

\DOE/NASA/0076-82/1
NASA CR-167975
SRD-81-097


Advanced AC Permanent Magnet Axial Flux Disc Motor for Electric Passenger Vehicle

Gerald B. Kliman
Corporate Research and Development
General Electric Company

October 1982

Prepared for
NATIONAL AERONAUTICS AND SPACE ADMINISTRATION
Lewis Research Center
Under Contract DEN 3-76

for
**U.S. DEPARTMENT OF ENERGY
Conservation and Renewable Energy
Office of Vehicle and Engine R&D**



NOTICE

This report was prepared to document work sponsored by the United States Government. Neither the United States nor its agent, the United States Department of Energy, nor any Federal employees, nor any of their contractors, subcontractors or their employees, makes any warranty, express or implied, or assumes any legal liability or responsibility for the accuracy, completeness, or usefulness of any information, apparatus, product, or process disclosed, or represents that its use would not infringe privately owned rights.

**U.S. AIR FORCE
VAFB TECHNICAL LIBRARY**

DOE/NASA/0076-82/1
NASA CR-167975
SRD-81-097

Advanced AC Permanent Magnet Axial Flux Disc Motor for Electric Passenger Vehicle

Gerald B. Kliman
Power Electronics Laboratory
Corporate Research and Development
General Electric Company
Schenectady, New York 12345

October 1982

Prepared for
National Aeronautics and Space Administration
Lewis Research Center
Cleveland, Ohio 44135
Under Contract DEN 3-76

for
U.S. DEPARTMENT OF ENERGY
Conservation and Renewable Energy
Office of Vehicle and Engine R&D
Washington, D.C. 20585

Under Interagency Agreement DE-AI01-77CS51044

Page intentionally left blank

Page intentionally left blank

FOREWORD

This final report, "Advanced AC Permanent Magnet Axial Flux Disc Motor for Electric Passenger Vehicle," was prepared for the National Aeronautics and Space Administration Lewis Research Center for the Department of Energy by Corporate Research and Development of the General Electric Company in Schenectady, New York. Mr. B.R. Hatvani of the Lewis Research Center was the Project Manager for the program.

ACKNOWLEDGEMENT

Many people contributed their talents and hard work to this project. Foremost among them must be Eric Whitely of the Canadian General Electric Company, who, pioneered the idea of the disc motor for many years before it became a reality. Working with Eric Whitely through many of the early days was Martin Van Duyn, who innovated the solutions to many of the mechanical and assembly problems of the early dc motors. Eric and Martin also designed and built the Proof-of-Principle motor stators.

The remainder of the Phase I(A) electromagnetic and stator design effort was led by Vern Honsinger. Roger Johnson designed and built the rotor and attended to other mechanical engineering tasks. Russ Tompkins saw to the procurement, fabrication, and charging of the rotor magnets. The modification of the load-commutated inverter and activation of the control systems for this experiment was carried out by Tom Nordahl. The building and assembly of the test stands and data systems, as well as much of the testing, was done by William Mischler.

In the system and electronics area, Al Plunkett was prominent in the conception of this project and in the implementation of the control. Mike Boyle contributed to the computer reprogramming and making the system work. Gene Johnson built and modified the breadboard inverter packages and provided the documentation.

The machine shops under Ed Stoodley and Ed Matthews and the winding shops under Joe Cammarere were key contributors to the project. Dan Evans contributed at all stages of the assembly and testing of the motors.

The Phase I(B) effort saw some changes in key personnel, Russ Oney took charge of the electromagnetic and stator design effort, Owen Fraking wound the stators, and Bill Mischler took over all aspects of the inverter, control, and testing.

Bob Hatvani, while functioning in his principal role as Project Manager for NASA, also contributed directly to the work and must share the credit.

Finally, and not the least, thanks to Tom Mangano of the Graphics Department for editing and assembly of this Final Report.

Gerald B. Kliman
Principal Investigator

EXECUTIVE SUMMARY

This program covers the design, development, and performance evaluation of an advanced ac permanent magnet axial flux disc motor for electric passenger vehicle propulsion. It was undertaken to support the Electric Vehicle Program of the Department of Energy (DOE) and NASA Lewis Research Center in an effort to reduce the dependency of the USA on petroleum in the transportation system.

The principal objective of this work was to establish the feasibility of the axial flux permanent magnet disc motor with load-commutated inverter as a candidate for an electric passenger vehicle drive system component. Subsidiary goals were to attempt the application of the then newly emerging Manganese-Aluminum-Carbon magnets to reduce costs and to attempt the implementation of amorphous metals to reduce iron losses and improve efficiency.

Several different forms of disc motor are possible. A concept selection study was made which resulted in the recommendation of a single rotating disc machine. The magnets were to be contained in the rotor with a stator winding cast into the frames on each side of the rotor. A low stress, limited performance, low risk version of this motor was built and tested to demonstrate the principle of the method and to generate basic design data. This motor became known as the Proof-of-Principle (POP) motor.

Upon the successful testing of the POP motor, a detailed analysis of the performance requirements was made. Then, utilizing the test experience of the POP motor, a full performance, fully stressed motor was designed, built, and tested. This was known as the Functional Model (FM) motor. Due to delays in the commercial development of Manganese-Aluminum-Carbon magnets, a special Alnico 8 was supplied to simulate it. Silicon steel was substituted for amorphous iron in order to save development costs when it was discovered that core losses were a minor problem.

Both motors (FM and POP) were tested by generating into a resistance load (dynamic brake), open loop motoring on sine wave at low power, and motoring at maximum power on a load-commutated inverter. The inverter had been developed for another project and was modified for these tests.

Preliminary design studies were made for an "Engineering Model" with recommendation for correcting the deficiencies noted in the testing of the functional model. The functional model did not perform as well as required primarily due to the inadequacy of the magnets and secondarily to problems in the windings. Subsequently, the contract was extended to redesign the FM motor to correct its problems. The redesigned motor became known as FM(B) and the original motor as FM(A). FM(B) exceeded the performance requirements of the contract.

The principal changes made in the design were using rare earth (CoSm) magnets and a single layer chain winding. Other design innovations and improvements were made to improve electromagnetic performance, heat transfer, and mechanical performance. New approaches to fabrication of the magnets, the stator winding, and the heat transfer systems were developed for the FM(B).

An important issue in this high-speed machine was windage losses. Hence, a careful experiment was designed, built, and successfully run to evaluate windage losses in the proposed structure.

The FM(B) motor was tested in a manner similar to that for the FM(A). Peak efficiency on inverter drive was measured and found to be almost 93% in the mid-

speed range. Mechanical stability and balance were excellent. Finally, recommendations for improved efficiency in the Engineering Model were proposed to complement the previous design study.

OVERALL SUMMARY

This volume contains two separate reports. The first is complete and deals with Phase I of NASA/Lewis Contract DEN 3-76 "Advanced Electric Vehicle Motor Development." Two operating motors were built in this phase. The first, known as the Proof-of-Principle (POP) motor, was a limited performance, low stress machine without cooling that was built to generate basic data. The second motor, known as the Functional Model (FM), was to be a full performance, fully stressed motor meeting all the requirements of the contract. This did not turn out to be the case, resulting in an extension of the contract to redesign the FM motor to bring its performance up to a satisfactory level. This work, which was eminently successful, is the subject of the second report in this volume. The second report depends for its completeness on elements of the first part which are not repeated. In the usage of these reports, the original Phase I became known as Phase I(A) and the extension became known as Phase I(B), corresponding also to the first and second parts of this volume. In like manner, the functional model motors become known as FM(A) and FM(B).

TABLE OF CONTENTS

Part I — Phase 1(A)

Section	Page
1.0 INTRODUCTION	1-1
2.0 MOTOR CONCEPT	2-1
2.0.1 Description	2-1
2.0.2 Concept Development	2-1
2.0.3 Alternative Constructions	2-4
2.0.3.1 Flux Shunts	2-4
2.0.3.2 Rotor	2-7
2.0.3.3 Stator	2-7
2.0.4 Technology Development and Associated Risks	2-8
2.0.4.1 Performance	2-8
2.0.4.2 Materials	2-9
2.0.5 Summary	2-9
2.1 Mechanical Design	2-10
2.1.1 Alternatives	2-10
2.1.2 Rotor Design	2-11
2.1.3 Rotating Flux Shunts	2-13
2.1.4 Stator Winding	2-13
2.1.5 Stator Casing	2-14
2.1.6 Assembly	2-15
2.1.7 Summary	2-15
3.0 THE PROOF-OF-PRINCIPLE MOTOR	3-1
3.1 Concept Selection	3-1
3.2 Performance Prediction of the Proof-of-Principle Motor	3-1
3.3 Areas of Concern	3-10
3.4 Mechanical Design	3-10
3.4.1 Overview	3-10
3.4.2 Basic Data of the Mechanical Design	3-10
3.4.2.1 Requirements	3-10
3.4.2.2 Materials Application	3-10
3.4.2.3 Stresses	3-12
3.4.2.4 Rotor Weight	3-12
3.4.2.5 Catalog Components	3-12
3.4.2.6 Assembly Drawing	3-12
3.5 Mechanical Design Analysis	3-12
3.6 Rotor Windage Loss	3-13
3.7 Proof-of-Principle Motor Assembly	3-13
3.8 Sine Wave Testing	3-16
4.0 FUNCTIONAL MODEL OF DISK MOTOR: DETERMINATION OF MOTOR RATING, SIZE, AND WEIGHT; PREDICTION OF PARAMETERS	4-1
4.1 General Considerations	4-1

TABLE OF CONTENTS (Cont'd)

Section	Page
4.0 FUNCTIONAL MODEL OF DISK MOTOR: DETERMINATION OF MOTOR RATING, SIZE, AND WEIGHT; PREDICTION OF PARAMETERS (Cont'd)	
4.1.1 Summary of the Specifications from the Contract	4-1
4.1.2 Extra-Contractual Assumptions	4-2
4.2 Road Resistance	4-2
4.3 Motor Requirements	4-2
4.4 J227 Cycle Requirements	4-2
4.5 Voltage — Frequency Break Point	4-2
4.5.1 Chopper-Inverter Operation	4-4
4.6 Prediction of Parameters and Performance of the Functional Disc Motor	4-5
4.6.1 Magnet Permeability: Effect on Performance	4-7
4.6.2 Effect of Boundaries on Inductance	4-10
4.6.3 Prediction of Parameters and Design Quantities	4-11
4.6.4 Prediction of Performance	4-11
4.6.5 Thermal Performance	4-16
4.7 Design Description	4-18
4.8 Mechanical Design	4-21
4.9 Magnetization in Place	4-25
5.0 TESTING OF THE PROOF-OF-PRINCIPLE AND THE FUNCTIONAL MODEL MOTORS	5-1
5.1 Summary	5-1
5.2 Introduction	5-1
5.3 Description of Motors Tested	5-2
5.4 Coil Voltages and Inductances	5-3
5.5 Performance Summary	5-5
5.6 SFM Machine Open Circuit and Generating Data	5-7
5.7 Load-Commutated Inverter Rating of a Synchronous Motor	5-10
5.8 Load-Commutated Inverter Tests	5-14
5.9 Conclusion	5-18
6.0 TEST SUPPORT EQUIPMENT FOR THE DISC MOTORS	6-1
6.1 Introduction	6-1
6.2 First Floor Test Facility	6-1
6.3 The Fourth-Floor Test Facility	6-2
6.4 Load-Commutated Inverter and Control	6-4
6.5 Inverter Schematic Diagrams	6-6
7.0 ENGINEERING MODEL PRELIMINARY DESIGN	7-1
7.1 Introduction	7-1
7.2 Electromagnetic Design	7-1
7.2.1 Motor Concepts	7-1
7.2.2 MnAlC, 30 cm Designs	7-1

TABLE OF CONTENTS (Cont'd)

Section	Page
7.0 ENGINEERING MODEL PRELIMINARY DESIGN (Cont'd)	
7.2.3 Rare Earth, 30 cm Designs	7-2
7.2.4 Rare Earth, 21.5 cm Designs	7-2
7.2.5 Engineering Model Design Applications	7-2
7.3 Mechanical Design	7-2
7.3.1 MnAlC, 30 cm Design	7-2
7.3.2 CoSm, 21.5 cm Design	7-2
7.4 Conclusions	7-3

Part II — Phase 1(B)

Section	Page
8.0 INTRODUCTION	8-1
8.1 Background	8-1
8.2 Problems of the Phase I(A) Motor	8-1
9.0 ELECTROMAGNETIC DESIGN	9-1
9.1 Performance Predictions	9-1
9.2 Temperature Prediction	9-4
9.3 Magnet Size	9-4
9.4 Winding Concept	9-10
10.0 STATOR FABRICATION	10-1
10.1 Winding	10-1
10.2 Heat Removal Devices	10-1
10.3 Frame, Carrier Plate, Yoke, and Wedges	10-2
10.4 Connections and Leads	10-4
10.5 Insulation and Potting	10-6
11.0 ROTOR DESIGN AND FABRICATION	11-1
11.1 Rotor Concept	11-1
11.2 Rotor Stresses	11-2
11.3 Magnet Concept and Activation	11-2
11.4 Rotor Balancing	11-3
12.0 WINDAGE TEST	12-1
12.1 Design and Fabrication	12-1
12.2 Test Results	12-1
13.0 PERFORMANCE TEST	13-1
13.1 Test Setup and Apparatus	13-1
13.2 Accuracy and Precision	13-1
13.3 Open Circuit Tests	13-4
13.4 Generating Tests	13-7
13.5 Motoring Tests	13-11

TABLE OF CONTENTS (Cont'd)

Section	Page
14.0 CONCLUSIONS AND RECOMMENDATIONS	14-1
14.1 Conclusions	14-1
14.2 Recommendations	14-1
14.2.1 The Functional Model Motor	14-1
14.2.2 Engineering Model	14-3
Appendix A — MECHANICAL DESIGN ANALYSIS	A-1
Appendix B — PERFORMANCE REQUIREMENTS	B-1
Appendix C — CONTROL SYSTEM SCHEMATICS	C-1
Appendix D — MAJOR ASSEMBLY DRAWINGS	D-1

LIST OF ILLUSTRATIONS

Figure		Page
2-1	Novel Motor Concept	2-2
2-2	Six-Pole Rotor with Alternate Magnet Configurations	2-2
2-3	Motor Losses at 19.4 kW (26 hp) Output	2-5
2-4	Propulsion System Comparison Summary	2-6
2-5	(a) Stationary Iron, Double Disc Concept; (b) Rotating Iron, Single Disc Concept	2-6
2-6	Preliminary Design Disc Motor for Electric Car; Alternative I — Stationary Flux Return Yokes	2-10
2-7	Preliminary Design Disc Motor for Electric Car; Alternative II — Rotating Flux Return Yokes	2-11
2-8	Preliminary Design Disc Motor for Electric Car — Pole and Coil Layout	2-12
3-1	Proof-of-Principle Motor	3-2
3-2	Proof-of-Principle Motor — 5.2 kW (7 hp), 240 Hz; Predicted Effect of Voltage on Efficiency, Power Factor, and Amperes	3-4
3-3	Predicted Effect of External Reactance	3-5
3-4	Predicted Variation of No-Load Amperes with Voltage and External Reactance	3-6
3-5	Predicted Variation of Amperes with Voltage and Load	3-7
3-6	Three Cases of Efficiency and Current Versus Load	3-8
3-7	Torque Angle Characteristics — δ° Versus Amperes	3-9
3-8	Fully Assembled Proof-of-Principle Motor	3-13
3-9	Full-Scale Model of Proof-of-Principle Motor	3-14
3-10	Proof-of-Principle Rotor Hub After Balancing	3-14
3-11	Finished Proof-of-Principle Rotor	3-15
3-12	Proof-of-Principle Motor Components	3-15
3-13	Magnet Test Fixture	3-16
3-14	Measured Flux Densities on Magnet Surface	3-17
3-15	Open Circuit Voltage E_o (Line to Neutral) Versus Speed	3-17
3-16	Variation of No-Load Amperes with Voltage-External Reactance in Line; Disk Motor, 5.2 kW (7 hp), 240 Hz, 8 Pole	3-18
4-1	Torque-Speed Requirements Summary	4-3
4-2	Acceleration Schedule Options	4-3
4-3	Illustration of the “Corner Point” Concept	4-4

LIST OF ILLUSTRATIONS (Cont'd)

Figure		Page
4-4	Battery-Controller-Motor System	4-4
4-5	Fixed Battery Voltage V_b Together with a Linear Open-Circuit Voltage E_o with Respect to Frequency	4-6
4-6	Illustration of Voltage Control Principle	4-7
4-7	Magnet Concept — Functional Model Disc Motor	4-8
4-8	Comparison of CoSm, Alnico 8E with Mn-Al-C	4-8
4-9	Alnico 8E — Operating Point; 3-Layer Winding, $L_m = 5.08$ cm, No-Iron Powder, Functional Model $B_r = .6900$ T, $H_c = 263$ kA/m	4-9
4-10	Approximate Three-Dimensional Field of the Magnet Flux and the Form Factor	4-10
4-11	Functional Model of Disc Motor Operating at 11.2 kW (15 hp), 732 Hz with Variable Sinusoidal Voltage	4-14
4-12	Functional Model of Disc Motor Operating at 29.8 kW (40 hp), 466 Hz with Variable Sinusoidal Voltage	4-14
4-13	Open-Circuit Voltage	4-15
4-14	Functional Model of Disc Motor Operating at 11.2 kW (15 hp), 732 Hz but with E_o Successively Phased-Back	4-15
4-15	Commutation Limits at Various dc Link Voltages and Inverter Frequencies	4-16
4-16	Prediction of Temperature Rise	4-17
4-17	Maximum Coil Temperature of Disc Motor	4-17
4-18	Layout of the Functional Model Motor	4-18
4-19	Cross Section of the Functional Model Motor	4-19
4-20	Completely Assembled Functional Model Motor	4-19
4-21	Finished Rotor of the Functional Model Motor	4-20
4-22	Active Face of a Stator Side	4-20
4-23	Functional Model Rotor Hub with Shaft	4-22
4-24	Rim Loading Model	4-22
4-25	Magnetizing Circuit for Alnico 8 Motor Magnets	4-25
5-1	Performance Specification for the Application of the Functional Model Disc Motor to an Electric Vehicle	5-2
5-2	Structure of the AC Disc Machines Tested	5-3
5-3	Steady-State Temperature Rise of Stator Windings During Open Circuit Heat Runs on FM Machine	5-7
5-4	Series-Connected FM Machine Data	5-8

LIST OF ILLUSTRATIONS (Cont'd)

Figure		Page
5-5	Series-Connected FM Machine Data	5-9
5-6	Series-Connected FM Machine Data	5-9
5-7	Projected Efficiency of SFM Disc Motor while Operating Along Profile of Continuously Rated Load	5-11
5-8	Projected Steady-State Winding Temperature Rise while Operating Along Profile of Continuously Rated Load	5-12
5-9	Vector Diagram for a Smooth-Gap Synchronous Machine With a Leading Power Factor	5-13
5-10	Single-Sided POP Motor Data	5-15
5-11	Series-Connected Functional Disc Motor Data	5-16
5-12	Series-Connected Functional Disc Motor Data	5-16
5-13	Series-Connected Functional Disc Motor Data	5-17
5-14	Series-Connected Functional Disc Motor Data	5-17
6-1	Proof-of-Principle Motor Installed in First-Floor Test Facility	6-1
6-2	Fourth-Floor Test Facility	6-5
6-3	Control and Test Instrumentation	6-6
6-4	Sample Data Printout	6-7
6-5	Sample DPO Printout: (a) Motor Voltage Waveform, (b) Motor Current Waveform, (c) Motor Instantaneous Power Waveform	6-8
6-6	Sample Temperature Recorder Output	6-10
6-7	Load Commutated Inverter Breadboard	6-11
6-8	Printed Circuit Cards and Card Rack	6-11
6-9	Third Harmonic Commutator and Relays	6-12
6-10	EAI Analog and Digital Computer	6-12
7-1	Proposed Magnet Dimensions — Engineering Model Motor	7-3
7-2	Ten-Pole Magnet Geometry	7-4
7-3	AlMnC Magnet Characteristics	7-4
7-4	Effect of Air Gap Length on E_o and X_d	7-5
7-5	Open Circuit E_o and Reactance X_d Corresponding to a Magnet Length of 3.81 cm with a Varying Air Gap	7-6
7-6	Armature Reaction Effects as the Air Gap Varies	7-7
7-7	Effect of Air Gap on Machine Performance	7-7
7-8	Effect of Magnet Length on Machine Performance	7-8
7-9	Armature Reation Effects as the Magnet Length Varies	7-8

LIST OF ILLUSTRATIONS (Cont'd)

Figure		Page
7-10	Open Circuit Voltage E_o and Reactance X_d Corresponding to an Air Gap Length of 0.15 cm with Varying Magnet Length	7-9
7-11	Effect of Magnet Length on Machine Performance	7-10
7-12	Armature Reaction Effects as the magnet Length Varies	7-11
7-13	Open-Circuit Voltage E_o and Reactance X_d Corresponding to an Air Gap Length of 0.15 cm with Varying Magnet Length	7-12
7-14	Effect of Magnet Length on Machine Performance	7-13
7-15	Armature Reaction Effects as the Magnet Length Varies	7-14
7-16	Open Circuit Voltage E_o and Reactance X_d Corresponding to an Air Gap Length of 0.15 cm with Varying Magnet Length	7-15
9-1	Vector Diagram — Motoring	9-1
9-2	Computer Program — Phase I(B) Motor/Generator	9-3
9-3	Effect of Motor Inertia	9-8
9-4	Revised Performance Requirements	9-9
9-5	Simplified Thermal Circuit Phase I(B) Motor	9-9
10-1	Slot Layout — 2 Cables, 3 Turns	10-1
10-2	Electromagnetic Components	10-2
10-3	Stator Assembly Before Impregnation	10-3
10-4	Detail of Stator Assembly End Region	10-3
10-5	Internal Wiring Diagram	10-4
10-6	External Connection Diagram	10-5
10-7	Lead Entry Area	10-5
10-8	Lead Construction	10-6
11-1	Finished Rotor	11-1
11-2	Magnet Concept	11-3
11-3	Magnetization Handling Fixture	11-4
11-4	Magnet Flux Summary	11-4
11-5	Radial Flux Scan	11-5
11-6	Azimuthal Flux Scan	11-6
12-1	Windage Test Sample Run	12-2
12-2	Windage and Bearing Losses vs. Axial Clearance Gap for a 26.7 cm (10.5 Inch) Diameter \times 3.81 cm (1.5 Inch) Thick Rotor Rotating in a Housing with Grease-Lubricated Bearings	12-3

LIST OF ILLUSTRATIONS (Cont'd)

Figure		Page
13-1	Completed Motor in the Mounting/Safety/Ventilation Enclosure	13-1
13-2	Test Setup Showing Terminals, Vibration Instrumentation, and Digital Processing Oscilloscope Cart.	13-2
13-3	Open Circuit Voltage Measurement	13-3
13-4	Voltage Waveform — Generating, Low Speed	13-5
13-5	Voltage Spectrum — Generating, Low speed	13-5
13-6	Open Circuit Loss Measurement	13-6
13-7	Circulating Current Waveform — Low Speed, Open Circuit, Cable-to-Cable	13-7
13-8	Circulating Current Spectrum — Low Speed, Open Circuit, Cable-to-Cable	13-7
13-9	Generating Performance Test Points	13-8
13-10	Phase A Voltage — Generating at 7000 rpm, 18.5 kW	13-10
13-11	Phase A Current — Generating at 7000 rpm, 18.5 kW	13-10
13-12	Phase A Power — Generating at 7000 rpm, 18.5 kW	13-11
13-13	Phase A Voltage Spectrum — Generating at 7000 rpm, 18.5 kW	13-11
13-14	Phase A Current Spectrum — Generating at 7000 rpm, 18.5 kW	13-12
13-15	Motoring Performance Test Points	13-12
13-16	Phase A Voltage — Motoring at 11,000 rpm, 11.2 kW	13-16
13-17	Phase A Current — Motoring at 11,000 rpm, 11.2 kW	13-16
13-18	Phase A Power — Motoring at 11,000 rpm, 11.2 kW	13-17
13-19	Phase A Voltage — Motoring at 7000 rpm, 23.9 kW	13-17
13-20	Phase A Current — Motoring at 7000 rpm, 23.9 kW	13-18
13-21	Phase A Power — Motoring at 7000 rpm, 23.9 kW	13-18
13-22	Phase A Voltage Spectrum — Motoring at 7000 rpm, 23.9 kW	13-19
13-23	Phase A Current Spectrum — Motoring at 7000 rpm, 23.9 kW	13-19
13-24	Peak Efficiency Determination	13-20
A-1	Dynamic Tensile Stress in Aluminum Alloy Proof-of-Principle Rotor Rim Versus Rim Thickness at 5000 rpm	A-7

LIST OF TABLES

Table		Page
3-1	Proof-of-Principle Motor: Design Parameters	3-3
3-2	Technology “Barriers”	3-11
3-3	Pop Motor Parameters: 240 Hz Estimated and Measured	3-18
4-1	Magnet Comparison	4-9
4-2	Tests on Exploratory Machine	4-11
4-3	A Listing of Design Data and Predicted Parameters	4-12
4-4	Functional Model Motor Mechanical Design Basis	4-21
4-5	Functional Model Motor Rotor Assembly Summary	4-23
4-6	Functional Model Motor Design Summary	4-23
4-7	Functional Model Motor Rotor Performance Verification	4-24
4-8	Functional Model Safety	4-24
4-9	Functional Model Motor Windage and Cooling	4-25
4-10	Magnetization in Place of Alnico 8 Magnets Circuit Parameters	4-26
4-11	Magnetization in Place Potential Magnetizing Force	4-26
4-12	Alnico Magnets Depth of Penetration	4-27
5-1	Design Data for Pop and FM Disc Machines	5-4
5-2	Motor Coil Test Data	5-5
5-3	Approximate Air Gap Flux Densities of Tested Motors	5-6
5-4	Performance Summary for Pop and FM Disc Motors	5-6
5-5	Series-Connected FM Generator Data	5-10
5-6	Series-Connected Functional Model Generator Heat Run Data	5-11
5-7	Functional Model Motor Series-Connected FM Disc Motor Heat Run Data While Operating on the Load-Commutated Inverter	5-18
6-1	Three-Phase and Single-Phase Digital Instrument Panels	6-2
6-2	Analog Instruments	6-3
6-3	System 6 Instrumentation	6-4
7-1	Implications of Using a Single Layer Winding with a Slotted Iron Core ...	7-16
7-2	Engineering Model Motor Preliminary Mechanical Design.....	7-17
7-3	Engineering Model Motor Preliminary Mechanical Design.....	7-17
7-4	Engineering Model Motor Rotor Preliminary Mechanical Design	7-18
7-5	Engineering Model Motor Preliminary Mechanical Design.....	7-18
7-6	Engineering Model Motor Rotor Preliminary Mechanical Design	7-19

LIST OF TABLES (Cont'd)

Table		Page
8-1	Project Teams	8-1
8-2	Phase I(A) Motor Performance Summary	8-2
8-3	Phase I(A) Magnets	8-2
8-4	Magnet Comparison	8-2
8-5	Goals of the Electromagnetic Design	8-3
8-6	Phase I(A) Open Circuit Loss	8-3
8-7	Phase I(A) Winding Balance	8-4
8-8	Heat Transfer Measures	8-4
8-9	Phase I(A) Motor Mechanical Problems	8-5
8-10	Case and Mount Concept Improvements	8-5
8-11	Balance Concept	8-5
9-1	Phase I(B) Functional Model Motor Performance Prediction and Loss Breakdown	9-2
9-2	Motoring Performance on Load-Commutated Inverter	9-6
9-3	Generating Performance with Resistance Load	9-7
9-4	Required Performance Extra-Contractual Assumptions	9-8
10-1	Insulating Materials — Primary	10-7
10-2	Insulating Materials — Support	10-7
10-3	Insulating Materials — Epoxies	10-8
11-1	Vibration Summary	11-7
11-2	Test Stand Resonance	11-7
13-1	Mechanical Power Measurement Uncertainty Due to Least Count of Himmelstein Display at Full Load	13-3
13-2	Winding Balance	13-4
13-3	Magnet Temperature	13-6
13-4	Generating Tests with Resistance Load	13-9
13-5	Motoring Tests on Load-Commutated Inverter	13-15
13-6	Motoring Tests — 5500 rpm Runs — Load-Commutated Inverter	13-21
14-1	Performance Improvement Winding	14-1
14-2	Performance Improvement Case and Core	14-2
14-3	Performance Improvement System	14-2
14-4	Engineering Model Option Phase I(B) Design	14-3

LIST OF TABLES (Cont'd)

Table		Page
14-5	Engineering Model Option Modified Designs	14-4
14-6	Engineering Model Option	14-4
14-7	Engineering Model Option	14-5

PART I – PHASE 1 (A)

SUMMARY – PHASE I(A)

This part of the report stands alone as a complete report of the initial Phase I activities of NASA/Lewis contract DEN 3-76 "Advanced Electric Vehicle Motor Development." The principal objective of this work was to establish the feasibility of the axial flux permanent magnet disc motor with load-commutated inverter as a candidate for an electric vehicle drive. Subsidiary goals were to attempt the application of the newly emerging manganese-aluminum-carbon magnets to reduce costs, and to attempt the implementation of amorphous metals to increase efficiency.

The tasks undertaken to accomplish these objectives are described below and correspond to the divisions of the report.

1. Concept Selection—Several different forms of the axial flux disc motor are possible. The final form consists of a single rotor containing the magnets with a stator cast into the frame on each side.
2. A low stress, limited performance, low risk motor without cooling provisions was designed, built, and tested to demonstrate the principle of the method and to generate basic design data (the Proof-of-Principle motor).
3. Based on this work, a full performance, fully stressed motor was designed, built, and tested (Functional Model). Due to delays in the development of manganese-aluminum-carbon magnets, a special Alnico8 was supplied to simulate the material. Silicon Steel was substituted for amorphous metal when it was discovered that iron losses were a minor problem, and to save development costs.
4. The details of the test support equipment and the test history are included in the report.
5. Preliminary design studies for an "Engineering Model" motor form the last section of the report.

The Functional Model motor did not perform to specification primarily due to the inadequacy of the magnets and secondarily to problems in the windings. Subsequently, the contract was extended to redesign the motor to correct these problems. That work is the subject of the second part.

1.0 INTRODUCTION

This project started with an internal GE study of possible electric vehicle drives. The conclusions of that study were as follows:

1. For the near term, the conventional dc motor with a transistor chopper was the best prospect.
2. In the intermediate term, an induction motor with transistor inverter offered improvements in cost, weight, and efficiency.
3. For the far term, with considerably less knowledge and higher risk, an axial flux disc type permanent magnet motor with load-commutated SCR inverter might offer improvements beyond that of the induction motor drive.

At the time the dc motor-transistor chopper system was under development for the DOE electric test vehicle ETV-1. Subsequent to the internal study, NASA/Lewis Research Center and DOE requested proposals for advanced electric vehicle drives. The work reported here on the Advanced Electric Vehicle Motor was based on the far-term option described above. In parallel, the induction motor drive of the intermediate term option was undertaken in a second contract and is reported separately.

2.0 MOTOR CONCEPT

2.0.1 Description

The motor proposed for this study may be described, very generally, as an inside-out, permanent magnet, disc-type synchronous motor with air gap windings. A cross-section sketch of the motor concept is shown in Figure 2-1. The magnetic field is supplied by permanent magnets mounted in the rotor, as in Figure 2-2. The rotor is made of a nonmagnetic material. The stators are radial arrays of conductors, with appropriate end turns and connections, fixed in a nonmagnetic, insulating matrix. The wound stator discs are fixed to the frame. To provide a return path for the magnetic fluxes, iron plates are positioned outboard of the stator discs. If the iron plates (flux shunts) are affixed to the shaft instead of the frame, the magnetic flux in them will be steady, thus eliminating almost all core losses. Note that Figures 2-1 and 2-2 are purely for the purpose of illustrating the main concepts

In this motor concept, the objectives for the design of an electric vehicle motor may be achieved. Efficiency will be high over the entire operating cycle since there will be no excitation or slip loss and no iron core loss. Weight will be low since most of the heavy iron flux paths and the copper field windings have been eliminated. The frame may be a lightweight aluminum die-casting. Production cost will be low since the fabrication of the components should be relatively simple and done "in the open." For example, contrast the wire laydown and casting required with conventional methods of winding wires into the slots of a small bore stator. With the possible exception of the magnets, materials costs should also be low since high quality thin steel laminations and coil insulation may not be required. Commutating inductance should be low because of the absence of slots and because of the large air gap. The motor will also run at leading power factor. These properties allow the use of a relatively inexpensive lightweight load commutated inverter (LCI) utilizing commercially available semiconductors. The permanent magnet rotor can be built for higher speed operation than earlier dc disc motors with windings on the rotor, thus providing a further opportunity for weight reduction. Finally, since there are no commutator, slip rings, brushes, or exposed end windings, no maintenance (other than for the bearings) is required and reliability should be very high.

2.0.2 Concept Development

Most electric vehicles have been propelled by dc motors, as is to be expected in view of the dc (battery) power supply and the availability of relatively simple controllers: first the switched resistor and now the chopper. The dc motors used have, for the most part, been adaptations of commercial products. With increased attention now being given to the performance, range, and cost of electric vehicles, the propulsion system has come under increasing pressure to attain higher efficiency and reduced weight while at the same time delivering a high level of performance. And all of this is to be achieved at low cost.

In pursuing these goals, the first steps are to improve existing motors and to exploit traditional motor concepts.

The efficiency of a conventional dc motor may be improved in the usual way (within limits) by increasing weight with additional copper and iron. Improved steels may be used. The same may be done for ac motors. The ac motor will be lighter in weight and higher in efficiency at the same speed, mainly because of the absence of the dc motor commutator. The main field poles of the dc motor may be replaced with

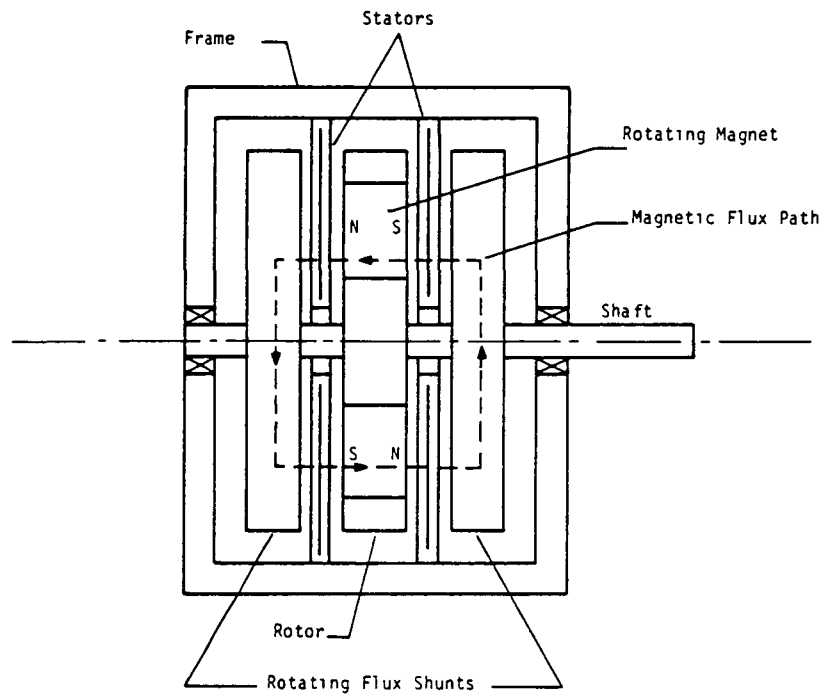


Figure 2-1. Novel Motor Concept (PM-synchronous-disc)

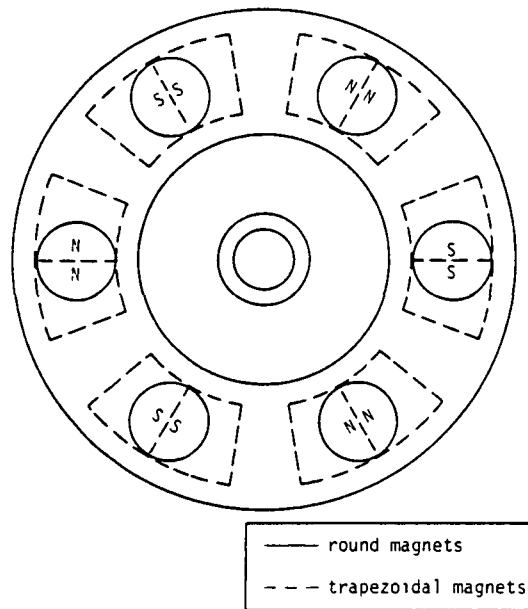


Figure 2-2. Six-Pole Rotor with Alternate Magnet Configurations

permanent magnets to eliminate excitation losses and to decrease weight. Interpoles will still usually be required, however. Further decrease in weight can only be achieved by increasing speed. Here again, the commutator is limiting. The rotor windings will also become a problem at high speeds.

The next step is to remove the commutator from the motor and replace it with an electronic switching system controlled by the position of the rotor. The windings may now be placed on the stator and the magnets placed on the rotor. The mechanical commutator, slip rings, and brushes are eliminated, and there are no windings on the rotor. Speed may now, in principle, be increased to the stress limits of the rotor in order to reduce size. This configuration is often referred to as an "electronically commutated motor" (ECM) or a "brushless dc motor," but is, in fact, a permanent magnet synchronous motor with feedback control. The stator resembles and is often identical to that of a conventional three-phase synchronous or induction motor. The magnets are variously arranged on the surface of the rotor or buried beneath the surface. Iron is required on the rotor to conduct magnetic flux from the magnets to the air gap and from pole to pole.

A permanent magnet synchronous motor may be optimized at a particular speed to achieve high efficiency. There are no excitation losses (slip losses in an induction motor), but copper losses, iron losses, and stray load losses remain. Iron losses are a particularly serious problem when the motor is applied in an adjustable speed drive. In wound field dc and ac motors and in the induction motor, the magnetic flux is reduced as the speed is increased. As a result, bulk iron losses remain in balance with the copper losses as speed and frequency increase. This is so because bulk iron losses vary (approximately) as the $3/2$ power of the frequency and as the square of the flux density. In the permanent magnet motor, however, the excitation is constant and independent of speed, and bulk iron losses will increase rapidly with increasing speed. For the electric vehicle drive, maximum efficiency may be high, but cycle efficiency will be low.

A partial solution to the problem may be in the use of very thin laminations to reduce eddy current losses. But this avenue is limited, and hysteresis losses may actually be increased. New materials such as amorphous metals may be used, but they will not be sufficiently developed for motors of conventional shape for some time. In addition to the bulk iron losses, there will also be comparable frequency-dependent losses because of the teeth in the stator and in the rotor iron. If a way of building motors without iron could be found, then high efficiency over a wide speed range in a lightweight motor would be achieved. The disc motor is a practical method of approaching this ideal.

The disc configuration removes the need for magnetic iron in the rotor to conduct the flux from pole to pole, as the flux is entirely axial, both in the air gap and in the magnets (Figure 2-1). Tooth ripple iron loss in the rotor is eliminated by removal of the iron, which also reduces the weight. Iron is still required at the ends of the motor to conduct flux from pole to pole azimuthally. If this iron is stationary, the flux in it will be ac and of relatively constant magnitude. However, the stator windings may be separated from the iron which is now fixed to the rotating shaft. The "stator yoke" is now rotating synchronously with the rotor magnets, and the iron flux is steady; hence there are no losses even if the iron is not laminated. The effect of an ironless motor has been achieved. Along the way, teeth and slots have also disappeared, eliminating losses due to leakage flux and ripple effects. The weight of the teeth is now also re-

moved. Additional thickness of the magnets is, however, required to drive the larger air gap.

The proposed motor concept (Figure 2-1) was developed as the result of an internal GE study of alternative drive systems. The objective of the study was to determine which motor/converter systems showed most promise for attaining the greatest electric vehicle range while remaining competitive in cost and meeting all other performance requirements. A principal result of the study was the conclusion that, if the motor was to be built in conventional form, the optimum system was a squirrel cage induction motor with a transistor inverter. But if a permanent magnet synchronous motor could be built without iron losses, it could be driven by a relatively simple SCR load commutated inverter to yield an even better system; that is, the inverter/motor combination ought to be lighter and more efficient.

The rationale for these conclusions may be seen in Figure 2-3, which shows a loss breakdown for a squirrel cage induction motor of conventional form. Note that for the induction motor as speed is increased, the iron core losses drop as a result of field weakening, and stator copper loss also decreases slightly. These decreases in loss are just overbalanced by a sharp increase in friction, windage, and stray load losses. Going to a permanent magnet synchronous motor would eliminate the rotor (slip) losses, improving efficiency at low speed. However, at high speed, iron core losses are drastically increased since there is no field weakening. If the iron and the iron core losses could be removed, a considerable gain in cycle efficiency would be achieved. The effect on system weight, efficiency, and range is shown in Figure 2-4 using the state-of-the-art dc motor/chopper propulsion system for a comparison and baseline. The ironless permanent magnet synchronous disc motor grew out of these considerations.

It was anticipated that the advanced permanent magnet synchronous disc motor will have roughly half the losses of a conventional PM synchronous motor yielding an efficiency between 94 and 96%. It will run with leading power factor for load commutation. The weight should be on the order of 45.4 kg (100 pounds).

2.0.3 Alternative Constructions

The preferred realization for highest efficiency of the motor has been described in Section 2.0.2. Uncertainties in the realization of the concept could lead to significant variations, and many of these uncertainties may not become evident until a motor is built and tested. Some of the more prominent problem areas and design variations are described below.

2.0.3.1 Flux Shunts

In the preferred concept, the flux shunts are simply solid iron discs affixed to the shaft. It may be necessary to affix the flux shunts to the stator, thus allowing ac flux in the iron, for two reasons. First, the inertia of the flux shunt discs could prove unacceptable in the electric vehicle drive. Second, it may be necessary to bond the cast stator to the flux shunt, which would provide a short heat transfer path for stator winding losses and make the thermal inertia of the iron discs more available to the stators. The necessity for such a change will depend on the effectiveness of the stator cooling and the strength of the stator matrix at elevated temperatures. Additional risks would, however, be incurred in making and maintaining good mechanical and thermal bonds. This form of the concept is shown in Figure 2-5a.

With the flux shunts stationary and carrying ac flux, core losses would again be present. These core losses can be reduced to a very low level, even at high frequen-

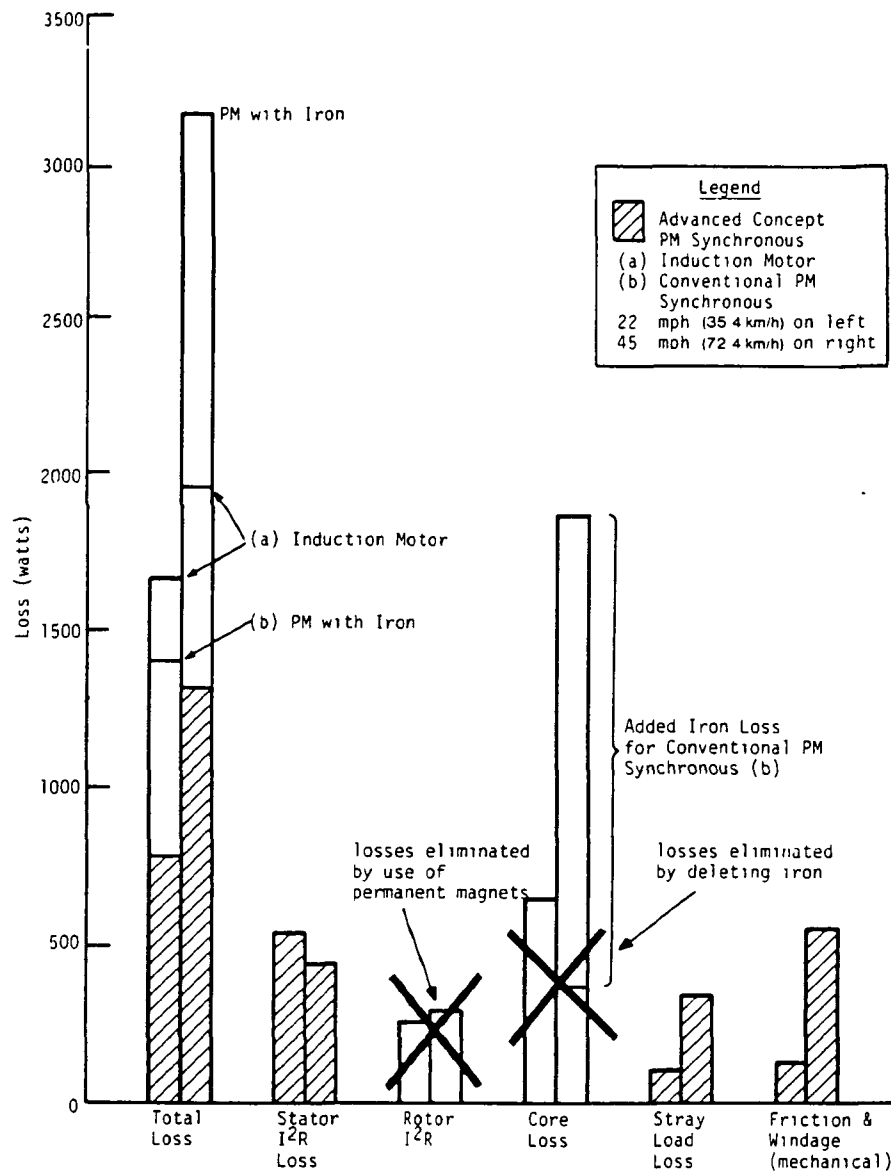


Figure 2-3. Motor Losses at 19.4 kW (26 hp) output

cies, by fabricating the disc as a spiral of amorphous metal tape. This form of magnetic material is very thin 0.0038 cm (~ 0.0015 inch) and has high resistivity and low hysteresis loss. It is now becoming available in widths suitable for this application and is supposed to eventually be comparable in cost to solid iron. The direction of the resultant lamination is correct for the direction of the fluxes. There will be about 172.4 kPa (25 psi) on the tape edges as a result of magnetic attraction, but this is easily overcome by friction between the layers due to the very high winding tensions used with this high strength material.

It may be desirable to use amorphous metal tape even for the rotating disc concept, as there will be leakage and stray fluxes from the stator windings flowing in it. There will also be considerable repetitive, high frequency transient fluxes due to inverter commutation.

It is desirable for the rotating flux shunt to be of great mechanical strength. It must be spun at the same speed as the rotor but will usually be of much higher densi-

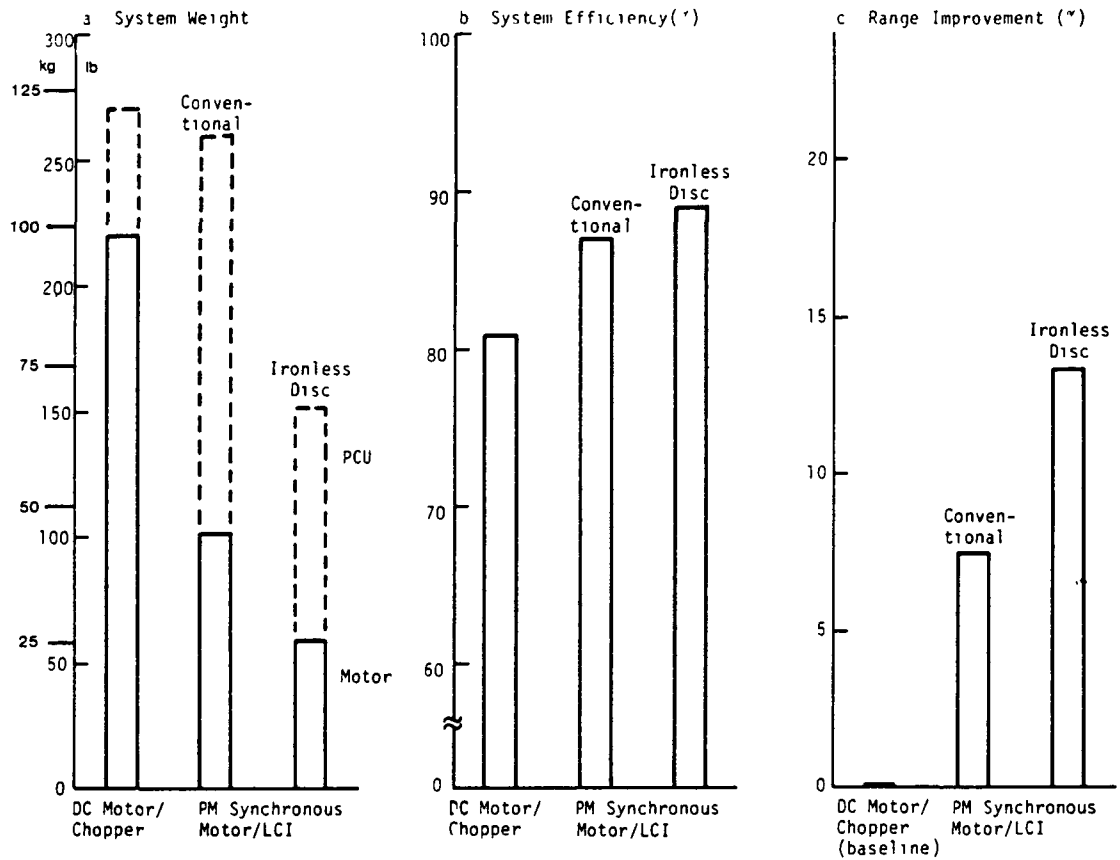


Figure 2-4. Propulsion System Comparison Summary

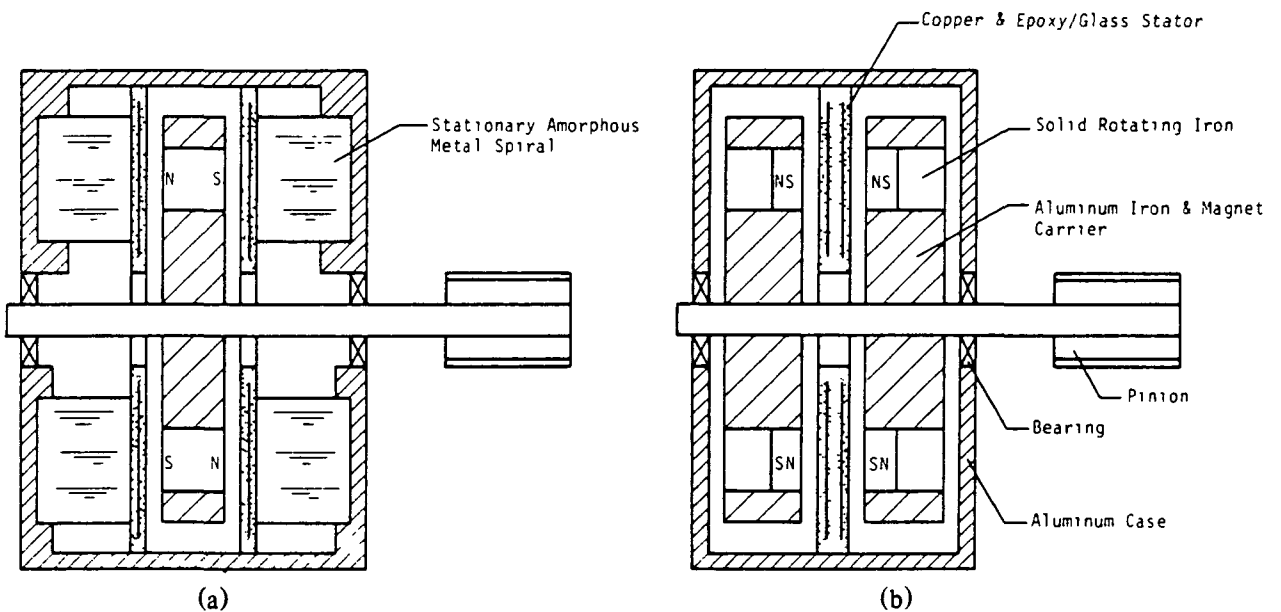


Figure 2-5. (a) Stationary Iron, Double Disc Concept; (b) Rotating Iron, Single Disc Concept

ty; hence, the stress levels will also be much higher than the rotor. In order to achieve the smallest motor, the speed should be as high as will be allowed by the centrifugal stresses and inverter limitations. At the same time, the flux shunt must have high magnetic permeability. The requirements of great strength and high permeability will usually conflict. Again, one exception is amorphous metal tapes.

Considerable uncertainty, however, is associated with the use of amorphous metal. This is a new material and much must be learned in the techniques of fabrication, effects of stresses, temperature, etc. Since core loss is already quite low compared to winding losses in this configuration, amorphous metal may be of marginal benefit.

The motor concept has been shown with two stator discs in order to realize the motor in the smallest outside diameter. If the heat transfer from the disc is sufficient, it may be possible to utilize a single disc within a reasonable outside diameter. This concept is shown in Figure 2-5b. Note that all of the magnetic iron is rotating with the magnets and therefore has a steady magnetic flux.

2.0.3.2 Rotor

There are a variety of permanent magnet materials now available for use in motors. New materials are currently under development. The choice, at this time, is between cobalt samarium, which is available and powerful but expensive, and a new alloy, manganese-aluminum-carbon now under development by Matsushita and others. Use of ferrites in this configuration will result in an unacceptably large motor.

The magnetic flux in the magnets and air gaps will be axial; thus, the capability of the motor may be increased by adding additional rotors and stators along the shaft. The flux will pass axially through each gap and magnet until it reaches the flux shunt. The flux in the shunt turns in the azimuthal direction and returns to the air gap under the next pole. The flux shunts are therefore required only at the ends of the stack of rotor and stator layers. In this way, the motor torque and power may be increased while decreasing the pounds per horsepower.

The rotor matrix may be either an insulator, such as the epoxy/glass laminates currently in use for flywheels, or a nonmagnetic conductor such as stainless steel or aluminum. A prime consideration is the strength of the materials required to withstand centrifugal and electromagnetic forces.

If the rotor is a conductor such as stainless steel, there will normally be no currents flowing in it, with the exception of the commutation interval. Such currents may be useful in reducing commutation inductance, but they will be a source of additional losses. Making the rotor entirely of aluminum or using aluminum cover sheets will give lower commutating inductance with low loss. The magnets will also be partially protected against demagnetization as a result of inverter shoot-through. A similar effect may be achieved by surrounding the magnets with aluminum sheaths.

Figure 2-2 shows the axially magnetized materials as trapezoidal or circular in shape. Many magnetic materials will be available only in the form of circular cylinders. It is clear that shaping the magnets to match the windings will yield a significant advantage in net flux per pole.

2.0.3.3 Stator

As noted in the preceding section, cooling of the stator windings will be difficult. Unlike conventional machines, the windings are not surrounded by iron but encased

in a thick epoxy or plastic matrix. The high thermal impedance and low heat capacity of such materials in thick layers will cause difficulty in cooling the windings. This will be especially so in maximum acceleration or in hill climbing, where a high power level will be sustained for considerable time. Several ways of removing heat are possible, including (1) directing an air flow radially over the surface of the disc, (2) extending the windings so that the end turns are close to the frame, (3) exposing the end turns directly to the air flow, (4) perforating the disc so that air can flow through it as well as over the surface, and (5) using rigid bar-type conductors only partially encased in the matrix for direct exposure to the air stream. Other more exotic means are possible.

Since the winding matrix is stationary, unlike the dc disc motor, there will be no centrifugal stresses. Forces due to the conductors reacting with the main magnetic fields and with each other will result in average stresses under 300 psi at full torque. Hence, even shoot-through stresses and high temperatures should not cause over-stressing of the stator matrix. There will then be considerable latitude in the selection of materials for castability, dielectric strength, convenience, and so on.

Multistranding of the stator conductors and, possibly, transposition are required. The windings are exposed to full air gap flux rather than just leakage flux, as in a conventional toothed iron motor. Eddy current and skin effect losses may then be greater than in a conventional motor. These losses can be largely eliminated by stranding and, if needed, by transposition.

2.0.4 Technology Development and Associated Risks

Most new motor designs are made in small, evolutionary steps from proven concepts, utilizing proven materials and proven production techniques. This is so, in part, because there is really no such thing as a motor breadboard. In large part, it is because motors are expected to perform reliably for many years (30 years, typically), suffering much abuse and still being low in cost. It is no surprise, then, that motor designers tend to be cautious and conservative.

In the case of the proposed motor, most of the forms, materials, and techniques are new. It is not possible to foresee all of the difficulties and problems that will arise in the pursuit of such a totally new design concept. Although many of the possibilities have already been discussed, it is worthwhile to reiterate some of the possible problem areas here.

2.0.4.1 Performance

The general equations for the behavior of permanent magnet synchronous motors can be set down in straightforward manner. The evaluation of the constants in those equations derived from the geometry and material properties must be carried out. Such evaluation always involves simplifying assumptions and approximations, the validity of which cannot be determined until a realistic model of the machine is built and tested.

The best cooling methods must be found, and the efficacy of these schemes and others must be predicted and tested. The heat transfer equation for such complex systems are often straightforward; however, the heat transfer coefficients are notoriously hard to compute. This is especially true for electrical insulation, laminations, and solid-to-gas interfaces.

Stray fluxes will give rise to additional heating, as well as influencing inductances, both in the active components and in the supports and frame.

2.0.4.2 Materials

The major structural material in the motor will be aluminum. There appear to be no serious problems in procuring or fabricating aluminum components of the required strength.

There are a variety of permanent magnet materials available in the current market. These range from low cost, low energy ceramic ferrites through the alnicos to the high energy, high cost cobalt-samariums. New materials are being developed that promise higher energies than the ferrites but at comparable cost. There is no problem in getting a magnet material that will work. However, materials under development will enable designs of smaller size and/or lower cost.

If the rotating iron option is used, the iron may be solid. Since the flux in the iron is dc, its loss properties are not of major interest. It should be strong, and this may affect the permeability. It is desirable to have a very high permeability to reduce dc leakage flux. Since steels will have relative permeabilities over 1000 even when hardened, this must be a minor consideration. Possibly more important are the losses induced in solid iron by space harmonics and leakage fluxes of the stator windings and inverter commutation transients. If these secondary effects prove to be a significant source of inefficiency, then lamination would be required as it is with stationary iron.

If it proves necessary to utilize stationary iron, then it must be laminated. Even with the best steels and thin laminations, there will be core losses reducing the efficiency. Fortunately, the recently developed noncrystalline metals have demonstrated greatly reduced losses compared with fine silicon steels, but at projected costs comparable to common iron. The normal form of this material is on the order of 0.005 cm (0.002-inch) thick, much thinner than any nonoriented steel available. This thickness and the very narrow widths [presently about 2.5 cm (1 inch) maximum] have prevented application of this new material to conventional electric motor construction so far. However, this form appears more natural for the proposed novel motor.

Glassy or noncrystalline metals (amorphous metals) are under intensive development at General Electric and elsewhere. At present they have significantly lower saturation flux densities than normal steels and much lower stacking factors. Both of these problems are the objects of much research with good prospects for improvement. These limitations would result in a requirement of at least 50% more material than would otherwise be required, with consequent increase in weight.

The remaining major area of concern is the fabrication of the stator. Problems of material selection, casting of large discs, windings, and producibility may be expected. Experience with the rotors of dc disc machines will be valuable here. There will probably be a period of experimentation to find the right winding and casting techniques.

Undoubtedly, there will be mechanical problems of construction assembly, disassembly, production, and so on, which will require much ingenuity in their solution.

2.0.5 Summary

There are several forms in which the ironless permanent magnet synchronous disc motor may be realized. The preferred form, for highest electromagnetic efficiency,

has flux-bearing iron portions rotating with the magnets. Mechanical considerations may force consideration of alternate forms, but techniques are available for reducing the effect on efficiency

2.1 MECHANICAL DESIGN

The design of the proposed permanent magnet synchronous disc motor may take one of many forms, depending on the final resolution of the design demands and constraints. For the purpose of discussing the many mechanical aspects of the proposed disc motor design, reference will be made to two alternatives. These designs are similar in many respects but Alternative I has a stationary flux return path (Figure 2-6) while Alternative II has a rotating yoke (Figure 2-7). In both cases the layout of the poles on the rotor and the shape of the winding is the same (Figure 2-8).

2.1.1 Alternatives

The design, shown in Figure 2-6, with the stationary winding is the preferred alternative from a mechanical design viewpoint. This design presents challenges to the electromagnetic engineer, but if these challenges can be met by selection of the newly developed amorphous or other low-loss metals or a somewhat reduced rotational speed, then this alternative offers many mechanical design advantages over Alternative II.

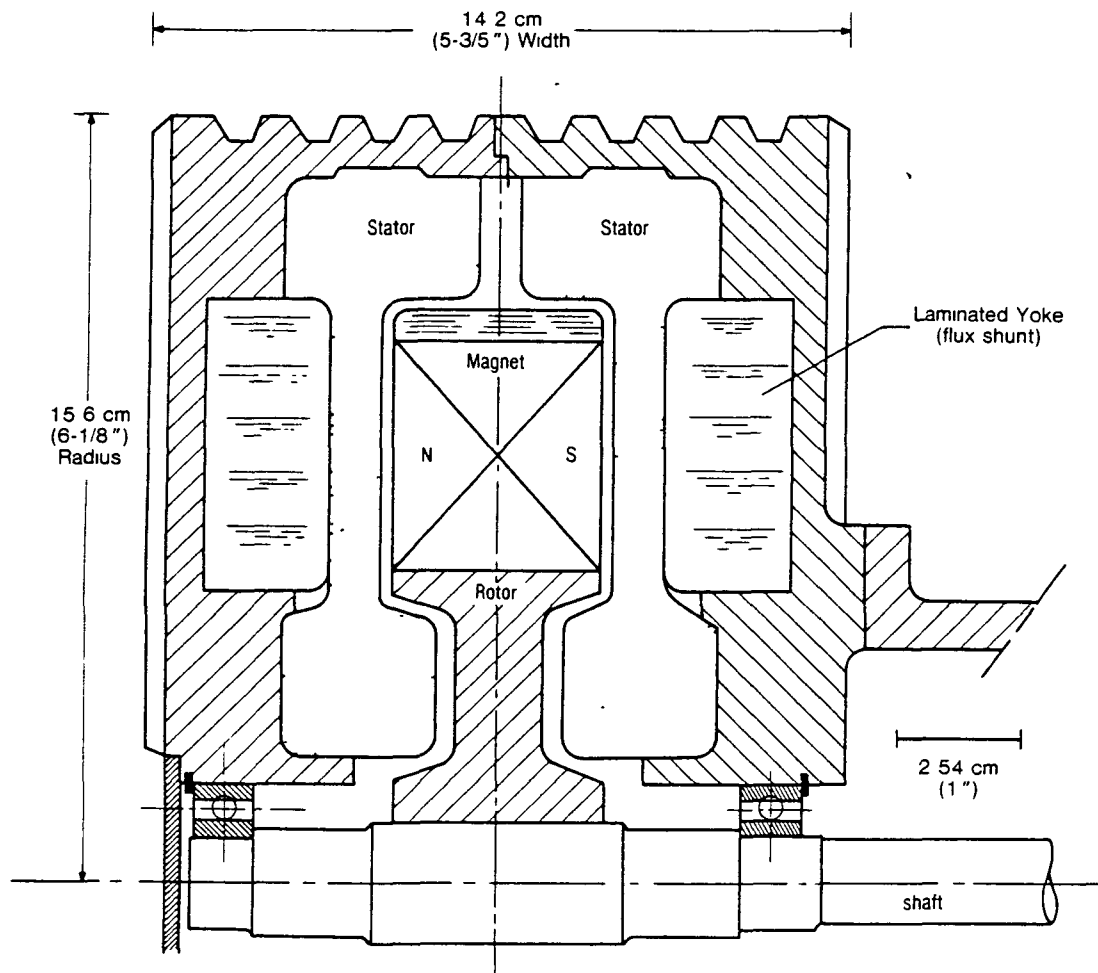


Figure 2-6. Preliminary Design Disc Motor for Electric Car; Alternative I – Stationary Flux Return Yokes

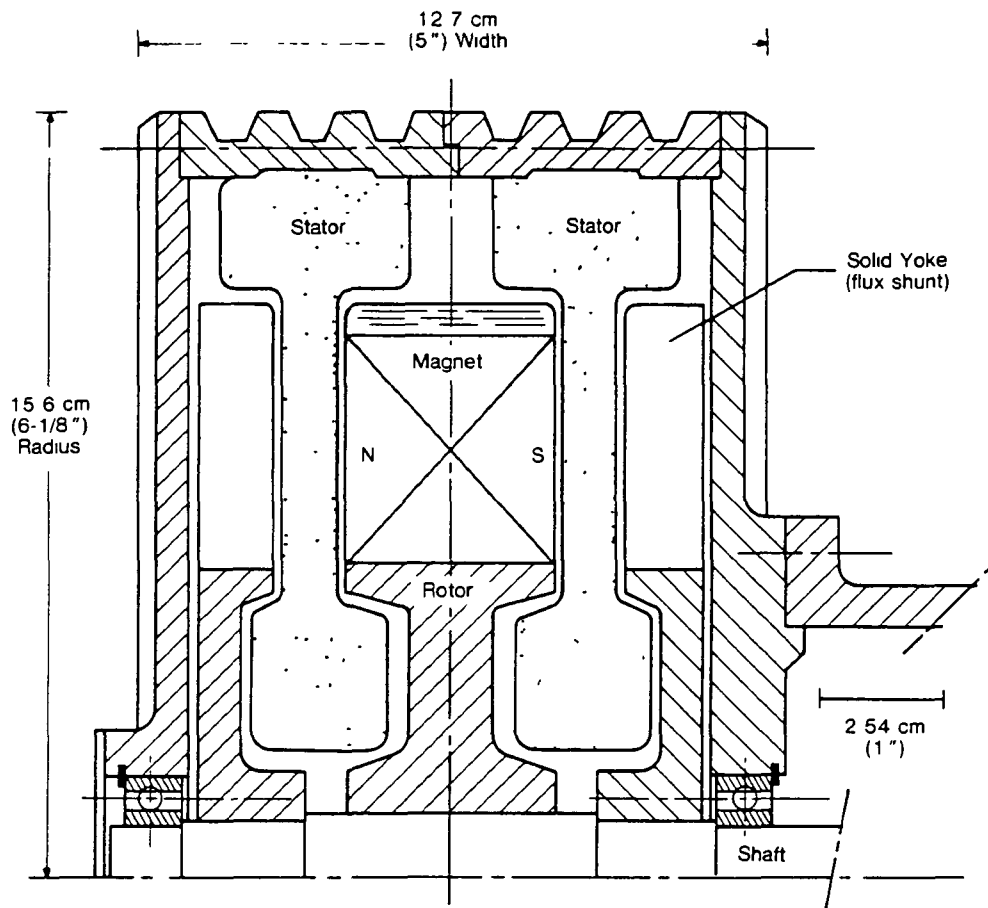


Figure 2-7. Preliminary Design Disc Motor for Electric Car; Alternative II – Rotating Flux Return Yokes

2.1.2 Rotor Design

A cross section of the rotor is shown as part of Figure 2-6. The rotor hub is made of an aluminum alloy for light weight and strength. This hub is pressed with an appropriate interference fit on a steel shaft. The shaft is supported on each side of the rotor to provide a good lateral stability when the motor is subjected to the maneuver loads inherent in the operation of a vehicle.

The aluminum hub has four radial spokes, integral with the hub, as may be deduced from the plan view in Figure 2-8. The configuration of four spokes coincides with the tentative selection of a 4-pole design, although alternatives will be investigated in any final design.

The spaces between the spokes form four pockets in which the magnets will be mounted. If a temporary ring is placed over the outside diameter of the spokes, four cavities will be formed between ring, spokes, and hub which make a very convenient jig for mounting the magnets, even in a magnetized state. Such a jig is necessary because of the strong repulsion resulting from the edge fluxes between individual magnets forming a pole.

In a 4-pole design, the pole face area of each pole is too large for the use of a single block of permanent magnet material as a result of processing limitations. Instead the present design proposes to build up each pole out of four identical blocks of a con-

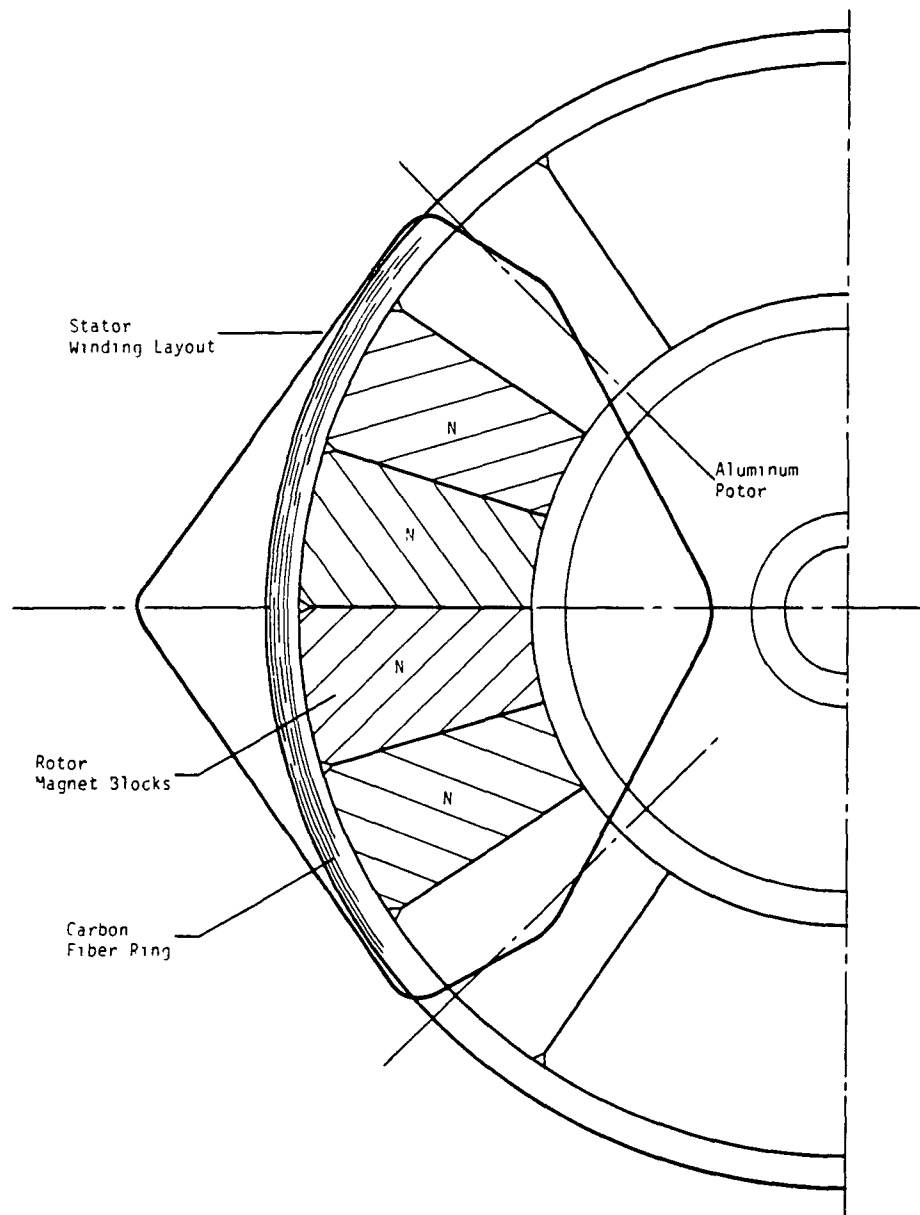


Figure 2-8. Preliminary Design Disc Motor for Electric Car – Pole and Coil Layout

venient shape as shown in Figure 2-8. In this manner a total of 16 blocks is required for the 4 poles of this motor. The magnets are mounted in the four cavities and cemented in place by means of a high strength, high temperature aerospace-type adhesive (such as some of the Hysol formulations). This procedure has already been used successfully in the dc disc motor designs with a conventional commutator mentioned earlier.

The design does not rely on any structural strength from the magnets. (In fact, careful design will ensure that the magnets will undergo very little stress.) Instead it is assumed that the entire centrifugal weight of the magnet blocks has to be carried by a retaining ring over the magnets and the hub spokes, which replaces the temporary ring. This retaining ring might be metallic, in the form of a suitable high strength

steel, or it may be a medium strength metallic band with a high strength, high modulus of elasticity composite material. An important goal here is the application of the newly developed graphite fibers which will be commercially available at low cost in the near future. The fibers may have an elasticity modulus of 2.2×10^{11} Pa (32 million psi), and a tensile strength of 2.8×10^9 Pa (400,000 psi). These fibers, already in use in aerospace applications, are now also being considered for automotive applications. The high modulus of elasticity makes these fibers more useful than the low modulus glass fibers in a design with metallic components.

In the conventional dc design with a commutator on the rotor, the I^2R heating and other losses occur in the rotor. Because of these losses, considerable design effort is required to obtain a satisfactory rotor. The location of the losses present a major barrier to transmitting the heating losses to the ambient air. Specifically three high transfer barriers have to be overcome for a totally enclosed conventional dc machine

- a. From rotor to internal air
- b. From internal air to casing
- c. From casing to external ambient air

In the proposed design, no significant heat is generated in the rotor, resulting in considerable improvement in the cooling capability for a given frame size. In fact, the rotor can only change its temperature in response to the changes in the internal air temperature. Hence the thermal response to a severe transient loading of the motor is very kind to the rotor. This should be very beneficial in the detail design for structural integrity of the rotor in the short and long term. With the proposed design it should be feasible to obtain mechanical speeds of up to 15,000 rpm. The introduction of aluminum in the interpolar space by means of the hub spokes is regarded as beneficial to commutation by the electromagnetic engineer.

2.1.3 Rotating Flux Shunts

In Alternative I the magnet carrier is the only rotating part. In Alternative II there are two additional rotating parts in the form of the magnetic flux return paths. (See Figure 2-7). Each of these additional rotors consists of an aluminum alloy hub pressed on the shaft and a magnetic steel ring shrunk into the hub. The flux shunt may be either a solid steel ring or a wound amorphous or other low-loss metal tape. The latter is feasible because of the inherent high strength of 1.4×10^7 Pa (200,000 psi) of this material and the possibility of winding the tape under tension on the hub.

2.1.4 Stator Winding

In both Alternatives I and II the stator winding is stationary. In Alternative I the winding is bonded directly to the stator casing and the flux shunt ring, which results in intimate contact over a very large area between the winding and the stator housing. Since the coil is the major source of heat-producing motor loss, there is a good heat conducting path from the winding to the casing and hence to the ambient air.

In Alternative II this direct contact is limited to the outside diameter of the winding, and it may be more challenging to the total heat transfer capability than in Alternative I.

In either case there will be excellent radial thermal conduction along the coil so that heat at the inner diameter is readily conducted to the outside diameter. However, there is an additional heat transfer consideration which speaks strongly in favor of

Alternative I. In this design the coil and housing behave more readily as a single thermal mass, which means that in situations in which there is high thermal loading of the winding, as is the case during acceleration or regenerative braking, heat can readily be stored in the larger thermal mass, to be dissipated at a longer time constant during the cruise portion of the cycle. Therefore, the danger of overheating the winding in a severe transient due to high thermal loading is much less in Alternative I than in Alternative II.

This situation has been clearly demonstrated in the conventional disc motor with rotating coils and a commutator. In that machine, the thermal time constant of the rotor is only a small fraction of the time constant of the casing; e.g., one could overheat the winding during an overload without any immediate evidence or warning in terms of the casing temperature.

In Alternative I, it appears that the motor may be run without the need for supplying internal cooling air. In Alternative II, it remains to be determined whether adequate cooling can be obtained without passing an external flow of filtered air through the casing. The latter might represent some complication of the more desirable situation of a totally enclosed motor without ventilation, as seems feasible in Alternative I.

In Alternative I, it is planned to deposit the wound form in the cavity presented by the die cast half stator shell. In fact the half shell may be thought of as one half of a mold for encapsulating the winding. Next a matching mold-half encloses the other side of the winding. This mold is evacuated and subsequently the coil is encapsulated in a suitable epoxy resin. It should be noted that the coil, after hardening of the epoxy, is fully locked into the stator shell by means of the peripheral groove at the outside diameter. Additional means of providing mechanical locking actions can be provided. These integral locks are a useful addition to the chemical bonding action.

2.1.5 Stator Casing

The stator casings for both alternatives will be made from aluminum die castings when in production. They would seem suitable candidates for the low pressure die casting process. Cooling ribs may be cast integrally with the casing in order to enhance the cooling capacity to the ambient. These ribs may run in a peripheral direction as shown on the cylindrical portion of the casing in Figures 2-6 and 2-7, or they may be run radially as indicated on the flat shell portions. The most suitable directions of the cooling ribs will in part be determined by the convenience of the die casting mold release action. For example, radial ribs on the flat plate might be combined with axially oriented ribs on the cylindrical portion.

A preliminary thermal analysis indicates that, especially in Alternative I, adequate cooling may be obtained if the relative air speed of the car in motion is utilized in part by ducting via an intake of some outside air over the housing. This would conveniently dissipate the excess heat accumulated during the thermally heavily loaded acceleration-deceleration periods.

In Alternative I the stator consists simply of two half-shells that meet on a rabbet on the centerline split. Furthermore, the magnetic attraction is likely to be sufficiently large between the two casing halves so that no axial bolting is required. Just a single tangential positioning lock should be provided to ensure correct installation of the shells with respect to the winding and individual coil positions.

It should be noted that for Alternative II axial bolting is required because the at-

traction magnetic forces act on the rotating flux shunts and the forces are transmitted through the center portion of the shaft.

2.1.6 Assembly

The assembly of the Alternative I configuration is straightforward. Special attention is required however in the case of Alternative II. As may be seen in Figure 2.1-2 the assembly feasibility requires that the cylindrical portion of the casing be split not only in the center but also at the cover plates. The coils are placed on each side of the magnet-carrying rotor. Then the rotating yokes are pressed on the shaft ends and finally the end covers with bearings are installed. For this alternative, provision should be made on the hubs of the flux shunt rotors to allow a pulling device to be attached to draw these rotors off the shaft if servicing is required. This procedure of assembly and disassembly is feasible, but again it emphasizes the relative simplicity of Alternative I.

2.1.7 Summary

Construction of a permanent magnet synchronous disc motor in both of the proposed forms appears to be feasible, economical, and adaptable to commonly used production techniques. Both designs will result in good structural integrity and adequate cooling of the stator. Alternative I is, from the mechanical point of view, much simpler in these respects. If the iron core losses can be reduced adequately by the use of amorphous metals or by choice of the operating parameters, Alternative I may be preferred.

3.0 THE PROOF-OF-PRINCIPLE MOTOR

3.1 CONCEPT SELECTION

Several alternatives for the design of an ac disc motor were discussed in Section 2. The concept selected for development was that of Figure 2-5a (or Figure 2-6) for the following reasons:

1. While core losses in the rotating yokes would be zero (or nearly so), windage losses would be virtually doubled due to the large number of rotating surfaces. It was felt from preliminary calculations that this windage loss addition would be greater than the core loss subtracted.
2. Removal of heat from the windings would be extremely difficult in all concepts except that of Figure 2-5a.
3. The mechanical problems of building and supporting the winding would be extremely difficult in all concepts except that of Figure 2-5a.
4. The rotating yokes would add a great deal of inertia to the system. This may be desirable in some cases, but was felt to be a disadvantage for an electric vehicle drive.
5. The rotating yoke structure could be very complex to assemble, requiring shaft clamps and partial assemblies.

In order to shorten the construction cycle of the proof-of-principle motor the stator windings were built according to a previously developed concept for a dc disc motor.

The proof-of-principle motor had no cooling system and ran at low speed.

3.2 PERFORMANCE PREDICTION OF THE PROOF-OF-PRINCIPLE MOTOR

Performance prediction is based on a computer program which is a modification of an existing proprietary program for conventional permanent magnet motors. The performance prediction applies to a double-sided, slotless disc motor with permanent magnet excitation. The magnets are of the cobalt-samarium type, having a remanent flux density B_r of about 0.8 T and a coercive force of about 64 kA/m (8000 oersted). Four of these magnets are stacked together; the final stacked magnet characteristic was devaluated by 10% to account for the aspect ratio and manufacturing variation. An assembly drawing of the motor is shown in Figure 3-1.

The design parameters are given in Table 3-1, together with the predicted values for motor resistances, reactances, and open-circuit voltage. The motor performance is predicted from these parameters using a sine wave power supply at 240 Hz (3600 rpm).

The proof-of-principle motor is rated at 110 volts. An external reactance of about 0.25 ohm is inserted in each of the three phase lines to enhance motor stability when operating open-loop or without inverter control of torque angle and motor current.

The motor is extremely sensitive to voltage. Since the reactance x_d is estimated to be very small (0.08 ohm), the *no-load current* can change radically with a lack of voltage balance (defined here as $V \simeq E_o$). Large, no-load currents are also alleviated by the use of external reactors.

Predicted performance of the proof-of-principle motor is shown in Figures 3-2 through 3-7 under various conditions.

Table 3-1
PROOF-OF-PRINCIPLE MOTOR: DESIGN PARAMETERS

General

rating (kW)	5.2 (7 hp)
rpm	3600
line voltage (rms)	110
amperes (rms)	32.4
frequency (Hz)	240
number of poles	8
class insulation	H
open circuit voltage (line-rms)	114

Stator Winding

strands per conductor	9
wire (strand) size AWG	26
turns/coil/phase	25
number parallel circuits	8
turns/phase, N_1	50
effective turns/phase, $N_1 k_w$	46.3
total gross conductor area (cm ²)	0.093
current density J_a (A/cm ²)	348
surface density K_a (A/cm)	339

Motor Parameters (ohms)

(Estimated at 240 Hz)

stator resistance, r_1	0.04
direct axis reactance, x_d	0.08
quadrature axis reactance, x_q	0.08
leakage reactance, x_l	0.02
subtransient reactance, $x_d'' = x_q''$	0.05
commutating reactance, x_c	0.05

Lengths (cm)

one air gap \times Carter factor	1.3
air gap area/pole (both sides) (cm ²)	75.2
pole pitch	7.17
magnet thickness, L_m	5.08
magnet area, (cm ²)	23.4
magnet OD, D_o	23.5
magnet ID, D_i	13.0
magnet av. dia $D_r = (D_o + D_i)/2$	18.25
stack length $k_s = (D_o - D_i)/2$	5.25
conductor effective length, l_s	5.25
active stator surface area (both sides) (cm ²)	602
$2(\pi D_r l_s) = 2(\pi/4)(D_o^2 - D_i^2)$	

Weights (kg)

stator assemblies (both sides) (52 lb)	23.6
rotor (32.5 lb)	14.7
spacer, bolts, caps, etc (7.0 lb)	3.2
Total (92.5 lb)	41.5

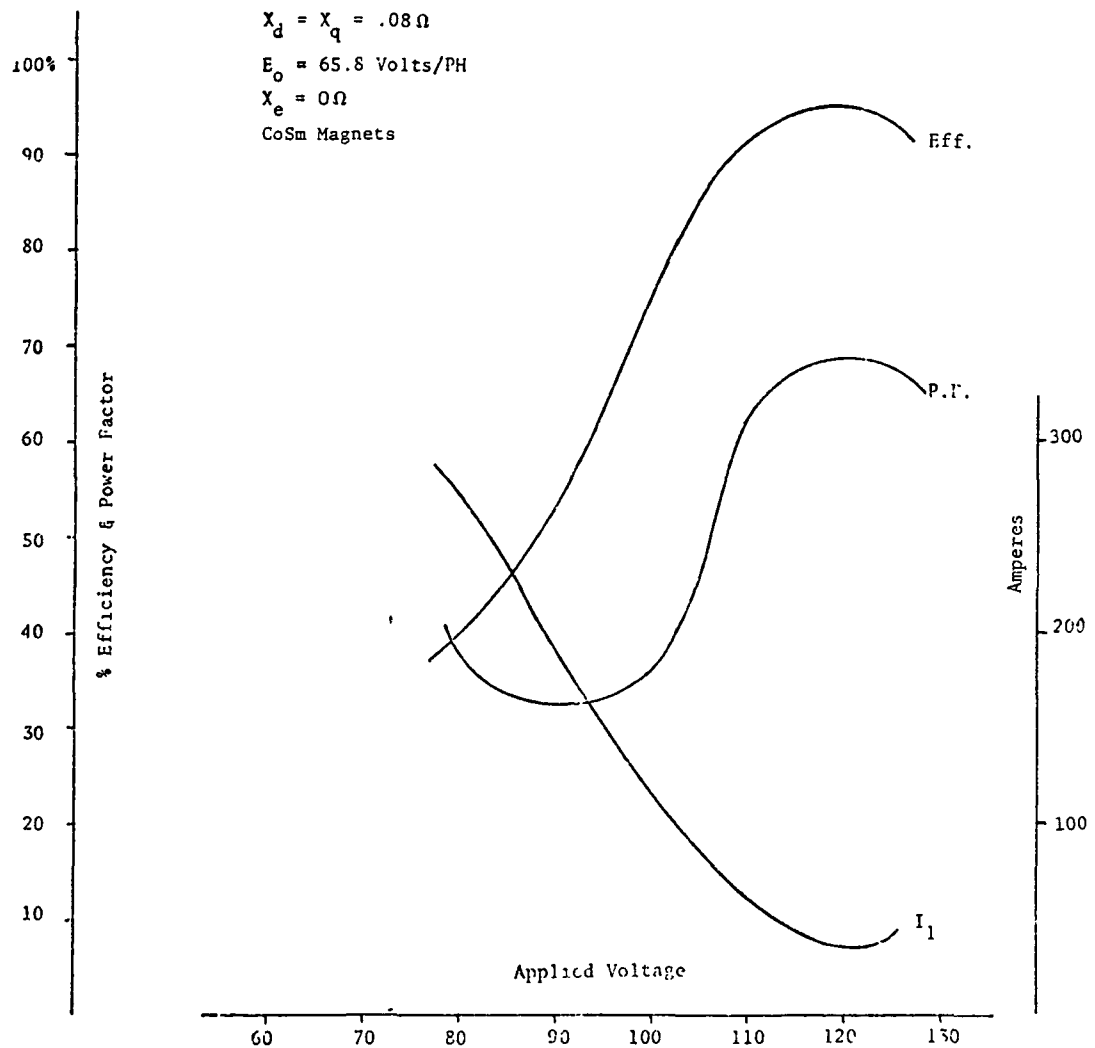


Figure 3-2. Proof-of-Principle Motor – 5.2 kW (7 hp), 240 Hz; Predicted Effect of Voltage on Efficiency, Power Factor, and Amperes

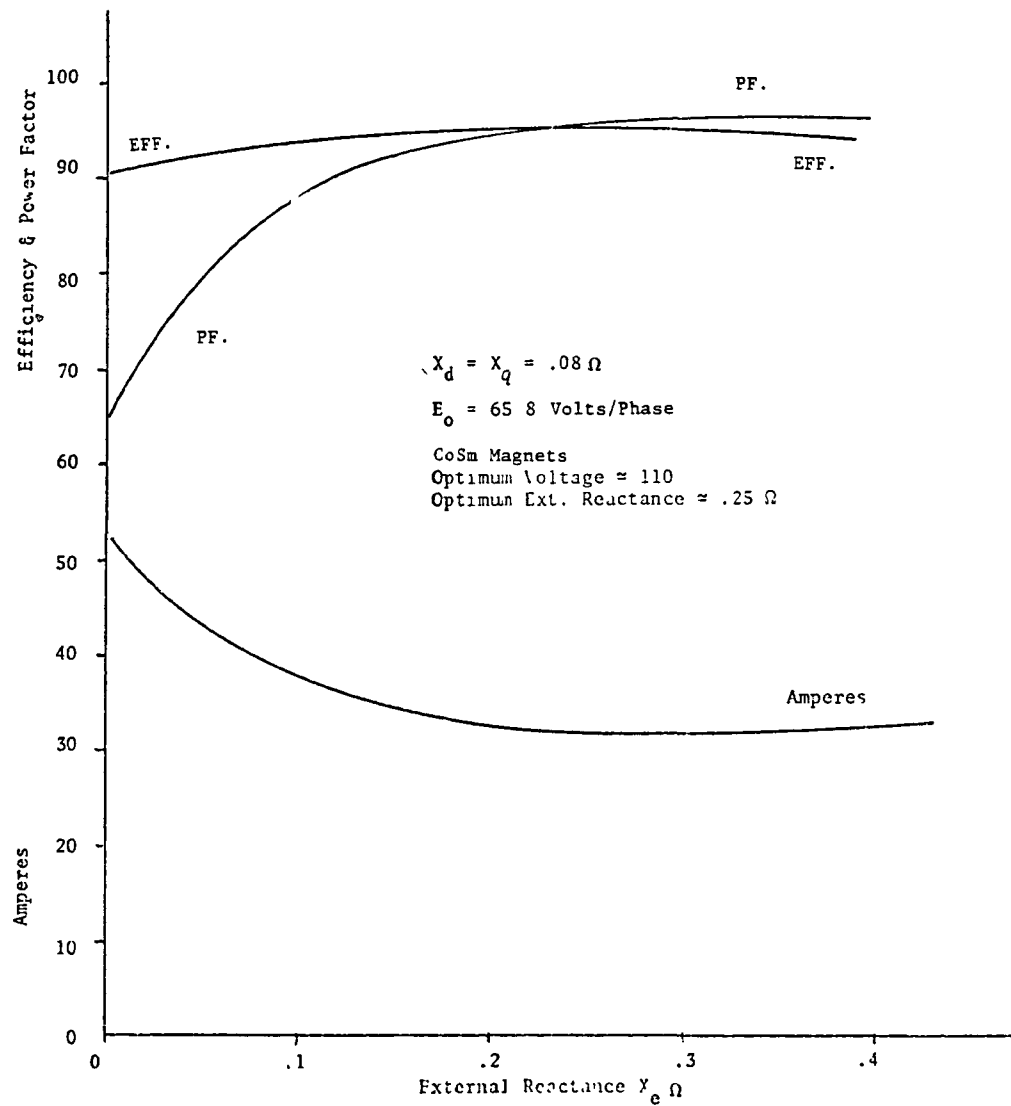


Figure 3-3. Predicted Effect of External Reactance

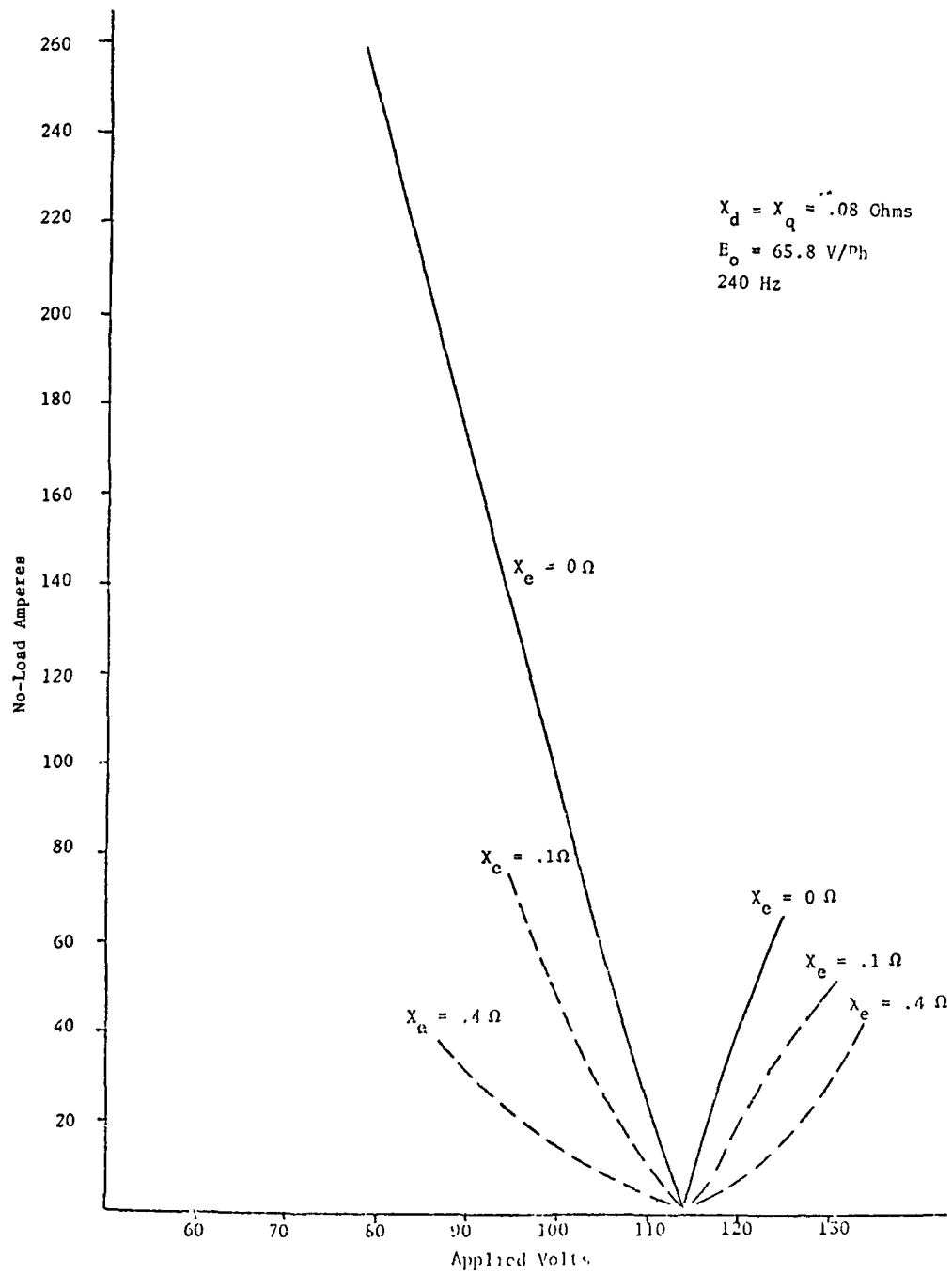


Figure 3-4. Predicted Variation of No-load Amperes with Voltage and External Reactance

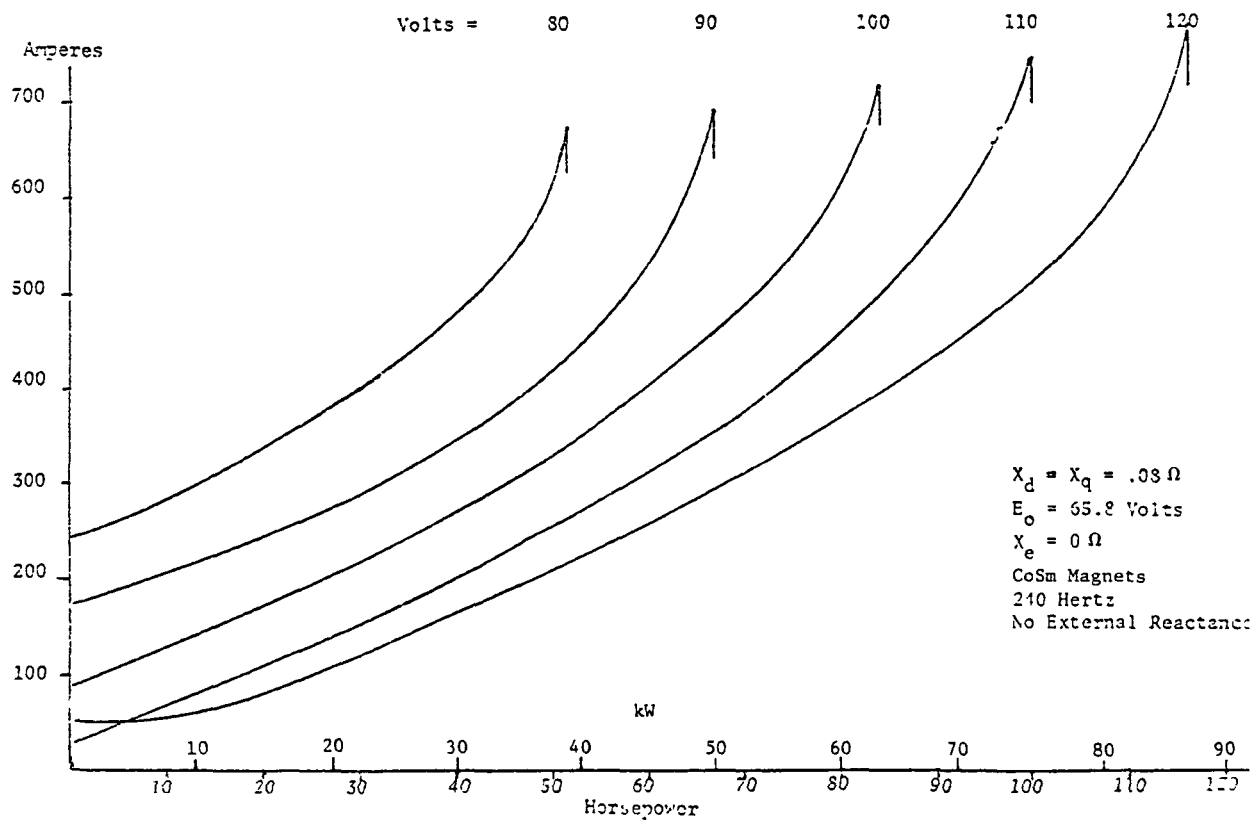


Figure 3-5. Predicted Variation of Amperes with Voltage and Load

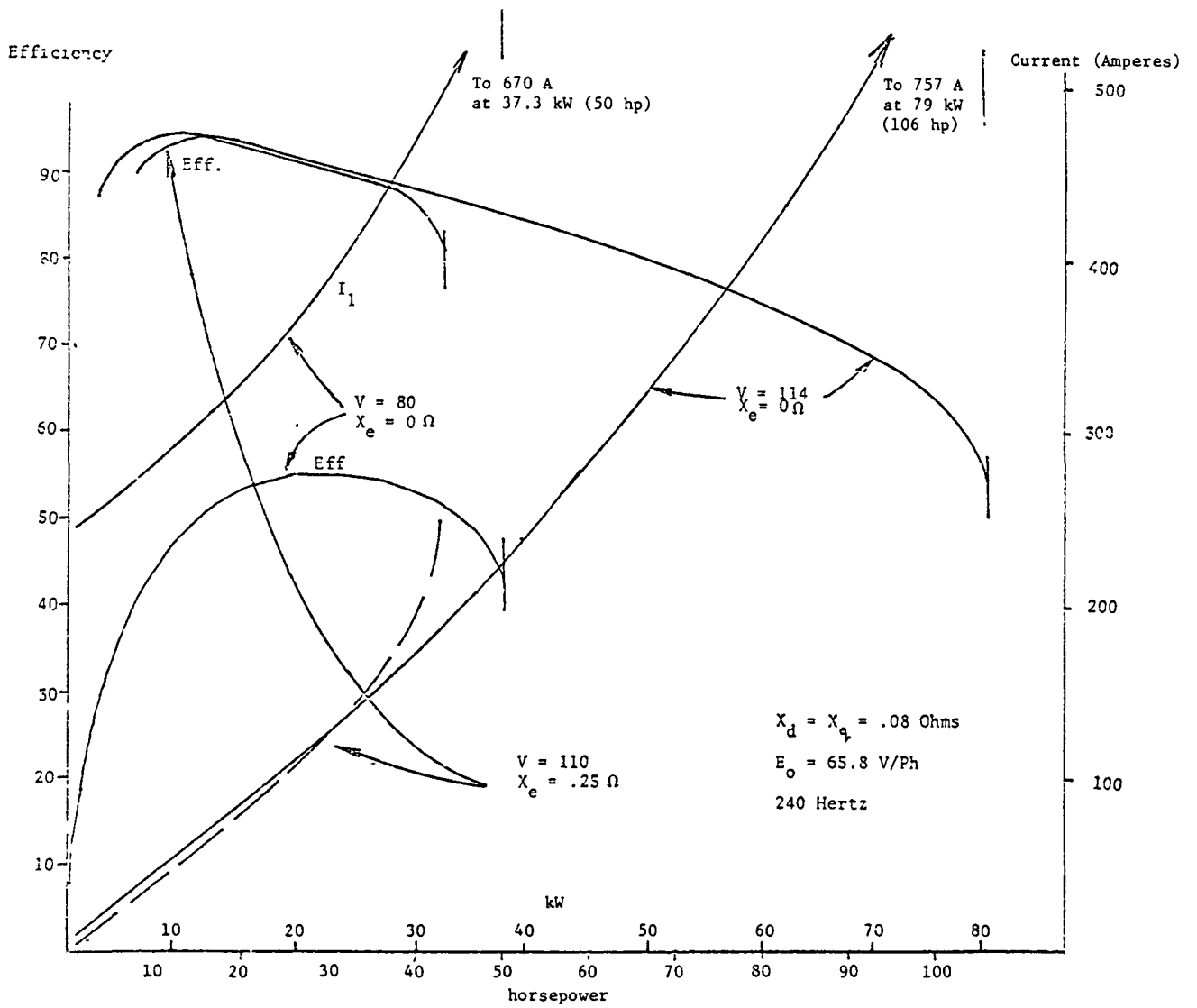


Figure 3-6. Three Cases of Efficiency and Current Versus Load (Predicted)

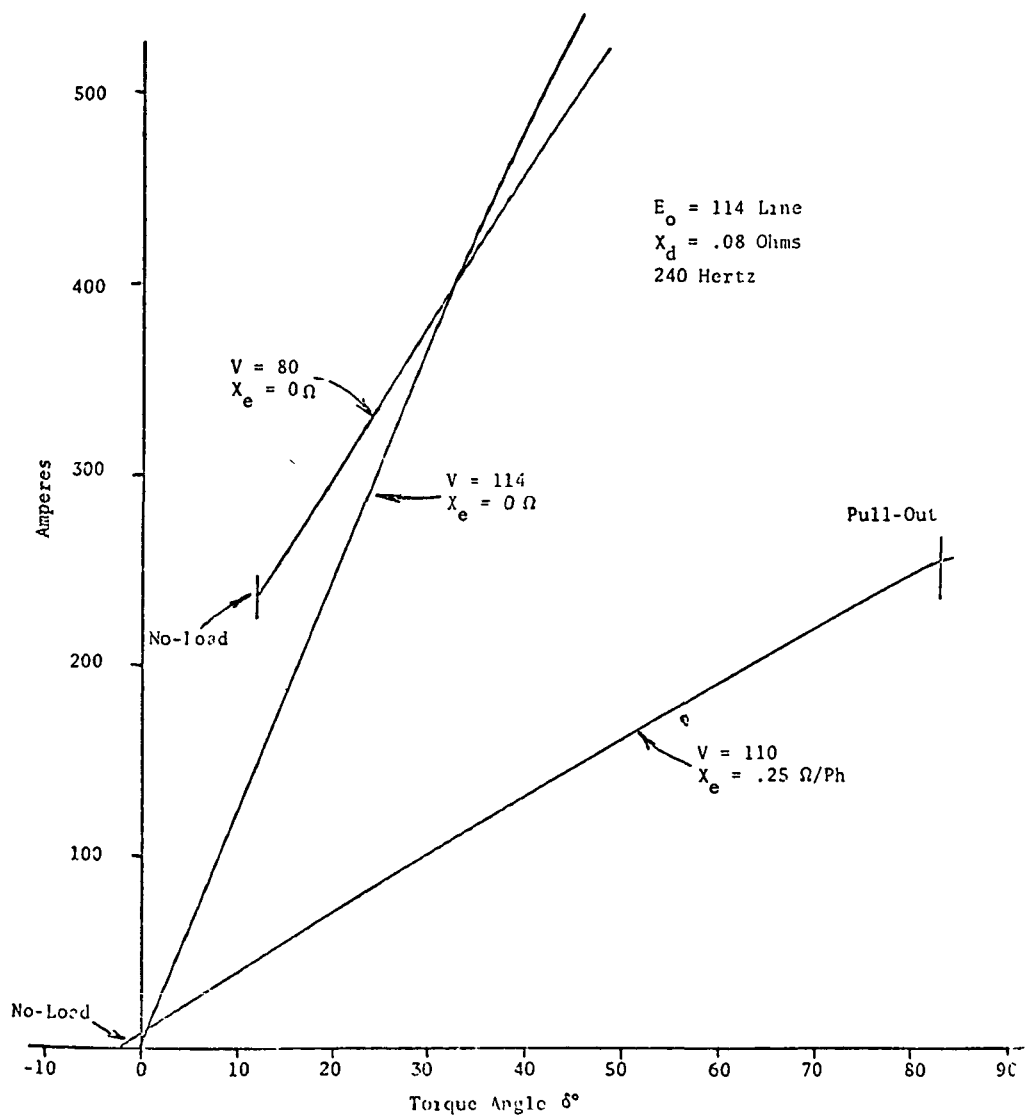


Figure 3-7. Torque Angle Characteristics — δ° Versus Amperes

The external reactance makes the motor more stable for sine wave testing and was not used in inverter testing. When operating on the inverter, stability is assured by the electronic control system. In sine wave testing, the motor is subject to classical synchronous motor hunting oscillations and instability. It was thought initially that it would not be possible to run the motor open loop for sine wave testing but the aluminum hub, spokes, and ring coupled well enough to the stator to provide some amortisseur action. The proof-of-principle motor was successfully run under load up to several kilowatts open loop. A motor generator set was used as the power supply.

3.3 AREAS OF CONCERN

Table 3-2 lists a number of areas which must be dealt with in the design and construction of a new concept motor such as this. Some of the concerns are common to all motors and some are unique to this one.

3.4 MECHANICAL DESIGN

3.4.1 Overview

The stator of the proof-of-principle motor, as mentioned in Section 3.1, is based on an existing proprietary design for a dc disc motor. Stresses in the stator frame are low; thus, the design is noncritical. On the other hand, the rotor design is unique to this motor. The design approach and calculations had to be developed from first principles with little production experience to guide the process. For this reason, and because integrity of the mechanical design is fundamental to safety, the design basis and calculations are given in detail.

3.4.2 Basic Data of the Mechanical Design

3.4.2.1 Requirements

Angular speed (max) = 5000 rpm

Torque (peak) = 158.6 N-m (117 ft-lb)

Operating Temperature (max) = 125°C

Magnets: eight, cobalt-samarium, approximately 5 cm (2-inch) cubes at 17.8 cm (7.0 inch) average diameter

Stators: two, supplied by Canadian GE, Peterborough, Ont.

Rotor Rim: To restrain 100% of magnet mass

3.4.2.2 Materials Application

<u>Steel</u>	<u>Aluminum Alloy 2024-T3</u>	<u>Epoxy, HYSOL #934</u>
• Bearing caps	[$S_y = 345 \text{ MPa (50 ksi)}$, $S_u = 483 \text{ MPa (70 ksi)}$]*	• Magnet-to-magnet
• Preload spring	• Rotor hub	• Magnets-to-hub
• Rotor bearings	• Rotor rim	
• Bolts	• Stator spacer	
• Shaft (1015-1035, cold drawn, stress relieved, $S_y = 241 \text{ MPa (35 ksi)}$, $S_u = 517 \text{ MPa (75 ksi)}$)		

* S_y : yield strength, S_u : ultimate strength

Table 3-2
TECHNOLOGY “BARRIERS”

1. *Winding and Casting Technique*
 - a. Phase insulation
 - b. Nesting of coils
 - c. Accuracy of coil alignment and placement and fabrication stability
 - d. Achievement of high copper factors and mould closure
 - e. Handling and treatment of force wave bundles
 - f. Handling and routing of leads for low inductance and resistance
 - g. Balancing of poles, circuits, sides and phases
 - h. Epoxy selection and void free mould filling and curing
2. *MnAlC Magnet Development*
 - a. Procurement of magnet material
 - b. Modeling
 - c. Magnetizing in place
3. *Amorphous Metal Development*
 - a. Procurement
 - b. Handling and stacking
 - c. Placement and securing
4. *Magnet Flux Prediction and Application*
 - a. Optimal use of materials
 - b. Control of stray fields
 - c. Prediction of open circuit voltage
 - d. Air gap field prediction
5. *Electromagnetic Performance and Design*
 - a. Prediction of open circuit voltage
 - b. Prediction of inductances
 - c. Sizing of motor and inverter
6. *Thermal Performance and Design*
 - a. Prediction of steady state temperature distribution
 - b. Prediction of transient temperature distribution
 - c. Provision of effective heat transfer paper from windings
 - d. Cooling of rotor magnets
 - e. Heat removal from exterior surfaces
7. *Rotor Performance and Design*
 - a. Securing magnets in rotor
 - b. Hub and magnet stress
 - c. Retainer ring stress
 - d. High speed
 - e. Bearing life
8. *Motor Performance*
 - a. Stability
 - b. Sensitivity to voltage
 - c. Very low reactance (large currents)
 - d. Voltage balance $V \simeq E_o$

3.4.2.3 Stresses

<u>Component</u>	<u>Source</u>	<u>Type Stress</u>	<u>Magnitude</u>	<u>Allowable*</u>
Rotor shaft, at keyway	Torque	Shear	88.3 MPa (12.8 ksi)	138 MPa (20 ksi)
Rotor shaft, under hub	Shrink fit	Compression	219 MPa (31.8 ksi)	241 MPa (35 ksi)
Rotor hub, at shaft	Shrink fit	Tension	277 MPa (40.2 ksi)	310 MPa (45 ksi)
Rotor rim	Shrink fit	Tension	91.7 MPa (13.3 ksi)	310 MPa (45 ksi)

3.4.2.4 Rotor Weight

<u>Component(s)</u>	<u>Method</u>	<u>Weight</u>
Shaft, hub bearing	Scale	4.9 kg (10.8 lb)
Magnets	Calculation	7.8 kg (17.2 lb)
Rim	Calculation	2.1 kg (4.5 lb)
		14.8 kg (32.5 lb)

3.4.2.5 Catalog Components

Rotor bearings: Barden Corp. #205FF5G18; Class 5
Grease Lubricated 149°C (300°F) max, sealed

Bearing Preload Springs: Associated Spring Corp. #W2028-022;
Wave-type: 113 kg (25 lb) compressive force
at 0.13 cm (0.05 in.) deflection per spring

3.4.2.6 Assembly Drawing

Proof-of-Principle Vehicle Motor, GE Drawing 146D4136 (Figure 3-1)

3.5 MECHANICAL DESIGN ANALYSIS

The mechanical design analysis is set out in some detail in Appendix A. The numbers used there are for the POP motor; however, the same analysis is reused for the functional models A and B. The results of the calculations are briefly summarized here.

Shaft Stress: The predicted shaft stress is about half the yield stress; hence the shaft should not fatigue.

Rotor Drawings: The bearings are deep groove ball type, grease lubricated. Under estimated vehicle operating conditions with preload, bearing life should be on the order of 2500 h, limited by grease life. Hence, the bearing in the POP motor should be more than adequate.

Shrink Fit: The shrink fit was calculated to transmit maximum torque without slipping. The resultant stress was less than yield with a design margin of 2.

* To preclude yielding

Differential Expansion of Hub to Magnets: A possible failure mode was predicted due to differential expansion of the hub to magnets. This was eliminated by introduction of an epoxy pad between the magnets and hub.

Rotor Rim: The rotor rim is a shrink fit on the hub. The rim material is the same as that of the hub to eliminate thermal stresses associated with differing materials. It is made thick enough to reduce possible problems with compression of the epoxy pads. As a result, the preload was well below the yield stress.

3.6 ROTOR WINDAGE LOSS

The rotor windage loss was estimated using standard formulae as detailed in Appendix A.2. The windage loss for the POP rotor at 5000 rpm and 100°C was predicted to be 39 W. An increase of 15% is predicted for 40°C.

3.7 PROOF-OF-PRINCIPLE MOTOR ASSEMBLY

The fully assembled proof-of-principle motor is shown in Figure 3-8. A full-scale cutaway model of the motor made to the same drawings (full scale) is shown in Figure 3-9 to make clear the relationship of the components. The rotor hub before installation of the magnet is shown in Figure 3-10. The completed rotor is shown in Figure 3-11. The stators and the partially assembled rotor are shown in Figure 3-12. In Figure 3-12, only the aluminum rim is lacking in the rotor assembly so that the layered structure of the magnets may be seen.

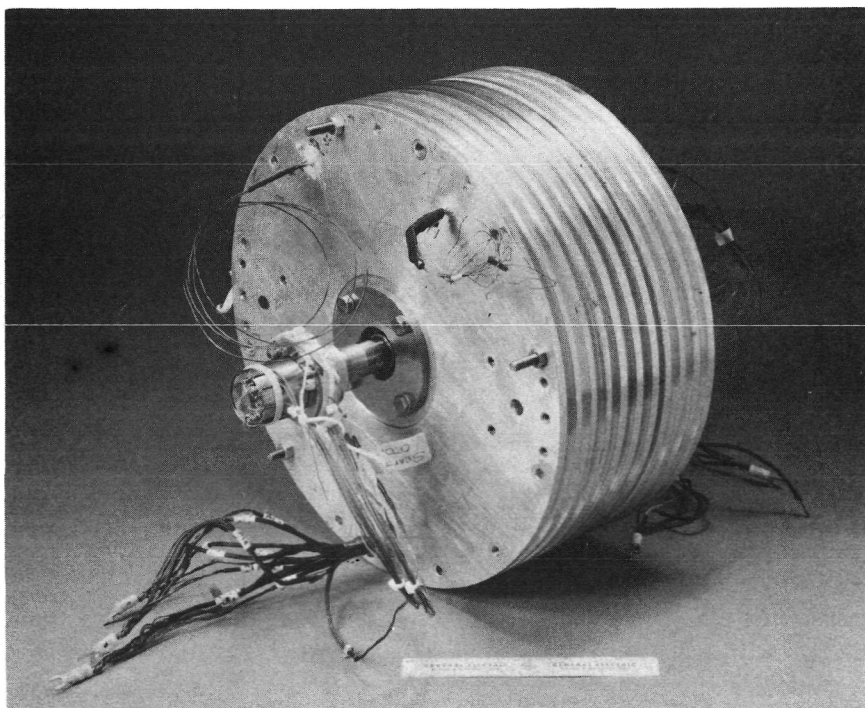


Figure 3-8. Fully Assembled Proof-of-Principle Motor

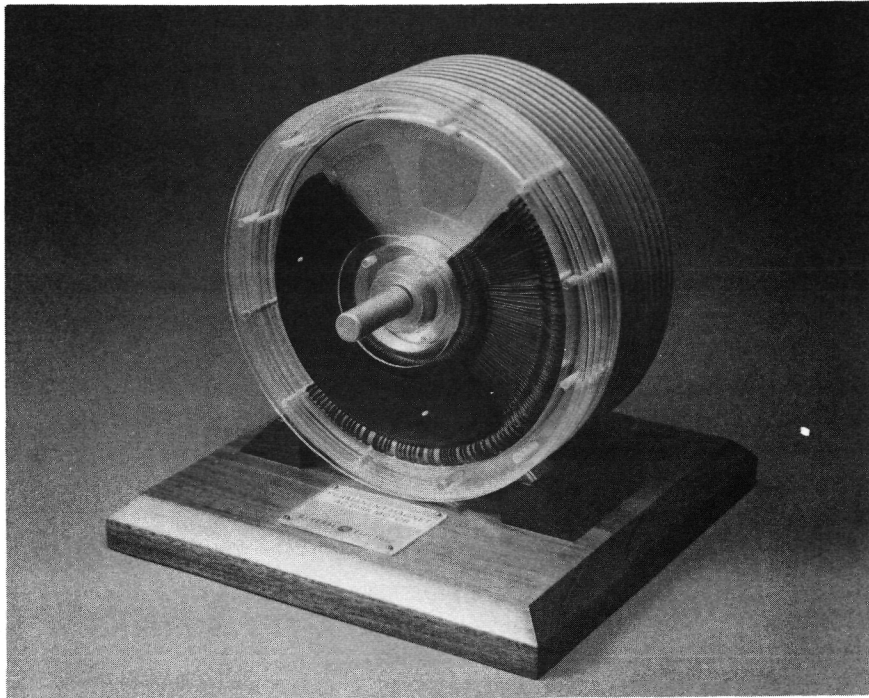


Figure 3-9. Full-Scale Model of Proof-of-Principle Motor

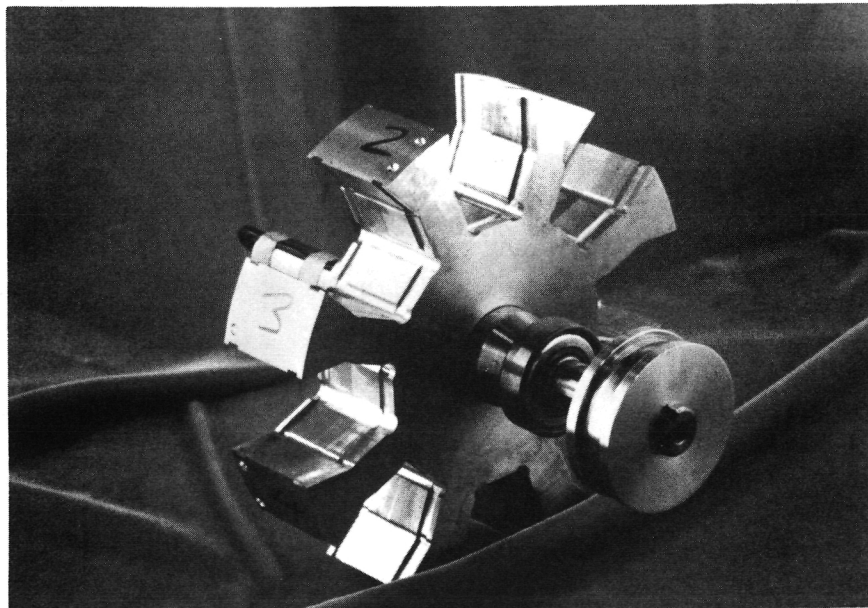


Figure 3-10. Proof-of-Principle Rotor Hub After Balancing

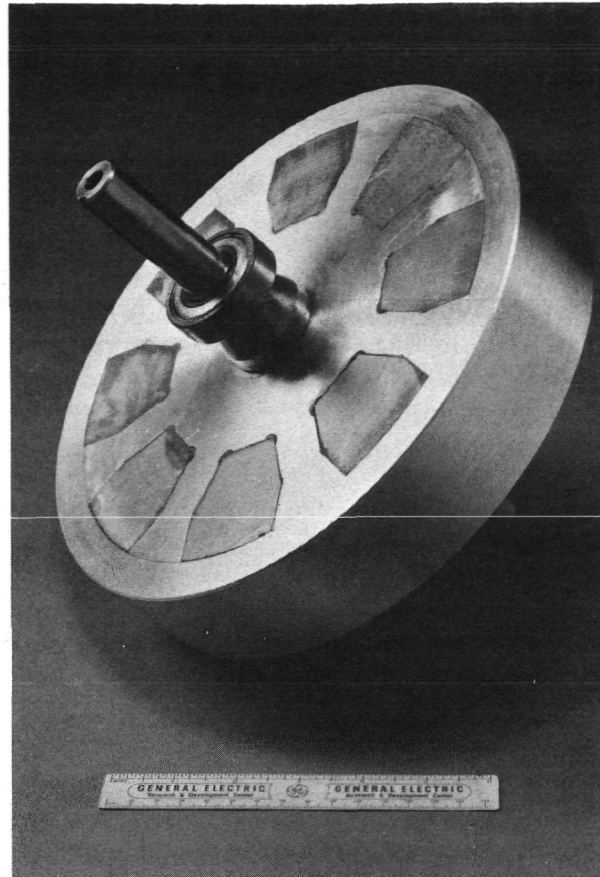


Figure 3-11. Finished Proof-of-Principle Rotor

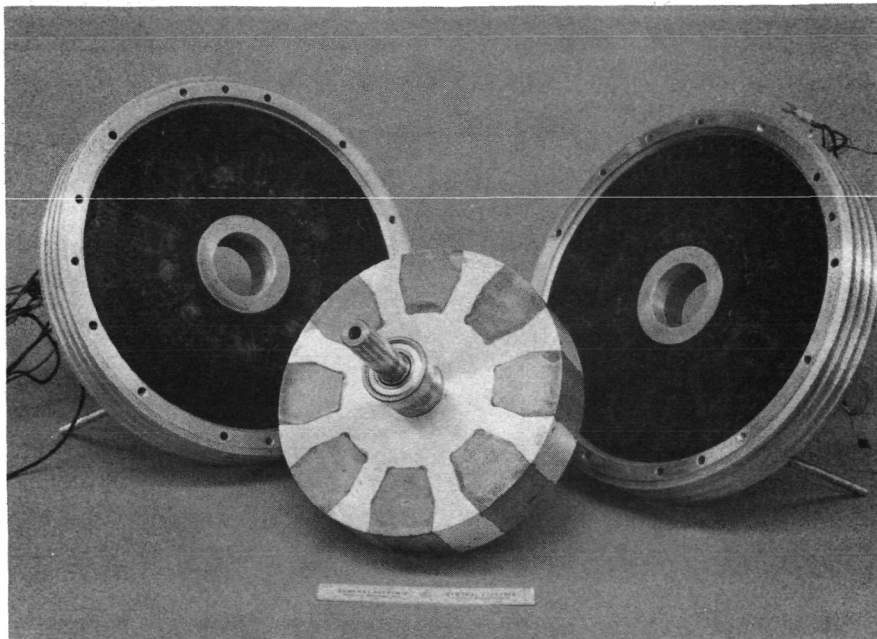


Figure 3-12. Proof-of-Principle Motor Components (Unfinished Rotor)

The magnets were formed by finishing the rough pressed bricks from the magnet vendor and then clipping the corners, resulting in the form shown in Figure 3-13. The magnets were then magnetized and glued together in stacks of four. The final form may be seen in Figure 3-12.

3.8 SINE WAVE TESTING

Certain tests were run on the proof-of-principle motor to verify that the performance was in line with predictions before proceeding to the design of the functional model motor. More extensive testing was done in both the generating mode (resistor load) and the motoring mode with the inverter. These results are reported along with the functional model tests in Section 5.

The first of the preliminary tests was not on the motor but on two of the magnets in a special test rig (Figure 3-13) to determine the distribution of magnetic flux density in this unusual configuration. The flux density was measured with a Hall effect probe at various points around the magnets in the test rig shown in Figure 3-13. Figure 3-14 shows the flux density measured at the magnet surface in the gap between the iron and the magnet. The magnitude of the "axial" flux density is plotted as a height above the magnet plane. The characteristic "dome" shaped distribution of flux over the magnet is accounted for by a special correction factor in predicting the open circuit voltage shown in Figure 3-15. The conventional synchronous motor parameters are also computed in the modified program. A comparison of predicted and measured values is given in Table 3-3.

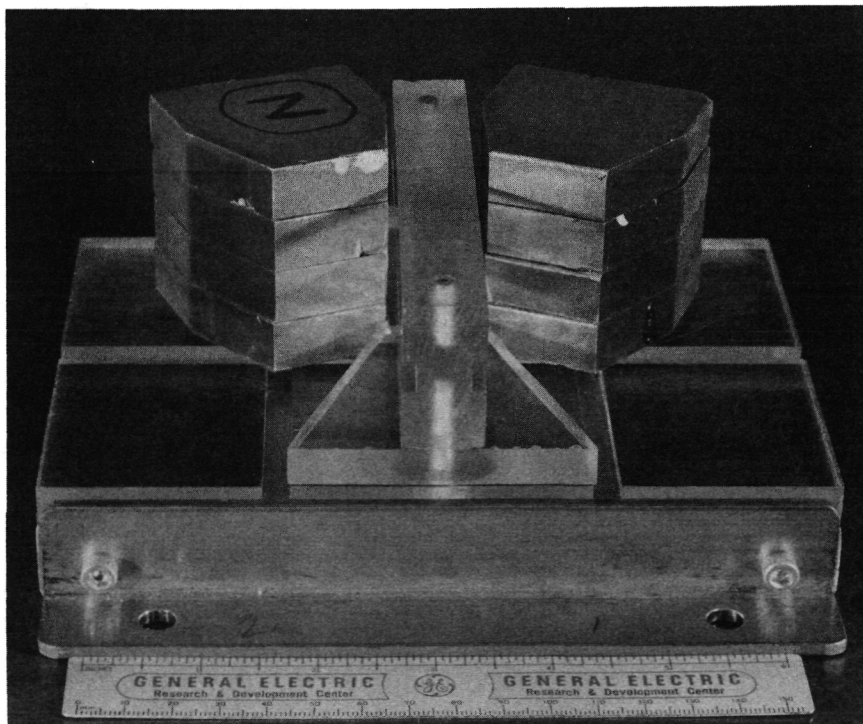


Figure 3-13. Magnet Test Fixture

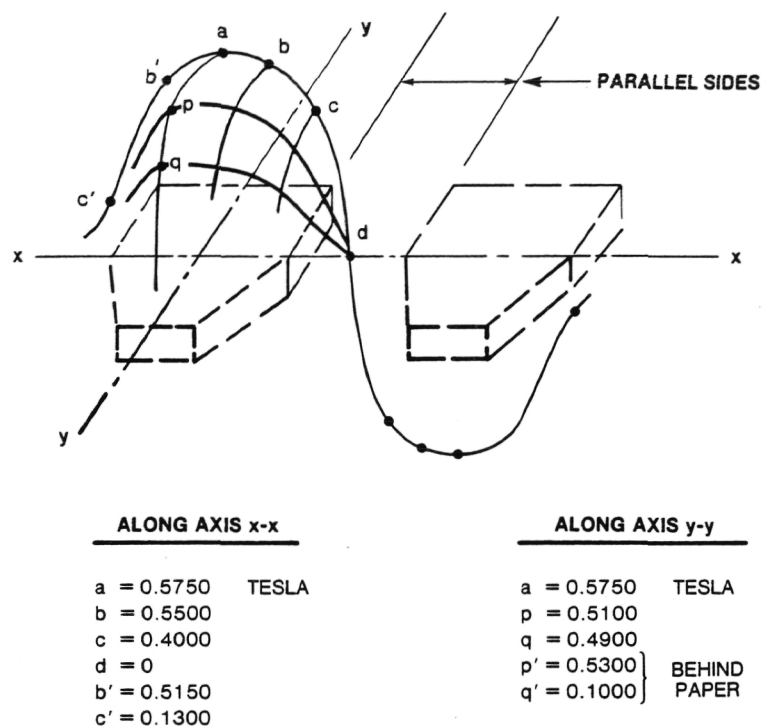


Figure 3-14. Measured Flux Densities on Magnet Surface

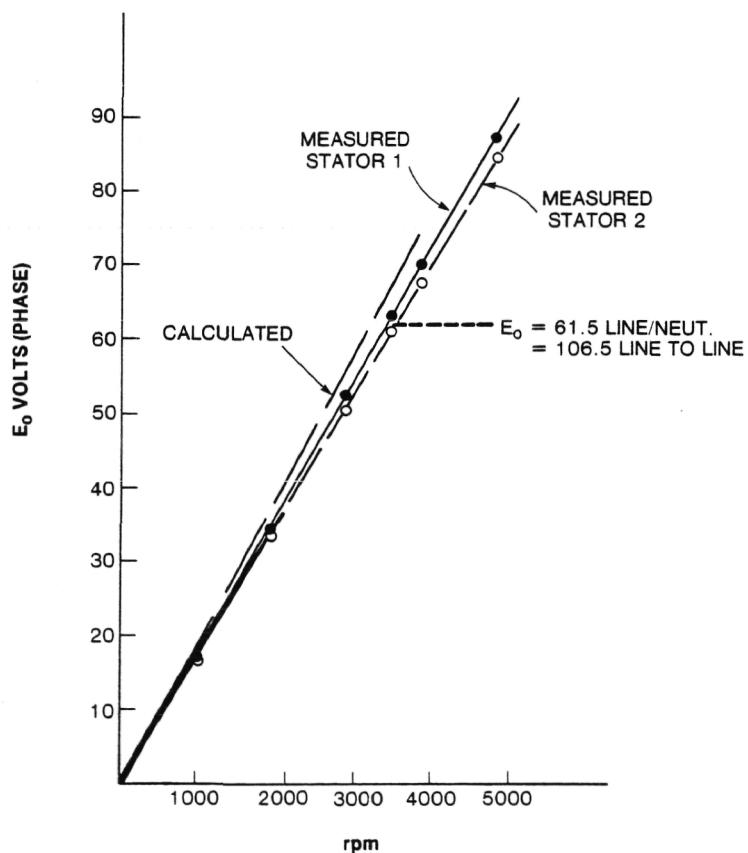


Figure 3-15. Open Circuit Voltage E_o (Line to Neutral) Versus Speed (POP Motor)

Table 3-3
POP MOTOR PARAMETERS: 240 Hz
ESTIMATED AND MEASURED

	<u>Estimate</u>	<u>Measured</u>
Stator Resistance, r_1 (100°C) Ω	0.04	0.039
Direct-Axis Reactance, x_d Ω	0.08	0.081
Quadrature-Axis Reactance, x_q Ω	0.08	—
Subtransient Reactance, $x_d'' = x_q''$ Ω	0.05	0.046
Open Circuit Voltage, E_o (line), V	114	106.5
Note: Synchronous Reactance, $x_d =$ Transient Reactance x_d'		

With the proof-of-principle motor running as a motor at no load, the characteristic "V" curve for a synchronous motor was obtained theoretically and experimentally. These curves are shown in Figure 3-16. The major difference in the predicted and measured curves results from the difference between open circuit voltage prediction and measurement.

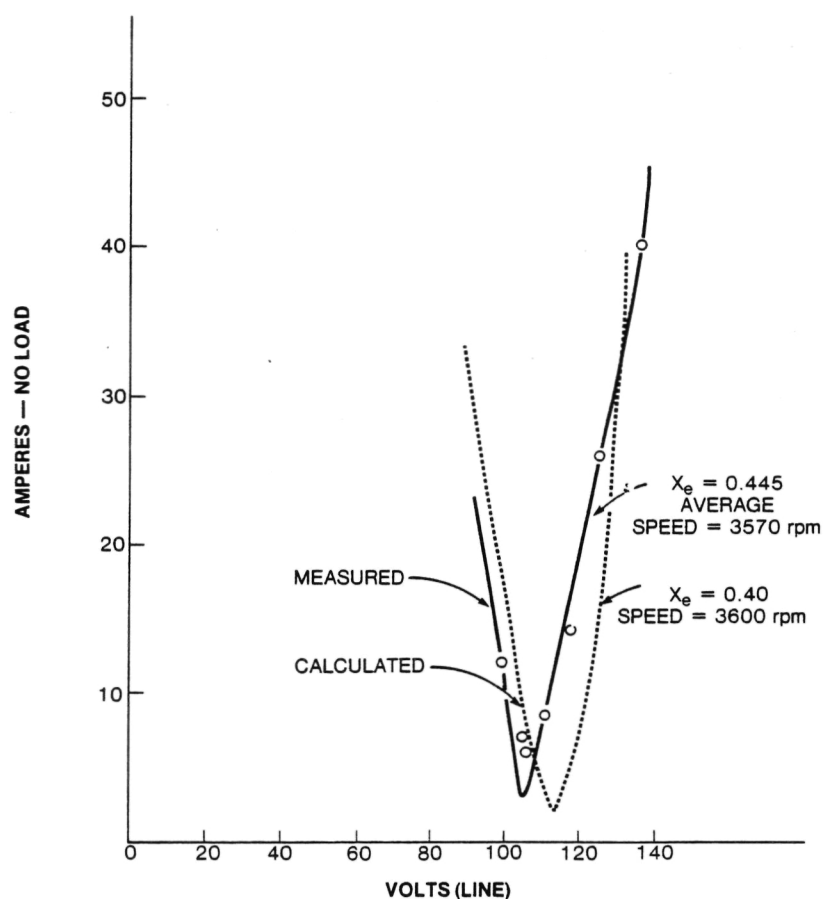


Figure 3-16. Variation of No-Load Amperes with Voltage-External Reactance in Line; Disk Motor, 5.2 kW (7 hp), 240 Hz, 8 Pole (POP Motor)

4.0 FUNCTIONAL MODEL OF DISK MOTOR: DETERMINATION OF MOTOR RATING, SIZE, AND WEIGHT; PREDICTION OF PARAMETERS

4.1 GENERAL CONSIDERATIONS

The motor size and its design are greatly influenced by the following requirements:

1. Maximum torque
2. Maximum speed
3. Acceleration schedule
4. Speed range for constant power
5. Inverter commutation requirements
6. Efficiency, cost, size, and weight goals.

The maximum torque at the wheel axle is determined by acceleration and gradeability requirements and not by cruising while level. The axle torque is reflected to the motor through a gear that increases the motor speed and reduces motor torque requirement.

4.1.1 Summary of the Specifications from the Contract

The following is a summary of motor specifications for the double-sided, slotless disk motor required by NASA:

- a) The drive system may, if necessary, use a two-speed transmission.
- b) The duty cycle, in summary, is
 1. Cruise for two hours at 88.5 km/h (55 mph).
 2. Two hours of repetitive SAE J227a cycles (schedule D).
 3. Operation on a 10% uphill grade at 56.3 km/h (35 mph) for five minutes.
 4. Downhill braking by generator action on a 15% grade at 48.3 km/h (30 mph).
- c) The motor shall be air cooled, assuming an ambient temperature of from -30 to $+50^{\circ}\text{C}$.
- d) The contract requirement for battery voltage is any voltage between 120 and 240 V dc, but a higher voltage is preferred (180 V dc is suggested).
- e) The drive system shall be designed for overall efficiency maximization over the duty cycle.
- f) The vehicle is characterized by the following data:

1. Weight including passengers

$$W = 3000 \text{ lb (1361 kg)}$$

2. Frontal area

$$A = 20 \text{ ft}^2 (1.86 \text{ m}^2)$$

3. Aerodynamic drag coefficient

$$D = 0.3 \text{ dimensionless}$$

4. Tire rolling resistance factor

$$K_r = 0.008 \text{ dimensionless}$$

5. Rolling radius

$$r = 0.292 \text{ m (0.96 ft)}$$

4.1.2 Extra-Contractual Assumptions

- a) It is assumed that the efficiency between the wheels and motor (bearings, gears, and miscellaneous moving parts) is 0.80.
- b) During acceleration, the change in kinetic energy must include the effect of rotating parts. This is equivalent to an increase in vehicle weight. It is assumed that the vehicle weight W is increased by 10%; e.g., $W' = 1.1 W$ (see Section 4.2.4) during acceleration, or from 3000 to 3300 pounds (1361 to 1497 kg).
- c) It is assumed that the vehicle speed will reach 66 mph occasionally. This corresponds to a motor overspeed requirement of 1.20.

4.2 ROAD RESISTANCE

The contractual and extracontractual requirements are given in terms of vehicle performance in Section 4.1. The method of transforming these vehicle requirements into motor requirements is discussed in detail in Appendix B. The effects considered are:

1. aerodynamic drag
2. rolling resistance
3. acceleration
4. grade

4.3 MOTOR REQUIREMENTS

The various motoring and braking requirements for the particular vehicle under consideration are summarized graphically in Figure 4-1 and in Appendix B.

4.4 J227 CYCLE REQUIREMENTS

Similar calculations to those in Appendix B become too complex for direct solution when windage is considered. Windage may not be neglected, however, hence various approximate and/or iterative methods must be employed (such as a simulation) to determine the best break point between constant torque and constant power acceleration. The results of such calculation (for three options) are shown in Figure 4-2 where the powers and tractive efforts are given without consideration of gear efficiency, which is assumed to be 0.8. The net result is that the required power is 19.4 kW (26 hp) at the motor shaft. A summary of the torque-speed requirements for the motor resulting from the contract and extra-contractual requirements is given in Figure 4-1.

4.5 VOLTAGE – FREQUENCY BREAK POINT

Figure 4-3 shows two curves, one being voltage versus frequency and the other being torque versus frequency for a typical ac motor traction drive. The frequency point on the voltage curve separating the constant V/f portion from the constant V portion is called the break point. In the case of the synchronous motor, the voltage-frequency

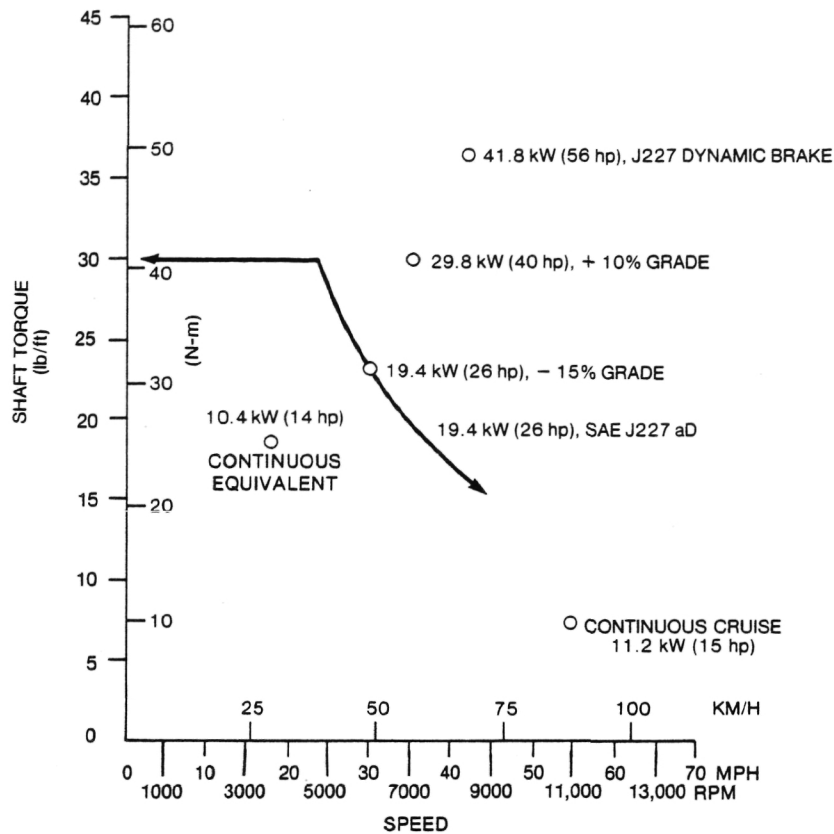


Figure 4-1. Torque-Speed Requirements Summary

ONLY POSSIBLE REGION OF OPERATION WITH $F_t = 155$ kg (342 lb) MAXIMUM CAPABILITY
 P_1 IS VARIABLE AND LESS THAN P_1 (MAXIMUM)

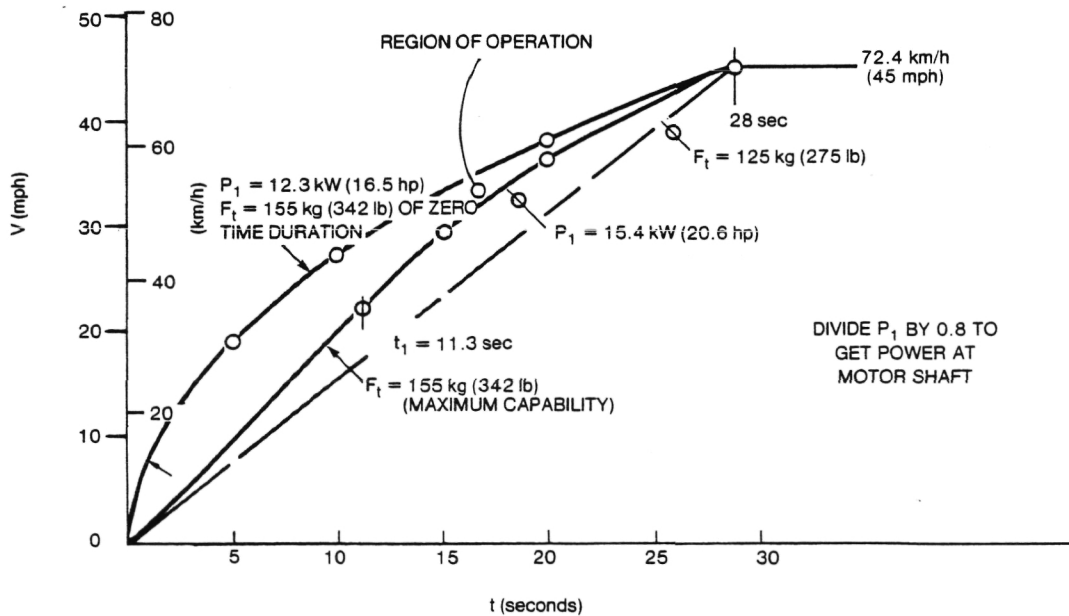


Figure 4-2. Acceleration Schedule Options

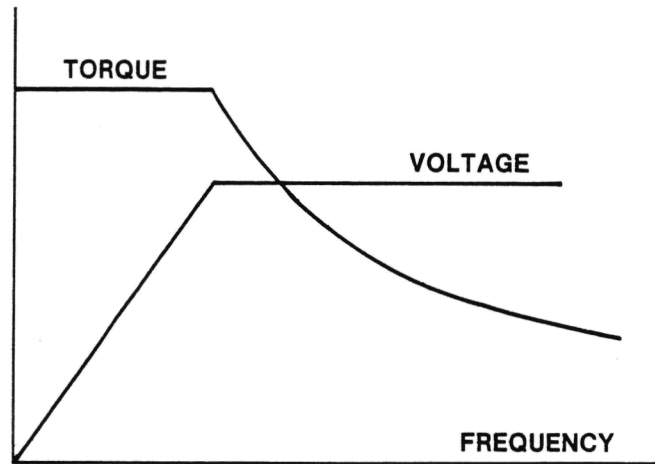


Figure 4-3. Illustration of the "Corner Point" Concept

break point is identical to the torque-frequency break point (this is usually not true for induction motors). The break point is often called the "corner point," and usually the curve is represented by "power" or "torque" plotted against speed which, in this case, is proportional to frequency.

The specifications summarized in Section 4.1 suggest that there is no "break" or "corner" point in the driving schedule, and hence there is no break point such as would define a voltage-frequency curve applicable to the inverter-motor system.

However, the inverter operating characteristic depends on the two modes defined by variable voltage and constant voltage segments that establish a definite break point, even though that break point may wander in an actual situation. Determination of the break or corner point is described in the next section.

4.5.1 Chopper-Inverter Operation

Figure 4-4 illustrates the battery-controller-motor system wherein V_b is the fixed dc battery voltage. V is the corresponding battery voltage after being processed through the inverter, changed to an ac voltage, and then placed across the motor terminals.

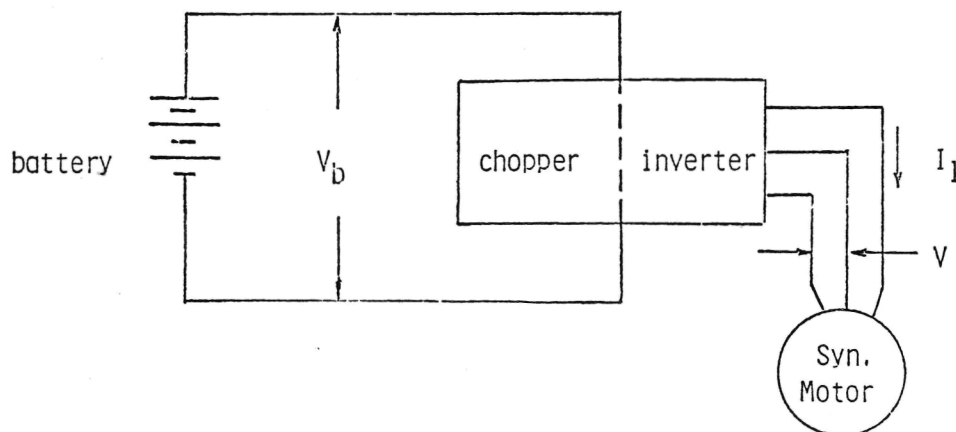


Figure 4-4. Battery-Controller-Motor System. Inverter is a load commutated type. V_b = battery voltage (fixed) while V = battery voltage referred to motor terminals through the inverter.

Four voltage equations are of immediate interest. These are, in phasor form,

$$V = E_o + I_1 x_m + I_1 z_1$$

$$V = E_i + I_1 z_1$$

$$E_o = E_i + I_1 x_m$$

$$E_o = k_3 f \hat{\phi}_1$$

The first equation lists the relation between V , the open-circuit voltage E_o , the armature reaction impedance drop $I_1 x_m$ and the leakage impedance $I_1 z_1$. The second equation lists the relation between the terminal voltage V , the internal (or air gap) voltage E_i , and $I_1 z_1$. The third equation follows from the first two. The open-circuit voltage E_o corresponds to the magnet flux or to the machine flux when there is no armature current. The internal voltage E_i corresponds to the magnet flux adjusted for armature reaction flux (which is the net flux in the air gap). The flux in the machine on open-circuit is due solely to the magnets and hence is constant at all frequencies. The voltage E_o in the last equation therefore is linear with respect to frequency or speed. The flux $\hat{\phi}$ is the magnet flux. It follows that the internal voltage E_i is nearly linear with respect to speed (the slight nonlinearity will be ignored).

Thus the situation exists where a fixed battery voltage V_b exists in conjunction with a variable voltage E_i which is nearly linear with respect to speed (see Figure 4-5). The chopper-inverter system lies between these two voltages. The inverter is a load (machine) commutated type where the voltage E_i is the forcing voltage required to quench the current in each thyristor. During inversion, the power factor must be leading or the ratio $E_o/V \approx E_i/V$ must be greater than unity.

It can be shown that, in this very low reactance system, the magnitudes of E_o and V are unusually close together, but nevertheless E_o must be slightly greater than V . This is accomplished by reducing the voltage V_b to a value V slightly less than $E_o \approx E_i$ to the left of the corner point in Figure 4-6. To the right of the corner point, the voltage $E_i \approx E_o$ is phased back by the inverter so that E_o is slightly greater than V .

This process defines a break or corner point given by the intersection of the linear E_o with the fixed V (when unprocessed) or, in another sense, the point that separates chopping operation from phase-back operation. This also means that the constant torque mode is on the left and the constant power mode on the right. The motor size will increase with the width of the constant power mode.

Normally the corner point is determined by the load requirement; the inverter voltage and frequency schedule is matched to the load. Figures 4-13 and 4-14 of Section 4.6 illustrate the performance of the disc motor corresponding to five different corner points.

Regardless of how the motor receives its voltage and at what frequency, the system must produce the performance summarized in Section 4.1.1.

4.6 PREDICTION OF PARAMETERS AND PERFORMANCE OF THE FUNCTIONAL DISC MOTOR

Some factors that influence the parameters of the functional disc motor, aside from the purely dimensional aspects of the machine, are:

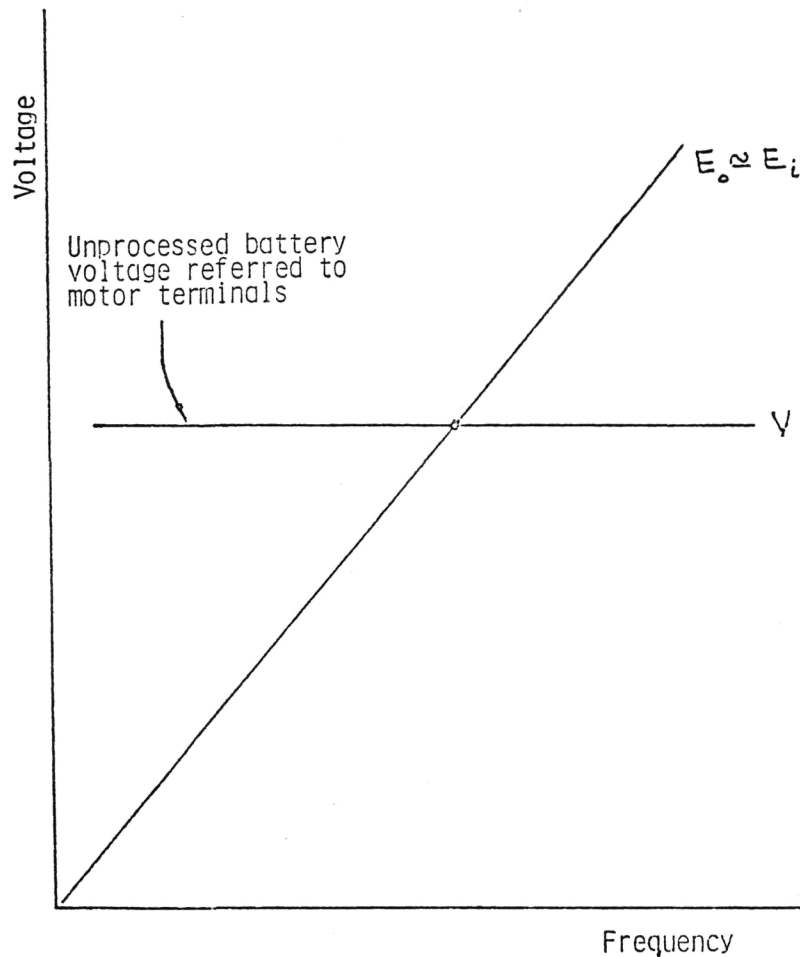


Figure 4-5. Fixed battery voltage V_b together with a linear open-circuit voltage E_o with respect to frequency.

- a) Use of a three layer winding instead of a single layer winding which augments the already large air gap. The reactances and open-circuit voltage are expected to be quite low. The use of iron-powder filled epoxy (if used) could alleviate this situation. But the presence of iron in a 3-layer winding could produce a magnetic path that partially short-circuits the magnet flux; this is less probable in a single layer winding.
- b) The permeability and nonlinearity of the magnet system affects the value of reactance and open circuit voltage.
- c) The essentially three-dimensional nature of the magnet field affects the open-circuit voltage.
- d) The aluminum housings and spacer act as flux dampening bodies through the agency of induced eddy currents.
- e) The state of magnetization of the magnets affects the open-circuit voltage. Magnetization of the magnets is planned to be achieved by use of the machine windings.

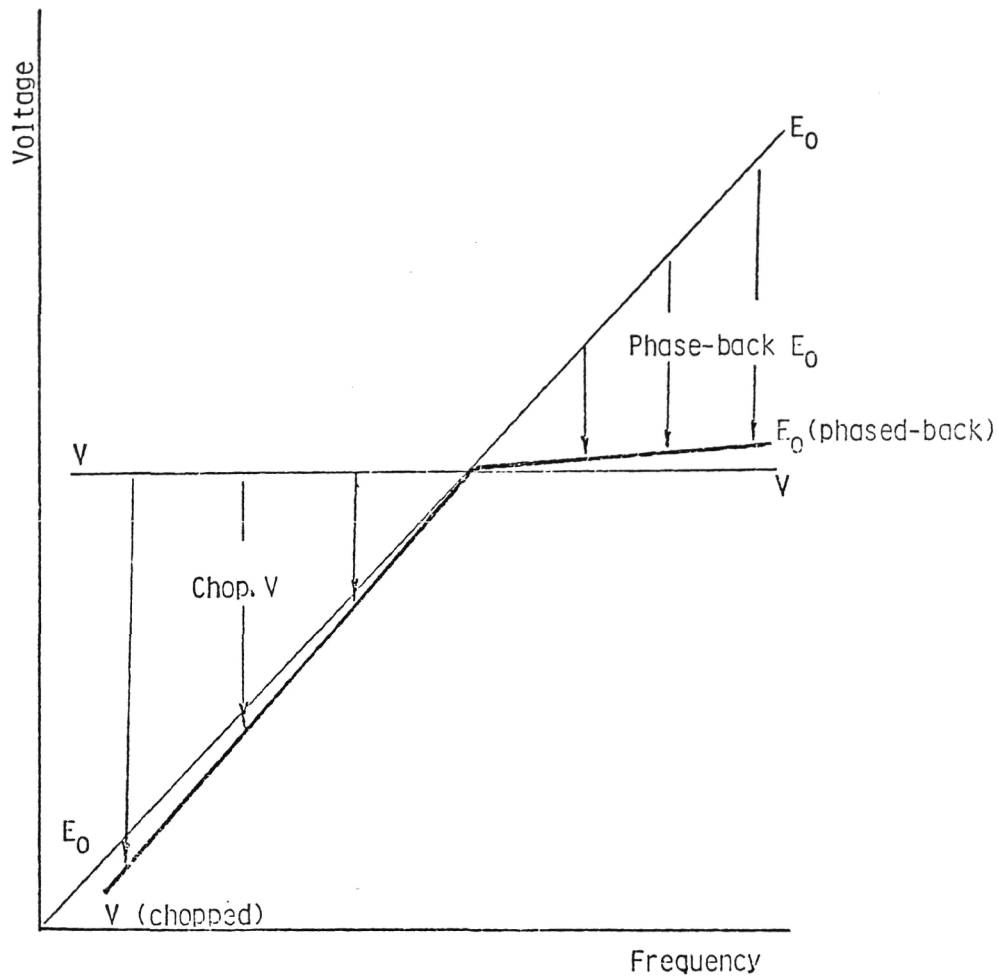


Figure 4-6. Illustration of Voltage Control Principle. Heavy lines show fixed V reduced by chopper and linear $E_o \approx E_i$ phased-back by inverter.

4.6.1 Magnet Permeability: Effect on Performance

Given two magnet systems of identical dimensions, specifically that shown in Figure 4-7. One system has a recoil permeability of 2.07 (Alnico 8E) and the other a permeability of unity. The remanent flux densities in both cases are identical and equal to 0.7900 T (illustrated in Figure 4-8).

Table 4-1 shows, for these two cases, the effect on reactances, magnet reluctances upon which the reactances depend, open circuit voltage, and magnet operating point.

Alnico 8E is used here as a stand-in for the Manganese-Aluminum-Carbon (MnAlC) magnets which were proposed originally. This was done because MnAlC was not available in sufficient quantities to construct the motor. This particular Alnico was chosen to simulate the electromagnetic properties and problems of MnAlC. In particular, the demagnetization due to armature currents ought to be worse in Alnico than in MnAlC due to the lower coercivity and increased slope of the third quadrant characteristic. Additionally, Alnico is now thought to be subject to further demagnetization as a result of field rotation.

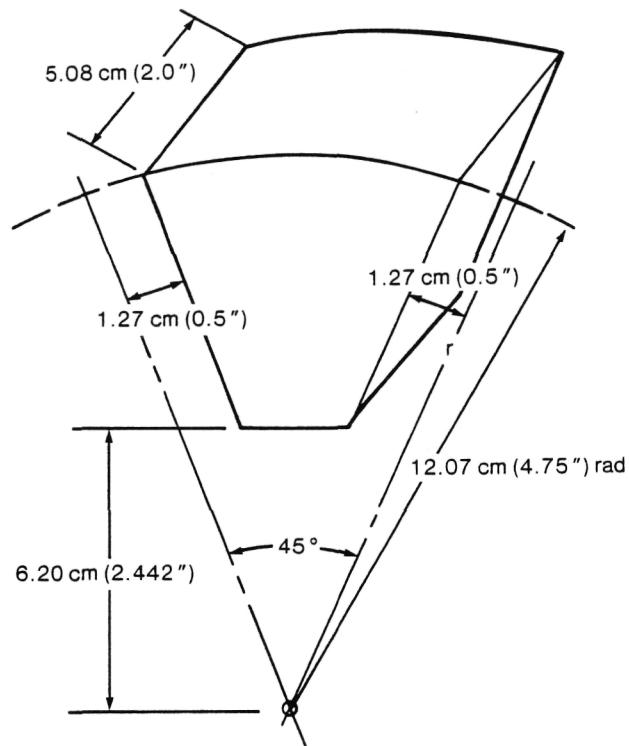


Figure 4-7. Magnet Concept - Functional Model Disc Motor

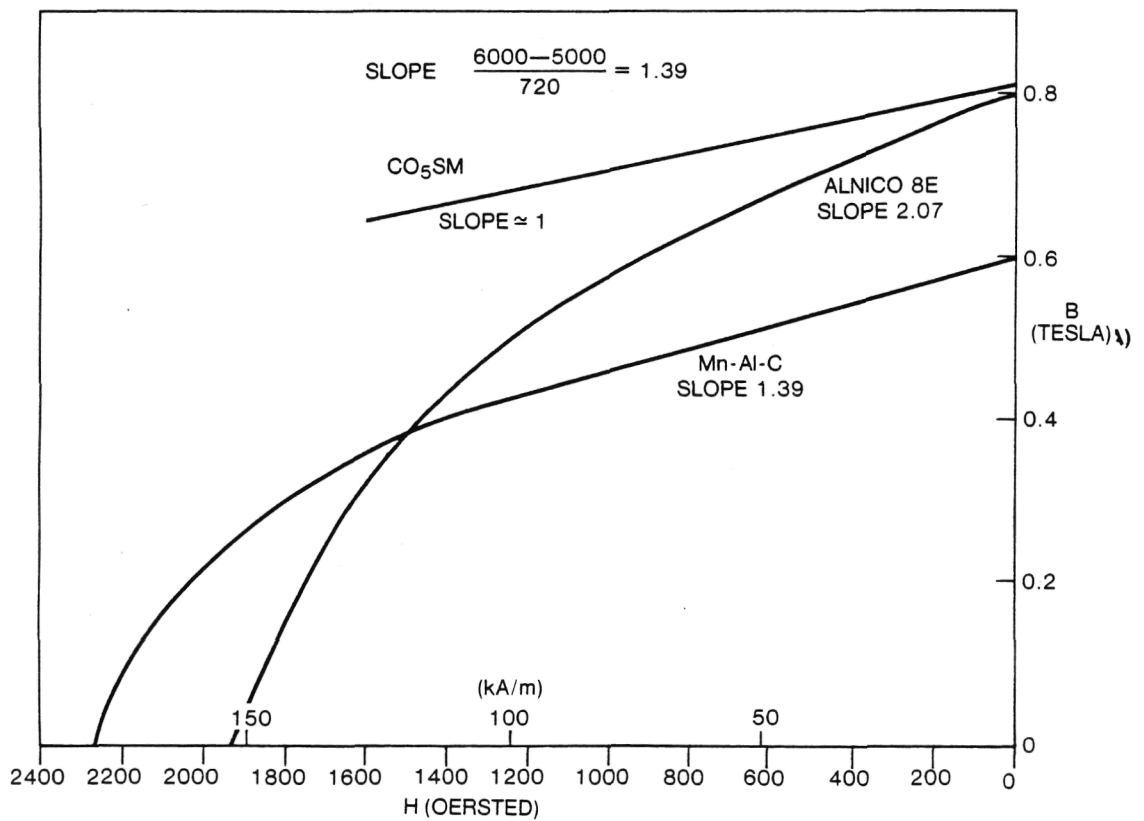


Figure 4-8. Comparison of CoSm, Alnico 8E with Mn-Al-C

Table 4-1
MAGNET COMPARISON

	<u>Alnico 8E</u>	<u>Fictitious</u>
B_r^*	.6900 T	.6900 T
Recoil Perm μ	2.07	1.0
Gap Rel. R_g	0.028	0.028
Magnet Rel. R_m	0.069	0.143
X_d , 732 Hz	0.14 Ω	0.11 Ω
E_o	175 V	217 V
ϕ_1	0.125×10^6 l	0.155×10^6 l
Magnet Flux Dens.	.5034 T	.5790 T

* Recoil line through operating point

Figure 4-9 shows the operating points for the final configuration of the functional model motor for no load, full load, and the recoil line along which the motor actually operates. The flux density shown at the operating point is actually valid only near the center of the magnet. Due to the large gap, the flux density drops off in all directions from the center resulting in the dome shaped distribution shown in Figure 4-10. If this dome is assumed sinusoidal in shape, a form factor K_f may be derived to modify the flux density of Figure 4-9 to an appropriate effective value.

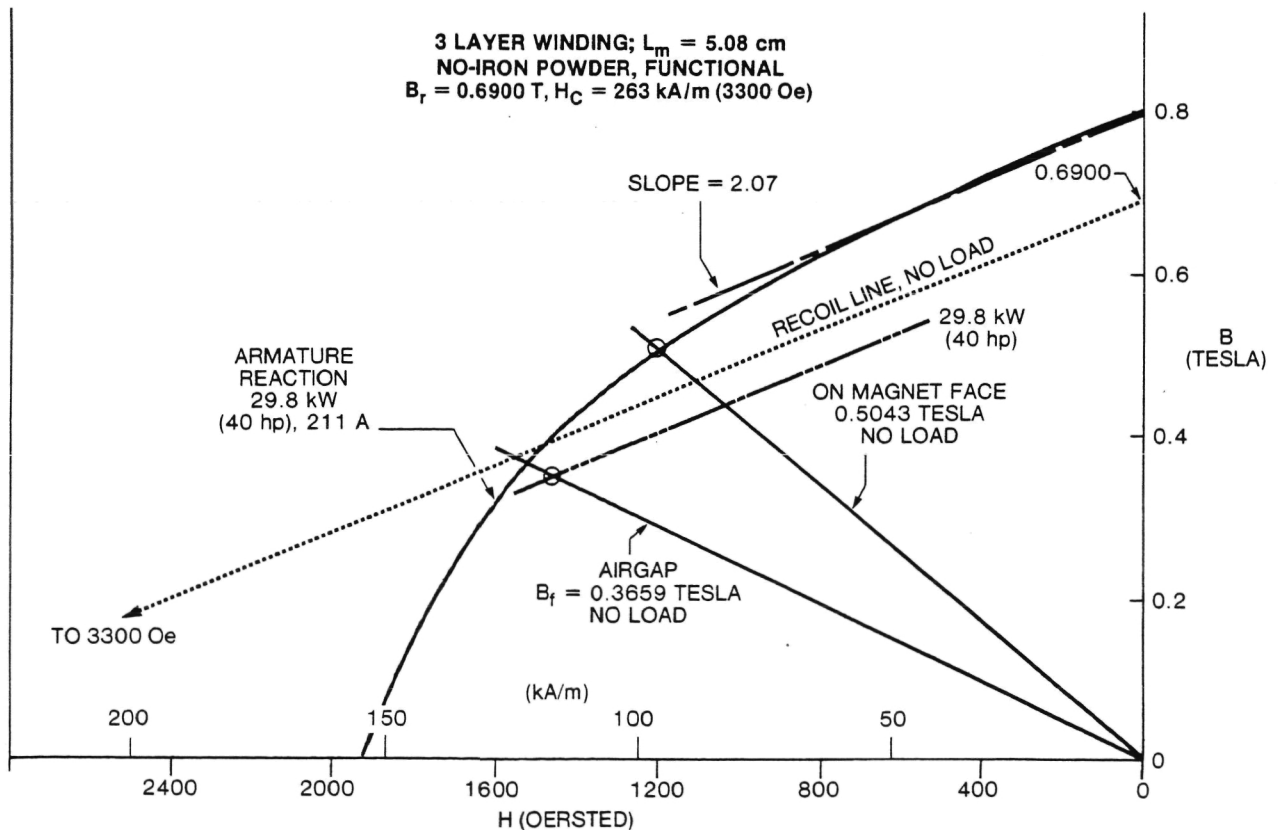


Figure 4-9. Alnico 8E - Operating Point; 3-Layer Winding, $L_m = 5.08$ cm, No-Iron Powder, Functional Model $B_r = .6900$ T, $H_c = 263$ kA/m (3300 Oe)

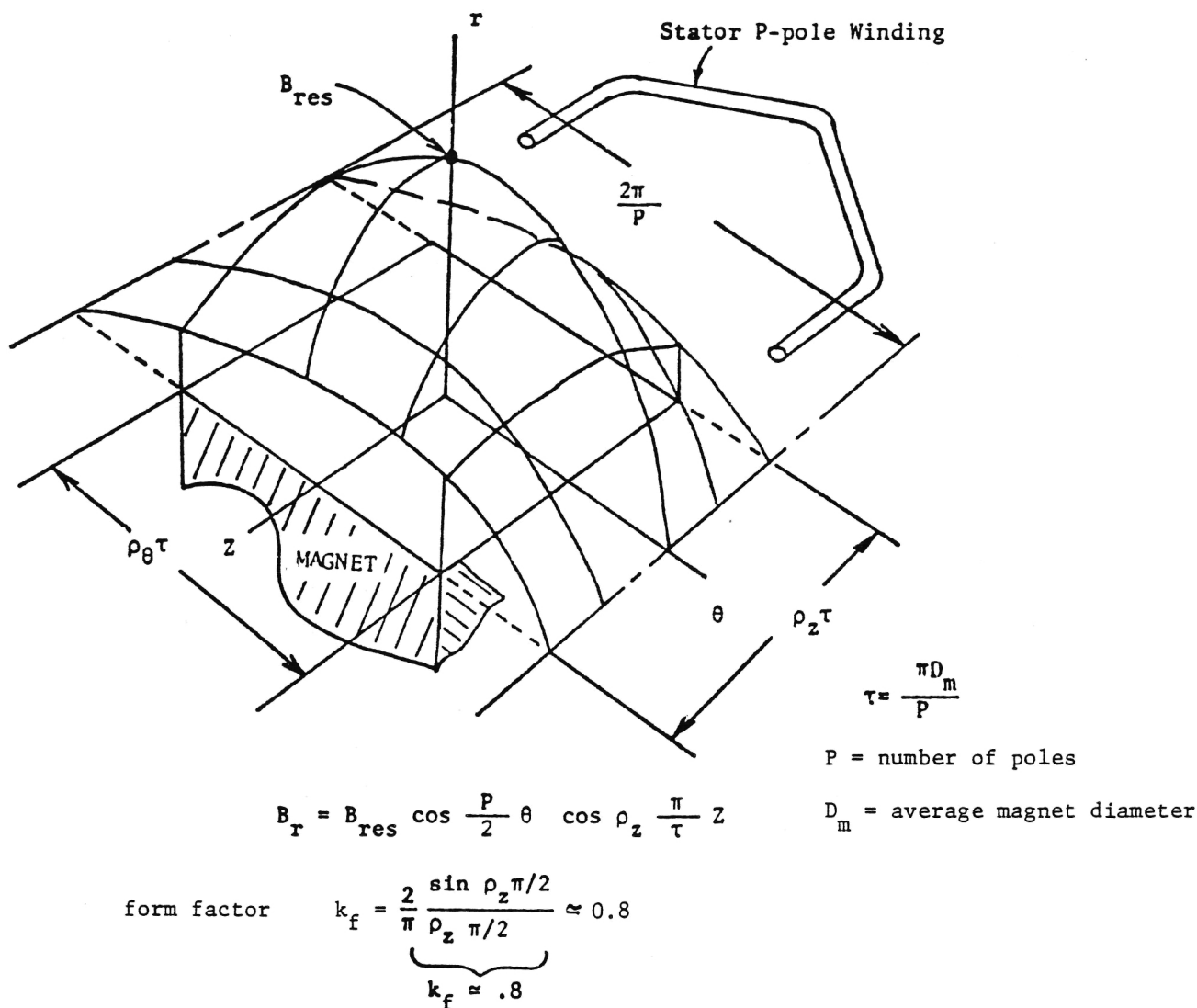


Figure 4-10. Approximate Three-Dimensional Field of the Magnet Flux and the Form Factor

4.6.2 Effect of Boundaries on Inductance

At synchronous speed, the fundamental flux wave travels at the same velocity as the rotor and induces no currents in the rotor. However, each harmonic of the stator field will induce rotor currents. The reactance associated with the fundamental wave is the synchronous reactance $x_d = x_q$, while the reactance associated with the harmonics essentially is the subtransient reactance, $x_d'' = x_q''$, which in this case is also the "commutating reactance," x_c .

The inductance of each stator winding of an exploratory machine (not the functional model) was measured in a variety of ways using a General Radio impedance bridge 1650-B operating at 1000 Hz. Table 4-2 shows the results of these tests. Emphasis was placed on the effect of the aluminum frame and the presence or nonpresence of the magnets.

Table 4-2
TESTS ON EXPLORATORY MACHINE

<u>Exploratory Machine</u> (not functional)	<u>Inductance (μH)</u>
1. One 32-turn stator winding in air	19.0
2. Stator placed on iron core with no aluminum housing	32.5
3. Stator placed on iron core with aluminum housing	29.5
4. Two stator assemblies laid flat and connected in parallel (no magnetic coupling)	15.9
5. Two stators assembled as in actual motor, windings connected in parallel, but with no rotor. Remaining phases are open.	15.5
6. Same as 5 except remaining two phases are connected in parallel but not externally excited. Neutral open. Did not change with neutral closed.	14.0
7. Same as 6 except with stationary rotor.	13.0

Measurements pertain to one stator winding with the other two windings not excited. This measurement, when transferred to a real machine with the mutual coupling of the other two phases considered, must be multiplied by $3/2$. In summary, with reference to Table 4-2,

- a) The presence of unshielded aluminum housings will decrease the inductance by 9% due to coupling with the aluminum (Tests 2 and 3).
- b) The coupling between two stators facing each other and separated by two 1.13-cm air gaps and a 5.08-cm magnet (of permeability unity) will decrease the inductance by only 3% (Tests 4 and 5).
- c) The disc motor employing Alnico 8E magnets with a recoil permeability of 2.07 will increase the inductance by 27% over magnets made from CoSm with a unity permeability (a calculated result).
- d) The synchronous inductance L_d is given by the inductance of Test 5. Multiplied by $(3/2 \times 1.27) = 1.91$ or

$$L_d = 15.5 \times 1.91 = 29.6 \mu\text{H}$$

4.6.3 Prediction of Parameters and Design Quantities

Table 4-3 gives a listing of the predicted parameters and design quantities.

4.6.4 Prediction of Performance

The results of the performance prediction and analysis codes are shown in Figures 4-11 through 4-15. These figures pertain to:

- (a) Performance with the machine at the cruising rating of 11.2 kW (15 hp), 732 Hz, 11,000 rpm (Figure 4-11).
- (b) Performance with the machine at the 5-minute rating of 29.8 kW (40 hp), 466 Hz, 7000 rpm (Figure 4-12).

Table 4-3

A LISTING OF DESIGN DATA AND PREDICTED PARAMETERS

a. General	Cruising	5 Min
rated power output	11.2 kW (15 hp)	29.8 kW (40 hp)
rpm	11,000	7,000
Vehicle speed	88.5 km/h (55 mph)	56.3 km/h (35 mph)
Current (amp)	62	190
Frequency, (Hz)	732	466
Voltage (line-rms)	127	105
b. Stator Winding		
Number of poles	8	8
Strands per conductor	6	6
Wire size (each strand)	0.145 cm × 0.1133 cm. (0.0571 × 0.0446 in.)	(over insul.)
Copper area (each strand)	0.0131 cm. ² (0.00203 in. ²)	
Turns per coil	4	
Number parallel circuits (two stators)	2	
Turns/phase, N_1	32	
Effective turns/phase	29.6	
Total conductor area	0.1574 cm. ² (0.0244 in. ²)	
Current density, J_a	394 A/cm. ² (2540 A/in. ²)	1266 A/cm. ² (7787 A/in. ²)
Surface current density, K_a	208 A/cm. (529 A/in.)	637 A/cm. (1617 A/in.)
$K_a = 2mN_1I_1/P\tau$		
c. Motor Parameters, ohms (Stator halves in parallel)		
	732 Hz	466 Hz
Stator resistance, r_1 at 25 °C	0.012	0.012
Magnetizing reactance		
x_{md}	0.11	0.07
x_{mq}	0.11	0.07
Stator leakage reactance, x_1	0.036	0.023
Synchronous reactance		
x_d	0.146	0.093
x_q	0.146	0.093
Rotor resistance, r_2 at 25 °C	0.09	0.09
Rotor leakage reactance, x_2	0.18	0.01
Transient reactance, $x_d' = x_q' = x_d$	0.146	0.093
Subtransient reactance, $x_d'' = x_q''$		
$X_d'' = x_1 + x_m x_2 / (x_m + x_2)$	0.10	0.064
Commutating reactance, $x_c \Delta x_d''$	0.10	0.064
Open circuit voltage (line-rms)	202	129
Windage loss (W)	400	162
Core loss (W)	120	61
Stray load loss (resistor-ohms)	0.009	0.009
d. Rotor and Stator Dimensions		
	in.	cm
Rotor OD, overall	10.50	26.7
Rotor OD, D_o (over magnets)	9.50	24.1
Rotor ID, D_i (under magnets)	4.88	12.4
Rotor diameter, $D_r = (D_o + D_i)/2$	7.19	18.3
Stack length, $l_s = (D_o - D_i)/2$	2.31	5.85
Conductor effective length = l_s	2.31	5.85
Stator surface area, both sides	104	673
$2(\pi D_r l_s) = 2(\pi/4)(D_o^2 - D_i^2)$		
Pole pitch, $\tau = \pi D_r / P$	2.82	7.17
Air gap, g (one side)	0.445	1.13

Table 4-3 (Cont'd)

e. Magnet Characteristic (see Figure 4-7)

Material	Alnico 8E
B_r	0.8000 T
H_c	154 A/in. (1940 oersted)
Slope of recoil line, μ'	2.07
Linear equivalent	
B_r (recoil) 7600/1.1	0.6900 T
H_c (recoil) = B_r/μ'	263 kA/m (3300 oersted)

	<u>in.</u>	<u>cm</u>
Magnet effective width w_m	1.2	3.05
Magnet length L_m	2.0	5.08
Magnet area	5.54 in. ²	36 cm ²
Magnet volume V_m	11.08	182
Magnet density	0.262 lb/in. ³	18.4 g/cm ³
Magnet weight (one)	2.8 lb	1.3 kg
Magnet weight (all)	22 lb	10.4 kg

f. Weights

	<u>lb</u>	<u>kg</u>
Housing (one)	7.2	3.3
Iron core	11.2	5.1
Winding (one)	4.3	2.0
Encapsulant (no iron)	8.3	4.8
One stator half	31.0	14.0
Two stators	62.0	28.0
Spacer	5.0	2.3
Rotor assembly	38.0	17.3
Miscellaneous (bearings, two blowers, end caps, etc.)	12.0	5.5
Total motor	117.0	53.1

Note: Reactances and open-circuit voltage are referenced for an encapsulated stator having no iron powder.

- (c) Open-circuit voltage with five possible corner points (Figure 4-13). This illustrates the extent of phase-back on E_o at the five speeds of 11,000 (no phase-back), 10,000, 9000, 8000 and 7000 rpm.
- (d) Performance at 15 hp, 732 Hz, with E_o phase back (Figure 4-14).
- (e) Commutation limits showing the overlap angle plotted against dc link amperes for constant values of dc link voltage (Figure 4-15). Hence the abscissa is proportional to dc link power $V_{dc} I_{dc}$ or roughly to the motor input power. Five curves are shown corresponding to

Frequency, Hz	Motor Speed (rpm)	Vehicle Speed (mph)	(km/h)
732	11,000	55	88.5
466	7,000	35	56.3
360	5,410	27	43.4
240	3,600	18	29.0
120	1,800	9	14.5

The inverter-motor system (as shown in Figure 4-15) commutates 30 kW at 732 and 466 Hz, and less but still adequate kW loads at the lower speeds.

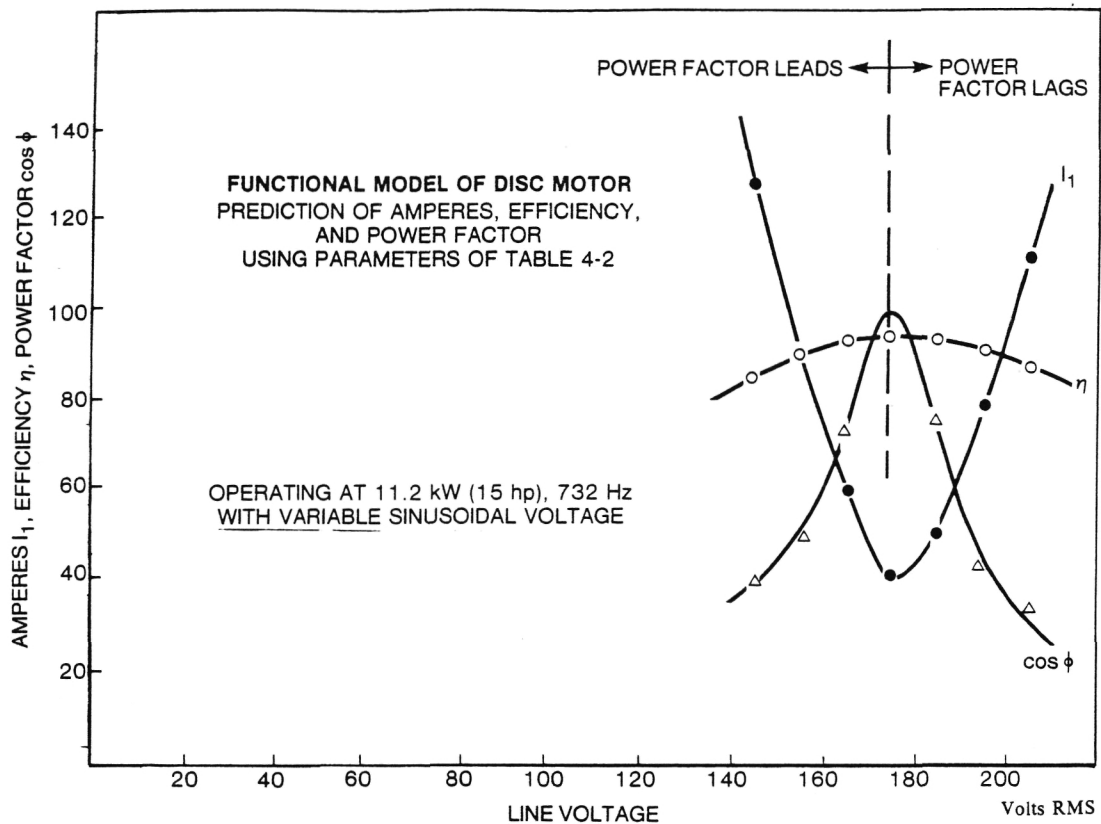


Figure 4-11. Functional Model of Disc Motor Operating at 11.2 kW (15 hp), 732 Hz with Variable Sinusoidal Voltage (Prediction of Amperes, Efficiency, and Power-Factor Using Parameters of Table 4-2)

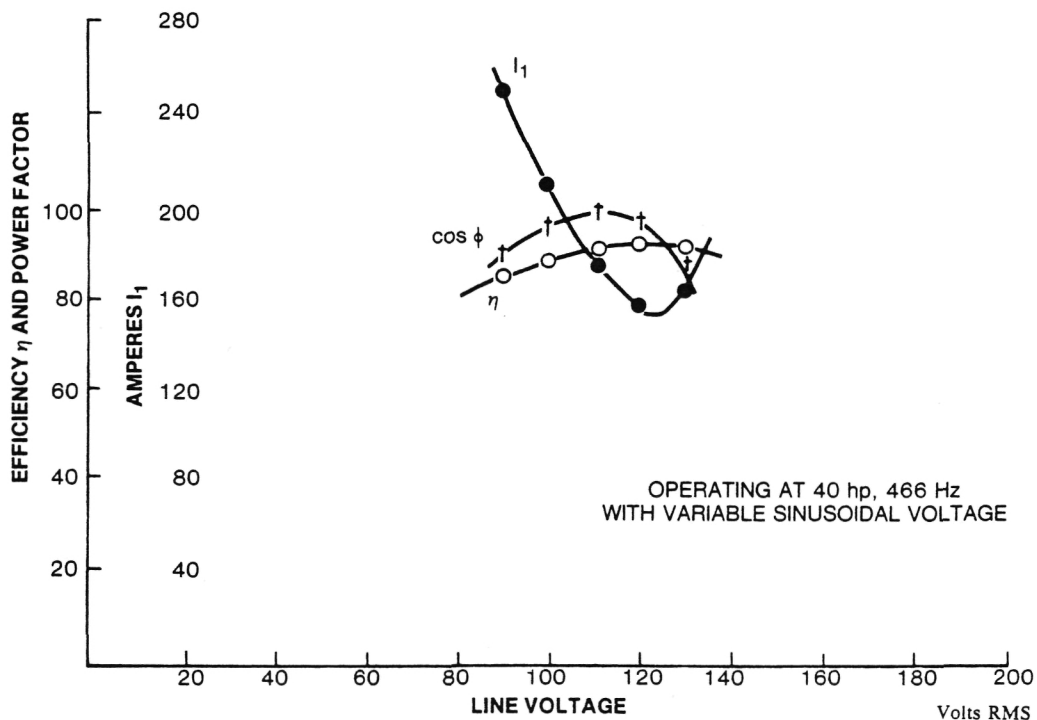


Figure 4-12. Functional Model of Disc Motor Operating at 29.8 kW (40 hp); 466 Hz with Variable Sinusoidal Voltage (Prediction of Amperes, Efficiency and Power-Factor Using Parameters of Table 4-2)

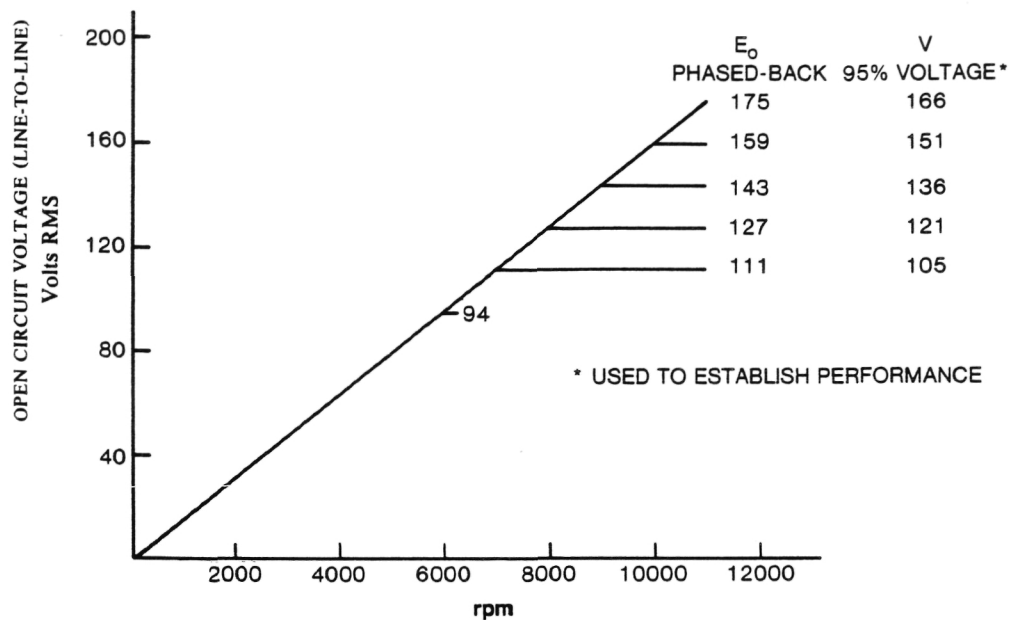


Figure 4-13. Open-Circuit Voltage (Line)

PREDICTION OF AMPERES, EFFICIENCY,
AND POWER FACTOR
USING PARAMETERS OF TABLE 4-2

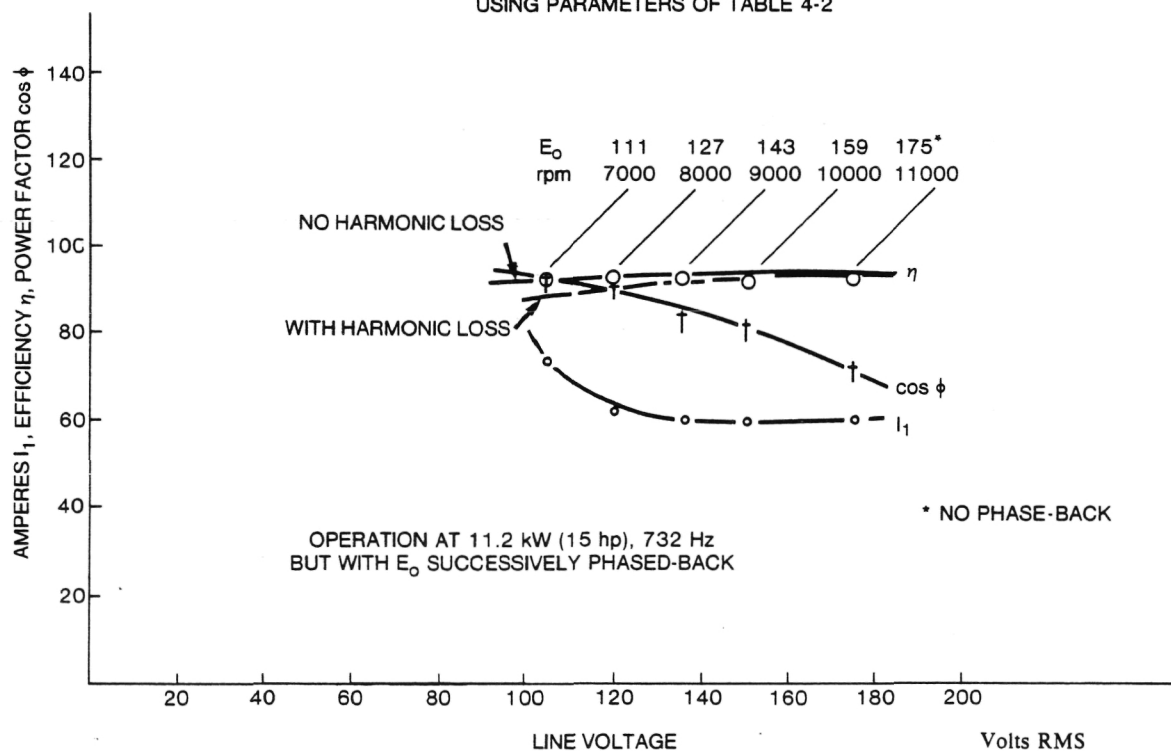


Figure 4-14. Functional Model of Disc Motor Operating at 11.2 kW (15 hp), 732 Hz but with E_o Successively Phased-Back (Prediction of Amperes, Efficiency, and Power Factor Using Parameters of Table 4-2)

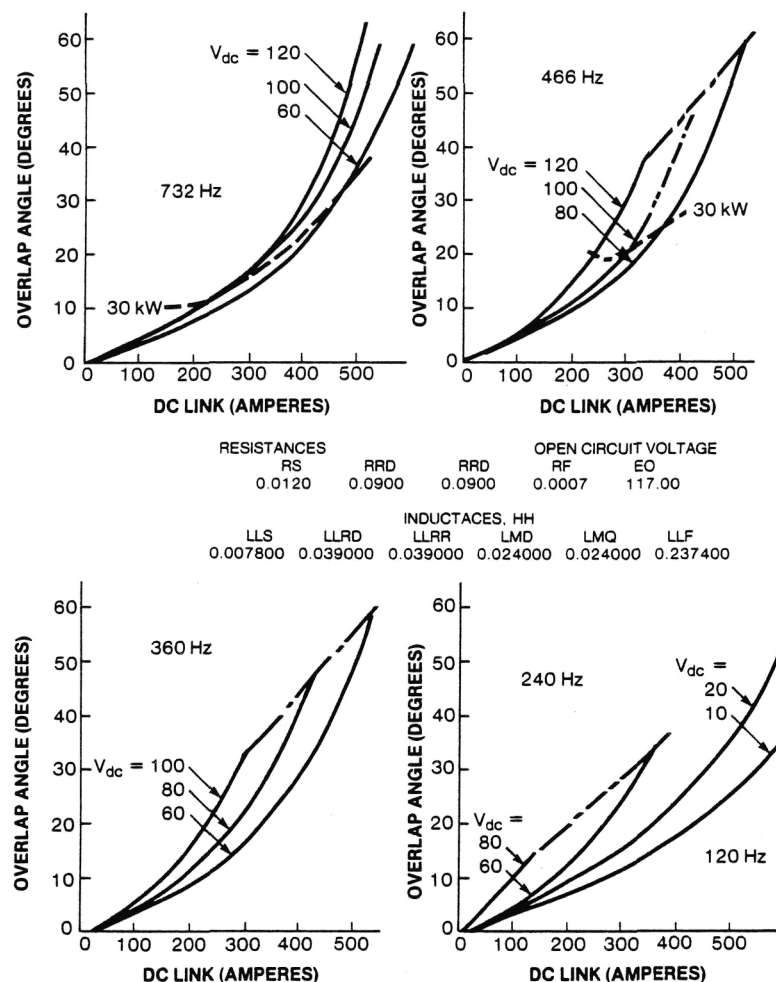


Figure 4-15. Commutation Limits at Various dc Link Voltages and Inverter Frequencies

The temperature rise of the motor was predicted by making a linear, lumped thermal network to represent the heat sources and heat transfer paths in the motor. For simplicity, the thermal resistances were considered to be linear. While a set of equations may be written to model the motor, the results must be treated very cautiously due to the great difficulty of determining the proper heat transfer coefficients and thermal impedances as well as the representation of a distributed and nonlinear complex system by linear lumped elements. A finite element approach would be better, but is beyond the scope of the study.

Figure 4-17 displays the maximum winding temperature as a function of power output at 7000 rpm for several assumed case eddy current losses and surface heat transfer coefficients.

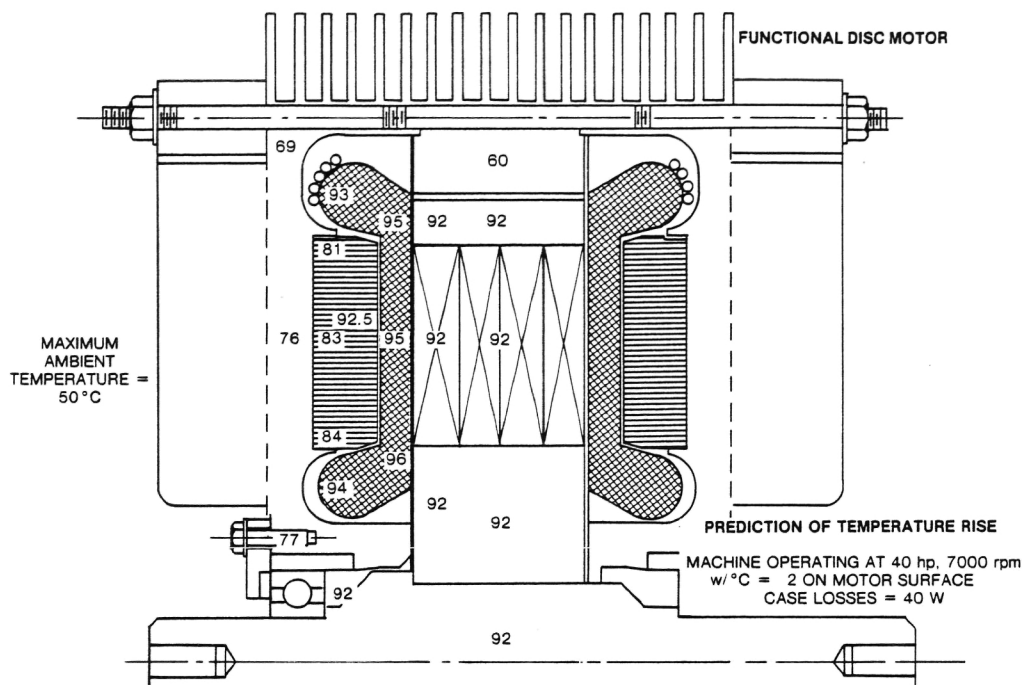


Figure 4-16. Prediction of Temperature Rise (Machine Operating at 29.8 kW (40 hp), 7000 rpm W/°C = 2 on Motor Surface; Case Losses = 40 W)

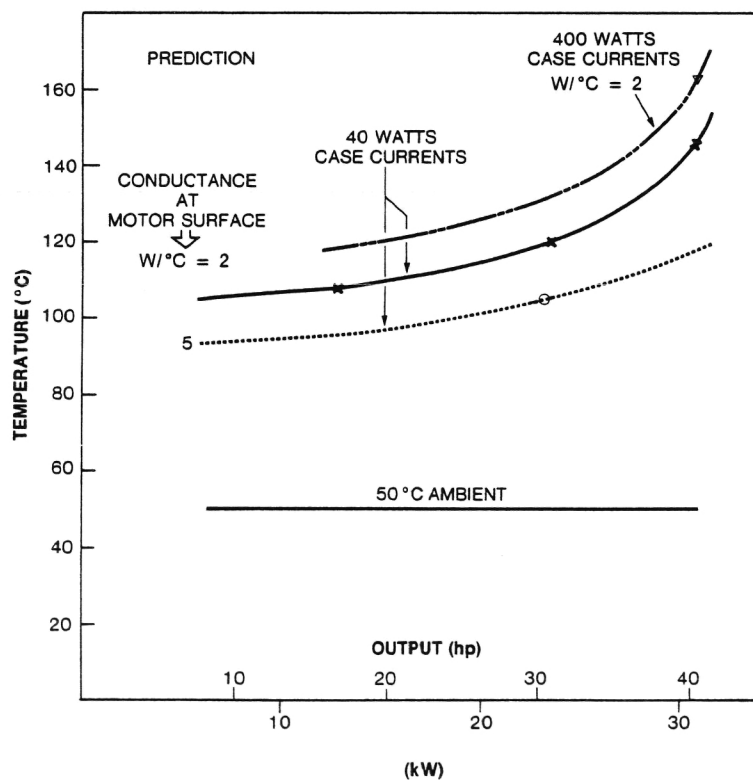


Figure 4-17. Maximum Coil Temperature of Disc Motor (Various Loads and Cooling Systems) - Prediction

4.7 DESIGN DESCRIPTION

The plan of the motor is shown in Figure 4-18. The cutaway portion shows part of the rotor consisting of an aluminum hub with pockets cut out to accept the trapezoidal magnets shown in Figure 4-7. Small semicircular slots are cut into the side of the pockets at their base for stress relief. These are also utilized to epoxy the magnets in place during assembly. The rotor hub is shrunk onto a steel shaft. The mechanical strength of the rotor is provided by an Inconel rim shrunk onto the hub and magnet assembly. The central part of the motor frame, called the spacer, extends to within 0.102 mm (0.040 in.) of the rotor to minimize windage loss and to provide emergency mechanical energy absorption.

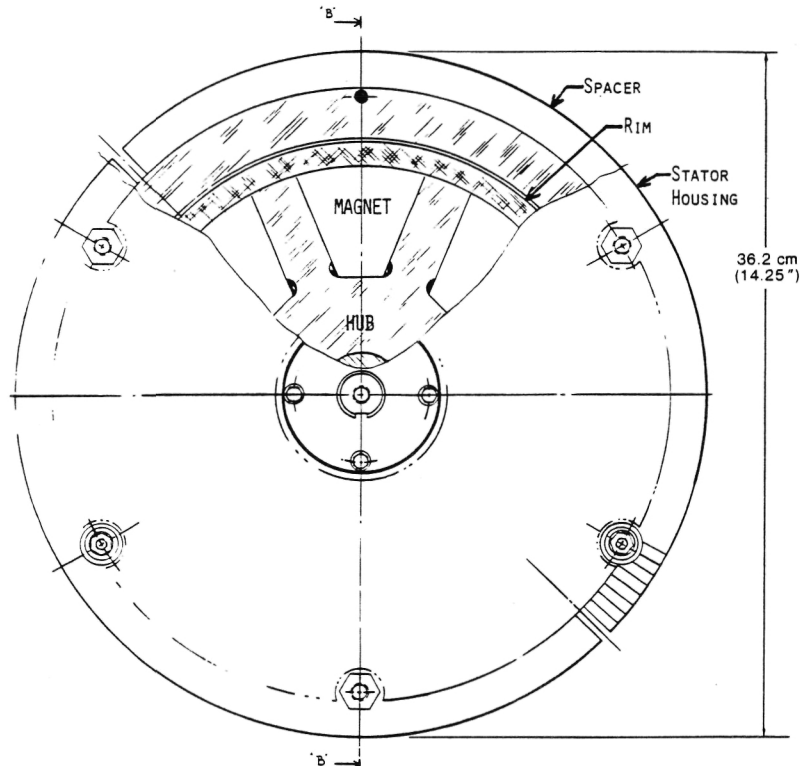


Figure 4-18. Layout of the Functional Model Motor

A cross section of the motor is shown in Figure 4-19. Additional detail of the rotor shows the three-layer construction of the magnets and the hollow shaft to accommodate thermocouple leads. The motor case is divided into three parts: the two stators and the spacer. All three parts have fins for effective heat transfer. The entire assembly is held together by through-bolts which also become part of the mounting system. The flux return path is provided by a spiral wound yoke of thin silicon steel epoxy bonded to the aluminum stator shell. The three layer winding rests, with suitable insulation, on top of this yoke. Each layer is separately fabricated and formed before installation. A thin layer of iron powder-epoxy composite is applied to the walls of the stator cavity to absorb stray fluxes from the end windings. After assembly, the entire structure is filled with a loaded epoxy and cured; the air gap is then machined to a flat surface. Figure 4-20 shows the completed functional model motor. Figure 4-21 is a view of the completed rotor, and Figure 4-22 is a view of one completed stator side.

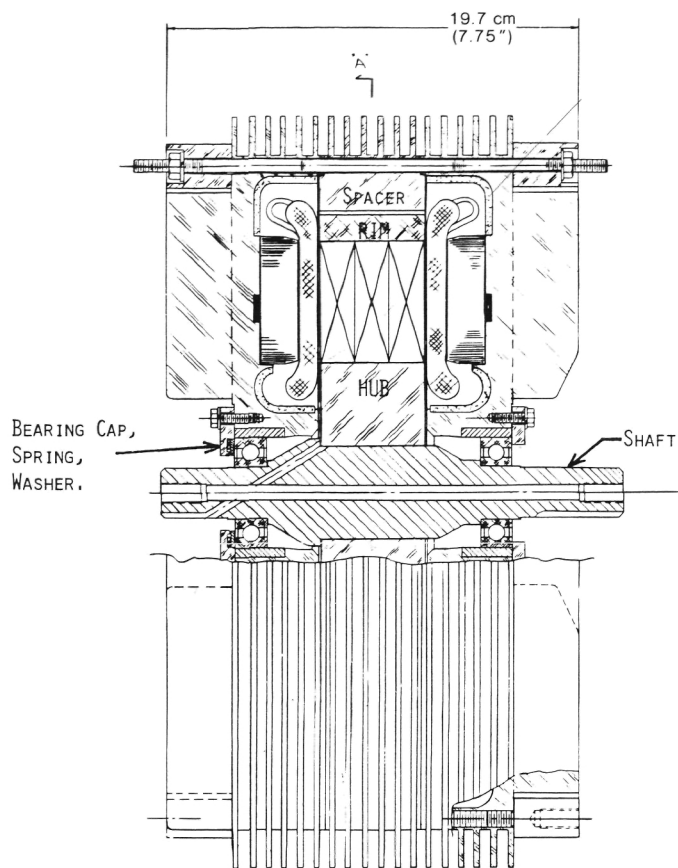


Figure 4-19. Cross Section of the Functional Model Motor

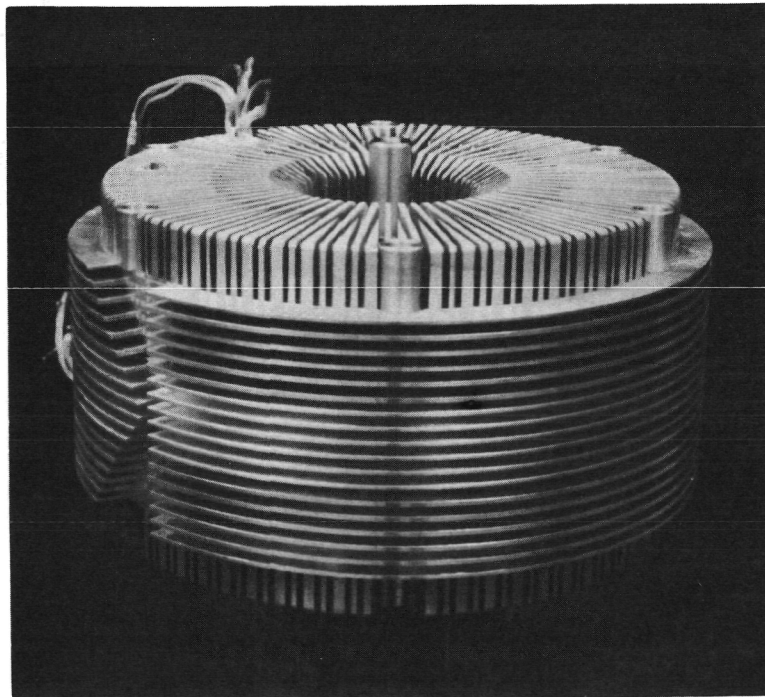


Figure 4-20. Completely Assembled Functional Model Motor

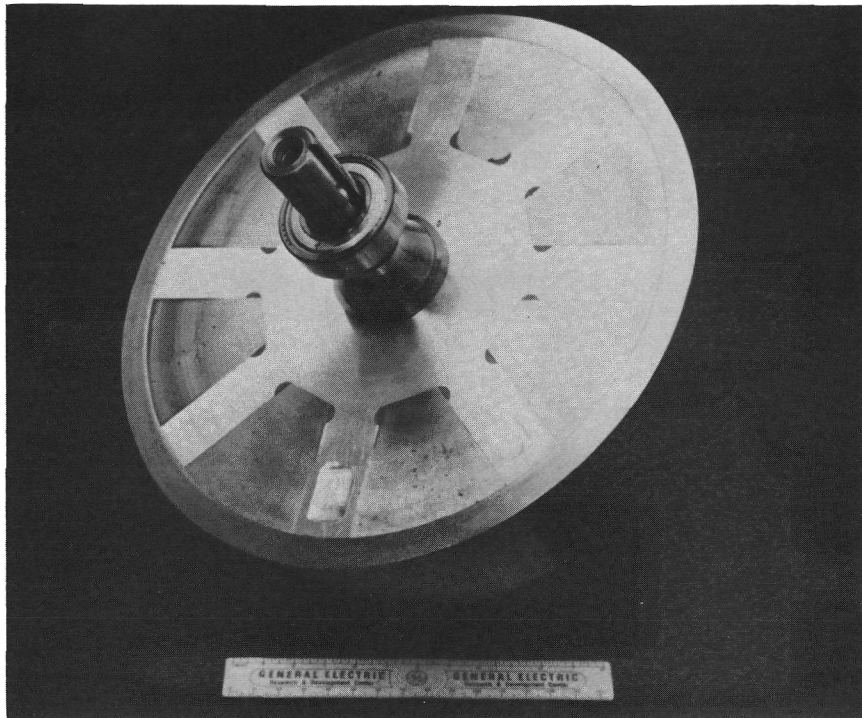


Figure 4-21. Finished Rotor of the Functional Model Motor

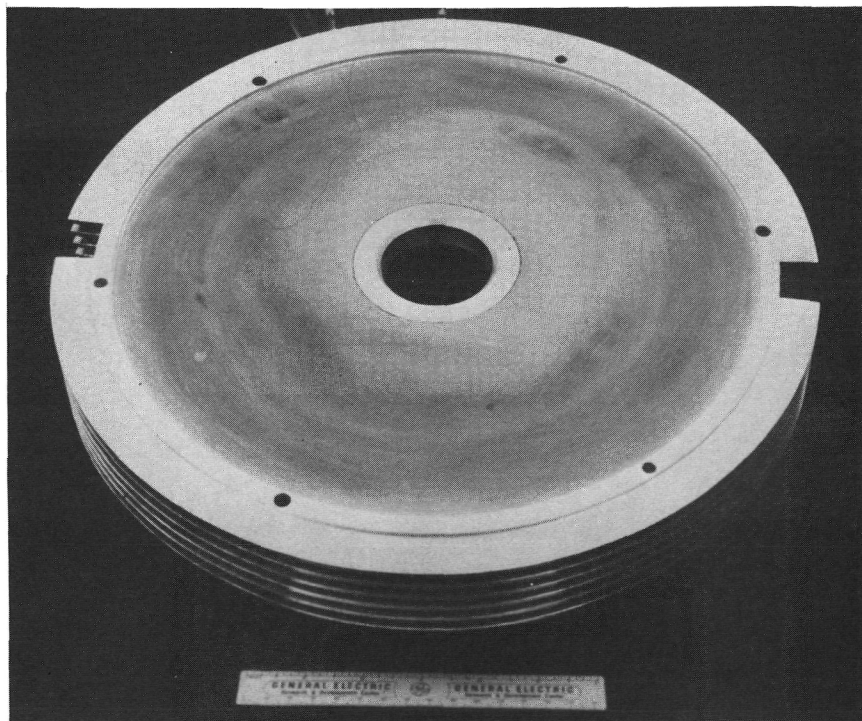


Figure 4-22. Active Face of a Stator Side (FM)

4.8 MECHANICAL DESIGN

The design basis for the mechanical engineering of the functional model is summarized in Table 4-4. The most critical element is again the rotor, but now attention must be given to the efficient removal of heat from the stator exterior; hence the extensive use of fins.

Table 4-4
FUNCTIONAL MODEL MOTOR
MECHANICAL DESIGN BASIS

Requirements

Speed (maximum)	—	11.0 krpm
Torque (peak)	—	237 N-m (175 ft-lb) at 7.5 krpm
Rotor	—	8 Alnico Magnets 12.1 cm. (4.75 in.) OR 6.2 cm. (2.44 in.) IR 5.1 cm. (2.00 in.) Thick Contain Thermocouples
Rotor/Frame	—	Minimum Axial Gap
Cooling	—	External, Air 1 kW Heat Load

The rotor geometry is somewhat different from that of the proof-of-principle motor in that the magnets are full trapezoids (no cut off corners), as shown in Figure 4-23. The stress analysis is very similar to that detailed for the proof-of-principle motor in section 3.5. A summary of the geometric basis of the calculation and the critical loads is shown in Figure 4-24.

The sequence of events in the fabrication of the rotor is shown in Table 4-5. A summary of the overall case dimensions, principal materials, and significant design speeds is given in Table 4-6. Note that three speeds are presented. The first is the maximum operating speed, which is the speed above which the motor must not be routinely operated, corresponding to 88.5 km/h (55 mph). The second is the design maximum speed, corresponding to 106 km/h (66 mph), at which the rim will start to separate from the hub, thus endangering the structure. The third, corresponding to 96.6 km/h (60 mph), is the verification speed which the motor may be allowed to reach occasionally.

There were some special problems associated with the rotor assembly. The first of these was that the Alnico8E magnets were received with many extensive cracks. This problem was handled by switching from titanium to Inconel for the rim material to minimize assembly stress. A program of verification testing of the magnets on a testing machine at maximum stress and temperature was carried out. Cycling of one magnet continuously eventually destroyed the epoxy bonding, but not the magnet itself. All magnets were checked for stress at temperature before being approved for use in the rotor.

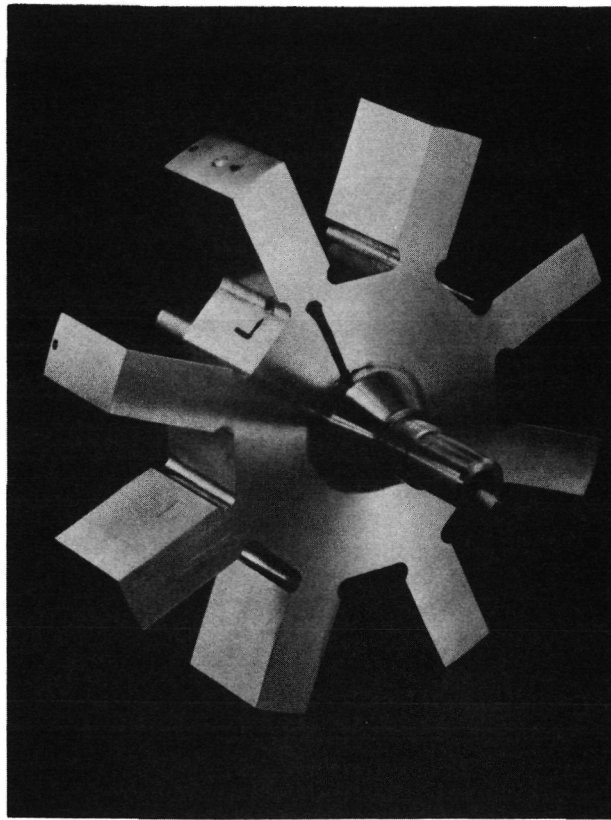
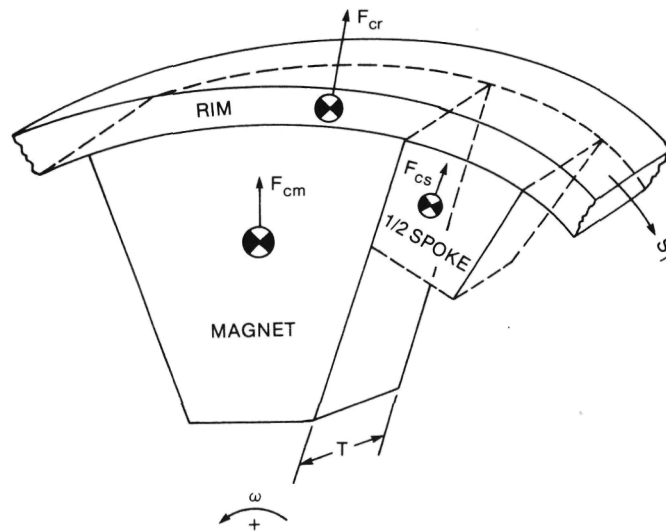


Figure 4-23. Functional Model Rotor Hub with Shaft



$$F_c = Mxa = M\frac{\omega^2}{T}$$

$$S_T = F [N(F_{cm} + F_{cs}) + F_{cr}]$$

AT 13.2 kRPM; $T = 5.1$ cm
(2.0")

8 F_{cm}	=	149 Mg (329 kLB)
8 F_{cs}	=	24 Mg (52 kLB)
F_{cr}	=	106 Mg (233 kLB)

Figure 4-24. Rim Loading Model

Table 4-5
FUNCTIONAL MODEL MOTOR
ROTOR ASSEMBLY SUMMARY

Rotor

- Hub machined, inspected
- Hub 0.086 mm (0.0034 in.) shrink-fit on shaft
- Hub/shaft dynamically balanced
- Magnets epoxied in hub, ground
- Rim heat-treated, finish machined
- Rim shrink-fit on hub
 - Tensile prestress > centrifugal forces
 - 0.810–0.838 mm. (0.032–0.033-in.) interference
 - 689 MPa (100K lb/in.²) maximum tension
- Final OD = 26.72 cm. (10.52 in.)
- Final dynamic balance on bearings

Table 4-6
FUNCTIONAL MODEL MOTOR
DESIGN SUMMARY

Rotor Speeds	—	11.0 krpm Maximum Operating 13.2 krpm Design Maximum 12.1 krpm Spin Test
Outline Dimensions	—	362 cm. (14.25 in.) Case OD 19.7 cm. (7.75 in.) Case Length 22.6 cm. (8.88 in.) Overall Length
Materials		
Shaft	—	303 Stainless
Hub	—	Aluminum Alloy 2024-T3
Rim	—	Inconel 718, Heat-Treated
End Frame	—	Aluminum Alloy 6061-T6
Spacer	—	2024-T3

The completed and balanced rotor was run up in the spin test facility. The results of these tests are summarized in Table 4-7.

Since the motor was to be tested in an open area, an examination of the failure modes was required. Following this, design changes were made in the motor and mounting frame to guarantee that there would be no injuries or damage to the laboratory as the result of a motor failure. A summary of this effort is given in Table 4-8.

Table 4-9 summarizes the remaining machine design data. The top section of the table relates to the axial and radial design clearance gaps, which in turn determine the windage loss; the axial preload is another, but less important, factor in the mechanical losses. The bottom section contains data on the fan system for removing heat from the finned surface.

Table 4-7

**FUNCTIONAL MODEL MOTOR
ROTOR PERFORMANCE VERIFICATION**

<u>Item</u>	<u>Prediction</u>	<u>Performance</u>
Rotor Bending Critical Speed	560 Hz	No resonances to 205 Hz
Rotor Torsional Critical Speed	135 Hz	No evidence to 167 Hz
Rotor Inertia	0.62 kg-cm-sec ² (0.54 lb in.-sec ²)	
Rim Separates from Hub	13.2 krpm	No evidence up to 12.3 krpm

Table 4-8

FUNCTIONAL MODEL SAFETY

Speeds	—	11.0 krpm Operating 13.2 krpm Design 12.1 krpm Spin Test (Passed)
Kinetic Energy of Magnets + Rim = 95 kJ (70K ft-lb) at 11 krpm		
Failure Modes and Safety Considerations		
Rim Breaks —		
Spacer absorbs 2/3 of kinetic energy		
Motor mount absorbs balance of energy		
Rotor Locks —		
Mounting studs shear		
Motor spins down within mounting frame		
External cables can absorb remaining kinetic energy		
Additional Precautions		
Each magnet load-tested		
Rim ultrasonically inspected		

Table 4-9
FUNCTIONAL MODEL MOTOR
WINDAGE AND COOLING

Rotor/Frame Interface

Clearance Gaps = 0.76 mm (0.03-in.) axial, 1.52 mm (0.06-in.) radial
Windage Loss = 350 W at 11 krpm
Axial Bearing Preload = 13.6 kg (30 lb)

Air Cooling

2 Blowers
1/2 Circumference Radial Flow
4 m³/min (140 cfm) volume flow rate

4.9 MAGNETIZATION IN PLACE

In dealing with permanent magnet motors of all descriptions, it is highly desirable to postpone activation of the magnets to the latest possible stage of the assembly process due to the obvious difficulties of handling individual magnets or the assembled rotor in an active state. The elimination of a special magnetizing rig could be another cost saving. The ultimate in this respect is to activate the magnets after the motor is assembled, which is a normal practice in PM dc machines. An auxiliary winding is usually included in the motor for this purpose. In an ac motor with magnets on the rotor, this option is not available.

An additional option was created that appears to be unique: magnetizing after motor assembly by using the stator windings as a magnetizing jig. In this procedure, one (or two in series) of the three phases of the stator are pulsed with a very high current obtained from the discharge of a capacitor bank (Figure 4-25). The position of the magnets on the rotor is referenced to a mark on the shaft, and the magnets are lined up with a stator phase (or two phases) before excitation. Before attempting to magnetize the motor in this way, a series of tests were done with model coils to verify that the large stresses resulting would be adequately borne and that the required flux densities could be achieved.

The parameters of the capacitor discharge circuit are given in Table 4-10, and an electromagnetic summary is given in Table 4-11.

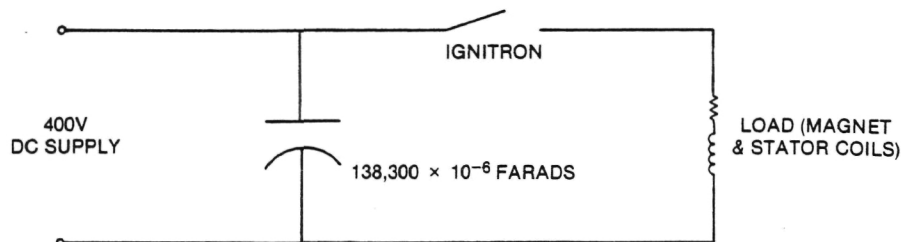


Figure 4-25. Magnetizing Circuit for Alnico 8 Motor Magnets

Table 4-10
MAGNETIZATION IN PLACE OF ALNICO 8 MAGNETS
CIRCUIT PARAMETERS

Capacitance — 138,300 μ F

DC Voltage — 400 V

Stored Energy — 11,064 J

Pulse Time — 0.030 sec

Current — 5500 A

4 Turns Per Coil

Flux Density in Gap — 0.3000 T

Table 4-11
MAGNETIZATION IN PLACE
POTENTIAL MAGNETIZING FORCE

2-4 Turn Stator Coils in Series

8 Turns Total

Peak Current — 5500 Amperes

Excitation — 44,000 Ampere Turns

Magnetizing Field — 875 kA turns/meter (22,000 ampere turns/in.)

Magnetizing Field — 11,000 Oersteds

A critical question in this method is "How long must the pulse be?" All of the data stated so far relates to the required magnitude of the current pulse. Table 4-12 provides a way of estimating how long the pulse must be. Here the depth to which the field pulse penetrates the magnet structure within the time that the pulse lasts is calculated approximately. The penetration of the field is resisted by induced circulating currents in the magnet itself. Hence, the magnet material resistivity and the initial permeability are involved. The frequency used is the dominant frequency of the pulse Fourier transform. For uniformity of magnetization, no dimension of the block should be greater at the maximum than twice the penetration depth. Since the largest dimension is 6.9 cm (2.7 inches) compared to a penetration depth of 6.2 cm (2.4 inches), uniformity of magnetization should be adequate, although technicians experienced in these methods would prefer much longer pulses to account for uncertainties in the approximations and eddy currents in the case (the iron will saturate). Recent investigations have also shown that the initial permeability is often larger than the recoil permeability used here.

Table 4-12

ALNICO MAGNETS
DEPTH OF PENETRATION

skin depth	=	$\frac{1}{2\pi} \sqrt{\frac{\rho \times 10^9}{f \times \mu}}$
resistivity, ρ (ohm-cm $\times 10^{-6}$)	—	50×10^{-6}
frequency, f (Hz)	—	16.6 (0.030 sec pulse)
relative permeability, μ	—	2
	=	$\frac{1}{2\pi} \sqrt{\frac{50 \times 10^{-6} \times 10^9}{16.6 \times 2}}$
	=	6.179 cm
	=	2.43 in.
largest magnet dimension	=	6.86 cm (2.7 in.)

5.0 TESTING OF THE PROOF-OF-PRINCIPLE AND THE FUNCTIONAL MODEL MOTORS

5.1 SUMMARY

This section of the report documents tests performed on two of the three synchronous disc machines built under sponsorship of the NASA Lewis Research Center, Cleveland, Ohio. These machines, designed for electric vehicle applications, were tested in two ways: as generators feeding power into a resistive load and as motors operating from a load-commutated inverter (LCI). One of the machines employed cobalt-samarium magnets on its rotor while the other machine used alnico magnets.

The machine which employed cobalt-samarium magnets performed close to expectations, producing approximately 13 hp at a speed of 3000 rpm and achieving a peak efficiency of 88% while driven from the LCI. The machine which employed alnico magnets did not meet its performance expectations primarily because of difficulty retaining the magnetization after the tests began. This motor produced 18 hp at 6000 rpm and achieved a peak efficiency of 86% while operating on the LCI.

5.2 INTRODUCTION

The motors described in this report were built in the early phase of the program. The purpose of this program was to explore the feasibility of lightweight, high-efficiency motors to extend the operating range of electric vehicles. The performance specifications which were to be met by these new motors are shown in Figure 5-1. It is seen that the motors were to be capable of producing 15 hp indefinitely and 40 hp for as long as five minutes.

The motors chosen for this study are ac disc type machines. An exploded view of an ac disc machine is shown in Figure 5-2. These machines have two stator halves on either side of the rotor. The rotor has embedded magnets which are magnetized in the axial direction. Each stator half has an aluminum housing which contains the armature winding and back iron. The back iron provides a low-reluctance path for the returning magnet flux. The stator windings are encapsulated in epoxy and placed between the magnets and back iron.

The advantages of this type of synchronous motor structure are:

1. No field excitation losses
2. Light weight because of few iron parts
3. No stator tooth losses
4. Short motor length in the axial direction
5. Operation on load-commutated inverter feasible.

The disadvantages of this type of motor structure are:

1. Low thermal conductivity exists between armature windings and case.
2. Coils of armature windings are difficult to position properly.
3. Armature conductors must be finely stranded to avoid high eddy current losses.
4. Magnetic air gap is large.
5. Stray fields induce hard-to-calculate losses in structural aluminum.

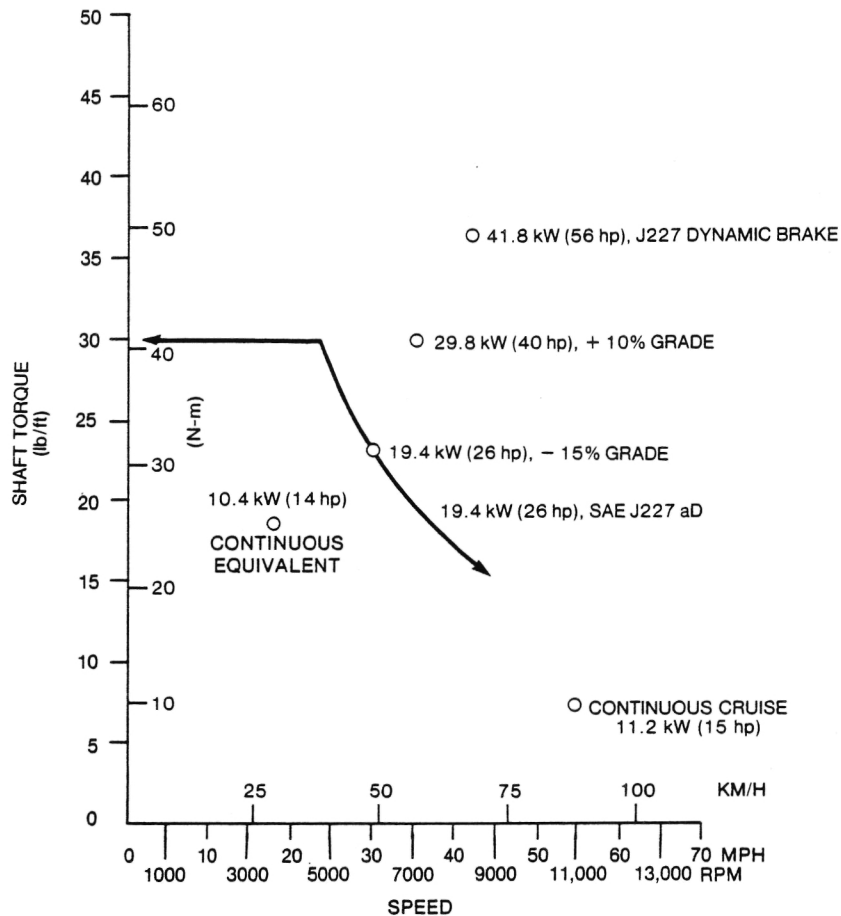


Figure 5-1. Performance Specification for the Application of the Functional Model Disc Motor to an Electric Vehicle.

6. Rotor outer diameter is larger than that of a conventional motor.

Overall, this type of machine appears to be a good candidate to achieve the high efficiency and low weight requirements of the electric vehicle project, although its construction poses a few difficulties.

5.3 DESCRIPTION OF MOTORS TESTED

The two motors described in this report are the Proof-of-Principle (POP) motor and the Functional Model (FM) motor. The POP motor was constructed to have the two stator sides operating with their respective coils paralleled electrically. However, when the two stators were connected in this manner, the slightly different coil voltages caused circulating currents to flow. Because these machines have relatively low stator impedances, these currents were quite large and caused rapid heating in the stators. To avoid this problem, the two stators were disconnected for this series of tests, and the motor was operated using only one stator. All references to the motor operating in this way are given in 1SPOP for one-sided Proof-of-Principle motor.

The FM motor was designed so that the two stators could be connected either in parallel or in series. Since connecting the stators in parallel gave large circulating currents, most of the tests were performed with the two stator sides in series. This condition is designated SFM (series-connected functional model motor). Table 5-1

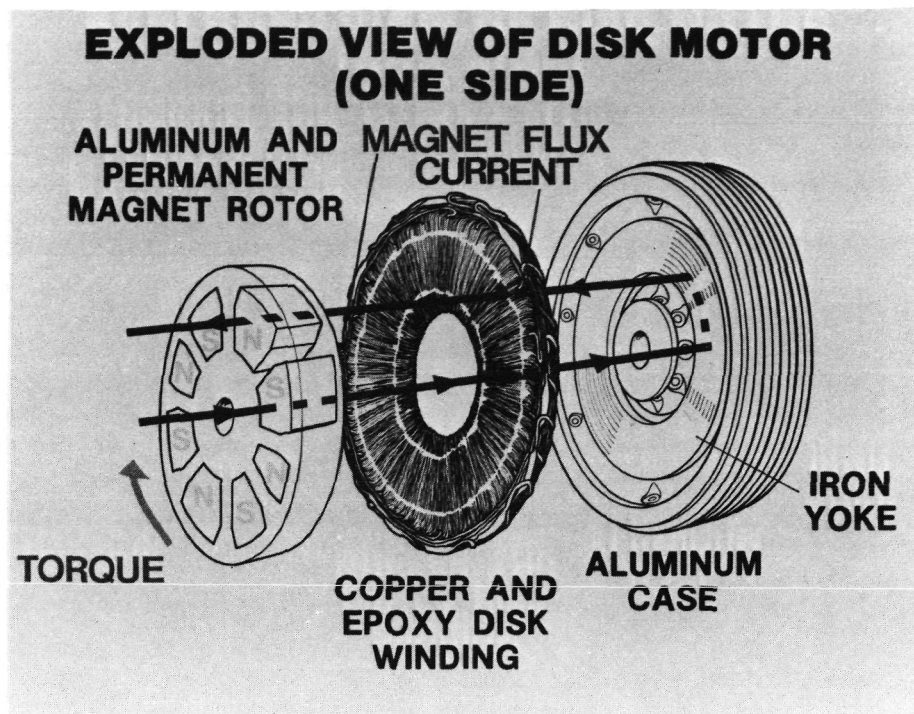


Figure 5-2. Structure of the AC Disc Machines Tested.

shows design data for both of these motors. The greatest differences between the two motors, other than the types of magnets employed, are the maximum rated speed and the cooling systems. The POP motor was limited to 5,000 rpm, while the FM motor was designed to operate up to 11,000 rpm. The FM motor had an elaborate cooling system while the POP had none.

5.4 COIL VOLTAGES AND INDUCTANCES

The first tests performed on the two motors were measurements of the open circuit voltages and inductances of the three-phase coils on each stator (six total coils). Table 5-2 shows this data. When the motors were tested on the inverter, only coils 1, 2, and 3 of the POP motor were used. The FM motor was tested on the inverter with coils 1 and 4, 2 and 5, and 3 and 6 in series.

The open circuit voltages of all coils were very close to ideal sine waves, but were not all 120° out of phase with one another. The voltages from the A, B, and C phase coils of the POP motor were displaced from one another by very close to 120° , but only phases A and C of the FM motor were displaced by this angle. The displacement between the coils of phases A and B was only about 105° .

Table 5-2 shows that the open circuit voltages from the coils of the POP motor were nearly equal. The voltages from the coils of the FM motor differed a bit more. The inductances of the various coils change as the magnets pass the coils, giving high and low readings. The inductances were measured using a 1000 Hz impedance bridge.

All coils of the POP motor were equidistant from the back iron. Thus their inductances, except for coil 6, are approximately equal. In the FM motor, the coils were arranged in layers, with coils 1 and 4 directly against the back iron, coils 3 and 6 next to the air gap, and coils 2 and 5 in the middle of the other coils. This gave coils 1 and 4

Table 5-1
DESIGN DATA FOR POP AND FM DISC MACHINES

<u>Stator Winding</u>	<u>ISPOP</u>	<u>SFM</u>
Number of poles	8	8
Strands per conductor	9	6
Strand size (cm)	0.040 dia.	0.145 x 0.113
Copper area/strand (cm ²)	0.0013	0.0131
Mean length of turn (cm)	28.5	25
Parallel circuits	4	1
Turns per coil per phase	25	4
Coils per phase	8	16
Effective series turns/phase	~45	59.2
<u>Calculated Parameters</u>		
Stator resistance at 25° (C)	0.070 Ω	0.048 Ω
Synchronous inductance, ($L_d=L_q$)	60 μH	100 μH
<u>Magnet Characteristic</u>		
Material	SmCo	Alnico 8E
B_r , T	0.81	0.80
H_c	0.64 MA/m (8000 Oe)	0.15 MA/m (1940 Oe)
Slope of recoil line, μ_r	1.0	2.07
<u>Rotor and Stator Dimensions</u>		
Rotor OD (overall) (cm)	24.9	26.7
Rotor OD (over magnets) (cm)	22.9	24.1
Rotor ID (under magnets) (cm)	12.7	12.4
Rotor length (thickness) (cm)	5.23	5.05
Clearance gap/side (cm)	0.127	0.076
Rotor to back iron gap/side (cm)	1.02	1.10
Stator surface area (cm ²)	570	680
Back iron thickness (cm)	1.90	1.97
Back iron outer diameter (cm)	23.2	24.6
Back iron inner diameter (cm)	12.4	12.1
Machine dimensions, excluding fins		
Diameter (cm)	31.8	32.4
Case length (cm)	13.6	13.3
<u>Magnet Dimensions per pole</u>		
Width at outer radius (cm)	5.08	6.8
Arc of magnet at OD (degrees)	26.3	34.4
Width at inner radius (cm)	3.05	2.4
Length (thickness) (cm)	5.23	5.05
Surface area (cm ²)	23	27
Volume (cm ³)	120	137
Number of magnet poles	8	8
<u>Weights, (kg)</u>		
Housing (both)	~5.0	6.5
Iron cores	8.7	10.2
Windings	3.6	3.9
Encapsulant	~6.3	7.5
Spacer	—	2.3
Rotor magnets	7.9	7.9
Rotor assembly	—	17.2
Miscellaneous	—	5.5
Total	41.5	53.1

Table 5-2
MOTOR COIL TEST DATA

Coil	Phase		Open Circuit Voltage (at 5000 rpm)		Inductance (μ H)	
	POP	FM	POP	FM*	POP	FM
1	A	A	84.4	34.9	46-56	28-33
2	B	C	84.2	36.0	45-57	28
3	C	B	84.3	37.5	48-50	26-27
4	A	A	84.6	34.6	47-57	34
5	B	C	84.4	35.4	42-56	26
6	C	B	84.2	37.3	34-37	20-26

*Directly after magnetization

the largest inductances and coils 3 and 6 the lowest. This inductance imbalance, combined with the coil angle imbalance, caused some stability problems while testing the FM motor on the load commutated inverter. The POP motor was much more stable.

While the open circuit voltage of the POP motor remained constant throughout the testing period, the voltage of the FM motor (with alnico magnets) did not. In addition, when the alnico magnets were magnetized using the stator windings, the design value of air gap flux was not achieved. Table 5-3 shows the estimated air gap flux densities of the two motors after various events. It is seen that most of the FM motor tests were performed with approximately two-thirds of the designed value of magnet flux density, which seriously decreased the output capability of the machine. It was initially calculated that the open circuit voltage with complete magnetization should have been 1.5 times higher than the value that was achieved. Later calculations showed that this was not correct and that the actual value with complete magnetization would have been only 1.1 times the value achieved. Thus most of the loss in magnetization occurred during testing, not during magnetization.

5.5 PERFORMANCE SUMMARY

A summary of the performance of the two disc machines is shown in Table 5-4. The open circuit losses at 5000 rpm are estimated from the steady-state temperature rise of the stator windings when the windings are open circuited. In the POP motor, the primary source of this loss was circulating currents flowing between the four paralleled coils in each stator circuit. In the FM motor, the primary source of open circuit losses was stranding loss, which is caused when eddy currents are induced in the stator conductors by the magnet flux. The smaller cross-sectional area of the POP stator conductor strands drastically reduced this loss in that motor. In both motors, these losses were approximately proportional to the square of rotor speed.

The efficiency of the two motors was not particularly high for a 15 hp motor. The highest efficiency observed in tests of the FM machine was 90% while generating into a resistor bank and 86% while operating from the LCI. The POP motor had similar efficiencies. The highest power attained from the FM motor was approximately 18 hp at 6000 rpm. The 1SPOP motor attained 13 hp at 3000 rpm. Neither of the motors

Table 5-3
APPROXIMATE AIR GAP FLUX DENSITIES OF TESTED MOTORS
(Values Are Ratioed from Open Circuit Voltages)

	Flux Density (Tesla)	
	POP (Co-Sm)	FM (alnico)
Design Value	—	0.3300
After Magnetization	0.5600	0.3000*
After Load Tests	0.5600	0.2850
After 1st Inverter Test	0.5600	0.2450
At End of Testing	0.5600	0.2330
After Motor Disassembly and Reassembly	0.5600	0.2270

*Measured at center of magnet

Table 5-4
PERFORMANCE SUMMARY FOR POP AND FM DISC MOTORS

	1SPOP	SFM
Maximum Rated Speed (rpm)	5000	11,000
Open Circuit Volts at 5000 rpm (volts-rms)	84.2 to 84.4	54.0 to 58.2*
Phase Resistance at 20°C (ohms)	0.062	0.042
Phase Reactance at 5000 rpm (ohms)	0.12	0.18 to 0.24
Open Circuit Losses at 5000 rpm (watts)	400	275
<u>Tested Performance with Resistive Load</u>		
Peak Efficiency at 5000 rpm, %	89	90
Winding to Case Thermal Resistance, °C/(kW)	70	53
Case to Ambient Thermal Resistance, °C/(kW)	58	17
Stator Winding Thermal Time Constant, min.	10	12
<u>Tested Performance with Load-Commutated Inverter</u>		
Stability	Good	Fair
Peak Torque	32 N-m at 3000 rpm	22 N-m at 6000 rpm
Peak Output Power	9.7 kW (13 hp) at 3000 rpm	13.4 kW (18 hp) at 6000 rpm
Peak Efficiency	88% at 2800 rpm	86% at 5500 rpm
Windings to Ambient Thermal Resistance, °C (kW)	130	65

*Stable values after start of inverter tests

attained the peak torque requirement of 41 N-m. For both motors, the peak powers listed are the largest electromagnetic values achieved while the motors were operated on the LCI. The power the motors could supply on a continuous basis was approximately two-thirds of the peak power listed in Table 5-4.

The thermal resistances for the two motors are calculated from steady-state temperature rises and estimates of stator winding losses. It is seen that the higher thermal resistance of the POP motor is largely due to poor heat transfer from the case to the ambient air. To give a number for comparative purposes, the thermal resistance of a 37 kW (50 hp) induction machine is approximately 15°C per kW of motor loss.

5.6 SFM MACHINE OPEN CIRCUIT AND GENERATING DATA

This section describes the heat runs and generating performance tests conducted on the SFM disc machine. Figure 5-3 shows the steady-state temperature rise (above ambient) for the machine with the stator terminals open-circuited. The machine was turned by the load motor to which it was attached. It is seen that the stator windings get quite hot with no external currents passing through them. This is due to the eddy-current loss induced in the stator strands by the passing magnet flux. The watts lost in the motor were estimated using the thermal resistances given in Table 5-4 and, at the higher power levels, closely matched the power supplied to the disc machine by the dc load machine. At low power levels the power was too small to measure accurately.

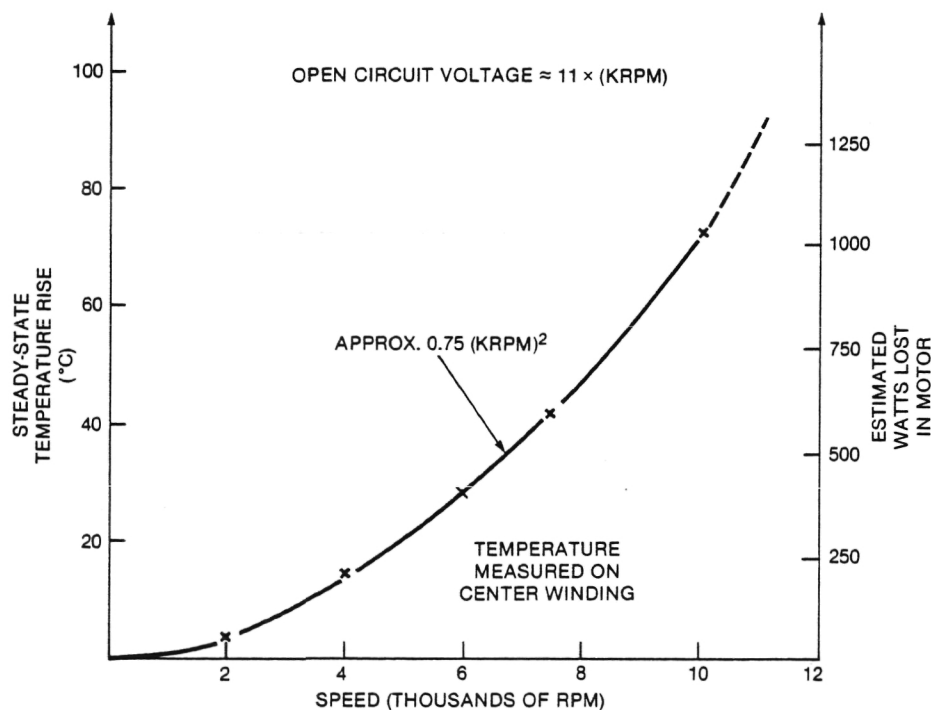


Figure 5-3. Steady-State Temperature Rise of Stator Windings During Open Circuit Heat Runs on FM Machine.

Figure 5-4, 5-5, and 5-6 show data for the FM machine generating into three different values of load resistors. The efficiency ranges from 80 to 90%. The only unusual characteristic is shown in Figure 5-6. In this case, the slope of the current versus speed curve changed at approximately 5000 rpm. Above this speed, it appeared that leakage flux saturation or armature reaction was starting to limit the generating capability of the machine. In addition, as the two data points at about 7800 rpm in Figure 5-6 show, the machine began to behave quite erratically.

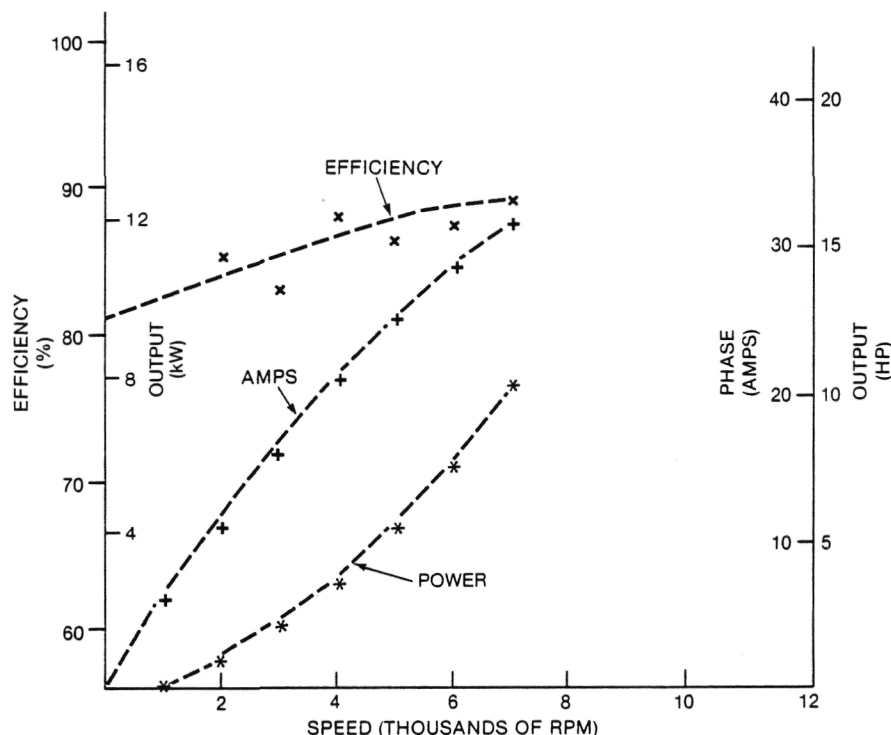


Figure 5-4. Series-Connected FM Machine Data. Performance for generating into a 2.0Ω /phase resistive load.

One explanation for this erratic behavior may be that the rotor was rubbing the stator during the tests at higher powers. Looking at the data in Figures 5-4 through 5-6, one can see that the FM machine was not tested up to its speed rating of 11,000 rpm. The reason for this was that during one of the last heat runs scheduled before the start of high-speed tests (in excess of 8000 rpm), the rotor rubbed one of the stators. This occurred when the stator temperature reached approximately 140°C . At that point, since enough low-speed tests had been performed to characterize the machine and since the motor had gone up to 12,000 rpm in a spin test, no more tests were run.

After disassembly of the motor, it was seen that two factors had contributed to the problem. A washer on one side of the stator had deformed, allowing the rotor to come closer to the stator on the side that rubbed, and the encapsulant on both stators had expanded into the air gap in some places and, in others, developed large radial cracks. The expansion of the encapsulant alone was enough to decrease the air gap from 0.076 to 0.005 cm when the machine was cool. When the machine was hot, the encapsulant expanded further, closing the air gap. The POP stator encapsulation did not exhibit this problem, probably because the coils were reinforced with glass cloth.

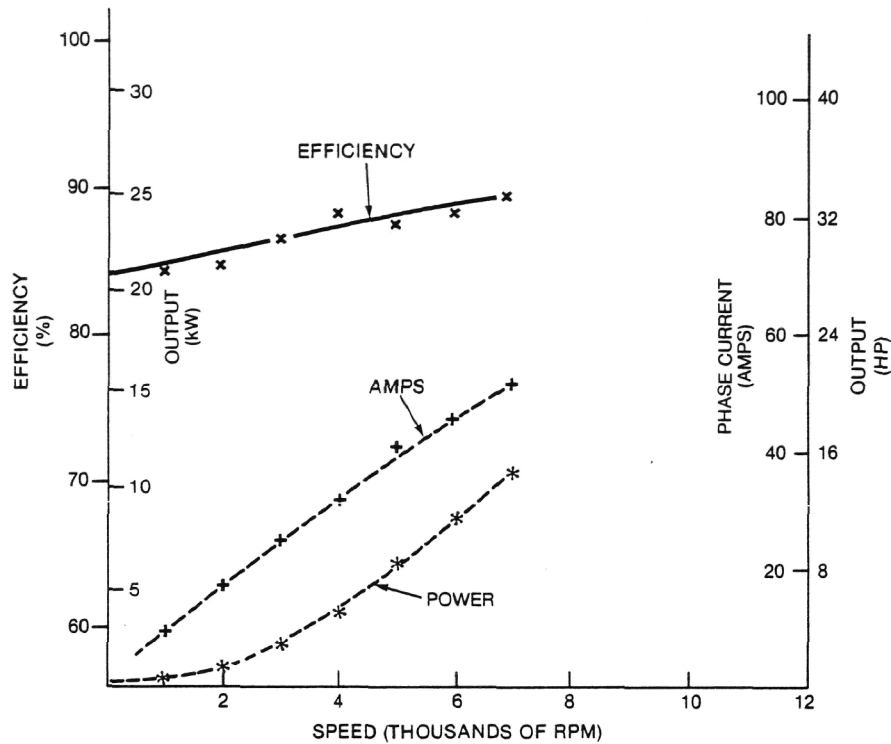


Figure 5-5. Series-Connected FM Machine Data. Performance for generating into a 1.5 Ω /phase resistive load.

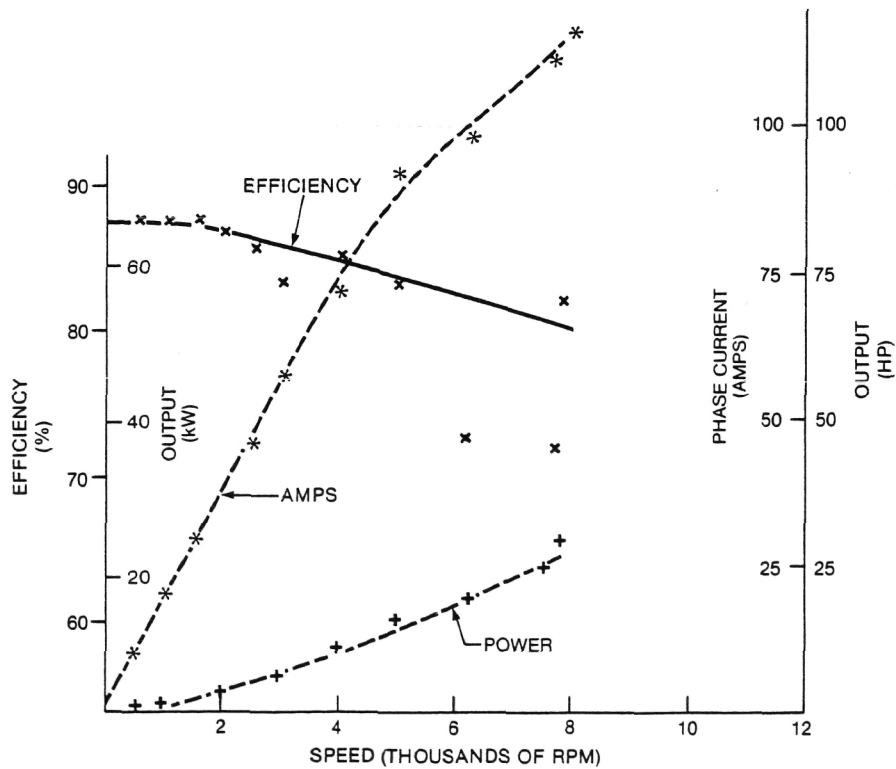


Figure 5-6. Series-Connected FM Machine Data. Performance for generating into a 0.5 Ω /phase resistive load.

Table 5-5 shows detailed heat run data for a particular value of load resistor. Table 5-6 analyzes this data from all the generating performance heat runs and performs a segregation of losses calculation. It is seen that the largest single loss component at the lower speeds was stator conductor loss due to winding resistance. At higher speeds, though, the stator conductor eddy current loss does get quite large.

Table 5-5
SERIES-CONNECTED FM GENERATOR DATA
(Load Resistance is 0.5 Ω /Phase)

Rotor Speed = 4030 rpm		Mech. Watts = -9370	
Shaft Power = 9.4 kW (-12.6 hp)		Elec. Watts = -8095	
Torque = 22.2 N-m		Efficiency = 86%	
Phase	A	B	C
Voltage (Volts, rms)	35.3	39.0	35.4
Current (Amperes, rms)	68.1	76.9	77.3
Average Power	-2415	-2960	-2720
Power Factor, %	100	98.7	99.4
Motor Part	Steady-State Temperature ($^{\circ}$ C)	Thermal Time Constant, Min. (Time to reach 63% Final Temperature)	
Coil 1	114	12	
Coils 2&3	135	12	
Coil 4	108	17	
Coil 5	123	15	
Coil 6	129	15	
Rotor	109	40	
Spacer	55	25	
Case	53	25	
Ambient	28	—	

Using the data of this section, a simple mathematical model of the FM machine was constructed to calculate the performance of the motor along the profile of continuously rated output power. Figure 5-7 shows some of the results. For a power factor of 100%, the motor can be expected to reach a peak efficiency of 90.5% when excited by a sine-wave source. At the best power factor possible with the motor driven from a load-commutated inverter (about 85%), the motor can be expected to reach a peak efficiency of 88.1% when powered by a sine-wave source. Figure 5-8 shows the calculated temperature rises along the profile of continuously rated output power.

5.7 LOAD-COMMUTATED INVERTER RATING OF A SYNCHRONOUS MOTOR

Before discussing the test results with the motors excited by the load commutated inverter, it is of interest to examine the operating characteristics of this type of inverter. A load commutated inverter, unlike most other types of inverter, does not require auxiliary thyristors to turn off the main thyristors. To have this be possible, it is necessary that the inverter be connected to a synchronous machine operating with a

Table 5-6

SERIES-CONNECTED FUNCTIONAL MODEL GENERATOR HEAT RUN DATA

Speed, rpm	2400	3000	3000	4030	5000	7000
HP Out	4.4	3.2	7.0	10.8	8.2	14.6
kW Out	3.28	2.39	5.22	8.06	6.12	10.89
Efficiency, %	86.0	88.0	82.4	86.4	90.0	90.0
Load, Ω /Phase*	0.5	1.1	0.64, Δ conn.	0.5	1.1	1.1
Temperature, Rise ($^{\circ}\text{C}$)	41	16	80	107	44	80
Phase Resistance (Ω)	0.051	0.046	0.057	0.061	0.051	0.057
Phase Amperes	47	26	67	74	41	54
Watts Loss	520	330	1120	1275	680	1196
I^2R Watts	338	93	768	1002	257	499
Open Circuit Watts†	58	90	90	162	250	490
Stray Watts	124	147	262	111	173	207
$^{\circ}\text{C}/(\text{kW Loss})$	79	48	71	84	65	67

*Load Resistor Y connected except 3000 rpm, 7 hp

† $10 \times (\text{rpm}/1000)^2 \text{ W}$

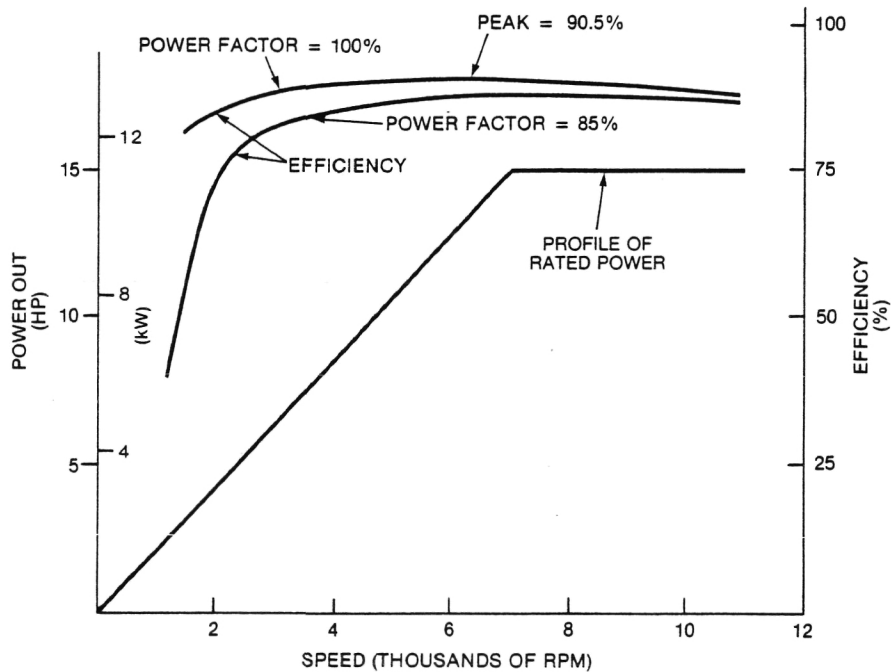


Figure 5-7. Projected Efficiency of SFM Disc Motor while Operating Along Profile of Continuously Rated Load. Values extrapolated from sine-wave generating data.

leading power factor. In this mode of operation, the current into a given phase winding reaches zero before the voltage does. In the interval between the zero crossings, the thyristor can turn off by itself.

This type of inverter is lighter and less costly than other types because it requires fewer high-power devices. However, neglecting magnetic saturation, the requirement

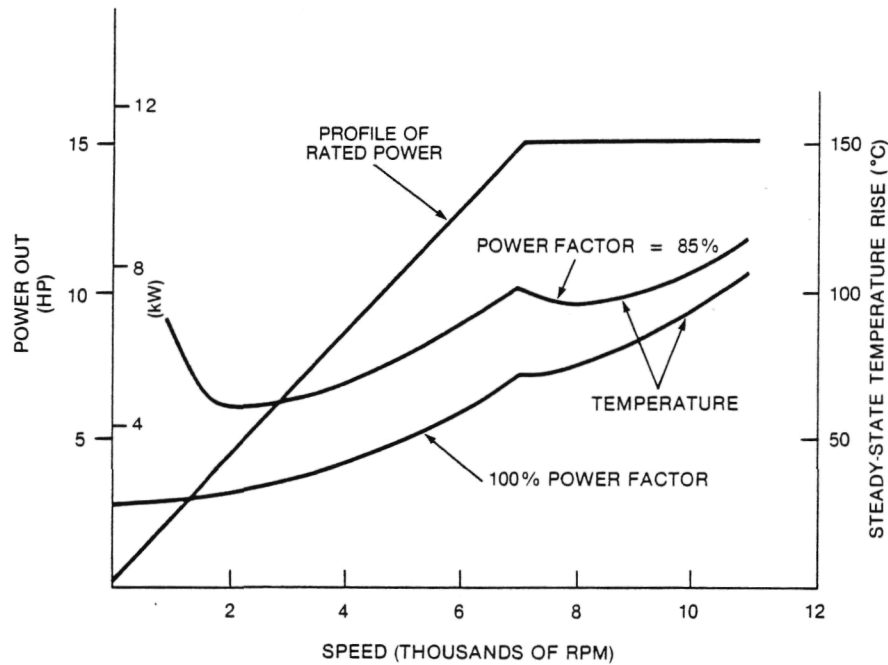


Figure 5-8. Projected Steady-State Winding Temperature Rise while Operating Along Profile of Continuously Rated Load. Values extrapolated from sine-wave generating data.

of a leading power factor lowers the peak electromagnetic power capability of the motor per ampere of armature current at a fixed value of field voltage. This can be illustrated by making a calculation based on an analysis for sinusoidal voltages and currents.

A vector diagram for a smooth-gapped synchronous machine operating with a leading power factor is shown in Figure 5-9. In this diagram,

I_s = Armature phase current

V_s = Armature phase voltage

E = Field (magnet) voltage

X = Synchronous reactance

ϕ = Power factor angle

δ = Torque angle.

The effect of armature resistance and saturation are neglected. From this figure,

$$V_s \cos(\delta) = E - X I_s \cos(\pi/2 - \delta - \phi) \quad (1)$$

$$V_s \sin(\delta) = X I_s \sin(\pi/2 - \delta - \phi) \quad (2)$$

Multiplying Eq. 1 by $\sin(\delta)$ and Eq. 2 by $\cos(\delta)$ allows V_s to be eliminated. This gives, after trigonometric reduction,

$$E \sin(\delta) = X I_s \cos(\phi) \quad (3)$$

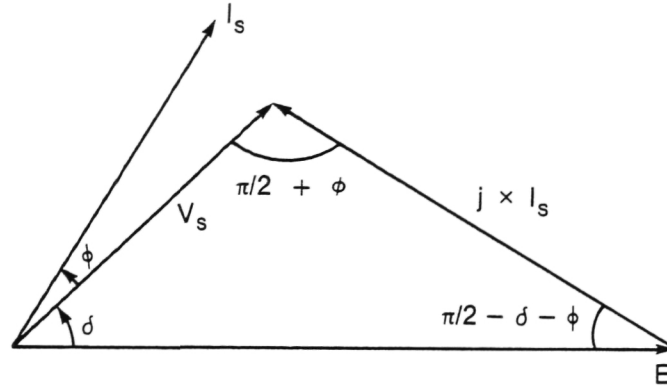


Figure 5-9. Vector Diagram for a Smooth-Gap Synchronous Machine With a Leading Power Factor.

The power out of the machine is given by

$$P = m E I_s \cos(\delta + \phi) \quad (4)$$

where m is the number of phases.

A permanent magnet motor operating on the LCI described in Reference 1 has the field voltage (at a constant speed) fixed by the magnet flux and the armature current fixed by the inverter. Thus operation at a fixed field voltage and constant armature current is of greatest interest. The phase voltage is not restricted to a fixed magnitude under these conditions.

Since Eq. 3 relates the field voltage and armature current, it is possible to solve for I_s and substitute the result into Eq. 4 to give:

$$P = (m E^2 / X) [0.5 \sin(2 \delta) - \sin^2(\delta) \tan(\phi)] \quad (5)$$

With the power-factor angle, ϕ , held constant, P in Eq. 5 varies as a function of δ . (Equation 3 shows the current is varying along with δ under these conditions.) To find the highest value of the output power at a given value of ϕ , Eq. 5 is differentiated with respect to δ . After setting the result equal to zero and solving for δ , it is found that the greatest output power, at a fixed leading power-factor angle, is achieved when:

$$\delta = (1/2)(\pi/2 - \phi). \quad (6)$$

Substituting Eq. 6 into Eq. 5 gives the maximum output power at a fixed value of ϕ as:

$$P_{\max} = \frac{m E^2}{2 X} [\cos(\phi) - \tan(\phi) (1 - \sin(\phi))] \quad (7)$$

The factor in brackets varies approximately linearly from a value of 1.0 at $\phi = 0$ to a value of zero at $\phi = 90^\circ$. It should be pointed out that the above equation is valid only for leading power-factor angles. For lagging power-factor angles, differentiation of Eq. 5 yields the minimum power, not the maximum.

When the motor is operating from the LCI, the minimum practical value of ϕ is approximately 30° . For this value, the maximum power obtainable on the LCI is

$$P_{\max(\text{LCI})} = 0.2887 m E^2/X. \quad (8)$$

The derivation leading up to Eq. 8 ignored the effect of stator resistance. To assess the effect of stator resistance drop, the computer model used to generate the data in Figure 5-8 and 5-9 was run with and without including stator resistance. Using a synchronous inductance of $100 \mu\text{H}$ and a hot stator resistance of 0.060Ω , the program calculated that the series-connected FM disc motor had the following values on the LCI at 5860 rpm:

shaft power = 8.95 kW (12.0 hp)
 phase current = 88 A rms
 phase voltage = 54 V rms
 efficiency = 78%
 power-factor angle = 36°
 torque angle (δ) = 19° .

These values closely match test data obtained from the FM motor when operating at this point. When the stator resistance was set to zero, the computer model showed the motor could produce a peak power of 16.5 hp at 5860 rpm with a leading power-factor angle of 30° . For this condition, the value of δ was 30° . Thus the resistance drop decreases the peak power capability of the motor by about 25%. Equation 8 gives a value of 20 hp because the rotational losses included in the computer program are ignored.

5.8 LOAD-COMMUTATED INVERTER TESTS

As has been mentioned previously, the thyristors in the LCI turn off between the time the phase current crosses zero and the time the phase voltage crosses zero. One way of adjusting the length of time between these zero crossings is to change the voltage of the inverter's dc power supply. As this dc voltage increases, the time between zero crossings decreases. If the voltage is increased too much, though, the thyristors do not have enough time to turn off and the inverter short circuits the dc power supply. It is best to avoid such a condition.

This condition is commonly referred to as "shoot through," and it may have other causes as well. At the same time the power supply is short-circuited, the motor is also short-circuited, at least on two phases. The details are complex but a major feature is large currents flowing in the motor limited mainly by motor inductance. These large currents could be destructive if on long enough. Even if on for only a short time, the large armature currents can drive the magnet operating point into the third quadrant, resulting in loss of magnetization. This effect is illustrated in Figure 4-9 for normal load current. For "shoot through" current, the recoil line will originate on the magnet characteristic in the third quadrant. The new operating point will then have a rather low flux. This effect is somewhat ameliorated by the conducting hub and the conductivity of the alnico magnets.

A plot of the 1SPOP motor's efficiency, output horsepower, and power factor versus the inverter's dc power supply voltage is shown in Figure 5-10. (The power factor is calculated as average power divided by the product of rms voltage and rms current.) When the dc voltage along the x axis of the plot reaches 100%, the thyristors do not have enough time to shut off. However, it is also seen that the motor performance improves as the dc voltage increases. Thus there is a trade-off between the time the thyristors are given to turn off and the motor efficiency and power factor.

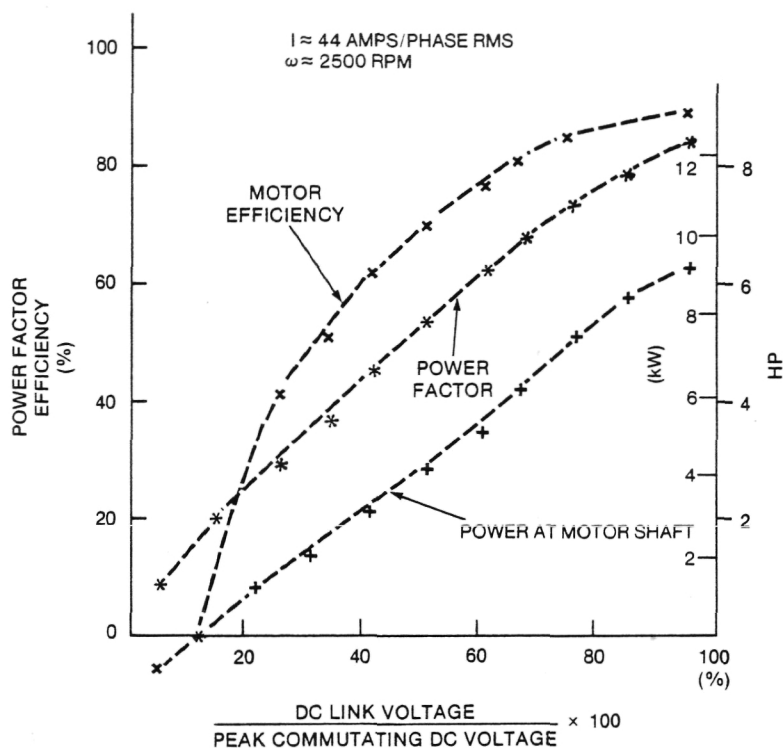


Figure 5-10. Single-Sided POP Motor Data. DC current of LCI power supply held constant.

In the plot of Figure 5-10, the voltage of the inverter's dc power supply was varied as the dc current was held constant. In Figure 5-11, the dc voltage was held constant while the dc current was varied. It is seen that the output power of the SFM motor first rises, then falls, as dc current is increased. After the peak power is reached, further increases of current cause the field and current vectors of Figure 5-9 to approach a relative displacement of 90° , which (by Eq. 4) gives less output power for more current. At currents higher than that which gives the peak power, the heating of the motor is very rapid.

Figure 5-12 and 5-13 give performance data for the SFM motor with the inverter's dc power supply current set at 40 and 75 amperes, respectively. During these tests, the dc voltage was raised to the largest value which gave sufficient thyristor turn-off time until the voltage limit of the power supply was reached. This limit was reached for speeds above 6000 rpm.

The curves of Figure 5-14 plot motor temperature versus speed and attempt to segregate the temperature rises into the components caused by eddy-current conductor losses (open circuit rotational losses), stator current losses, and stray losses. At the phase current shown for the test points, the torque of the SFM motor is approximately 12 N-m. Table 5-7 gives heat run data for LCI operation.

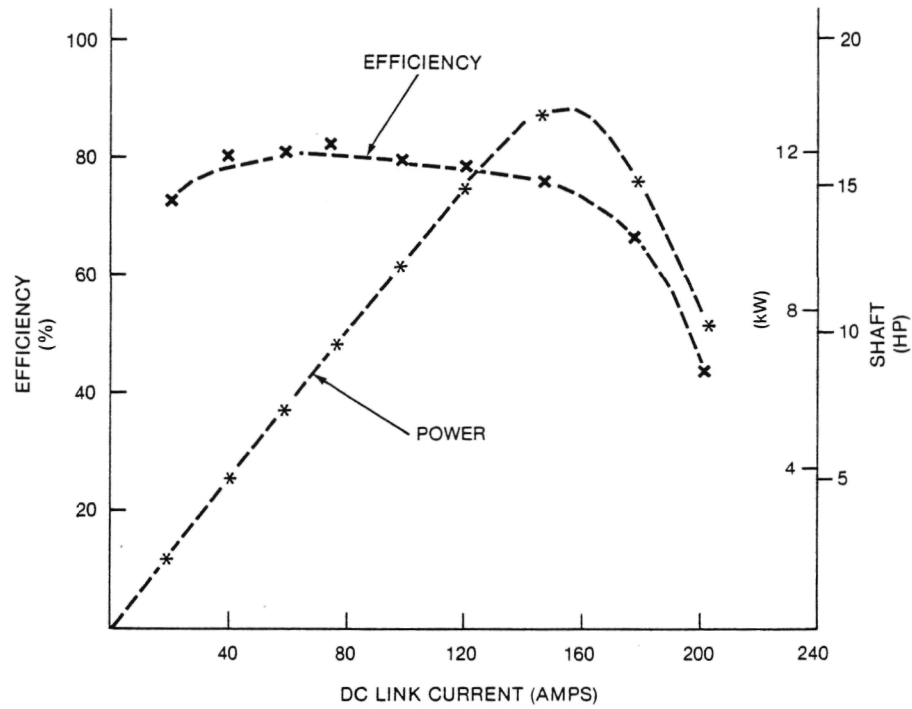


Figure 5-11. Series-Connected Functional Disc Motor Data. Performance as a function of LCI power supply current.

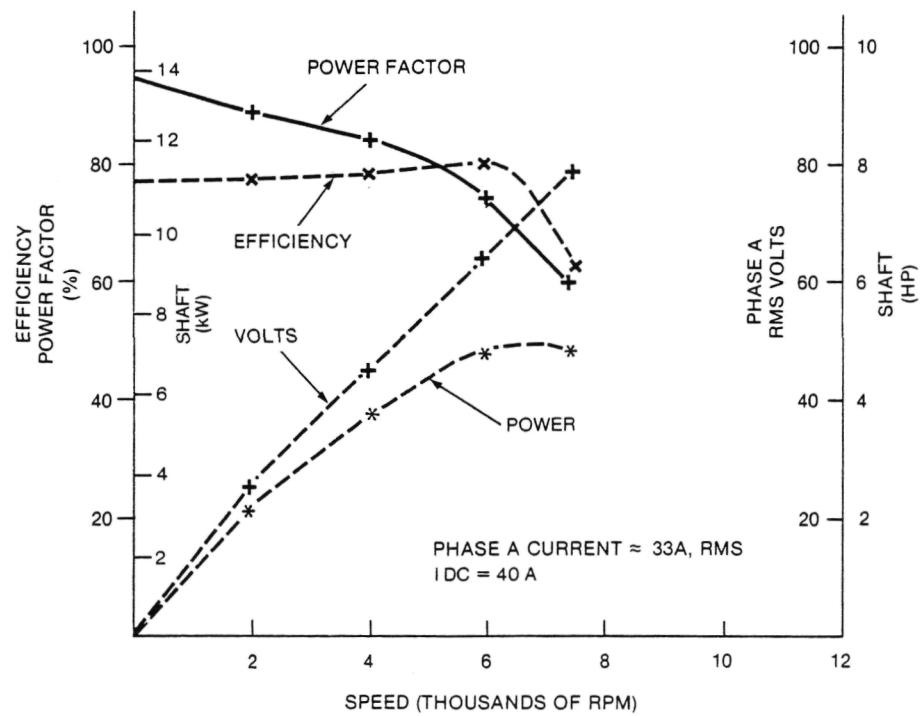


Figure 5-12. Series-Connected Functional Disc Motor Data. Performance with LCI power supply set to 40 A dc.

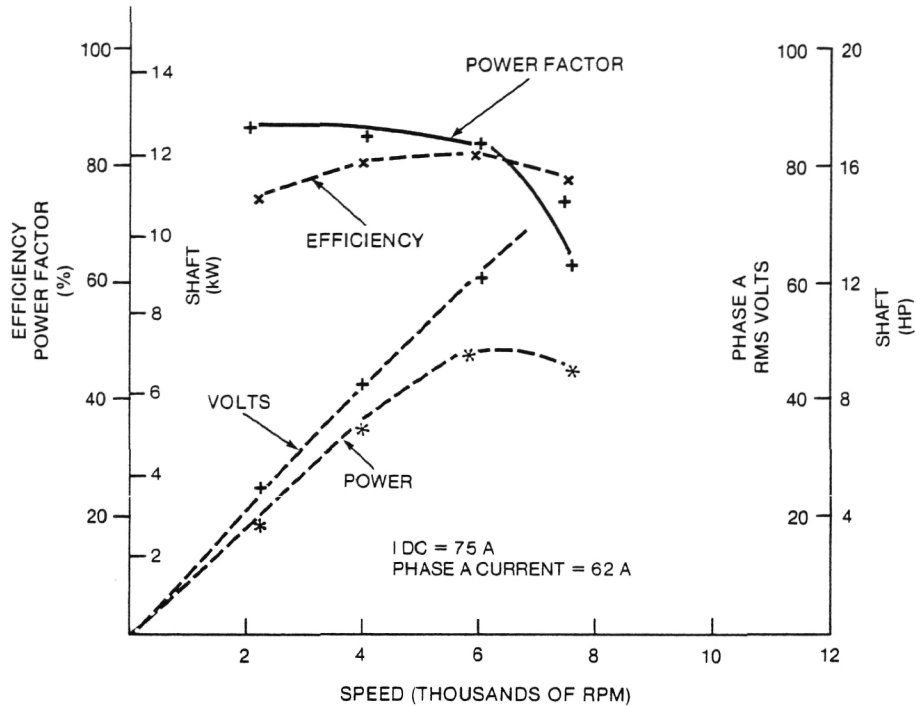


Figure 5-13. Series-Connected Functional Disc Motor Data. Performance with LCI power supply set to 75 A dc.

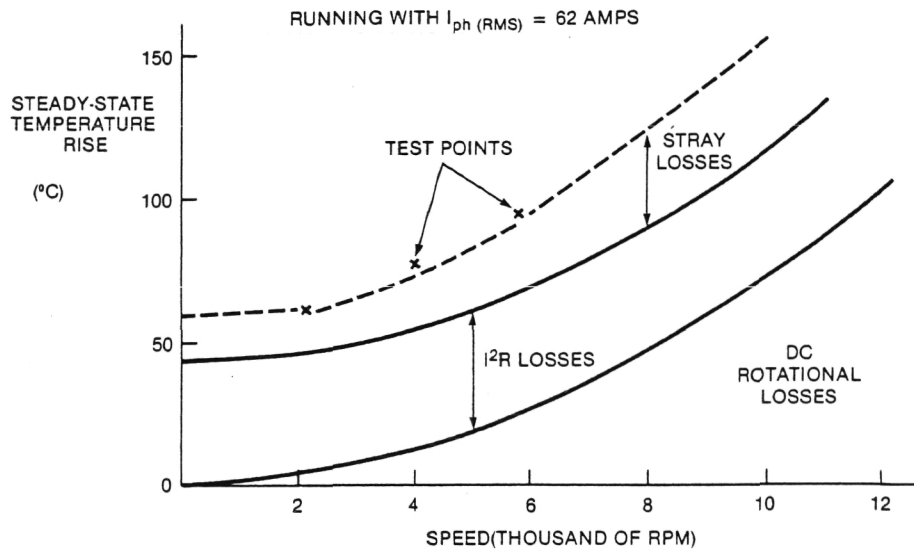


Figure 5-14. Series-Connected Functional Disc Motor Data. Estimated components of stator winding steady-state temperature rise as a function of rotor speed.

Table 5-7
FUNCTIONAL MODEL MOTOR
SERIES-CONNECTED FM DISC MOTOR HEAT RUN
DATA WHILE OPERATING ON THE LOAD-COMMUTATED INVERTER

Speed (rpm)	2230	4080	4300	5860	7640
Shaft Power (hp)	3.8	7.3	8.5	9.9	9.3
Shaft Power (kW)	2.83	5.45	6.34	7.39	6.94
Motor Efficiency (%)	72	82	83	83	77
Motor Power Factor (%)	84	83	82	77	59
Temperature Rise (°C)	62	75	87	91	125
Phase Reactance (Ω)	0.052	0.096	0.101	0.137	0.179
Phase Resistance (Ω)	0.054	0.056	0.057	0.059	0.064
Phase Current (Amperes)	62	62	65	63	66
Phase Voltage (Volts)	25	44	48	62	77
Total Loss (Watts)	1100	1190	1280	1510	2050
Winding Loss (Watts)	620	645	722	702	850
Open Circuit Loss (Watts)	50	165	185	345	585
Stray Loss (Watts)	430	380	370	463	615
Thermal Resistance (°C/(kW))	56	63	68	60	61
Shaft Power (kW)	6.34	2.83	5.45	7.39	6.94

* $10 \times (\text{rpm}/1000)^2$ watts

5.9 CONCLUSION

This section documents test results on the FM and POP axial-flux, ac synchronous, permanent magnet, disc machines. These tests showed the motors reached a peak efficiency of approximately 89% and produced peak torques in the range of 20 to 30 N-m. The motors did not achieve the desired efficiency and required performance for their electric vehicle application.

The POP motor was designed as a demonstration motor and was not expected to achieve the electric vehicle performance specifications. Its primary problem was large circulating currents which flowed between the paralleled coils of the machine. The FM motor was tested with its coils in series, which eliminated the problem with circulating currents. However, the tests of the FM motor revealed the following problems:

1. The alnico magnets used in the rotor partially demagnetized during the generating and inverter tests. After the motor was disassembled and reassembled at the conclusion of the tests, the open circuit voltages decreased by only a few percent.
2. The motor had large open circuit rotational losses because of eddy currents induced in the stator strands by the magnet flux.
3. The three-layer stator winding gave unequal stator winding inductances.
4. One of the coils was not positioned 120° in space with respect to the other two coils.
5. The rotor rubbed the stator because of a deformed washer and because the epoxy encapsulant expanded into the gap between the rotor and stator.
6. The heat transfer from the stator windings to the case is poor because the windings were completely surrounded by the epoxy encapsulant.

The problems in the FM motor were largely due to the method of construction. Two design changes, namely changing from alnico to Co-Sm magnets and using more finely stranded wire in the armature coils, should raise the peak efficiency of the FM motor to approximately 94% and raise the peak power capability from 13.4 to 37.3 kW (18 to 50 hp). These values would meet the performance requirements.

REFERENCE

- 5-1. A.B. Plunkett and F.G. Turnbull, "Load Commutated Inverter/Synchronous Motor Drive Without a Shaft Position Sensor," *IEEE Transactions*, Vol. IA-15, No. 1, pp. 63-71, Jan/Feb 1979.

6.0 TEST SUPPORT EQUIPMENT FOR THE DISC MOTORS

6.1 INTRODUCTION

The test support equipment is comprised of two basic groups which will be called "First-Floor Test Facility" and "Fourth-Floor Test Facility". The essential differences are that the first-floor facility uses an adjustable speed motor-generator set as a power supply, while the fourth-floor facility uses a solid-state inverter power supply. More significant is that the fourth-floor facility uses an EAI (Electronic Associates, Inc.) Pacer 600 computer for control of the inverter with data acquisition by an auxiliary DEC (Digital Equipment Corp.) computer.

Initial tests were run using a sine-wave, motor generator power supply on the first floor. After these tests, the motors were transferred to the fourth floor and mounted on the higher-speed test stand. The motor was then driven by the load-commutated inverter.

6.2 FIRST FLOOR TEST FACILITY

Figure 6-1 shows the proof-of-principal motor being tested in the first-floor facility.

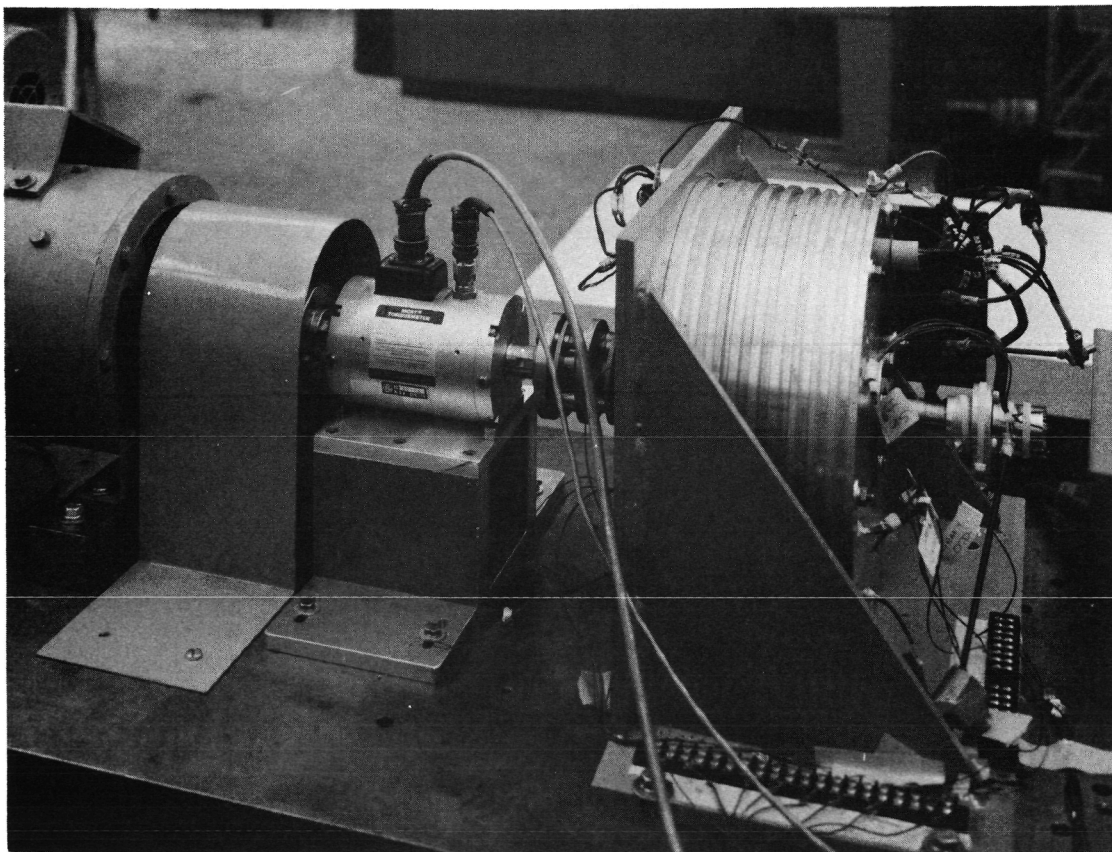


Figure 6-1. Proof-of-Principle Motor Installed in First-Floor Test Facility

The first-floor facility uses three basic sets of instruments:

- 1) Digital instruments applied to three-phase and single-phase instrument panels (Table 6-1)
- 2) Analog instruments with acceptable accuracies to at least 10 kHz (Table 6-2)
- 3) System 6 instrumentation and data processing (Table 6-3)

Table 6-1

THREE-PHASE AND SINGLE-PHASE DIGITAL INSTRUMENT PANELS

	<u>Full-Scale Accuracy</u>	<u>Frequency Range</u>
DIGITEC voltmeters and ammeters with their true rms adaptors		
DIGITEC wattmeters	$\pm 0.1\%$	45 to 1000 Hz
DIGITEC speed (rpm)		
DIGITEC torque		
Potential transformers are not required for these voltmeters and wattmeters.	---	---
Current transformers for ammeters and wattmeter GE JP-1 750×99G2 (1st Set)	$\pm 0.1\%$ * $\pm 0.5\%$ *	25 - 60 Hz 100 - 500 Hz
Watt Transducer for Wattmeter (Scientific Columbus)	$\pm 0.1\%$	45 to 400 Hz
Torque Signal (Himmelstein Torque-Meter)	$\pm 0.1\%$	28.24 Nm (rated)
Speed Signal (Himmelstein Torque-Meter)	± 1 Digit	7500 rpm or 1500† rpm

NOTE: ± 1 digit means if true reading is 7000 rpm, actual reading can be 6999 or 7001.

*If instrument burden is 1.0 PF, 0.75 VA, and 5 amps (the load on the transformer)

†high-speed transducer

6.3 THE FOURTH-FLOOR TEST FACILITY

Some facilities on the first floor are moveable and transferable to the fourth floor, particularly the analog instrumentation whose instrument accuracies were given in Section 6-2.

Figure 6-2 shows the essential equipment associated with the fourth floor. The following is a description of this equipment:

DC Load Machine

27 hp, 94.7 volts, 254 amperes, 1654 rpm, 50 volt separately excited field

Table 6-2
ANALOG INSTRUMENTS

	<u>Full-Scale Accuracy</u>	<u>Frequency Range</u>
Greibach ammeters, model 500	$\pm 0.5\%$	5 to 10,000 Hz
Greibach voltmeters, model 500	$\pm 0.5\%$	5 to 10,000 Hz
Greibach wattmeters, model 560	$\pm 1.0\%^*$	50 to 10,000 Hz
Current Transformers for ammeters and wattmeter (3rd Set)	$\pm 0.1\%$	25 to 60 Hz
GE JP-1 750×99G2	$\pm 0.5\%$	100 to 500 Hz

*If power factor is unity

Cotta Speed Reducer

Speed Ratio 2.5/1, maximum speed 30,000 rpm

Torque Meter

113 N-m (1000 in.-lb) , 15,000 rpm

A block diagram for the test facility is shown in Figure 6-3. It is seen that the disc machines could be tested either while generating into a three-phase resistor bank or while operating from a load-commutated inverter. The inverter and its control scheme are described in Reference 6-1. The five major data acquisition devices and their functions are:

- 1) DEC computer
 - a. Records torque and speed from Himmelstein unit
 - b. Records volts and amperes from power supply
 - c. Records power from inverter
- 2) Tektronix Digital Processing Oscilloscope (DPO)
 - a. Simultaneously records motor terminal volts and amperes
 - b. Computes rms and mean values and calculates average power
- 3) Greibach meters record phase volts, amperes, and watts
- 4) Digital voltmeters record dc load machine volts and amperes
- 5) 24-channel temperature recorder monitors ambient and 16 locations in motor.

The DEC computer and the DPO, fitted with a 100A F.W. Bell current probe, were the two primary data acquisition devices for electrical performance.

Table 6-3
SYSTEM 6 INSTRUMENTATION

	<u>Full-Scale Accuracy</u>	<u>Frequency Range</u>
Data Display 19 Channels	± 1 digit*	NA
Volt Transducers Ohio Semitronics	$\pm 0.5\%$	50 to 400 Hz
Current Transducers Ohio Semitronics	$\pm 0.5\%$	20 to 2000 Hz
Isolation Stepdown Transformers 220/110 V GE Jv 20 (Supplies wattmeter, varmeter, and voltmeters)	$\pm 0.1\%$ $\pm 0.5\%$	25 to 60 Hz 100 to 500 Hz
Current Transformers for ammeters and wattmeters (2nd set) GE JP-1 750 \times 99G2	$\pm 0.1\%$ $\pm 0.5\%$	25 to 60 Hz 100 to 500 Hz
Watt Transducer Scientific Columbus	$\pm 0.1\%$	45 to 400 Hz
Var Transducer Scientific Columbus	$\pm 0.15\%$	60 Hz
Torque Signal (Himmelstein Torque-Meter)	$\pm 0.1\%$	28.24 Nm (rated)
Speed Signal (Himmelstein Torque-Meter)	± 1 digit*	7500 rpm or 1500 \dagger rpm

* ± 1 digit means if true reading is 7000 rpm, actual reading can be 6999 or 7001.

\dagger high-speed transducer

Figure 6-4 shows a sample motor performance printout from the DEC computer. It shows the FM motor producing approximately 14 hp output at 7500 rpm while operating on the LCI. Figure 6-5 shows the DPO output which was taken, along with the data of Figure 6-4. Figure 6-6 shows the temperature traces taken during that same 14 hp run. Channels 1, 2, and 3 record stator winding temperatures.

6.4 LOAD-COMMUTATED INVERTER AND CONTROL

The inverter and control utilized to perform the motoring tests were originally built and used in subcontract 8990503 for Lawrence Livermore Laboratories. Details of the inverter design and construction and of the hybrid computer control are found in Sections 5.4 and 6.2 and Appendices A and B of Reference 6-1 (*Regenerative Flywheel Energy Storage System*).

The relatively complex system of control for the flywheel system contained the hardware and software required to test the disc machine. Modes 4, 5, and 6, which refer to recharging of the flywheel, are the modes of interest, in that the synchronous machine is motoring. The motor test setup was arranged for constant load operation,

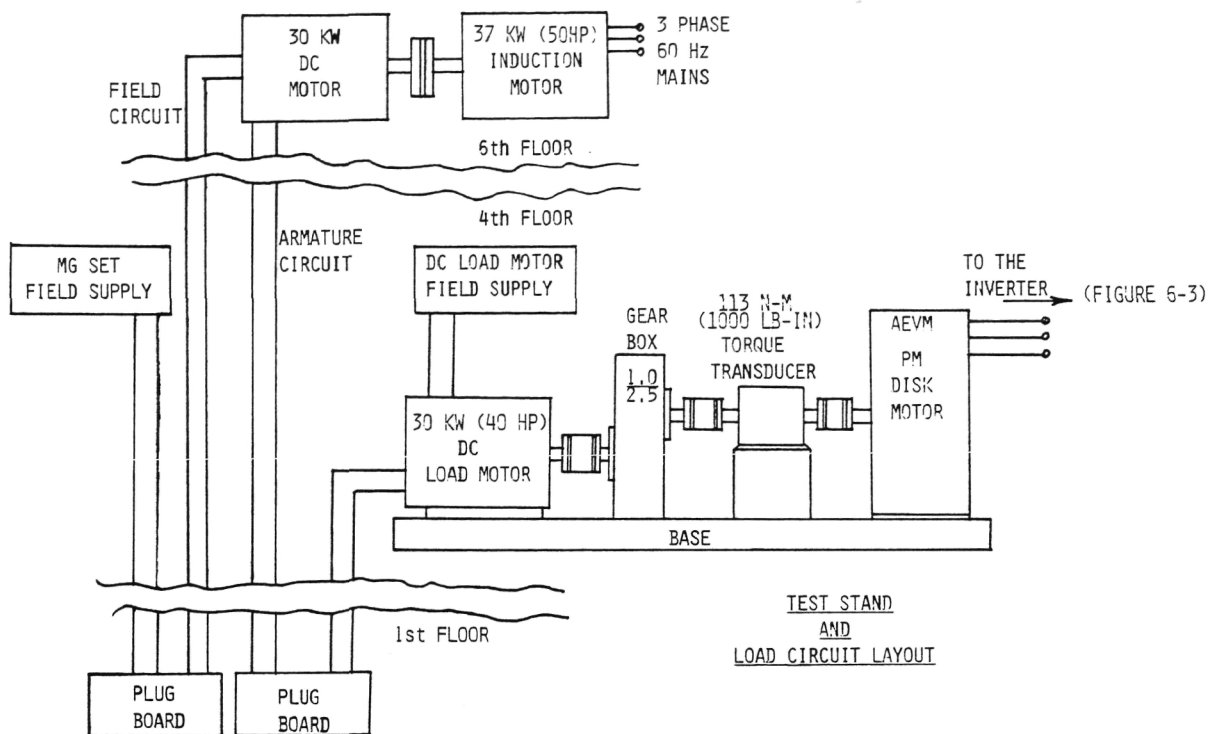


Figure 6-2. Fourth-Floor Test Facility

not for cycling as in the flywheel tests, and the appropriate changes were made to the digital control program in the hybrid computer. The basic functions of the control (the angle controller and current regulator in Reference 5-1) were utilized, while dc traction motor control and related portions were not.

In setting up test points, the dc machine was used to obtain approximately the correct test speed, the inverter started up, and the dc bus voltage adjusted to the desired level according to speed. The current was set by the current command input to the hybrid computer, and the dc machine adjusted to achieve the desired load point. All of these adjustments interacted so that setting of a desired load point frequently required an iterative approach. The relatively small number of load points required did not justify construction of a more sophisticated test control.

The inverter and its card rack are shown in Figures 6-7, 6-8, and 6-9. The inverter used for the test uses essentially the same circuitry but exists in an already installed "breadboard" form. Both are current-controlled, load (machine)-commutated inverters.

Neither has a chopper section for low-speed operation, and each requires the equivalent of an EAI (Figure 6-10) control for its operation. Low-speed tests can be accomplished on the fourth floor by substituting the controlled rectifier bridge power supply for the chopper.

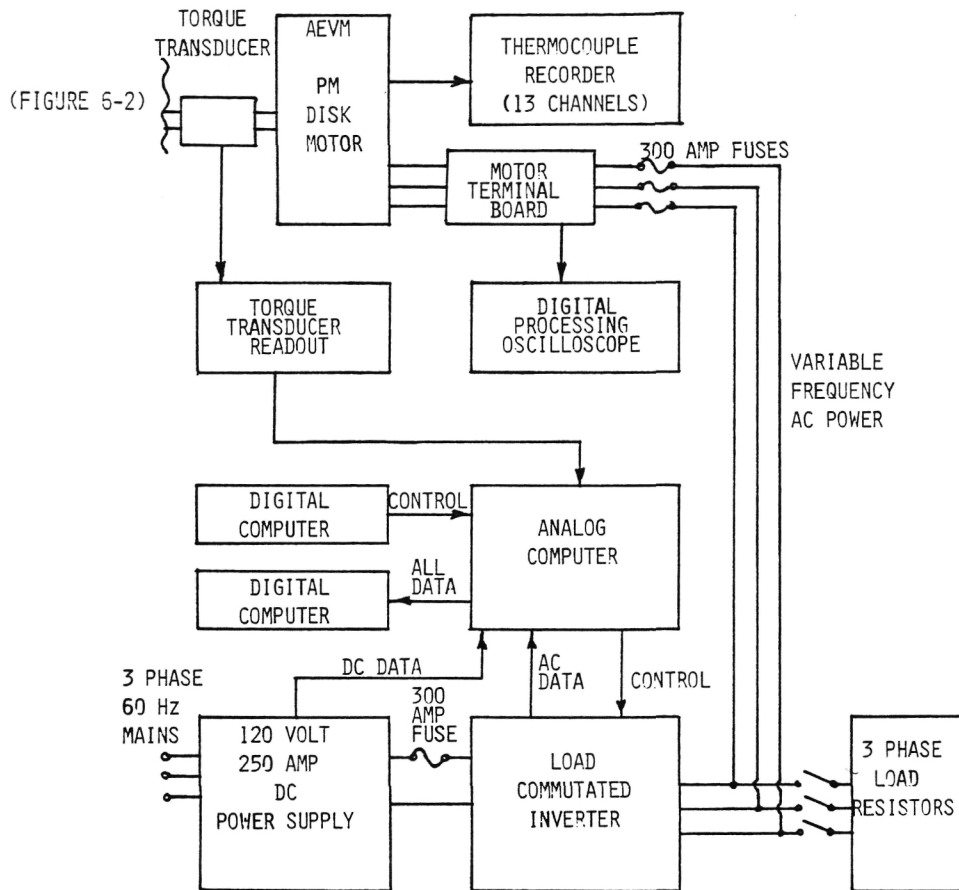


Figure 6-3. Control and Test Instrumentation

6.5 INVERTER SCHEMATIC DIAGRAMS

The inverter schematic diagrams are given in the nine drawings of Appendix C.

- IEX - 101 - Overall inverter diagram with its seven printed circuit cards
- IEX - 102 - Switching and commutator schematic
- 216B7527 - Frequency Generator, Card 1
- 216B7528 - SCR Steering, Card 2
- 216B7529 - SCR Main and Auxiliary Firing, Card 3
- 216B7530 - Current and Flux Magnitude, Card 4
- 216B7531 - Flux Measurement, Card 5
- 216B7532 - Torque, Card 6
- 217B7533 - Angle, Card 7

The field power supply shown on IEX-101 is not required for the disc motor and is to be omitted. The inputs and outputs to the EAI analog and digital computer are shown at the bottom left of IEX-101.

The theory of operation of these components and the system is given in Reference 6-1.

```

10-JUL-80                                TIME 10:37:13

      MOTOR                                INVERTER
CALCULATIONS                            CALCULATIONS
-----
TORQUE      SPEED      :::  DC CURRENT      DC POWER
NT-M        RPM        :::  AMP              WATTS
13.53      7509.77    :::  220.46          15694.79
-----
MECH. POWER  AC POWER  :::  DC VOLTS      AC POWER
WATTS        WATTS    :::              WATTS
10636.69    15087.89  :::  71.19          15087.89
-----
AC CURRENT   EFFICIENCY :::  EFFICIENCY      FREQ
MAGNITUDE    %          :::  %              HZ
218.99      70.50     :::  96.13          522.51
-----

TEST POINT H.P= 14.26    EST. S.S. TEMP. RISE= 247. DEG. C
-----

```

```

10-JUL-80                                TIME 10:37:22

      MOTOR                                INVERTER
CALCULATIONS                            CALCULATIONS
-----
TORQUE      SPEED      :::  DC CURRENT      DC POWER
NT-M        RPM        :::  AMP              WATTS
13.69      7500.00    :::  220.46          15780.90
-----
MECH. POWER  AC POWER  :::  DC VOLTS      AC POWER
WATTS        WATTS    :::              WATTS
10752.41    15112.30  :::  71.58          15112.30
-----
AC CURRENT   EFFICIENCY :::  EFFICIENCY      FREQ
MAGNITUDE    %          :::  %              HZ
219.24      71.15     :::  95.76          522.51
-----

TEST POINT H.P= 14.41    EST. S.S. TEMP. RISE= 242. DEG. C
-----

```

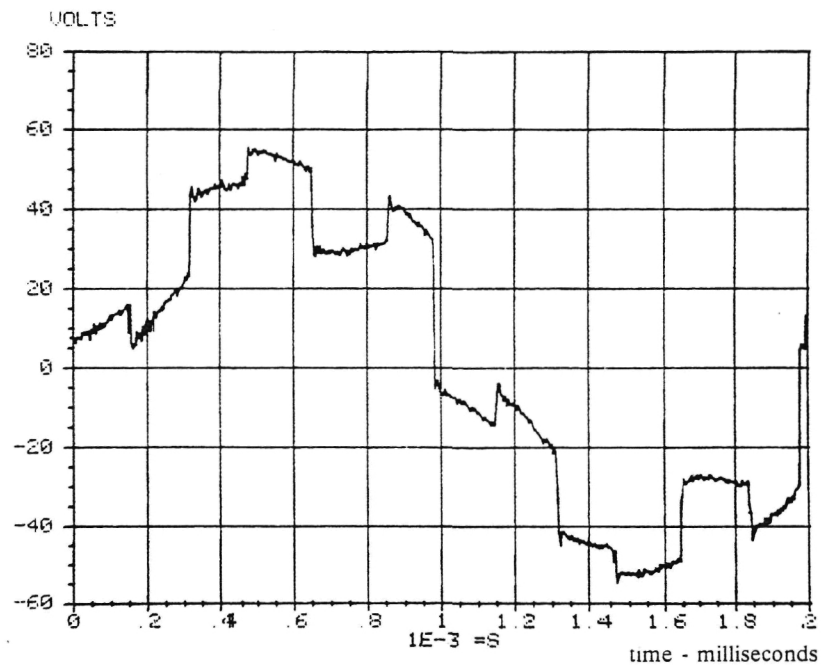
Figure 6-4. Sample Data Printout

REFERENCE

- 6-1. *Regenerative Flywheel Energy Storage System*, Volume II; Final Report, Subcontract No. 8990503; Prepared for Lawrence Livermore Laboratories, Univ. of California, Livermore, CA 94550; Prepared by General Electric Company, Corporate Research and Development, Schenectady, NY 12301, Report SRD-79-148-2.

RMS VALUE IS 34.7131

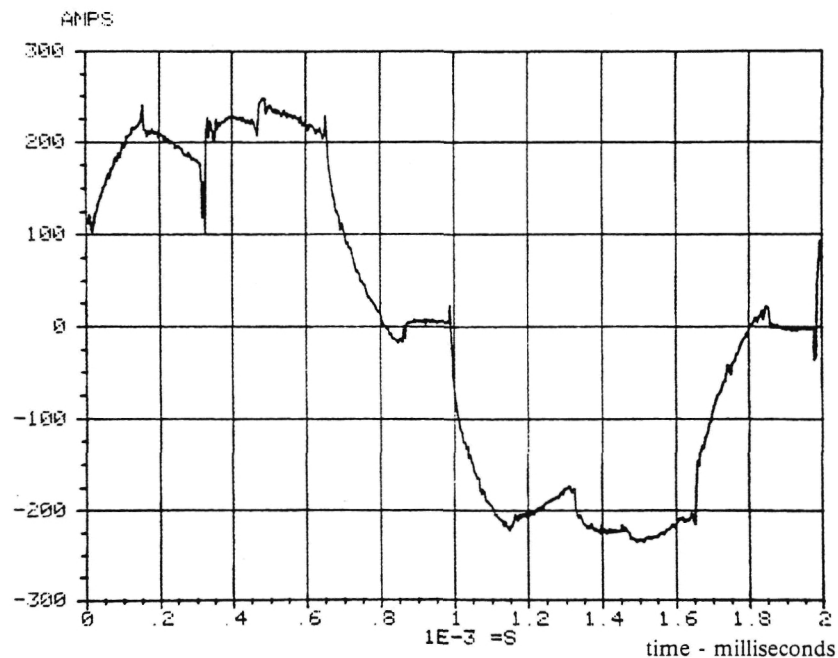
MEAN VALUE IS .626278



(a)

RMS VALUE IS 169.587

MEAN VALUE IS 1.79553



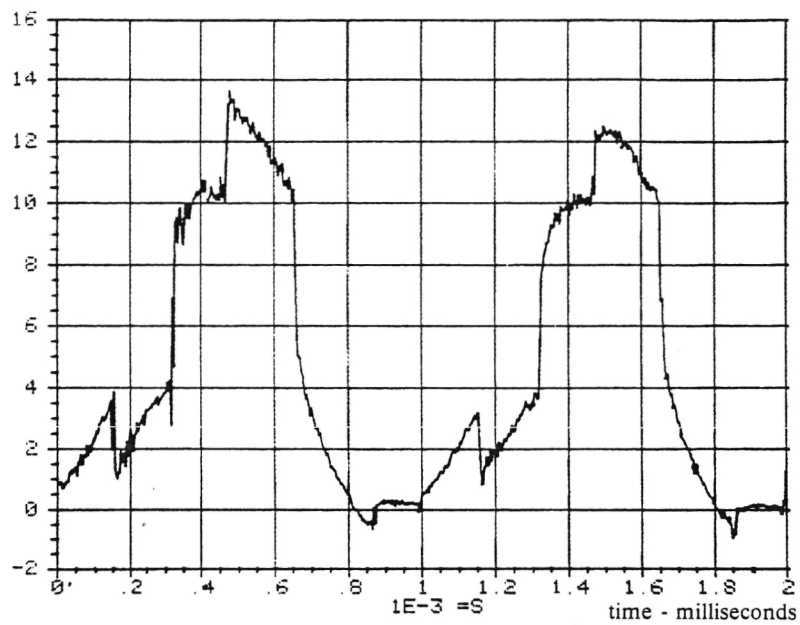
(b)

Figure 6-5. Sample DPO Printout: (a) Motor Voltage Waveform, (b) Motor Current Waveform, (c) (next page) Motor Instantaneous Power Waveform

RMS VALUE IS 6521.47

MEAN VALUE IS 4659.91

1E 3 WATTS



(c)

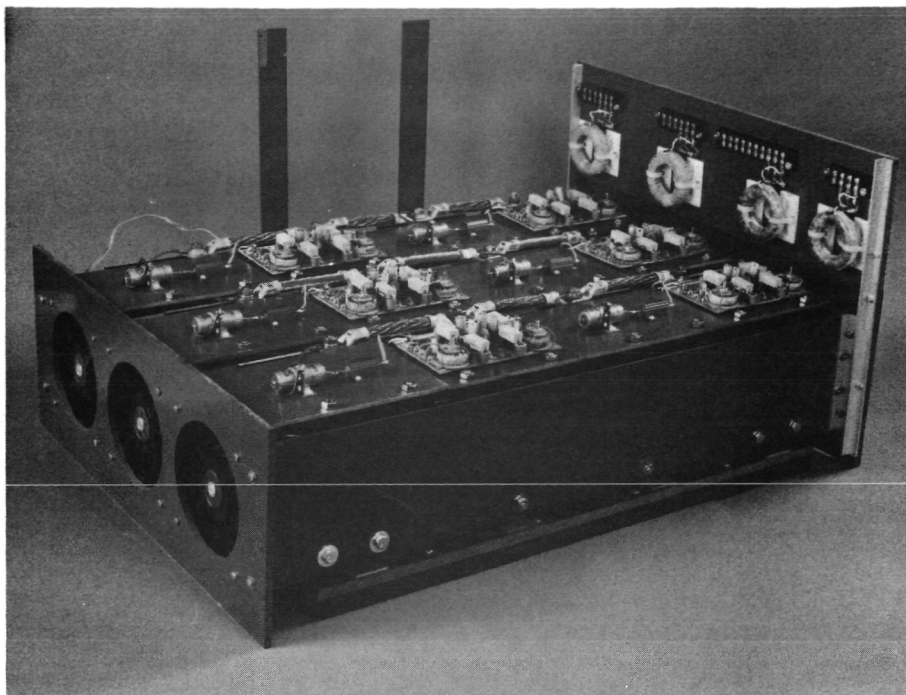


Figure 6-7. Load Commutated Inverter Breadboard

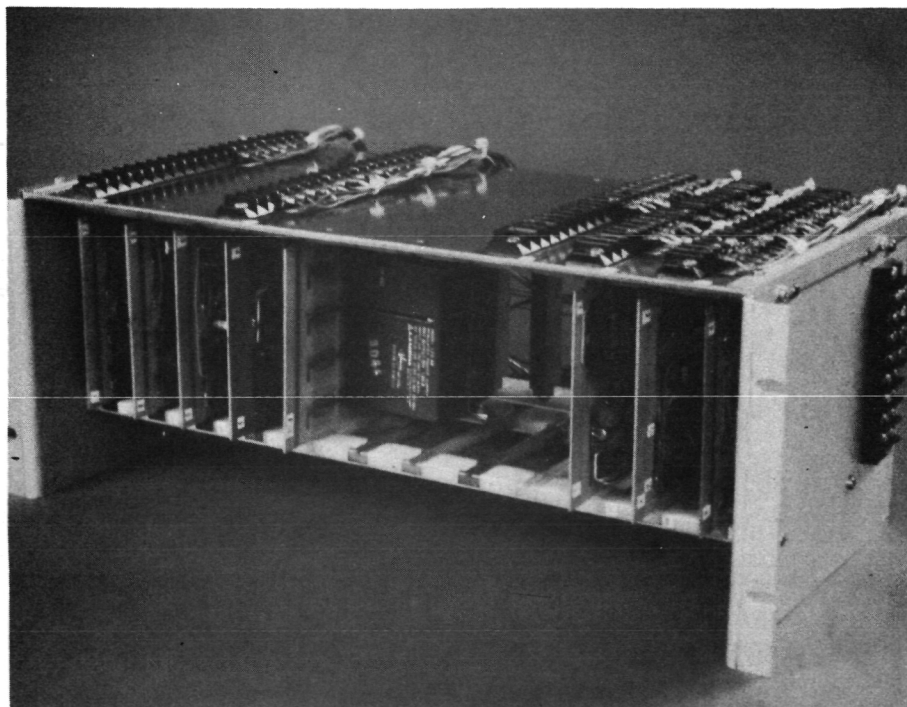


Figure 6-8. Printed Circuit Cards and Card Rack

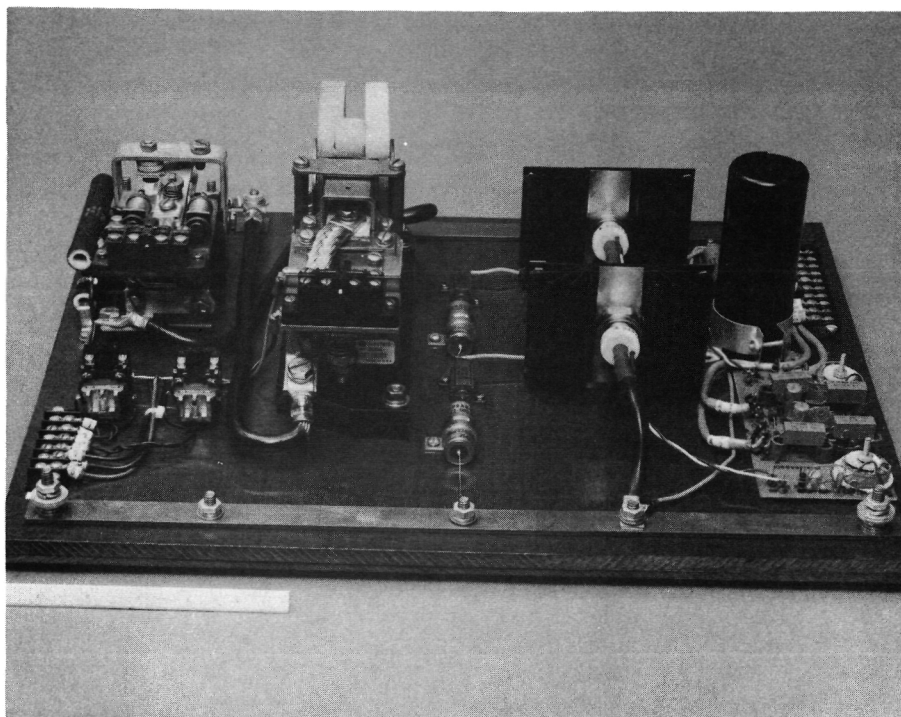


Figure 6-9. Third Harmonic Commutator and Relays



Figure 6-10. EAI Analog and Digital Computer

7.0 ENGINEERING MODEL PRELIMINARY DESIGN

7.1 INTRODUCTION

This section summarizes studies carried on during and following testing of the Phase I(A) motor but before the start of Phase I(B). As a result of the Phase I(B) activity, the conclusions stated here have been modified.

The preliminary engineering model design work is in two parts. The first consists of a series of parameter sensitivity studies, principally on magnetic gap length, to explore the differences, advantages, and disadvantages of air gap windings versus toothed steel cores, such cores being a low loss material such as powdered iron or amorphous metals. The second portion of the work examines the mechanical adequacy of the designs, principally with respect to the rotor containment ring.

7.2 ELECTROMAGNETIC DESIGN

7.2.1 Motor Concepts

All of the designs considered here are ten pole, compared to the eight-pole designs for the POP and FM motors. All motors have a top speed of 9470 rpm at 105 km/h (65 mph), which is considerably less than the FM(A). These choices grew out of some preliminary studies, the desire for lower stresses, and the desire for a smaller magnet. Three motor classes are examined:

1. A motor which utilizes manganese-aluminum magnets and has a magnet OD of 30 cm (11.81 in.), which is considerably larger than the FM(A).
2. A motor which has a magnet OD of 30 cm but uses rare earth magnets instead of manganese-aluminum-carbon.
3. A motor which uses rare earth magnets but has a magnet OD of 21.5 cm (8.46 in.), which is somewhat smaller than the FM(A).

The magnet geometry for the 30 cm diameter, ten-pole motor is shown in Figure 7-1. The manner of calculating the magnet area and other dimensions is shown in Figure 7-2. The magnet characteristic used for the manganese-aluminum-carbon magnet designs is shown in Figure 7-3. This characteristic is somewhat conservative in coercive force in view of the recent development of MnAlC with 0.26 MA/m (3300 Oe) coercive. A straight line [$0.8 \text{ T} \times 0.64 \text{ MA/m}$ ($8000 \text{ g} \times 8000 \text{ Oe}$)] is used for the CoSm magnet.

7.2.2 MnAlC, 30 cm Designs

Figure 7-4 shows how two critical parameters of the motor, the open circuit voltage E_o and the direct axis reactance X_d , vary with magnet length and effective gap. Since the sensitivity to magnet length is not great, succeeding curves are drawn for a nominal length of 3.81 cm for optimization of the gap after which the magnet length is reoptimized. Figure 7-5 shows a more complete variation of E_o and X_d for the selected magnet length. Figure 7-6 illustrates the air gap flux density under various conditions. Overall motor performance is shown in Figure 7-7. It may be seen that the best performance is obtained at an effective gap of about 0.15 cm. This, in turn, implies a slotted steel stator rather than an air gap winding. Figures 7-8, 7-9, and 7-10 repeat the previous charts as a function of magnet length at the apparent optimum gap of 0.15 cm. It may be seen that the relative insensitivity allows the choice of a short magnet to minimize cost, provided the inverter can accommodate a slightly increased

30 kW (40 hp) current. Since this appears to be the case, a magnet length of 2.54 cm (1 in.) is selected.

7.2.3 Rare Earth, 30 cm Designs

Based on the results of Section 7.2.2, an effective gap of 0.15 cm is selected. Sensitivity to magnet length is now rather marked, as shown in Figures 7-11, 7-12, and 7-13. Note in Figure 7-11 that minimum current is reached at a magnet length of 1.75 cm. However, since the efficiency peak is rather broad, the selection should be for minimum inverter current at 1.3 cm, which is also less magnet cost. Note also that the maximum efficiency is about 95.5% compared to 92.5% for the MnAlC magnets, and the 30 kW (40 hp) current is 130 versus 170 amperes. This suggests that the performance is in excess of that required and that considerable cost savings may result by reducing performance.

7.2.4 Rare Earth, 21.5 cm Designs

This section examines a reduced size, lower cost motor with reduced performance. Again, an effective air gap of 0.15 cm is utilized, and the magnet length is varied with results shown in Figures 7-14, 7-15, and 7-16. It may be seen that the sharp optima have disappeared and that a satisfactory motor is achieved at a magnet length of 1.5 cm. The maximum efficiency is now 93%, which is comparable to the MnAlC motor, but the 30 kW (40 hp) current is 200 amperes, which is higher than the MnAlC motor.

7.2.5 Engineering Model Design Applications

The preceding results indicate that a lower speed, smaller diameter motor will meet the contract requirements, provided rare earth magnets and a slotted core are used. The implications of using a slotted core with a single layer winding are listed in Table 7-1.

7.3 MECHANICAL DESIGN

7.3.1 MnAlC, 30 cm Design

The stresses in this motor were examined with essentially the same techniques used for the POP motor, as detailed in Section 3.5. The assumptions of the rotor design are listed in Table 7-2. Additional assumptions in connection with the case are listed in Table 7-3. The results for two different rim constructions, with an outside diameter of 30 cm (11.8 in.), are shown in Table 7-4. As a result of lower speed, even with increased diameter, it is now possible to consider high-strength aluminum instead of Inconel for the rim. Diameter may be reduced, to reduce windage and inertia, by use of Inconel.

7.3.2 CoSm, 21.5 cm Design

The assumptions for the CoSm magnet, 21.5 cm diameter design are shown in Table 7-5. Again, the analysis methods of Section 3.5 are utilized. In this design, the magnets are denser, but the diameter is smaller. The results of the study show that aluminum is a practical choice for the rim. The principal results are summarized in Table 7-6.

7.4 CONCLUSIONS

At this point, in view of the test results, several options for the engineering model have been considered. First is to continue with a very similar design using Alnico 8 or MnAlC magnets but redesigned to minimize demagnetization. The second option is similar to the first except that the magnets would be rare earth. This is a sensible option in view of the continuing high prices for MnAlC (and Alnico 8) and uncertainties as to its supply. Coupled with this is the drop in prices of CoSm magnets and the possibility of making a form of Mischmetal magnet at a viable price. The third option changes the concept of the motor from air gap winding to a slotted steel stator making it more like a conventional motor. This approach will entail the development of slotted tape winding techniques as well as a completely new winding concept. The magnet size, machine size, and efficiency of following these paths has been explored in some detail in this chapter.

Overall, the best course for proceeding to an Engineering Model at this point, with the minimum of lost time, is to retain the same motor concept (that is, air gap windings) but utilize rare earth (CoSm) magnets. At the same time improvements may be made in the electromagnetic design, structures, and fabrication methods that will result in further efficiency improvements.

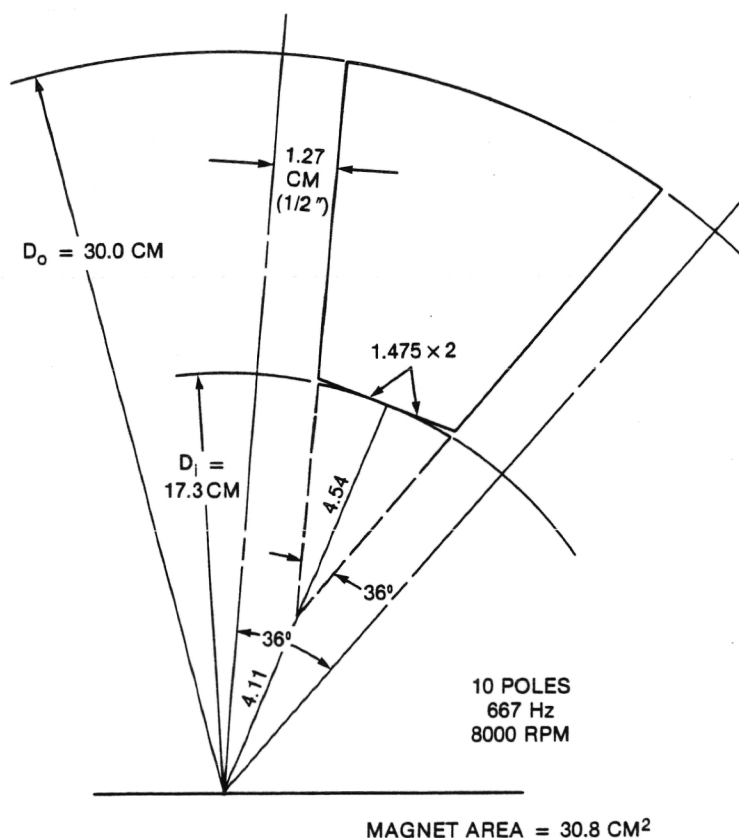
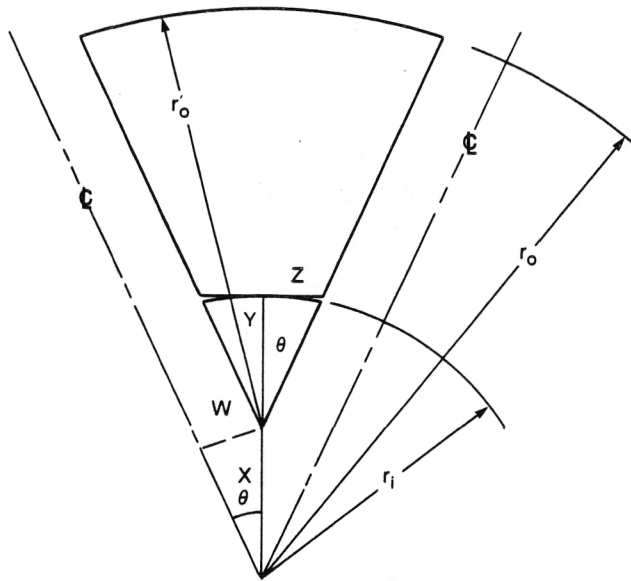


Figure 7-1. Proposed Magnet Dimensions—Engineering Model Motor



$$\left. \begin{aligned} \frac{W}{X} &= \sin \theta \\ Y &= r_i - X \\ Z &= Y \tan \theta \end{aligned} \right\} \quad \begin{aligned} \theta &= 36/2^\circ \text{ 10 POLE} \\ W &= 1.27 \text{ CM} \\ r_o &= 30/2 \text{ CM} \\ r_i &= 17.3/2 \text{ CM} \end{aligned}$$

$$\begin{aligned} X &= W/\sin \theta = 4.11 \text{ CM} \\ Y &= r_i - X = 4.54 \text{ CM} \\ Z &= Y \tan \theta = 1.475 \text{ CM} \\ r_o' &= r_o - X = 10.89 \text{ CM} \end{aligned}$$

$$\begin{aligned} \text{AREA} &\simeq \theta(r_o')^2 - \theta y^2 \\ &= .314 (10.89^2 - 4.54^2) \\ &= 30.8 \text{ SQ. CM} \end{aligned}$$

Figure 7-2. Ten-Pole Magnet Geometry

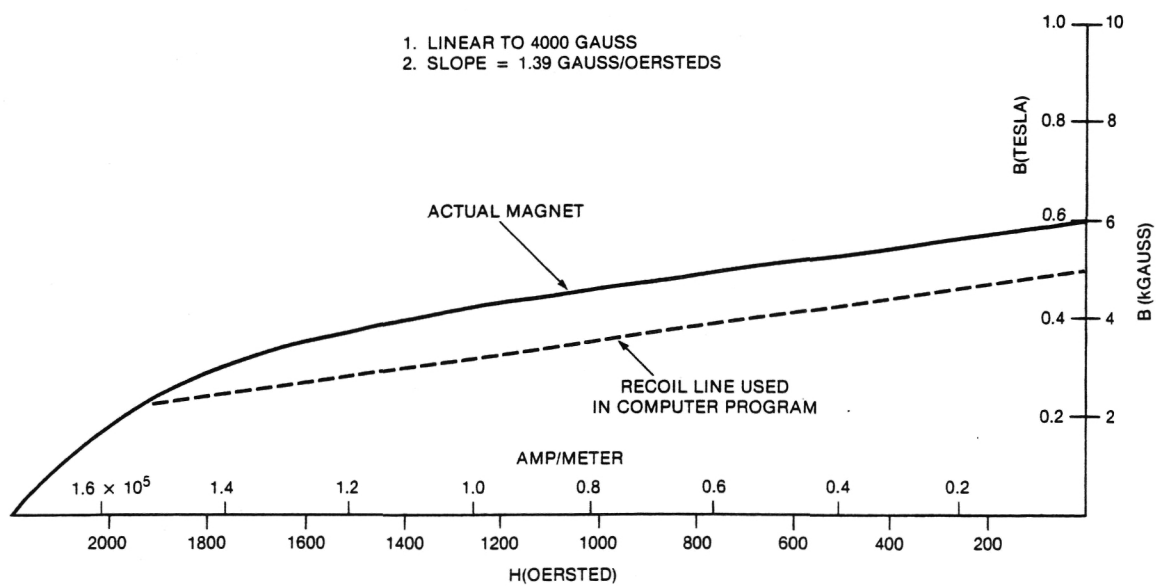


Figure 7-3. AlMnC Magnet Characteristics

AlMnC MAGNETS, 10 POLE, 30 TURNS, 425 Hz

STATOR $D_o = 30.0$ CM
STATOR $D_i = 17.3$ CM

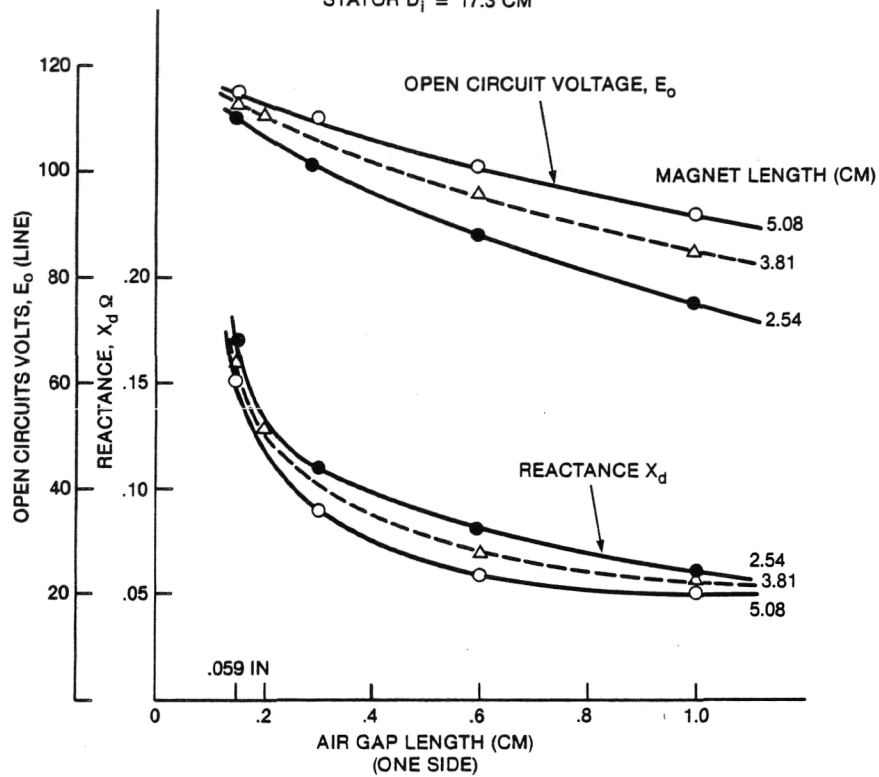


Figure 7-4. Effect of Air Gap Length on E_o and X_d

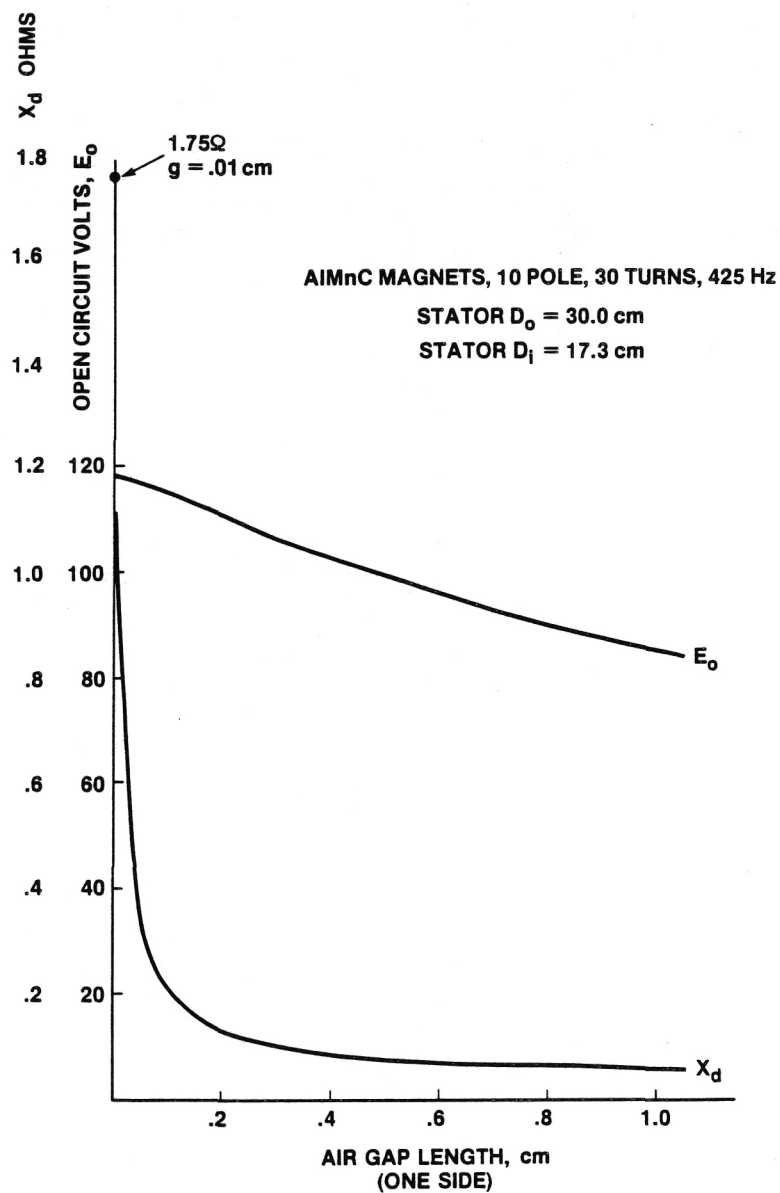


Figure 7-5. Open Circuit E_o and Reactance X_d Corresponding to a Magnet Length of 3.81 cm with a Varying Air Gap

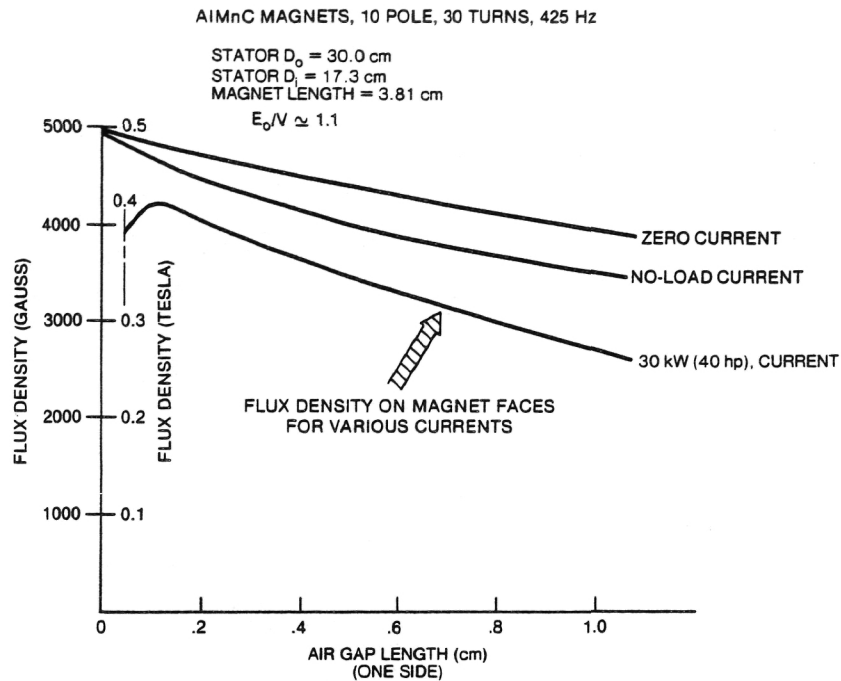


Figure 7-6. Armature Reaction Effects as the Air Gap Varies

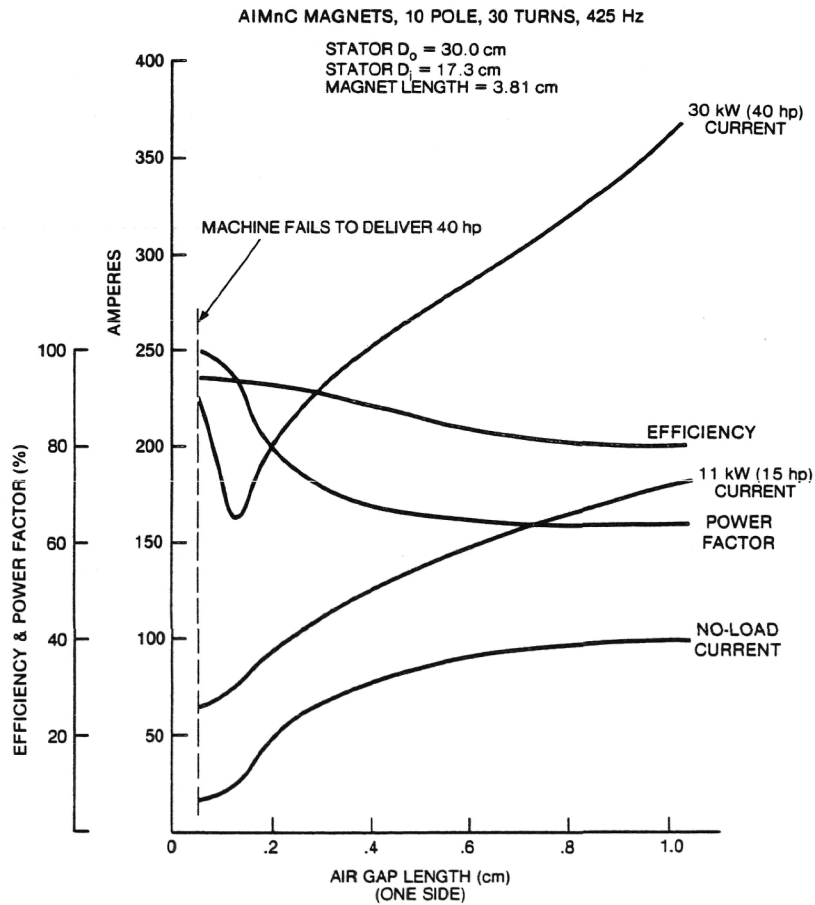


Figure 7-7. Effect of Air Gap on Machine Performance

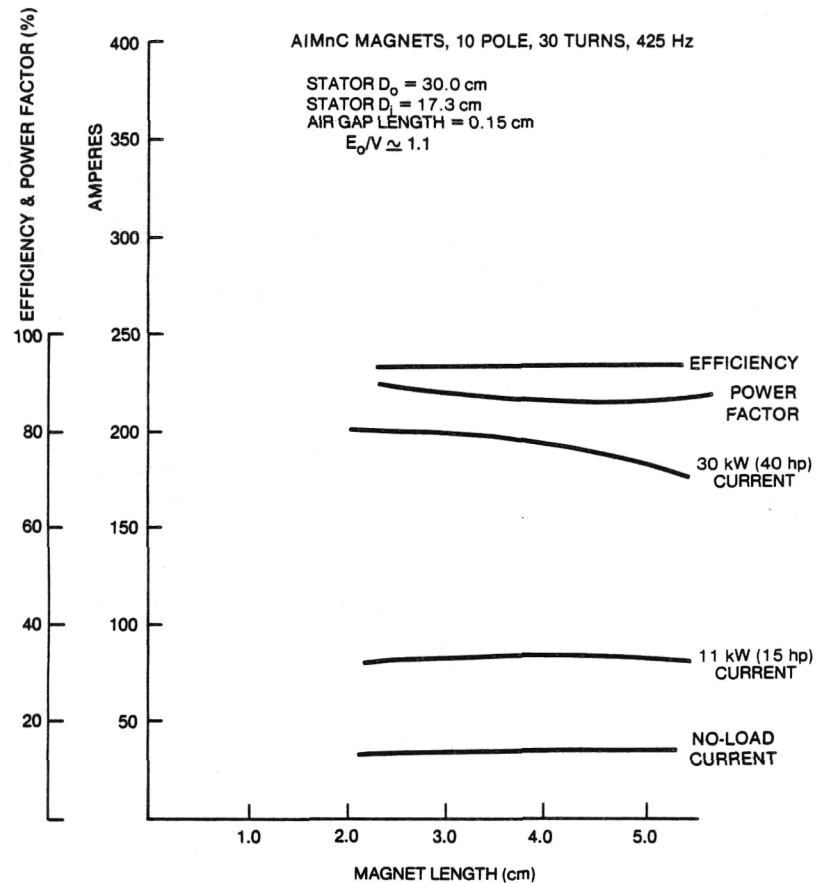


Figure 7-8. Effect of Magnet Length on Machine Performance

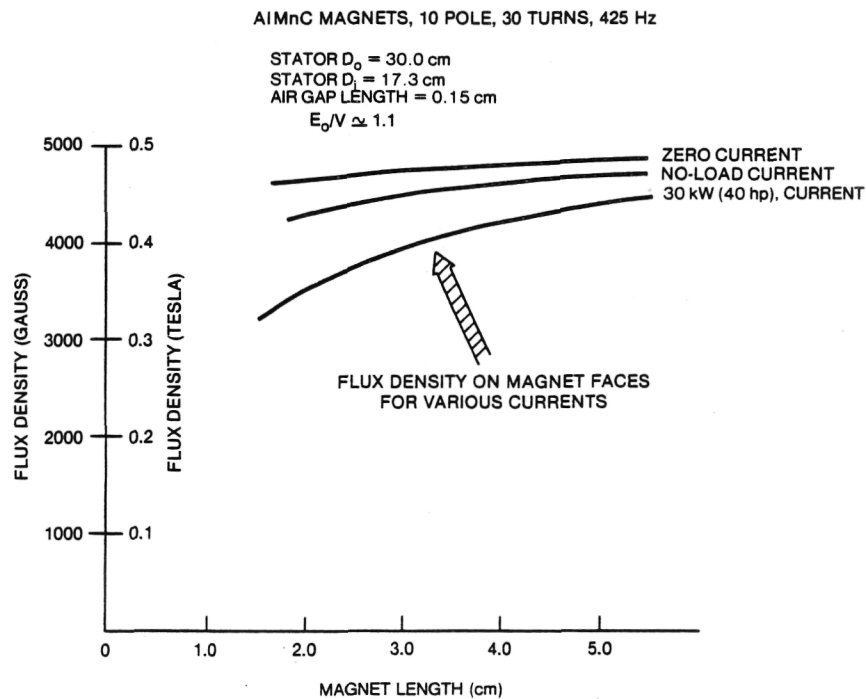


Figure 7-9. Armature Reaction Effects as the Magnet Length Varies

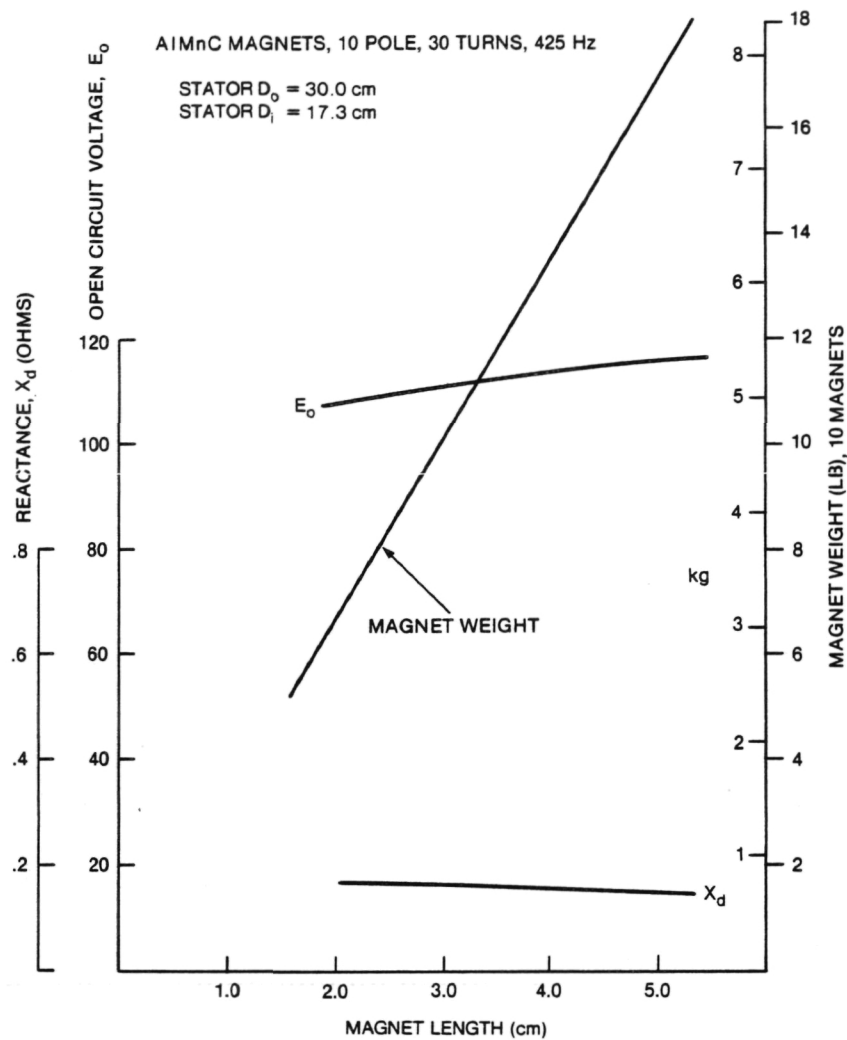


Figure 7-10. Open Circuit Voltage E_o and Reactance X_d Corresponding to an Air Gap Length of 0.15 cm with Varying Magnet Length

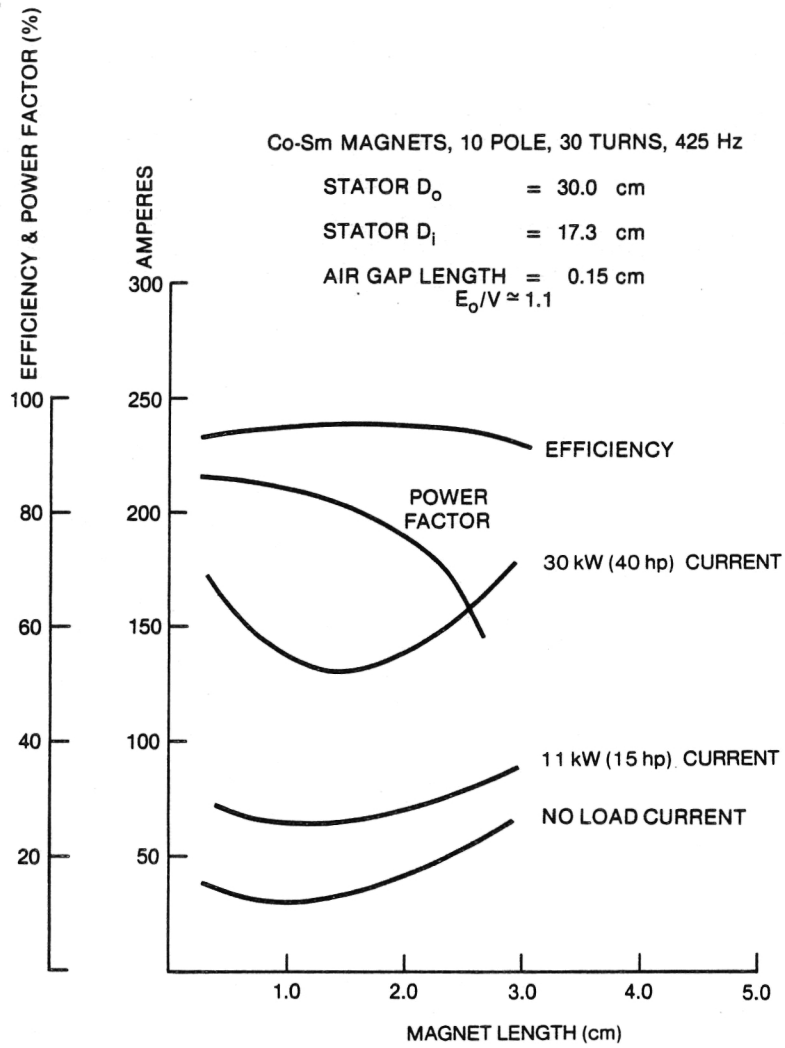


Figure 7-11. Effect of Magnet Length on Machine Performance

Co-Sm MAGNETS, 10 POLE, 30 TURNS, 425 Hz

STATOR D_o = 30.0 cm

STATOR D_i = 17.3 cm

AIR GAP LENGTH = 0.15 cm
 $E_o/V \approx 1.1$

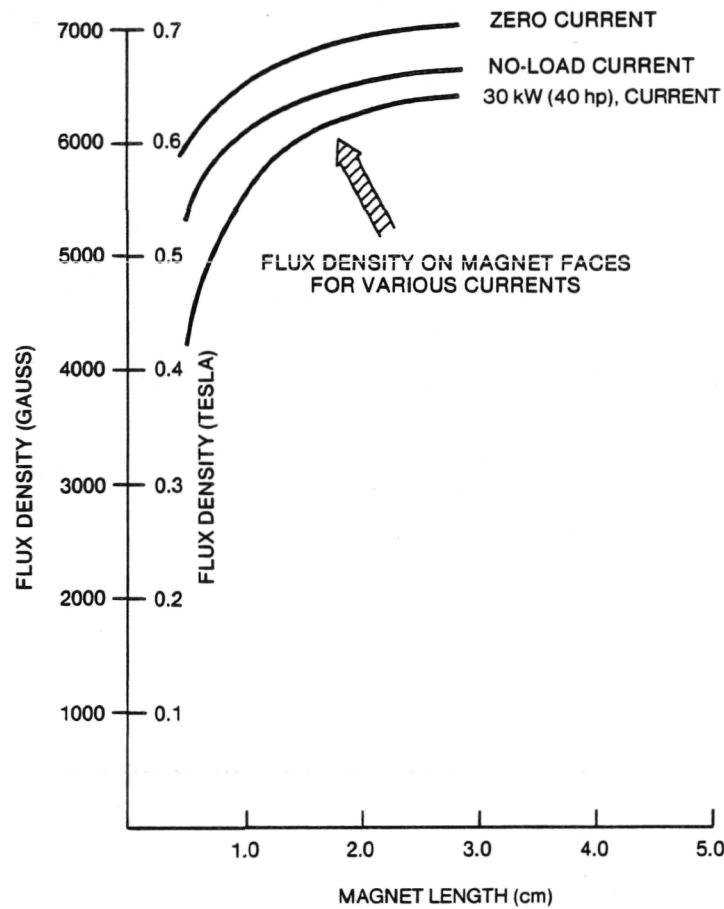


Figure 7-12. Armature Reaction Effects as the Magnet Length Varies

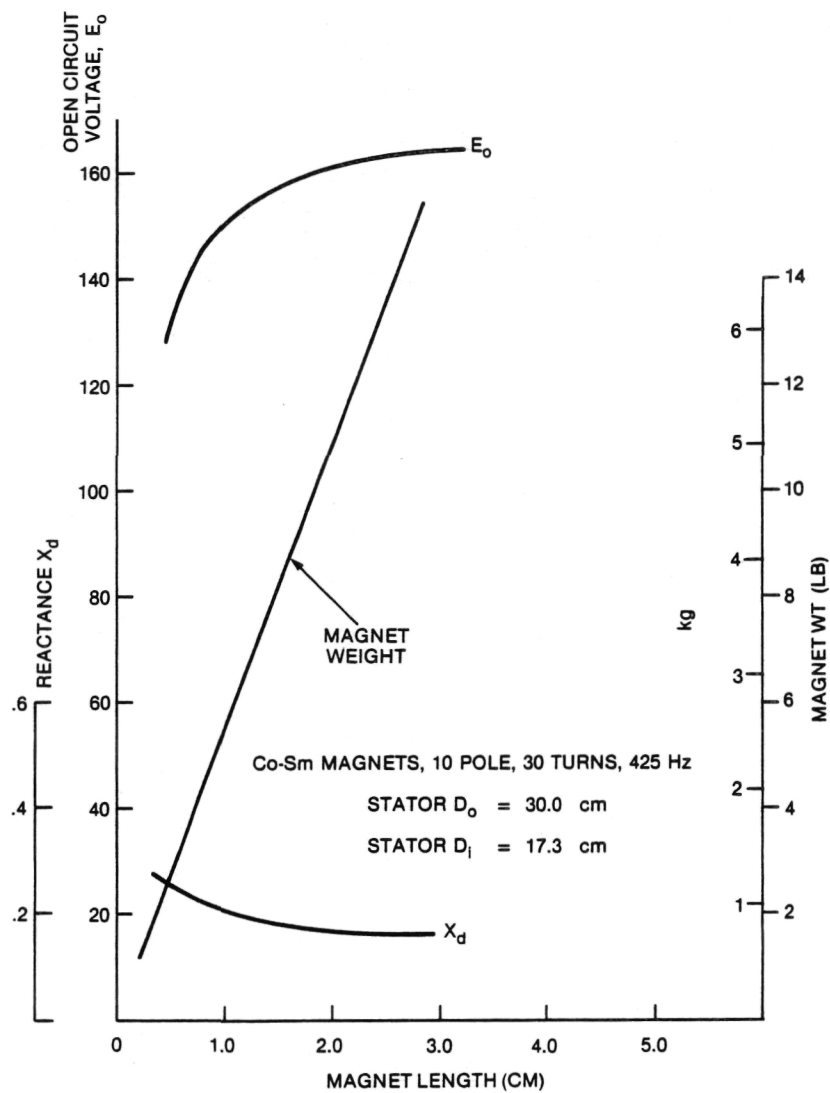


Figure 7-13. Open-Circuit Voltage E_o and Reactance X_d Corresponding to an Air Gap Length of 0.15 cm with Varying Magnet Length

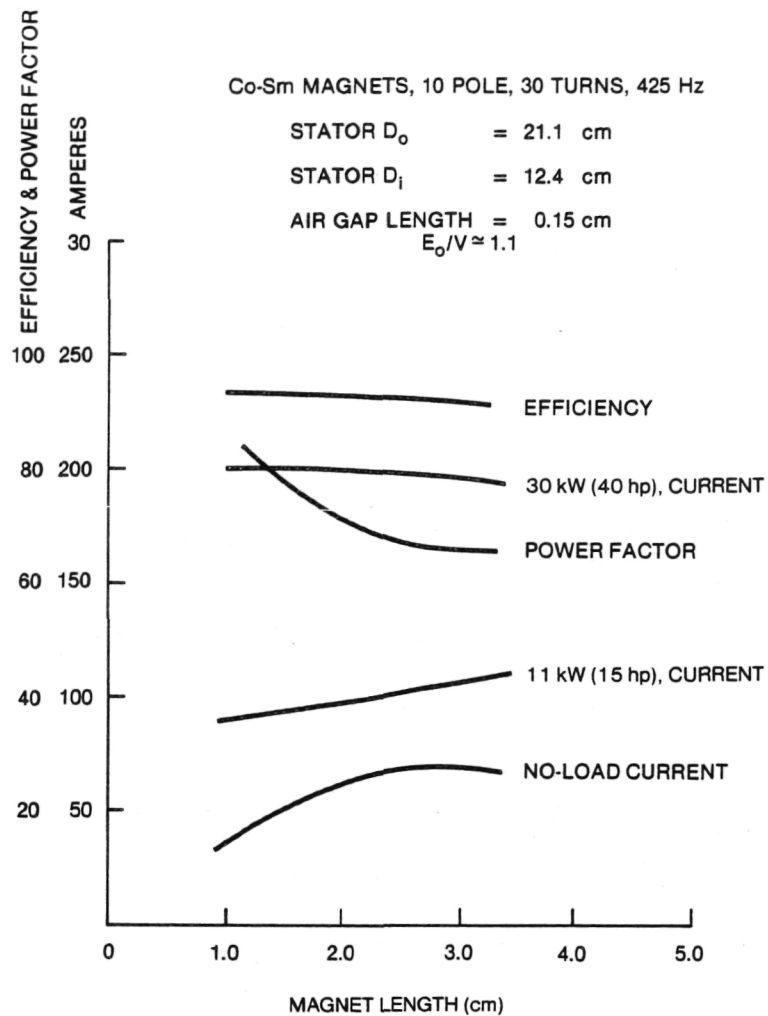


Figure 7-14. Effect of Magnet Length on Machine Performance

Co-Sm MAGNETS, 10 POLE, 30 TURNS, 425 Hz

STATOR D_o = 21.5 cm

STATOR D_i = 12.4 cm

AIR GAP LENGTH = 0.15 cm
 $E_o/V \approx 1.1$

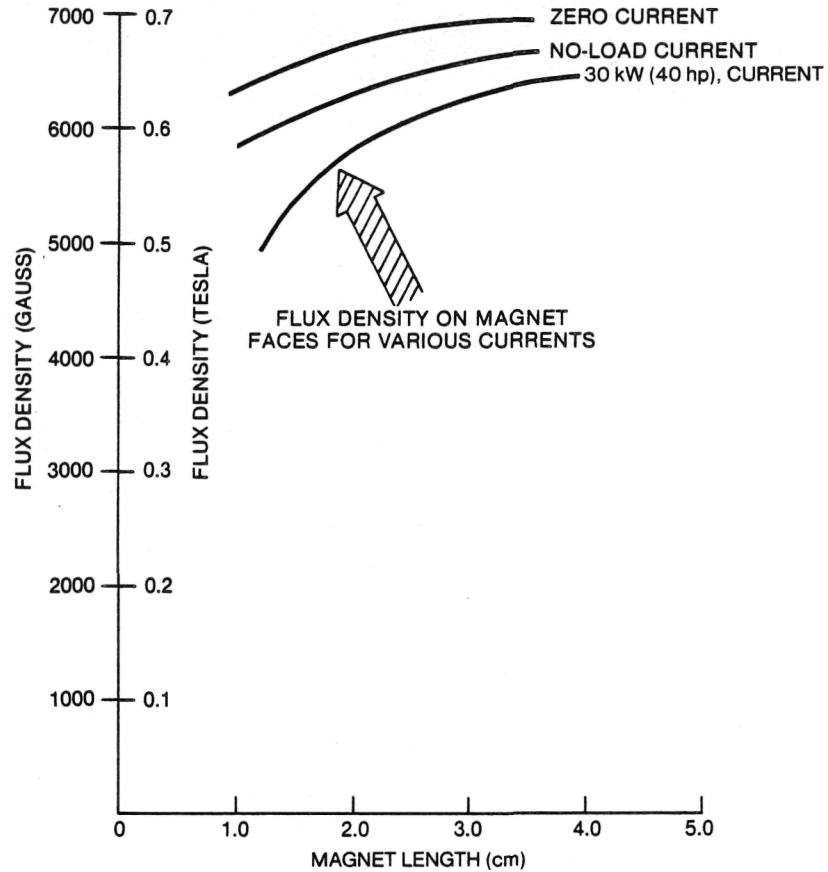


Figure 7-15. Armature Reaction Effects as the Magnet Length Varies

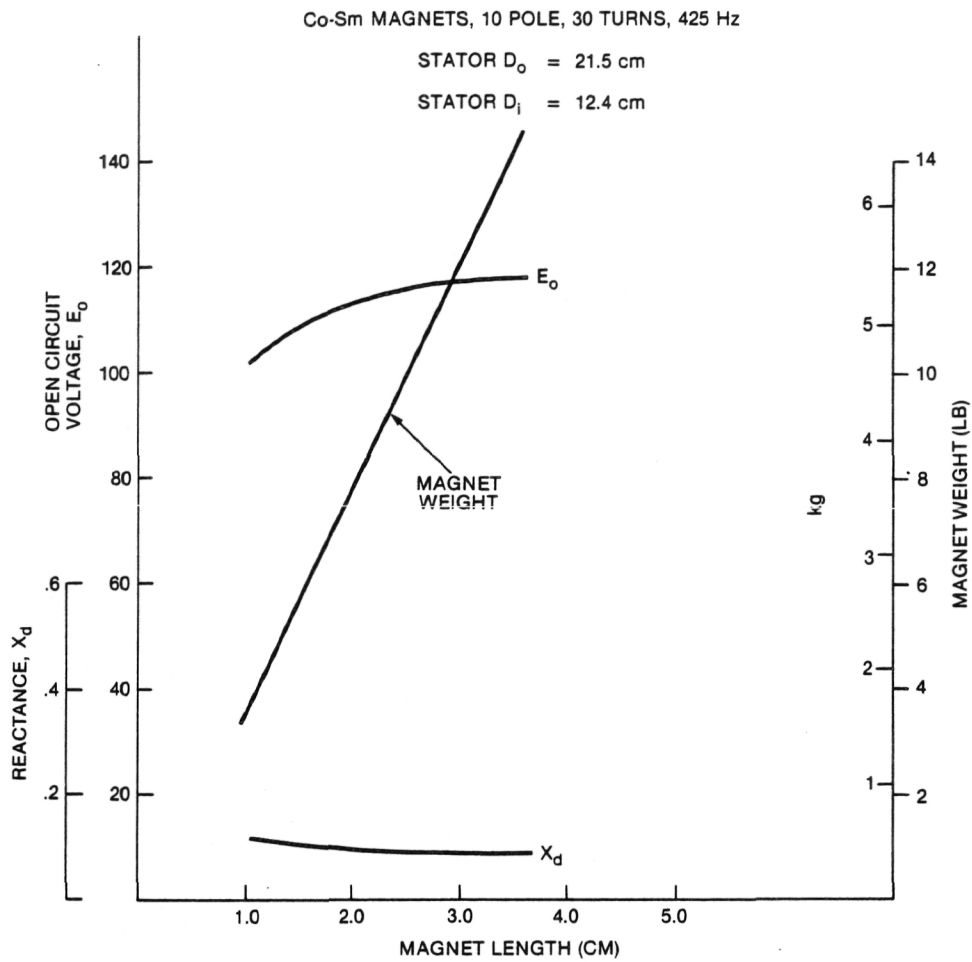


Figure 7-16. Open Circuit Voltage E_o and Reactance X_d Corresponding to an Air Gap Length of 0.15 cm with Varying Magnet Length

Table 7-1

**IMPLICATIONS OF USING A SINGLE LAYER
WINDING WITH A SLOTTED IRON CORE**

- **Larger Open Circuit Voltage**
 - 1. Permits inverter commutation despite larger reactance
- **Larger Reactance**
 - 1. Provides motor stability
 - 2. Machine less sensitive to voltage change
 - 3. LCI operation more difficult
- **Better Heat Transfer**
 - 1. Less temperature gradient between winding and frame
 - 2. Iron-toothed stator and single-layer winding reduce the thermal resistance
- **Eddy Currents In The Copper Strands Are Reduced**
 - 1. Stator winding subjected only to slot leakage and not the main flux
- **Magnet Operating Point Is High On The B,H Line**
 - 1. Makes possible operation on linear part of B,H line
- **Thinner Magnets Can Be Used**
 - 1. Excitation requirements reduced
- **Greatly Improved Flux Focusing**
 - 1. Less leakage flux
 - 2. Less case currents and case I^2R losses
 - 3. Increase (of a second kind) in open circuit voltage
- **Magnetization After Assembly Using Machine Winding**
 - 1. Small air gap and toothed stator provide minimum ampere turns for magnetization
- **Inexpensive Random Wound Stator Coils Can Be Used**
 - 1. Winding is positioned in stator slots
- **Winding Is Inherently Balanced**
 - 1. Slotting eases mechanical precision requirements
- **Disadvantages**
 - 1. Armature reaction is greater, hence easier demagnetization
 - 2. Tooth losses must be countered

Table 7-2
ENGINEERING MODEL MOTOR
PRELIMINARY MECHANICAL DESIGN

Speeds

Cruise = 88.5 km/h (55 mph)	8.00 krpm
Maximum = $\frac{65}{55} \times \text{Cruise}$	9.46 krpm
Design = $1.15 \times \text{Maximum}$	10.88 krpm

Magnets (From Electromagnetic Design)

Number	10
Material	AlMnC
Shape	Trapezoidal
Outside Radius	15 cm (5.9 in.)
Inside Radius	8.6 cm (3.4 in.)

Environmental

-30 to +50°C
3500 hr Life
Shock, Vibration

Table 7-3
ENGINEERING MODEL MOTOR
PRELIMINARY MECHANICAL DESIGN

Case

Cast Aluminum Alloy
Maximum OD 45.7 cm (18 in.)
Non-Ventilated

Cooling

External Air
1 Blower

Safety

<u>Failure Mode</u>	<u>Safety Feature</u>
Rim Fracture	Spacer and cooling duct absorb kinetic energy
Rotor Locks	Entire motor spins down within duct

Table 7-4

ENGINEERING MODEL MOTOR
ROTOR PRELIMINARY MECHANICAL DESIGN

Manganese-Aluminum-Carbon Magnets
30 cm Active Diameter

Construction

Metal rim shrunk on hub

Requires chilled hub

Rim

	Aluminum Alloy	Inconel and Aluminum Sandwich
OD	35.6 cm (14 in.)	33 cm (13 in.)
Windage	405 watts	275 watts
Design Stress	276 MPa (40 ksi)	931 MPa (135 ksi)

Bearings

Grease Lubrication

ABEC 5 (Target)

Table 7-5

ENGINEERING MODEL MOTOR
PRELIMINARY MECHANICAL DESIGN

Reduced Performance Option

Speeds

Cruise = 88.5 km/h (55 mph); 8000 rpm

Maximum = 104.6 km/h (65 mph); 9460 rpm

Design = 1.15×65 ; 10,890 rpm

Magnets

Number	10
Material	CoSm
Shape	Trapezoidal
Outside Radius	21.5 cm dia. (4.23 in.)
Inside Radius	12.4 cm dia. (2.44 in.)
Thickness	2.54 cm (1.00 in.)
Spacing	1.83 cm (~0.72 in.)

Table 7-6
ENGINEERING MODEL MOTOR
ROTOR PRELIMINARY MECHANICAL DESIGN
Reduced Performance Option

- Construction — Metal rim shrunk on hub
 - Requires chilled hub
 - 167°C (332°F) temperature differential
- Rim — Aluminum Alloy 7050-T3651
 - OD 9.3 in.
 - Windage loss 100 W
 - Design stress 298 MPa (43.2 ksi)
- Rotor Weight 6.8 kg (15 lb)

PART II – PHASE 1(B)

SUMMARY – PHASE I(B)

This part of the report deals only with work done during the extension of Phase I of NASA/Lewis Contract DEN 3-76 "Advanced Electric Vehicle Motor Development". It is not "free standing" in that it depends for completeness on various sections of the first part. The work reported here concerns the redesign, rebuilding, and test of the Functional Model motor. The resultant motor exceeds the performance specifications of the contract.

The tasks undertaken in the extension are described below and correspond to the sections of the report.

1. The redesign called for rare earth magnets and a single layer chain winding as the major approaches to correcting the deficiencies of the original model.
2. An account of the stator fabrication and special methods of heat transfer are given.
3. New magnet fabrication concepts were used. An account of the rotor fabrication and special balancing measures is given.
4. A task was added to carefully evaluate windage losses under realistic conditions in a simulated motor.
5. A summary of the test procedures and the results of testing are given.
6. Conclusion and recommendations with a new look at the engineering model forms the last section.

8.0 INTRODUCTION

8.1 BACKGROUND

At the conclusion of Phase I [now known as Phase I(A)], the performance of the motor was presented. As noted in Section 5 of the first part of this report, the performance did not meet the requirements of an electric vehicle drive. The principal reasons for this were identified, and solutions were proposed in each case.

Subsequently, an extension to Phase I of the contract was funded [now known as Phase I(B)] to redesign, rebuild, and retest the motor, including the proposed improvements. The results of that effort are the substance of this second part of the report. This work is, of course, heavily based in the work of Phase I(A); hence material covered in the first part is not repeated in the second. Only the newly developed materials are reported here. Thus the first part may stand on its own as a complete document, but the second part depends on the first for completeness.

There was also a change of staff (summarized in Table 8-1) between the first and second parts. The contributors listed are also the authors of the two sections of the report.

Table 8-1
PROJECT TEAMS

	<u>Phase I(A)</u>	<u>Phase I(B)</u>
Principal	G.B. Kliman	G.B. Kliman
Electromagnetic	V.B. Honsinger	W.R. Oney
Mechanical	R.N. Johnson	R.N. Johnson
Magnets	R.E. Tompkins	R.E. Tompkins
Test	T.A. Nondahl W.R. Mischler	W.R. Mischler W.R. Oney
Winding	J. Cammarere	O.H. Fraking
Concept and POP Motor	E. Whitely M. VanDuyn	

8.2 PROBLEMS OF THE PHASE I(A) MOTOR

The detailed performance of the Phase I(A) motor is given in Section 5 of the first part. A brief extract of this data is presented in Table 8-2. The achieved performance levels fall short of those required. Note also that the inductance is fairly high and that the internal thermal impedance is also quite high.

As previously mentioned, the most crucial problem was that of the magnets. Table 8-3 summarizes the performance history of the magnets showing the decay of flux due to armature reaction and faults, as suggested in the proposal as a principal risk. In order to assure the maximum resistance to demagnetization, a magnet of the highest coercive force (H_c) is required. At the same time, the highest possible flux density will yield the best motor performance. The principal choices of magnet type are shown in Table 8-4. The clear choice for performance (but not cost) is CoSm.

Table 8-2
PHASE I(A) MOTOR
PERFORMANCE SUMMARY

Phase Inductance	75 to 100 μ H
Phase Resistance	0.042 Ω
• <u>Generating into Resistive Load</u>	
Peak Efficiency	90%; 5000 rpm; 6.1 kW (8.2 hp)
Peak Output	66%; 8000 rpm; 19.4 kW (26 hp)
• <u>Motoring on Inverter</u>	
Peak Efficiency	86%; 5500 rpm; 6 kW (8 hp)
Peak Output	75%; 6000 rpm; 13.4 kW (18 hp)
• <u>Thermal</u>	
- Temperature Limited	
- Internal Drop Approximately 3X External	

Table 8-3
PHASE I(A) MAGNETS

Design Value	0.3660 T
Calculated Value	0.3300 T
Magnetized in Place	0.3000 T
After Load Tests	0.2850 T
After First Inverter Test	0.2450 T
At End of Testing	0.2330 T

Table 8-4
MAGNET COMPARISON

	<u>B_R</u>	<u>H_C</u>
Alnico 8E	0.8000 T	154 kA/m (1940 Oe)
MnAlC	0.5000 T	263 kA/m (3300 Oe)
CoSm	0.8000 T	637 kA/m (8000 Oe)
Ceramic	0.3800 T	302 kA/m (3800 Oe)

The goals of the electromagnetic design are listed in Table 8-5. The best performance will be obtained with the maximum flux for the selected magnets. Then the winding must be arranged to make maximum utilization of that flux.

Load losses were minimized by maximizing flux and packing as much copper into the motor as is possible. Unfortunately, packing of copper is limited by the size of the components, and increasing flux density increases the no-load and parasitic losses. Measures to combat those losses are listed under "Parasitic Current Reduction." An illustration of the effect of these losses is presented in Table 8-6, which shows that unusual measures such as fine wires, etching, surface insulation, etc. are justified.

Table 8-5
GOALS OF THE ELECTROMAGNETIC DESIGN

- Maximize Flux
 - Maximize Magnet Area
 - Minimize Air Gap
 - High-Energy Magnet
- Concentrate Winding
 - Maximize Use of Flux
 - ECM Effect
- Parasitic Current Reduction
 - Multistrand Twisted Cable
 - Transpose Cables
 - Precision Winding Placement
 - Insulated Structures
 - Etched Yoke
 - Shaped Yoke

Table 8-6
PHASE I(A)
OPEN CIRCUIT LOSS

<u>rpm</u>	<u>W</u>	<u>Temperature Rise (°C)</u>
5000	275	22
10,000	1100	75

Note: At 0.2400 T, scaling to 0.5400 T
and 7000 rpm yields 2729 W

Precision winding placement and the single-layer winding will assure balance. Imbalance of the Phase I(A) motor (Table 8-7) resulted in improper inverter operation and artificially high lead angles as well as some instability.

The best way to reduce temperature rise is to reduce losses, as already described. However, the losses that do occur must be brought out; hence, a number of measures were taken to reduce the internal thermal impedance. These are listed in Table 8-8.

In the mechanical area, several deficiencies were identified in the Phase I(A) motor and are listed in Table 8-9. The first item impacts losses, and the remainder influence vibrations and resonance. The solutions involved the windage loss study to optimize gap and stiffening of the motor fastening and support system (Table 8-10). The influence of the magnets indicated low confidence in balancing machine methods; hence, the procedure shown in Table 8-11 was proposed to achieve balance.

As will become evident in this section of the report, all proposed improvements were made with outstanding success. Some design options to improve efficiency (such as a nonconducting spacer) were not done in the interests of safety or were not within the scope of the project.

Table 8-7
PHASE I(A)
WINDING BALANCE

	<u>Inductance (μH)</u>	<u>Open Circuit Voltage (5000 rpm)</u>
Phase A	63.3	69.5
Phase B	52.7	74.8
Phase C	54.0	73.3

	<u>Angle</u>
A-C	120°
A-B	105°
B-C	140° (?)

Table 8-8
HEAT TRANSFER MEASURES

- Precision Fit of Surfaces
- Heat Conducting Epoxy
- Bonded Slot Liners and Surfaces
- Anisotropic Heat Conductors
- Impregnation with Heat Conducting Epoxy
- Retain Fins and Fans

Table 8-9

**PHASE I(A) MOTOR
MECHANICAL PROBLEMS**

- Nonoptimum Clearance Gap
- Weak Bearing Support
- Doubtful Balance
- Nonrigid Mounting

Table 8-10

CASE AND MOUNT CONCEPT IMPROVEMENTS

Case

- Phase 1A Stator Housings Reused
- Longer Spacer Required

Mount

- Stiffen Mounting
 - Weld Six Standoffs One End
 - Special Fasteners Attach Motor
- Lengthen Phase 1A Mount 1.11 cm (7/16 inch)

Table 8-11

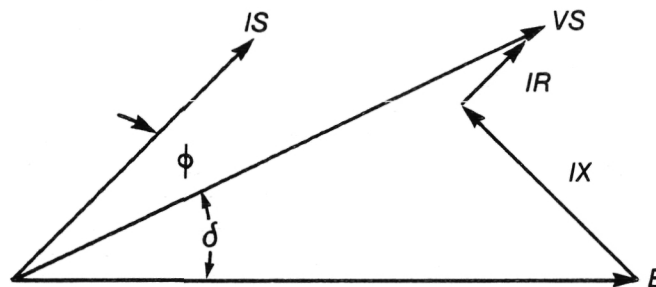
BALANCE CONCEPT

- Spin Balance Hub and Shaft on Bearings
- Weight-Match Opposite Magnets
- Static Balance Rim

9.0 ELECTROMAGNETIC DESIGN

9.1 PERFORMANCE PREDICTIONS

The software program adopted and modified to help design and predict performance of the Phase IB motor is that originally written by Dr. T.A. Nondahl to model and analyze the Phase IA motor performance. Inputs to the program are horsepower and speed. Printout is a table of performance characteristics for different vector angles (built into the program) between source current, IS , and back emf, E . The program finds a current magnitude that satisfies the program inputs (horsepower, speed, and vector angle) and prints out a line of characteristics which satisfy the vector diagram of Figure 9-1. It then repeats this procedure until all vector angles are solved.



ϕ	POWER-FACTOR ANGLE
δ	POWER ANGLE
IS	SOURCE CURRENT
VS	SOURCE VOLTAGE
IR	DROP — OHMIC AND STRAY LOAD LOSS
IX	REACTANCE DROP
E	BACK EMF

Figure 9-1. Vector Diagram — Motoring

Printout of performance predictions indicate all the possible ways the system can operate but not the way it will operate. The load-commutated inverter (LCI) selects (via computer control) the correct power-factor angle which will match source voltage, VS , and motor back emf, E . For conditions requiring a small power-factor angle, the inverter may fail to commute. Test data was obtained with a power-factor angle as low as 25° , but past experience with other motors indicates an angle of 30° to 35° is probably a more usual condition. The low angle is due to the extremely low inductance of this motor.

This angle is not an independent variable, but may be influenced by raising and lowering source voltage, VS , within a band determined by the limits of the dc power supply and the ability of the inverter to commute. The dc source used in the tests supplied enough voltage when full on at 120 V dc to enable the inverter output voltage to reach 55 V ac, which is a good operating voltage for a speed of 5500 rpm with no phase advance in the inverter.

Above 5500 rpm the power-factor angle had to be increased by the inverter control through phase advance because the source voltage, VS , had reached a plateau. For

example, at 9000 rpm and 19.8 kW (26.5 hp), the test power-factor angle is 50° and the calculated efficiency is 84.8%. If a higher dc voltage, say 190 volts, were available, the ac voltage would be 85 volts, the power-factor angle would be reduced to 25°, and the calculated efficiency would be increased to 91.5%. The increased efficiency results primarily from a reduction of phase current by about half.

A similar phenomenon may be seen in the performance predictions presented to NASA early in the program (Table 9-1). Here the early data was based on a low lead angle. As the design was refined, it became clear that the given operating point must have a larger lead angle to operate on the laboratory power supply. The breakdown of rotational losses shown in the early prediction is approximately correct. A similar breakdown is not shown for the later prediction since an empirical figure was being used.

Table 9-1
PHASE I(B) FUNCTIONAL MODEL MOTOR
PERFORMANCE PREDICTION AND LOSS BREAKDOWN
7000 rpm and 11.2 kW (15 hp)

<u>Stator Winding*</u>	<u>As Presented to NASA in July 1981</u>		<u>Final Design</u>
	<u>3 Cable</u>	<u>2 Cable</u>	<u>2 Cable</u>
Peak Flux Density, T	0.4900	0.5500	0.5450
Temperature Rise, °C	68.5	68.5	43.0
Stator Resistance, Ω	0.01535	0.02301	0.01654
Power Factor Angle (calc.)	32°	32°	43°
Losses (W)			
Stator I^2R	288	347	441
"Rotational"	738	674	706
Stray	242	194	—
Eddy	250	210	—
Friction and Windage	150	150	—
Frame	48	60	—
Core	48	60	—
Total Loss (W)	1026	1021	1147
Efficiency, %	91.60	91.64	90.7

*See Figure 10-1 for layout of 2-cable, 3-turn final design

A listing of the program in its final state is given in Figure 9-2. The mathematical model has been calibrated from empirical data, so agreement with test data is very good.

Terminal voltage was neither a trapezoid nor a sine wave, but its shape was intermediate and rounded. Source current, IS , was nearly at 120° quasi-square wave (except at high speeds when the sides of the wave begin to slope). Therefore, the input

```

10*#RUN = (CORE=22K)
20C PROGRAM TO CALCULATE TEMPERATURE PERFORMANCE OF DISK MOTOR
30C
40 COMPLEX E,IS,VS
50 REAL KRPM
60C
70 CALL OPENF(02,"DISCOUT: ")
80 IOUT=2
90C
100 SMG=1
110C SMG = 1 FOR MOTOR, = -1 FOR GENERATOR
120C
130 PI=4.*ATAN(1.)
140 ELS=25.8E-6
150 RS25=0.0142
160 EPKRPM=9.75
170 TEMP=50.
180 WPDCA=50.
182 WPDGS=50.
190 PHII2=65.
200C
210 10 WRITE(6,25)
220 25 FORMAT(" TYPE SPEED (IN THOUSANDS OF RPM) & SHAFT HP")
230 READ(5,5)KRPM,PSHAF1
240 5 FORMAT(V)
250 WRITE(IOUT,27)KRPM,PSHAF1
260 27 FORMAT("//" SPEED =" ,F8.3," KRPM. SHAFT H.P.=",F6.1, /
270& " NASA PHASE IB DISC MOTOR",35X,"+ WHEN LEADING")
280 PSHAF1=PSHAF1*746.
290 E=(1.,0.)*KRPM*EPKRPM
300 XS=ELS*120.*PI*KRPM/0.900
310C
320 WRITE(IOUT,35)
330 35 FORMAT(2X,"KWTERM",3X,"EFFIC.",2X,"P.F.",2X,
340& "TEMP.RISE",3X,"E",7X,"VS",6X,"IS",5X,"PHII",2X,"P.F.ANGLE")
350C
360 PHII=50.
370C
380 30 PHII=PHII+1.
390 IF(PHII.GT.PHII2) GO TO 200
400 ICOUNT=0
410 CUR=20.
420 IS=CUR*CMPLX(COS(PHII*PI/180.),SIN(PHII*PI/180.))
430C
440 40 TEMP=TEMP
450 ICOUNT=ICOUNT+1
460 RS=RS25*(1.+0.0384*TEMP)
462 PSTRAY=0.014*(1.+KRPM/8.)*CABS(IS)**2
465 RRS=RS+PSTRAY/(3.*CABS(IS)**2)
470 VS=E+SMG*IS*CMPLX(RRS,XS)
480C
490 PTERM=3.*REAL(VS*CONJG(IS))
492 PTERM=1.10*PTERM
500 PI2R=3.*RS*CABS(IS)**2
510C PROT=15.*KRPM**2
512 PROT=411.38-105.37*KRPM+21.882*KRPM**2
520
530 PLOSS=PI2R+PROT+PSTRAY
540 PSHAFT=PTERM-SMG*PLOSS
550 TEMP=(PLOSS/WPDCA)+(PI2R+.45*PROT+.3*PSTRAY)/WPDGS
552C
560 IF(TEMP.GT.1E3)GO TO 50
570 IF(ABS(TEMP-TEMP1).LT.0.5)GO TO 50
580 GO TO 40
590C
600 50 PERR=(PSHAF1-PSHAFT)/PSHAF1
610 IF(ABS(PERR).LT.0.005)GO TO 100
620 IF(ICOUNT.GT.300)WRITE(IOUT,55)
630 55 FORMAT(" *** TOO MANY ITERATIONS ***")
640 IF(ICOUNT.GT.300)GO TO 30
650 IS=IS*(1.+0.5*AMOD(PERR,2))
660 GO TO 40
670C
680 100 PHIV=ATAN2(AIMAG(VS),REAL(VS))*180./PI
690 PF=100.*COS((PHII-PHIV)*PI/180.)
700C
710 IF(ABS(SMG-1.).LT.0.01)EFF=100.*PSHAFT/PTERM
720 IF(ABS(SMG+1.).LT.0.01)EFF=100.*PTERM/PSHAFT
730C
740 WRITE(IOUT,155)PTERM/1000.,EFF,PF,TEMP,CABS(E),CABS(VS),
750& CABS(IS),PHII,(PHII-PHIV)
760 155 FORMAT(F9.2,F8.1)
770C
780 GO TO 30
790C
800 200 WRITE(6,205)
810 205 FORMAT(" TYPE '1' TO STOP")
820 READ(5,5)ISTOP
830 IF(ISTOP.NE.1)GO TO 10
840 CALL DETACH(02,IS,)
850 STOP
860 END

```

Figure 9-2. Computer Program – Phase I(B) Motor/Generator

power at the terminals is greater than the simple vector product of volts and amperes.

The sine-wave motoring program has been modified to handle the increase in torque due to the square wave of current reacting with the flux. A good empirical fit with motoring test data resulted when input power, which is based on sine waves, is increased 10%. Calculated motoring performance and test results are compared in Table 9-2.

Performance in the generating mode was computed with the same program. Computed and tested characteristics are shown in Table 9-3 for generating into an (almost) unity power-factor load. However, two changes were made in the program: first, the 10% increase in terminal power had to be removed because the voltage and current waves were nearly sinusoidal; secondly, the phase inductance was cut almost in half. This latter change is an empirical necessity which should be investigated. Calculated results in Table 9-3 are so near the test results that they are worthy of special note.

Performance requirements were assumed to be identical to those of the Phase I(A) motor. However, at the request of NASA, the performance requirements were reexamined in terms of a new "Diesel Equivalent" specification. As part of this reexamination, the effects of motor inertia and drive system efficiency were recalculated. While the mass of the vehicle is the principal inertia in the system, the rotational inertia of the motor and wheels must be taken into account (the gears may be neglected). The effect of these additional inertias have no effect other than to increase the effective mass of the vehicle, as shown in Figure 9-3. The net effect is to require some additional power during acceleration to achieve the specified performance. In this study the added rotational inertia was assumed to be 10% initially but revised to 20% for Phase I(B). Similarly the 80% figure for mechanical system efficiency was judged to be overly pessimistic and hence changed to the more realistic value of 95%. These reevaluations resulted only in changes to the extra-contractual assumptions, as shown in Table 9-4. The net result for the original specification and the "Diesel Equivalent" is shown in Figure 9-4. Testing was done only in terms of the original performance specification.

9.2 TEMPERATURE PREDICTION

The thermal design for the Phase I(B) motor was an extension of the Phase I(A) motor design. Although a great number of enhancements were made in the thermal circuit, only two significant nodal points existed, as shown by the temperature recorder: first, all windings were at a uniform temperature; secondly, the frame, core, and spacer were at another uniform temperature.

The thermal circuit in Figure 9-5 was calibrated from test results, assuming losses are divided as shown. The program calculates steady-state conditions or heat runs which are marked with asterisks in Tables 9-2 and 9-3. Calculated and tested temperature rises are in very good agreement.

9.3 MAGNET SIZE

Test experience with low coercive magnets in Phase I(A) indicated a need for rare earth magnets to withstand the demagnetization effects of inverter shoot-throughs. Dimensions of the magnet face for the Phase I(B) motor were influenced by (1) the ID of the available frame, (2) spoke (or spacer) width between magnets required for sufficient rotor strength, and (3) the configuration of available magnet materials. The

thickness of the magnet was influenced by the nonmagnetic gaps which were sized for the copper conductors and a small clearance gap to minimize windage losses.

Surface area for the Phase I(A) and I(B) magnets are 27.0 cm^2 and 26.5 cm^2 , respectively. The latter magnets are shorter top to bottom, but they are a little wider. The extra width is tolerable because stator coil sides lie in a narrow radial band at a full pole pitch.

Table 9-2
MOTING PERFORMANCE ON LOAD-COMMUTATED INVERTER
Calculated and Tested (in Parentheses)

FOR THESE CONDITIONS				KW AT MOTOR		%	RMS VOLTS (1)		RMS AMPS (2)		WINDING (3)	
RPM	SHAFT HP	P.F.	ANGLE	TERMINALS	TERMINALS		EFFICIENCY	TERMINAL (ℓ-n)	TERMINAL (ℓ)	TERMINAL (ℓ)	TEMPERATURE RISE °C	TEMPERATURE RISE °C
4000 (4000)	4.83 (4.83)	22.6 (22)		4.00 (3.91)		89.6 (92.0)	39.1 (39.6)	33.6 (37.1)			12.5 (13.6*)	
4000 (4000)	14.06 (14.06)	25.8 (25)		11.49 (11.42)		91.1 (91.1)	38.9 (40.0)	99.4 (107.9)			34.3 (36.1*)	
4000 (4000)	21.65 (21.65)	30.4 (30)		18.58 (18.78)		86.6 (86.0)	37.9 (39.4)	172.3 (192.0)			54 (54)	
3999 (3999)	23.13 (23.13)	29.4 (29)		20.02 (19.86)		85.8 (86.9)	38.0 (40.3)	183.5 (194.5)			66 (66)	
5511 (5511)	10.24 (10.24)	27.4 (27)		8.30 (8.21)		91.6 (93.0)	53.3 (54.1)	53.2 (58.6)			26 (26)	
5532 (5532)	25.27 (25.27)	32.1 (32)		20.88 (20.78)		90.0 (90.7)	51.6 (52.3)	144.7 (152.3)			56 (56)	
5505 (5505)	25.65 (25.65)	27.5 (27)		20.98 (20.99)		91.0 (91.2)	52.2 (54.4)	137.4 (154.0)			49 (49)	
6992 (6992)	25.53 (25.53)	43.3 (43)		21.25 (21.21)		89.2 (89.8)	62.7 (63.5)	141.1 (158.6)			56 (56)	
6990 (6990)	30.15 (30.15)	43.3 (43)		25.54 (25.58)		87.7 (87.9)	61.3 (63.4)	173.4 (192.8)			64.4 (64.4)	
9003 (9003)	5.01 (5.01)	56.4 (56)		5.05 (4.79)		73.9 (78.0)	85.6 (85.4)	32.3 (34.9)			38.7 (35.5*)	
8996 (8996)	10.58 (10.58)	56.0 (56)		9.40 (9.32)		8.37 (84.6)	83.6 (82.8)	60.9 (67.4)			46.1 (45*)	
8995 (8995)	14.77 (14.77)	56.7 (56)		12.81 (12.70)		85.6 (86.8)	81.7 (81.1)	86.5 (92.9)			57.1 (57*)	
8926 (8926)	25.81 (25.81)	55.9 (54)		22.49 (22.64)		85.2 (86.0)	75.8 (78.5)	160.2 (170.3)			62 (62)	
9002 (9002)	26.47 (26.47)	56.5 (56)		23.29 (22.96)		84.6 (86.0)	75.7 (79.3)	169.1 (174.4)			62 (62)	
10977 (10977)	15.63 (15.63)	62.9 (63)		14.31 (14.35)		8.21 (81.3)	97.7 (98.3)	97.3 (105.4)			56 (56)	
10997 (10997)	15.65 (15.65)	62.9 (63)		14.31 (14.28)		81.3 (81.8)	97.9 (99.1)	97.3 (104.7)			40 (40)	

NOTES: (1) Calculated values are based on sine waves. See pictures of waveshapes.

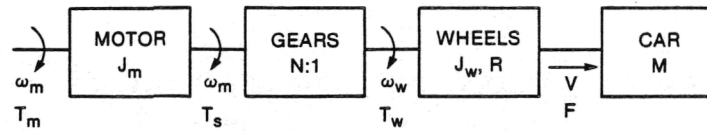
(2) RMS tested current quasi-square wave approximately 120° conduction. RMS fundamental component is 0.953 x Tested RMS value.

(3) Steady State conditions denoted by *'s - all others are transient temperatures.

Table 9-3
GENERATING PERFORMANCE WITH RESISTANCE LOAD
Calculated and Tested (in Parentheses)

FOR THESE CONDITIONS				KW AT MOTOR		% EFFICIENCY	RMS VOLTS (ℓ-n)		RMS AMPS TERMINALS	WINDINGS	
RPM	SHAFT HP	P.F.	ANGLE	TERMINALS	TERMINALS		TERMINALS	TEMPERATURE RISE °C			
3998 (3998)	14.41 (14.41)	-10.3	(-10)	9.81 (10.05)	36.6 (36.9)	91.6 (93.5)	90.8 (91.0)	26.8 (25.5*)			
4033 (4033)	23.53 (23.53)	-10.9	(-11)	15.53 (15.92)	35.2 (35.6)	88.9 (90.7)	150.0 (150.3)	45 (45)			
5443 (5443)	26.69 (26.69)	-14.0	(-14)	18.20 (18.44)	49.2 (49.2)	91.8 (92.6)	127.1 (126.8)	31 (31)			
7005 (7005)	24.83 (24.83)	-13.8	(-14)	17.10 (17.29)	65.3 (65.5)	92.7 (93.3)	89.9 (89.3)	34 (34)			
7091 (7091)	43.70 (43.70)	-14.0	(-14)	29.79 (29.87)	63.6 (63.5)	91.6 (91.6)	160.9 (159.7)	39.4 (39.4)			
9000 (9000)	9.60 (9.60)	-22.0	(-22)	5.85 (6.16)	86.7 (86.4)	82.0 (85.9)	24.2 (24.2)	33.1 (34.4*)			
9005 (9005)	10.31 (10.31)	-19.9	(-20)	6.37 (6.16)	86.8 (87.7)	83.2 (83.0)	26.0 (24.8)	10 (10)			
9000 (9000)	27.86 (27.86)	-15.0	(-15)	19.01 (19.36)	84.8 (84.8)	91.8 (93.1)	77.4 (77.0)	34 (34)			
11005 (11005)	15.33 (15.33)	-21.8	(-22)	9.41 (9.72)	105.8 (105.3)	82.6 (85.0)	31.9 (33.1)	40 (40)			

* Denotes Heat Run



$$\begin{aligned} \bullet \quad T_m &= \left[J_m + \frac{MR^2 + J_w}{N^2} \right] \dot{\omega}_m \\ &= \left[\left(J_m + \frac{J_w}{N^2} \right) + \frac{MR^2}{N^2} \right] \frac{N}{R} \dot{V} \end{aligned}$$

- $J_m = 0.0168 \text{ kg-m-s}^2 \text{ (1.46 lb-in-sec}^2\text{), PHASE IA}$
 $0.0136 \text{ kg-m-s}^2 \text{ (1.18 lb-in-sec}^2\text{), PHASE IB}$

MAY BE HALVED IN ENGINEERING MODEL

- $\frac{MR^2}{N^2} = 0.0631 \text{ kg-m-s}^2 \text{ (5.48 lb-in-sec}^2\text{)}$
- $\text{ETV-1 } J_m = 0.0092 \text{ kg-m-s}^2 \text{ (0.798 lb-in-sec}^2\text{)}$
 $\text{HYBRID } J_\theta = 0.0939 \text{ kg-m-s}^2 \text{ (3.813 lb-in-sec}^2\text{)}$
[including ICE inertia]

Figure 9-3. Effect of Motor Inertia

Table 9-4
REQUIRED PERFORMANCE
EXTRA-CONTRACTUAL ASSUMPTIONS

- Mechanical Drivetrain Efficiency = 80%
- Rotational Equivalent Inertia = 10%
- 66 mph Ultimate Overspeed
- No Gear Shift

Revised Assumptions

- Mechanical Drivetrain Efficiency = 95%
- Rotational Equivalent Inertia = 20%

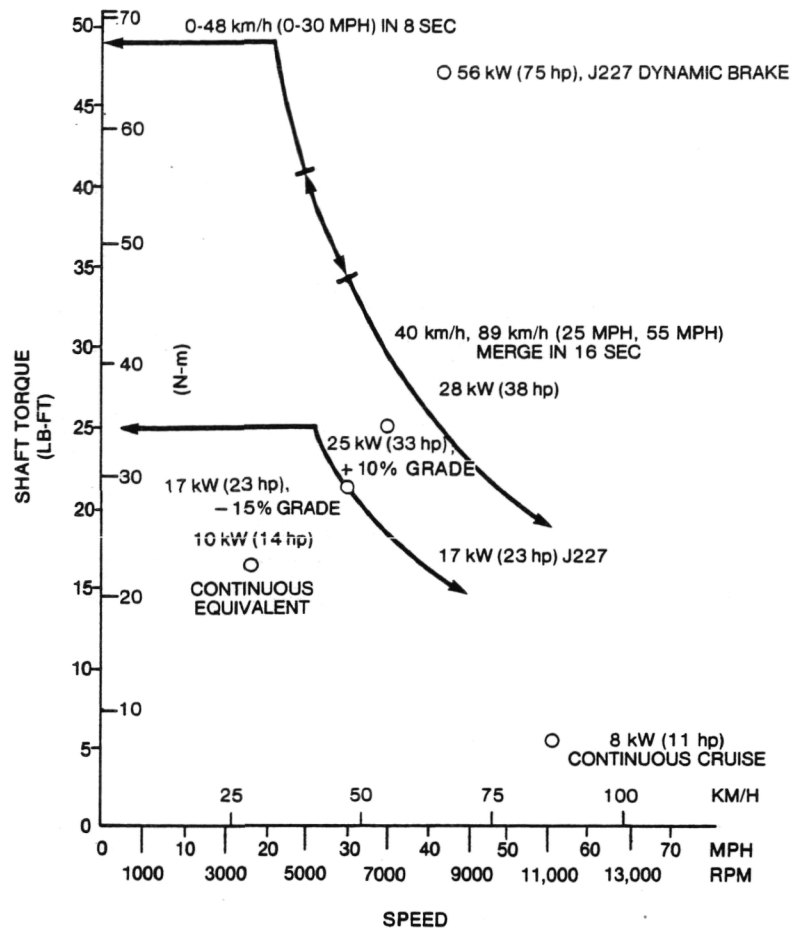


Figure 9-4. Revised Performance Requirements

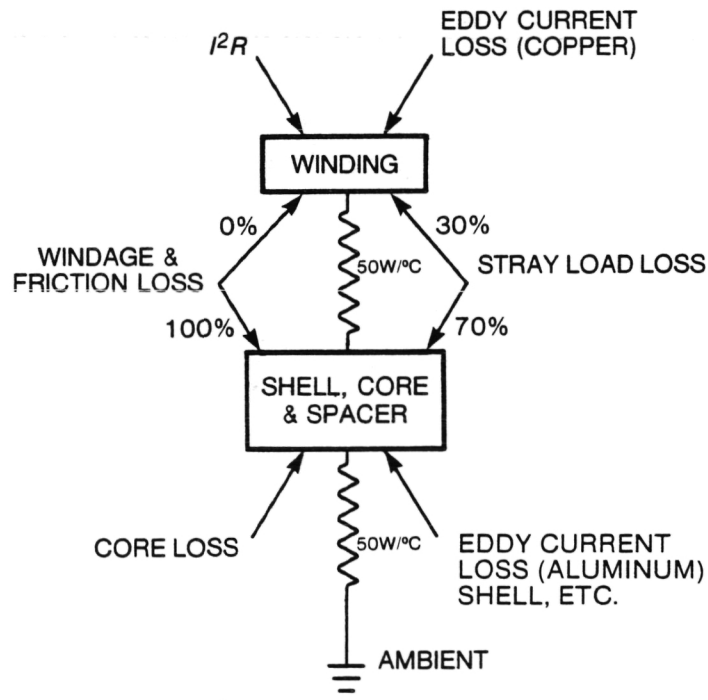


Figure 9-5. Simplified Thermal Circuit Phase I(B) Motor

9.4 WINDING CONCEPT

A surface wound machine is the perfect marriage with a load-commutated inverter (LCI). The large nonmagnetic gap results in very low reactance — a necessary condition for the LCI to function. Also, a large gap minimizes armature reaction effects. It seems, also that an open face machine could be more easily wound on automatic machines.

The major disadvantage of surface wound machines is the large amount of excitation energy required for the gap. This means more magnet material is required in PM machines. Another disadvantage is that the exposed copper is subject to eddy losses which are induced by the main field. The result is more drag and heat and lower efficiency at high speeds.

The winding that appeared most appropriate for the axial gap disc motor in Phase I(B) was the concentrated (100% pitch) half coiled (4 coils for 8 poles) in a chain or series configuration. The coils nest perfectly where alternate coils in a phase have their coil ends bent down away from the gap.

Phases were wound as a unit with no joints or connections terminal-to-terminal. Stranded cables were transposed between the second and third coils to balance resistance, reactance, and flux linkages.

10.0 STATOR FABRICATION

10.1 WINDING

An outstanding feature of the stator coils is their few turns. Two effects favored few turns: first, the frequency is high because the field has many poles and operates at a high speed; secondly, the maximum source voltage is only 55 volts ac. Because the coils are concentrated at 100% pitch, the winding can be shaded 1/2 turn per pole by half-coiling.

The best compromise is a three-turn coil (1.5 turns per pole) with two cables in hand of 19 strands of #22 copper wire with heavy film insulation. This stranding exceeded the requirements for skin effect due to phase current. However, eddy current drag resulting from the main pole of flux is still very significant at high speeds. More copper and finer stranding appear desirable for future machines.

A slot section layout is shown in Figure 10-1. No effort was made to tightly pack the slots, as is usually done, since the extra copper could not be accommodated in the end regions. This should be considered in future designs.

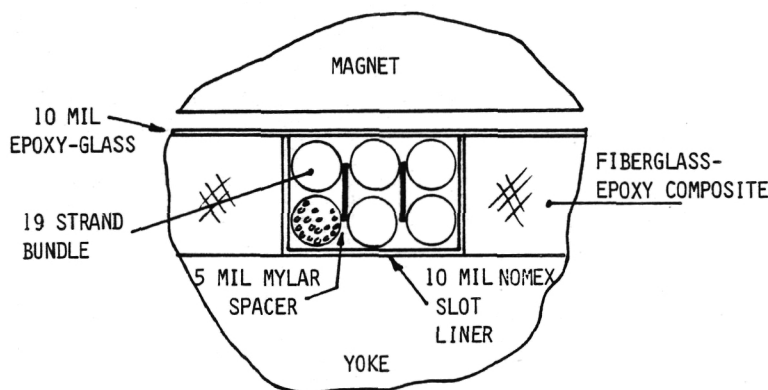


Figure 10-1. Slot Layout - 2 Cables, 3 Turns

10.2 HEAT REMOVAL DEVICES

All heat must exit the motor via the frame or fins. While a few losses occur in the frame due to stray fields, most of the losses occur deep in the machine and must be conducted to the frame.

The usual heat conduction path is from the winding to the iron. However, in this machine, the winding touches the iron on only one of its sides: the bottom. This was deemed inadequate, so auxiliary parallel paths of high thermal conductivity were invented and built into the stator to conduct heat away from the winding to the shell.

Copper and aluminum are good thermal conductors; they are also good electrical conductors. Hence, they should be stranded to minimize eddy losses resulting from the field around the coil conductors as well as the stray fields from the main poles of flux.

Half of the stator coils have end turns bent downward toward the carrier plate heat sink. Hence, short blocks of thermal conducting material with a large surface area were used to conduct heat from the bent-end turns to the carrier plate. Aluminum

strands embedded in epoxy are best here. Its electrical resistance is high enough to keep eddy losses low, and its thermal conductivity is high enough to hold the calculated thermal drop to only a few degrees Celsius.

Nested between the bent coils are an equal number of unbent coils. The heat flow path from their end turns to carrier plate is much farther than for the bent coils, so copper stranding is used to minimize cross section of the bundle and to enhance heat flow. A large interface surface is needed between copper strands and end turns to pick up the heat. This is achieved by fanning out the bundle of copper strands — half in each direction — along the sides of the coil end turns. The heat conducting devices are shown in the schematic (Figure 10-2) and in Figures 10-3 and 10-4.

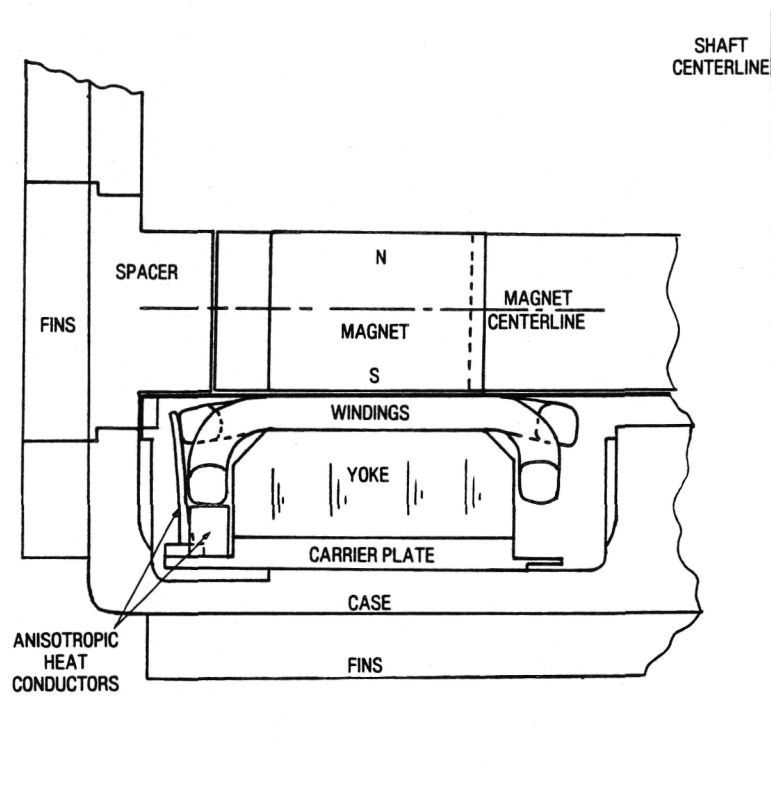


Figure 10-2. Electromagnetic Components

10.3 FRAME, CARRIER PLATE, YOKE, AND WEDGES

In an axial gap machine, the end bell becomes the stator frame and, as such, it supports the active material of the stator. Assembling and winding the stator within the confines of the frame is difficult. So, the active material was fabricated into a subassembly on the carrier plate and then mounted in the frame as shown schematically in Figure 10-2 and in finished form in Figures 10-3 and 10-4. Assembly drawings, with major dimensions, pertaining to both Phase 1(A) and 1(B) are contained in Appendix D. The assembly drawings show the internal configuration of Phase 1(A). Modifications for Phase 1(B) are shown in Figure 10-2.

The stator yoke or back iron is a tape-wound core of fully impregnated 12 mil silicon steel. A skim cut was made on the top and bottom faces, and the edges were beveled so the flux would enter the steel edgewise. Tool smear was removed with a

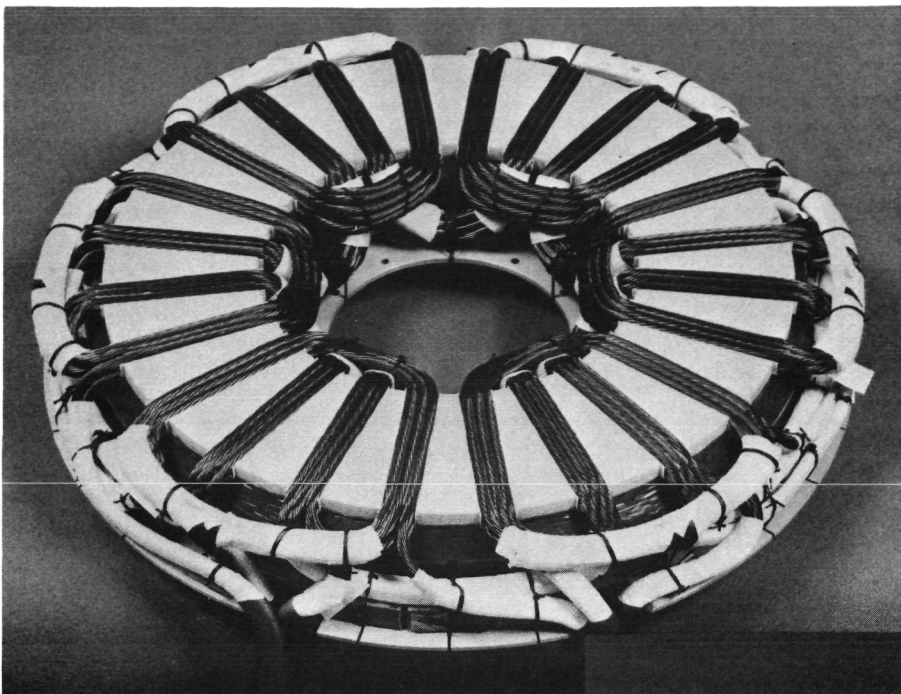


Figure 10-3. Stator Assembly Before Impregnation

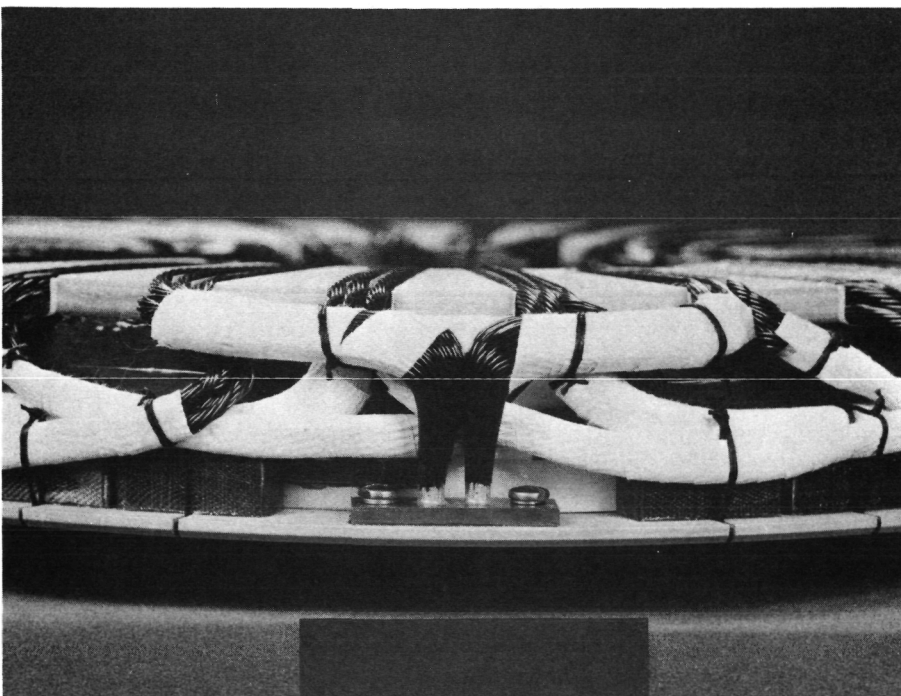


Figure 10-4. Detail of Stator Assembly End Region

5% solution of nitric acid etch which also improved all surfaces in preparation for bonding. The iron core was bonded to an aluminum disc or carrier plate which became the heat sink for the subassembly.

Accurate mechanical (and electrical) spacing of the coil sides enabled the LCI and motor to operate at a lower and more optimum power-factor angle than the Phase IA motor. Spacers or wedges of NEMA grade G-10 epoxy-glass were milled from a disc, but before parting the wedges on their IDs and ODs, they were all bonded as a single unit to the iron. Then the superfluous material was milled away, leaving only the wedges positioned as accurately as they were milled. These wedges served two important functions: first, they accurately positioned the coil sides; secondly, they supported much of the side thrust of the conductors, which is very large in a surface-wound machine.

10.4 CONNECTIONS AND LEADS

The phase winding was made without joints from terminal to terminal. Each of the two cables "in hand" had individual terminals to share the phase current and to reduce the connection resistance. The absence of internal joints eliminated the possibility of sneak paths for circulating current. The internal wiring diagram is shown in Figure 10-5, and the external connection diagram is shown in Figure 10-6.

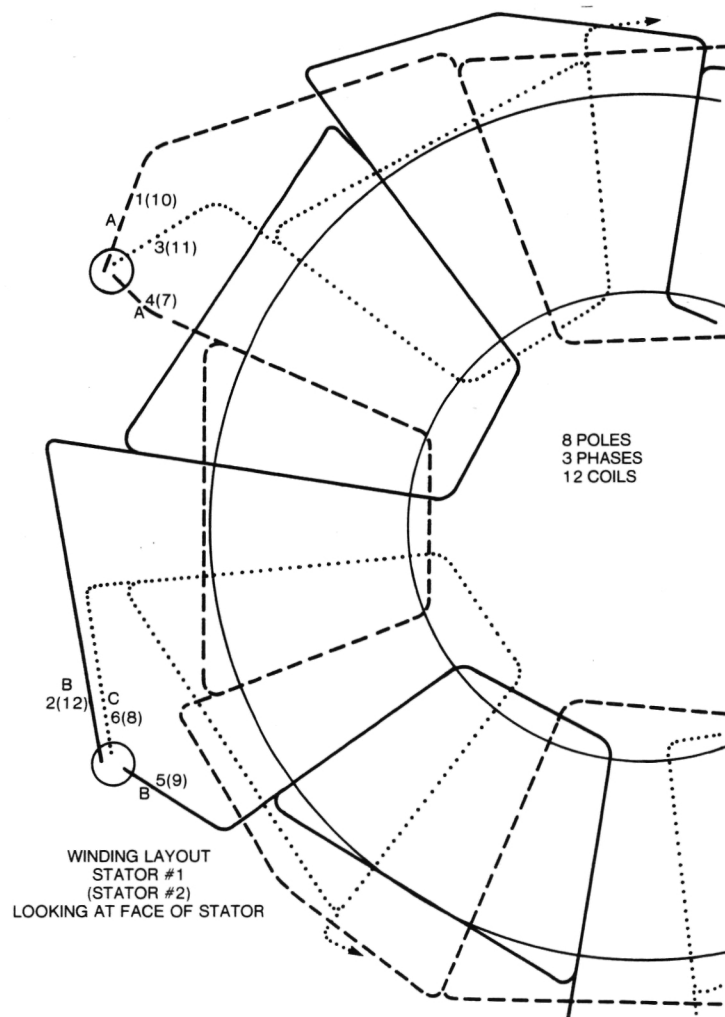


Figure 10-5. Internal Wiring Diagram

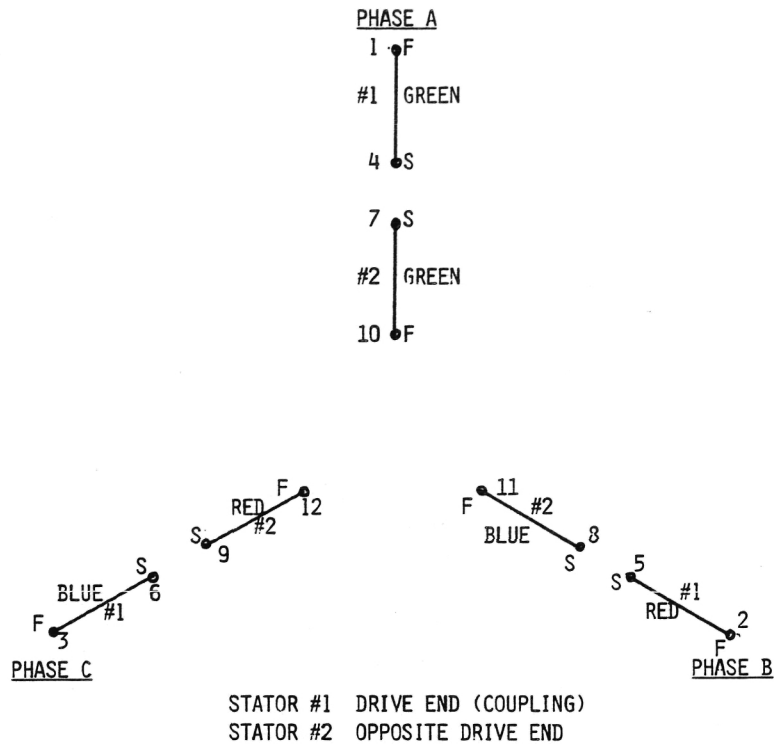


Figure 10-6. External Connection Diagram

The #22 size strands of the cables made the leads flexible. They were wrapped with half-lapped tapes of NomexTM in opposite directions. Mechanical protection of the Nomex surface was provided by a half-lapped layer of plastic tape. This made a very flexible lead with good electrical insulation and mechanical protection. Details of lead construction are shown in Figures 10-7 and 10-8.

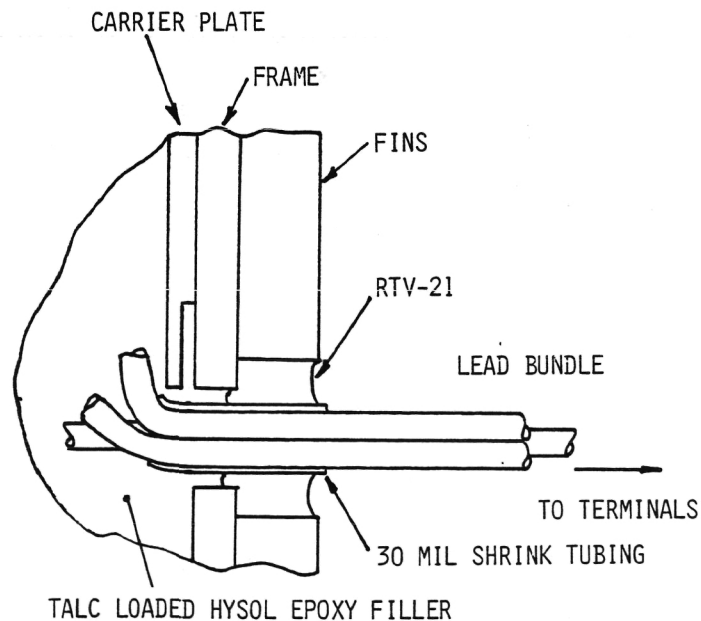


Figure 10-7. Lead Entry Area (Materials Data in Tables 10-1, 10-2 and 10-3)

TM Trademark of E.I duPont de Nemours and Co., Inc.

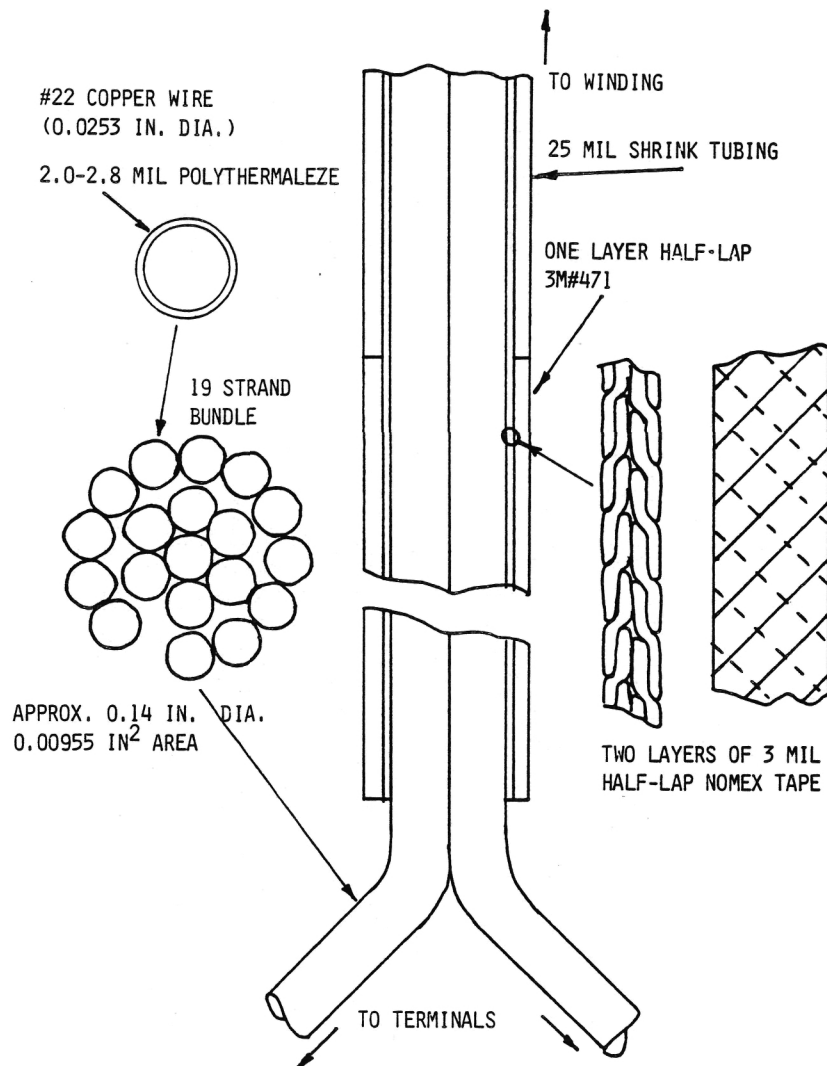


Figure 10-8. Lead Construction (Materials Data in Tables 10-1, 10-2 and 10-3)

10.5 INSULATION AND POTTING

The hottest part of a motor is its winding. Therefore, a very durable high-temperature film insulation is the first requirement. Next, the insulation materials in contact with the conductor must withstand the high temperature of the winding. Nomex was used for this insulation throughout the motor. Details of the insulation materials are given in Tables 10-1 and 10-2.

A very careful control of the potting or vacuum pressure impregnation process was necessary to ensure entry of epoxy into the smallest spaces. Elevated temperatures lowered viscosity for deep penetration, and prior deairing eliminated bubbles. Only high-temperature epoxies were used. Fillers enhanced heat transfer and minimized shrinkage during cure. Details of the potting material are given in Table 10-3.

Table 10-1
INSULATING MATERIALS – PRIMARY

- Poly-Thermaleze 2000 (armored)
 - Phelps-Dodge
 - 3800 Volts/mil (typical) at 100°C
 - 200°C Continuous
 - Strand Insulation 0.005 to 0.007 cm (2.0 to 2.8 mils)
 - Nomex
 - DuPont
 - 220°C Continuous (mil 1-24204)
- 0.008 cm (3 mil); 1.3 cm (1/2-Inch) Tape
- 500 Volts/mil (rapid rise)
 - Turn Insulation – Half Lapped
 - Single Layer in End Windings
 - Double Layer in Leads
- 0.025 cm (10 mil) Sheet
- 750 Volts/mil
 - Slot Liners

Table 10-2
INSULATING MATERIALS – SUPPORT

- Alphlex Fit Shrinkable Tubing (black)
 - Alpha Wire
 - 1300 Volts/mil
 - 135°C Continuous
 - Lead Entry 0.064 cm (25 mils)/Lead
 - Lead Entry 0.076 cm (30 mils)/Bundle
- 3M No. 471 Plastic Tape (white)
 - 3M
 - 800 Volts/mil
 - 105°C
 - Mechanical Protection of Leads
- RTV-21 (pink)
 - GE
 - ~400 Volts/mil
 - ~230°C for 4300 hr
 - Mechanical Support of Leads

Table 10-3
INSULATING MATERIALS – EPOXIES

- Stycast 2850 Ft (black)
 - Emerson and Cummings
 - 550 Volts/mil Minimum Dielectric Strength
 - 205°C Service Temperature
 - Winding Impregnant
- Deltacast 153C (blue)
 - Wakefield
 - 500 Volts/mil Minimum Dielectric Strength
 - 175°C Service Temperature Continuous
 - 250°C Intermittent
 - Bonding Surfaces, Surface Insulation
- Hysol HD-3537 Hardener; R9-2039 Resin (grey)
 - Dexter
 - ~650 Volts/mil Dielectric Strength
 - ~200°C Service Temperature
 - Stator Filler (talc loaded – mostly $\text{SiO}_2\text{--MgO}$)

11.0 ROTOR DESIGN AND FABRICATION

11.1 ROTOR CONCEPT

The Phase IB rotor (Figure 11-1) differed from the Phase IA rotor as follows:

	<u>IB</u>	<u>IA</u>
Magnets	Sm-Co	Alnico 8
Hub spoke width	2.29 cm (0.90 in.)	2.54 cm (1.00 in.)
Rotor thickness	3.89 cm (1.53 in.)	5.05 cm (1.99 in.)
Inertia	0.0136 kg-m ² -s ² (1.18 lb in.-sec ²)	0.0165 kg-m-s ² (1.43 lb in.-sec ²)

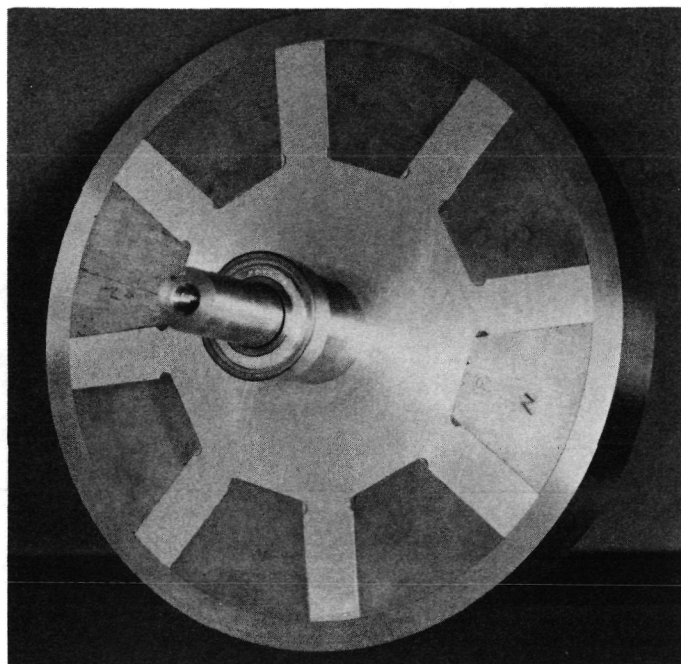


Figure 11-1. Finished Rotor

At the design speed of 13.2 krpm, the normalized centrifugal force of the Phase IB magnets and outer-half of spokes is 11.5% larger than in Phase IA, primarily due to greater magnet density. With the same thickness of the Inconel 718 retaining ring, the nominal diametral interference fit is increased for Phase IB from 0.084 to 0.094 cm (0.033 to 0.037 in.) to provide the required preload.

The assembly concept was basically the same as Phase IA except that, for shrink-fitting the rim to the hub/magnet subassembly, the latter was cooled to -40°C instead of remaining at ambient temperature. This was done to minimize the amount of thermally induced demagnetization. A drawing of the rotor assembly with dimensions pertaining to both Phase IA and IB is contained in Appendix D.

11.2 ROTOR STRESSES

The only significant change from Phase IA to Phase IB was the rim tensile stresses. Design tensile stress at 13.2 krpm increased approximately 10% from 689 MPa (100 ksi) to 758 MPa (110 ksi) (see Section 11.1).

The zero speed rim stress was calculated, based on a measurement of the rotor OD after assembly. The maximum tensile stress occurs at the rim ID (always) and, for zero speed, is 648 MPa (94 ksi). Then, by interpolation, rim tensile stress at an operating speed of 11 krpm is 724 MPa (105 ksi).

Rotor Stress Summary:

Component	Material	Maximum Stress, mPa (ksi)*	Condition	Minimum Yield, mPa (ksi)†
Shaft	303 SS	193 (28) C	-40°C	241 (35)
Hub	2024-T351	241 (35) T	-40°C	290 (42)
Magnets	Co-Sm	54 (7.8) C	13.2 krpm**	—
Rim	718 Inconel	758 (110) T	13.2 krpm**	1172 (170)

*C—Compression

T—Tension

†0.2% offset, room temperature

**Design rim/hub separation speed

11.3 MAGNET CONCEPT AND ACTIVATION

The eight rare earth magnets shown in Figure 11-2 were made from 5.33 cm × 5.08 cm × 1.27 cm (2.1" × 2" × 0.5") ingots secured through Permag of Hicksville, New York, and manufactured by Hitachi at their Edmore, Michigan, plant. The magnet poles are built up from six segments. The ingots are not large enough for a one-pole laminate. The six-piece design was also developed to increase mechanical stiffness of the pole structure by overlap. The specification drawing for the magnets is contained in Appendix D.

The ingots received from Permag were "as cast" and had a ± 0.076 cm (± 0.030 inch) tolerance. For this reason, much cutting and grinding was necessary to bring the poles into the acceptable size range. Magnet ingots were cut, coarse ground, and magnetically tested. An energy product of 0.12 Joule/cm³ (16 million gauss oersted) was the minimum acceptable for our use as segments for the magnet poles. The segments were then thermally demagnetized at 450°C. The polarity of the magnet segments was noted and stamped on each piece. There was a small magnetic residual (B_R) in each segment, which was acceptable as long as the magnets were remagnetized to the same polarity. The magnet segments were then matched according to magnetic energy product for each pole and then fine ground and assembled. The magnet segments were joined together using Hysol EA934 epoxy applied per manufacturer's instructions with maximum joint gaps of 0.006 cm (0.002 inch).

The magnet dimensions were checked and weighed using laboratory scales accurate to 0.01 gram. The magnets weighed about 868 grams each. The magnets were then weight-matched to within 0.01 gram by polishing the magnet faces. The matched magnet pairs were mounted 180° apart in the rotor as a necessary step in maintaining balance. This procedure was very beneficial, as evidenced by the vibration test data.

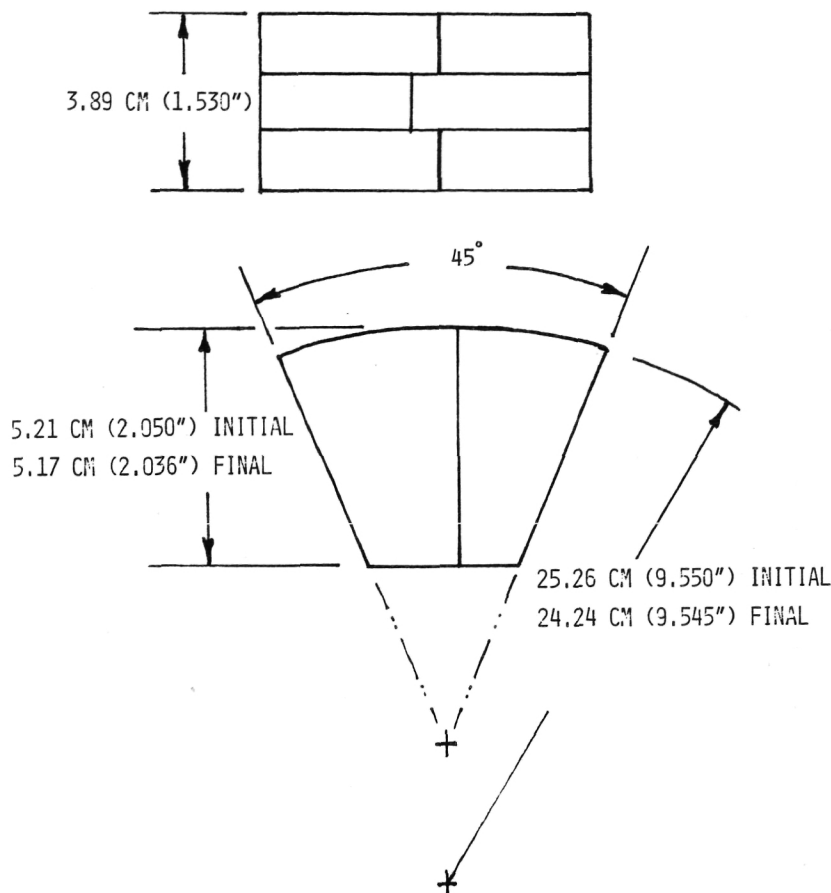


Figure 11-2. Magnet Concept

The magnets were individually magnetized before they were mounted in the motor. The magnetization was accomplished with a 25.4 cm (10 inch) Walker scientific 50/20 magnet and power supply using cobalt iron pole tips 7.94 cm (3.125) inches in diameter with a field of 1512 kA/m (19,000 oersteds). It was found necessary to use special jigs for holding and handling the magnets during this process to prevent damage or chipping (and thus upsetting the balance). A magnet in the jig is shown in Figure 11-3. The results of the selection, fabrication, and magnetization process were excellent, and are summarized in Figure 11-4. These measurements were made by setting the keepers on the rotor to the same magnetic gap as would exist in the motor. The axial flux density was measured at the middle of the magnet face in the center of the gap. The measurement was repeated on both ends of the magnet. The radial (Figure 11-5) and azimuthal (Figure 11-6) flux scans were made in the same apparatus but along the respective centerlines of the magnet.

11.4 ROTOR BALANCING

Rotor balance was achieved by a combination of subassembly dynamic balancing and component static balancing. Experience gained during Phase IA indicated that post-assembly dynamic balancing of the rotor was impractical due to interaction of strong rotating magnetic fields with commercial balancing machines. Rotor balance was obtained to within 3.31 g-cm (0.046 in. oz) [equivalent to 4.54 kg (10 lb) centrifugal force at 11 krpm] as follows:

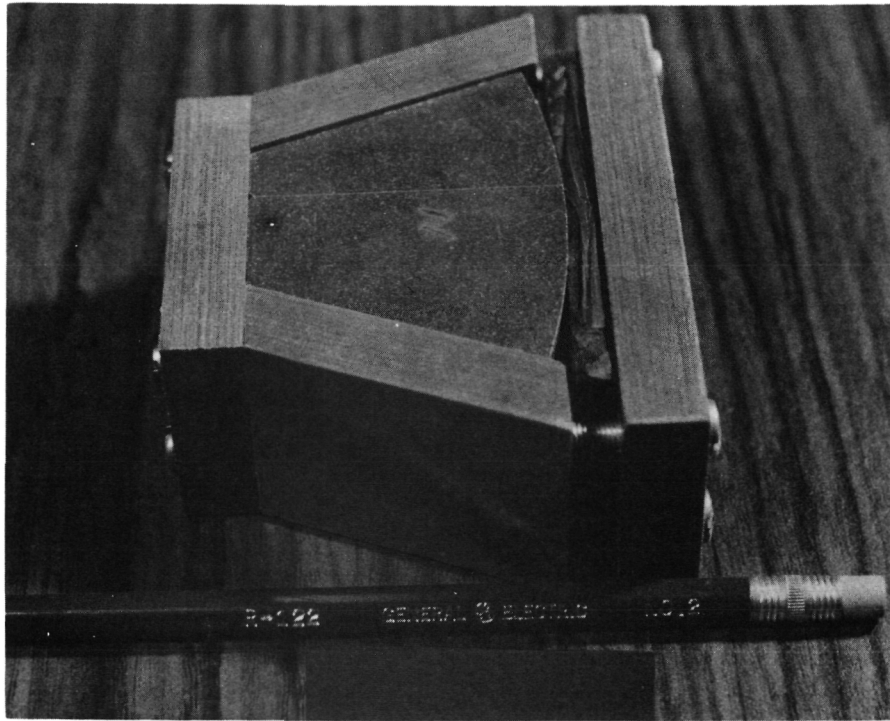


Figure 11-3. Magnetization Handling Fixture

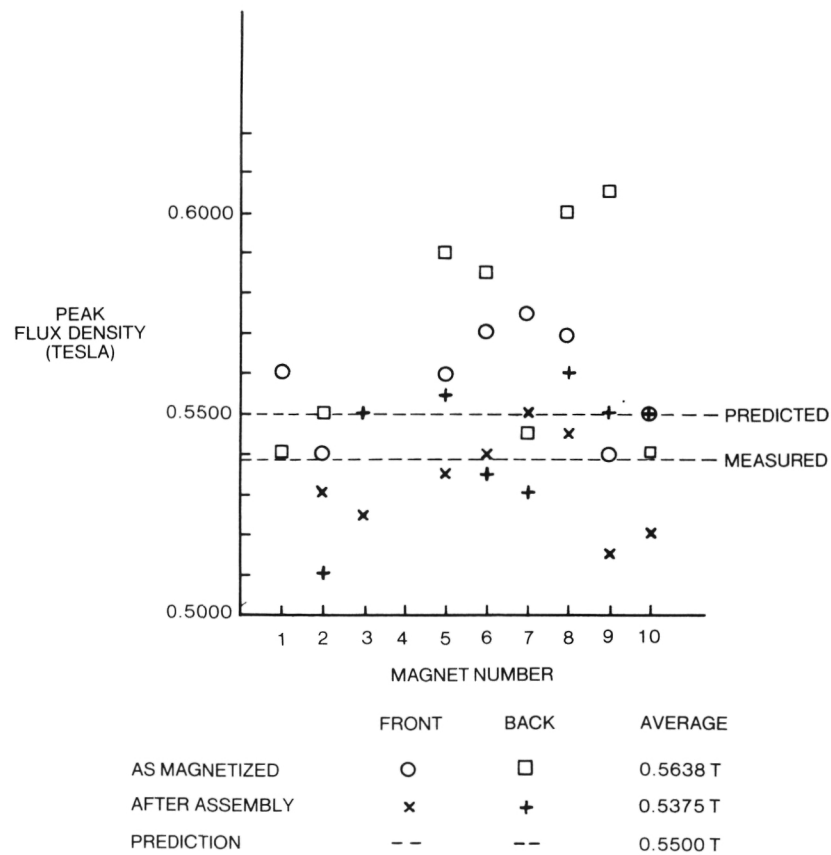


Figure 11-4. Magnet Flux Summary

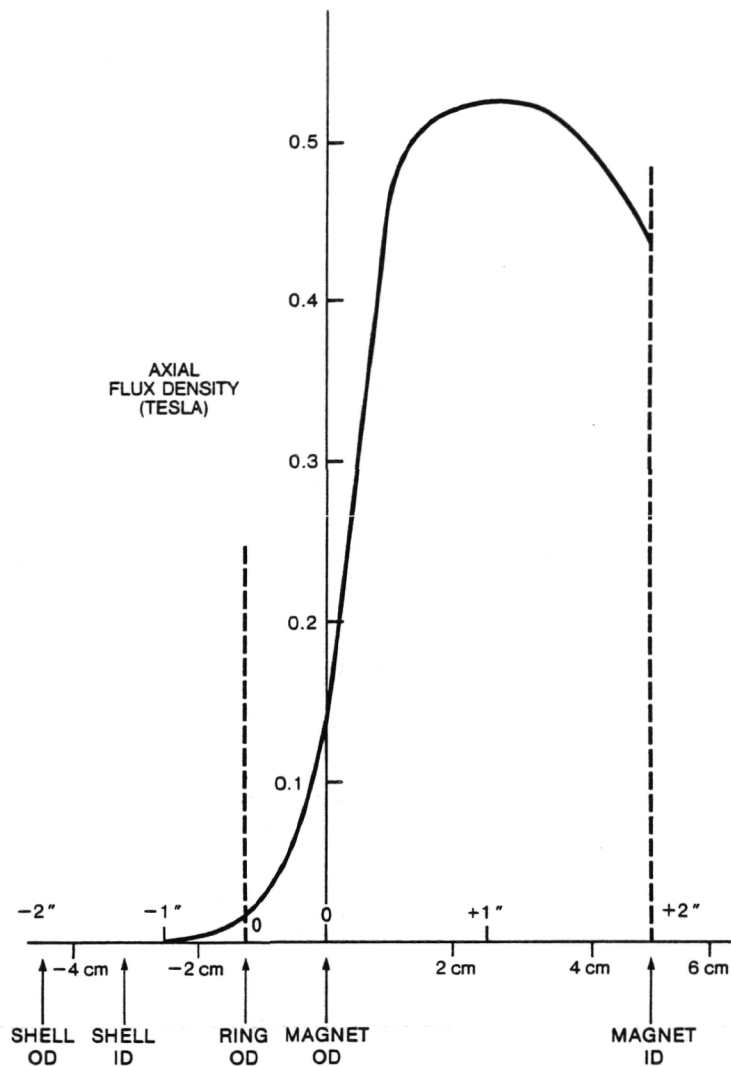


Figure 11-5. Radial Flux Scan

- The hub/shaft subassembly was dynamically balanced on the rotor bearings to 2.3 g-cm (0.002 in. oz.)
- Opposite magnets were matched within 0.01 gram, which is equivalent to 3.5 g-cm (0.003 in. oz) imbalance per pair.
- The static balance of the rim was established within 4.6 g-cm (0.004 in. oz) by close control of machining tolerances.
- After assembly, and before and after motor testing, the rotor static balance was checked on a fixture made of low permeability materials. Balance remained within 53 g-cm (0.046 in. oz.)

Rotor balance was confirmed by vibration measurements made with the motor being driven on the test stand. A summary of these tests is presented in Table 11-1.

In the course of testing, a resonance was observed leading to an investigation of its source, as summarized in Table 11-2.

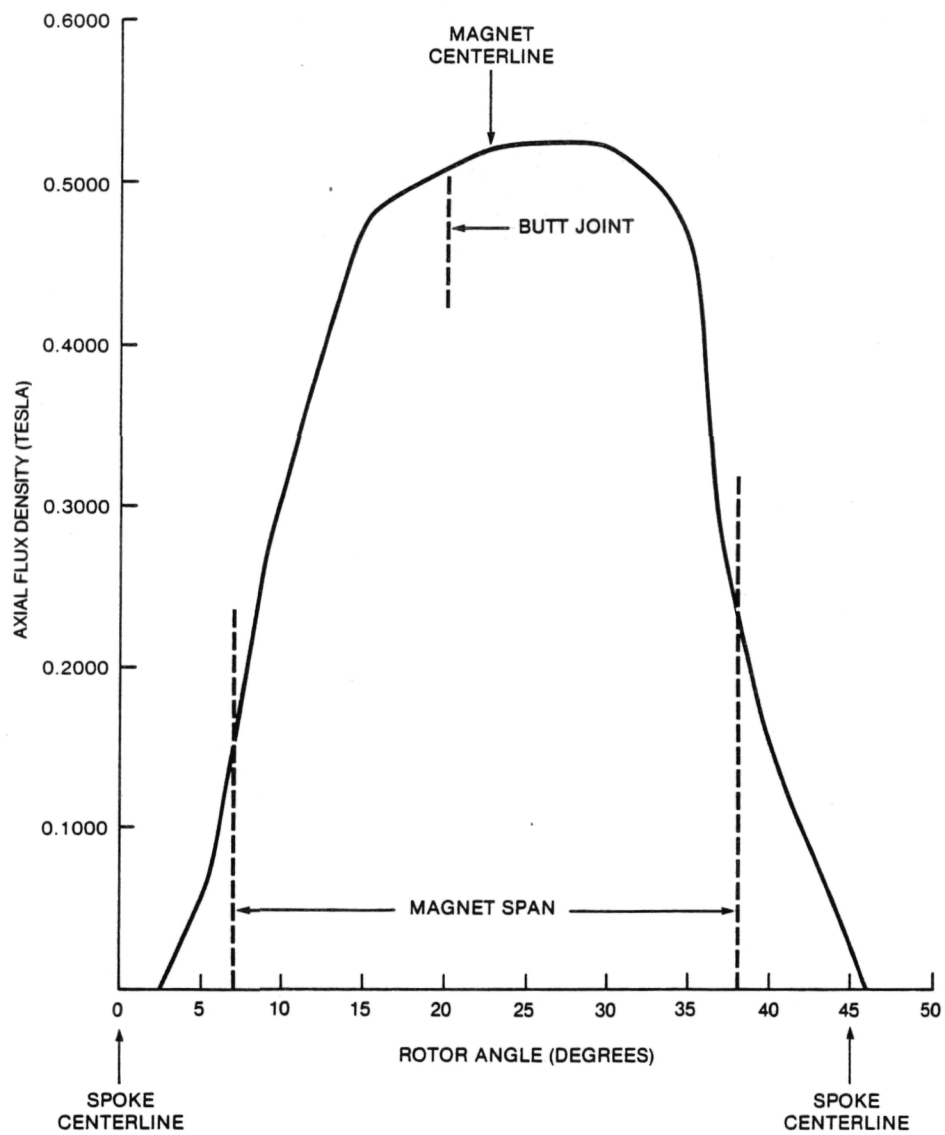


Figure 11-6. Azimuthal Flux Scan

Table 11-1
VIBRATION SUMMARY

Instrumentation

Accelerometers

- 1 B&K Model 4344 on Each Stator Housing in Plane of Rotor Bearing

Readout

- B&K Model 9500 Vibration Analyzer
- Oscilloscope

Results

krpm	Acceleration, G's, P-P
7	0.6
9	1.4
11	1.2

- Calculated Force at 11 krpm = 19 lb
- Calculated Amplitude of center of gravity at 11 krpm = 0.00017 in.

Table 11-2
TEST STAND RESONANCE

- Severe Resonance Observed
Approximately 9.2 to 10 krpm
- Calculated Test Stand Bending, F_N
8.5 to 9.6 krpm
- Calculated Rotor Bending, F_N
53 krpm (treated as simply supported
beam, center load)

12.0 WINDAGE TEST

12.1 DESIGN AND FABRICATION

The windage test utilized a solid aluminum alloy rotor within the proof of principle motor stators installed in an in-house spin test facility. The rotor OD and thickness are the same as the Phase IB motor. By changing shims, the axial rotor-to-housing test clearances were 0.0508, 0.1143, 0.3429, 0.5080 cm (0.020, 0.045, 0.135, and 0.200 inch); radial clearance was fixed at 0.1524 cm (0.06 inch) for all runs.

A slideable shaft provided positive decoupling of the rotor from the facility drive turbine to permit total loss determination (windage and bearing friction) by a coast-down technique. Heating tapes were wrapped around the housing OD to provide loss data nearer motor operating temperatures. Instantaneous angular speed measurements were obtained by a noncontact pickup sensing each passing of the shaft keyway, and output was recorded on a strip chart.

12.2 TEST RESULTS

Two coast-down runs were performed from 13 krpm at clearance gap temperatures of 35 and 65°C for each axial gap setting. Rotor angular speed vs. elapsed time during coast was recorded as shown in Figure 12-1.

The instantaneous power dissipation is given by

$$P = (I \alpha) \omega,$$

where

I = Moment of inertia = 0.0053 kg-m-s² (0.46 lb in.-sec²)

α = Angular acceleration, rad/sec²

ω = Angular speed, rad/sec

P = Power, watts

The angular acceleration at specific values of angular speed was determined by "differentiating" over small increments of the speed vs. time charts.

Coast-down data for 35°C was not reduced because of the close agreement with the 65°C coast curves. Theoretically, the windage loss at 35°C should be 7% to 10% greater than at 65°C. The results for 65°C are summarized in Figure 12-2.

The precision of the results is estimated at $\pm 10\%$ due, in part, to the manual differentiation of the speed-time curve. Since the windage and friction losses in this motor are approximately 1/2% of the output power or 7% of the losses, this level of precision is quite acceptable.

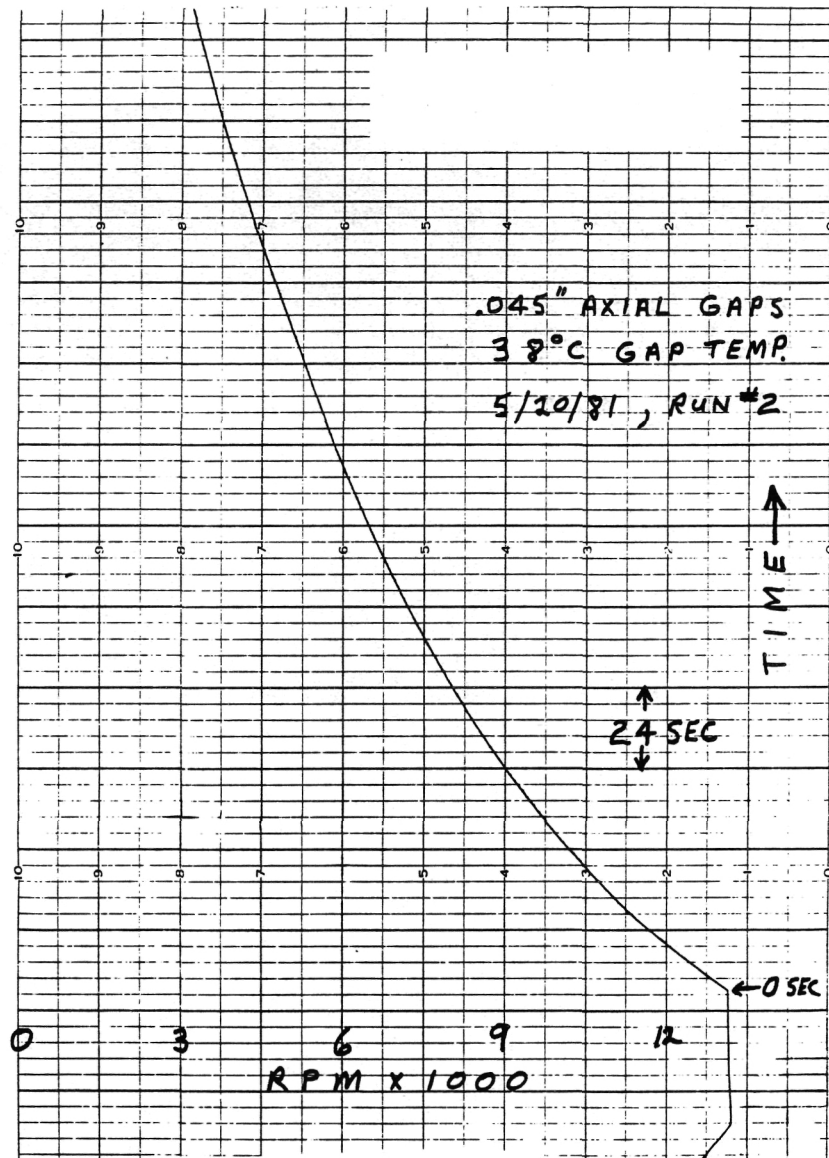


Figure 12-1. Windage Test Sample Run

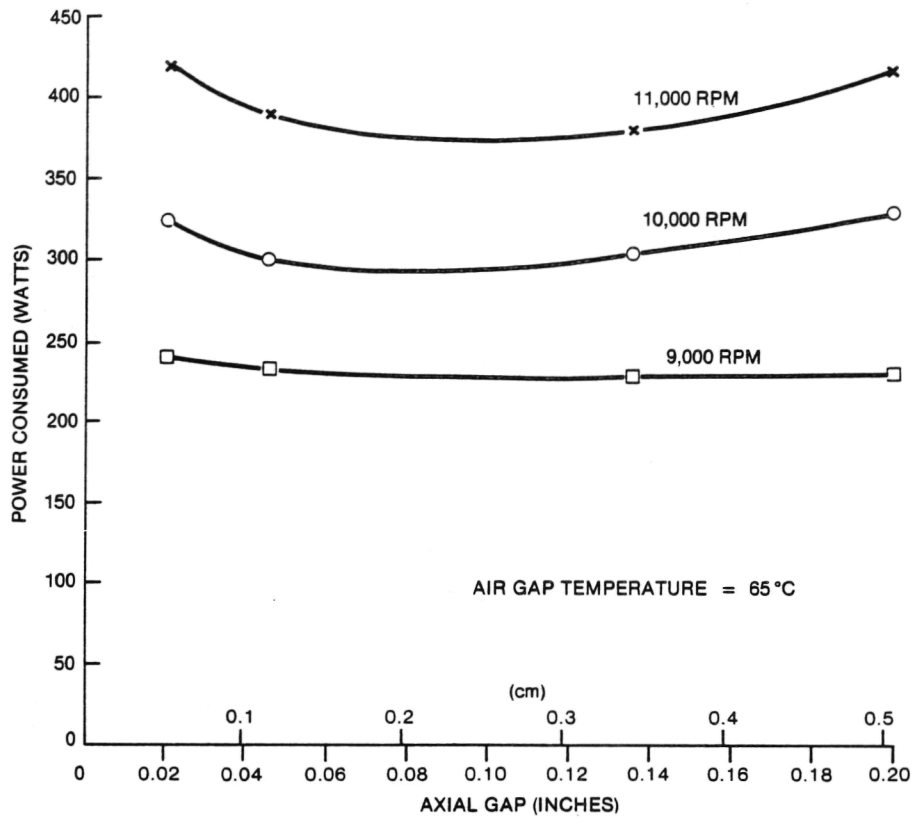


Figure 12-2. Windage and Bearing Losses vs. Axial Clearance Gap for a 26.7 cm (10.5 Inch) Diameter × 3.81 cm (1.5 Inch) Thick Rotor Rotating in a Housing with Grease-Lubricated Bearings (Air Gap Temperature = 65°C)

13.0 PERFORMANCE TEST

13.1 TEST SETUP AND APPARATUS

The basic data acquisition equipment and power supply for this series of tests was the same as used for Phase IA, and is described in Section 6 of the Phase I(A) report.

Figure 12-1 shows the motor installed in the safety frame/cooling shroud before mounting on the test stand. The completely assembled test stand is shown in Figure 12-2. The motor is completely enclosed, but the shaft extension and some fins may be seen in the center. The terminal block is mounted on top of the frame. Safety plates and cables may also be seen. The DPO scope cart is on the right. The vibration measuring equipment is on the left.

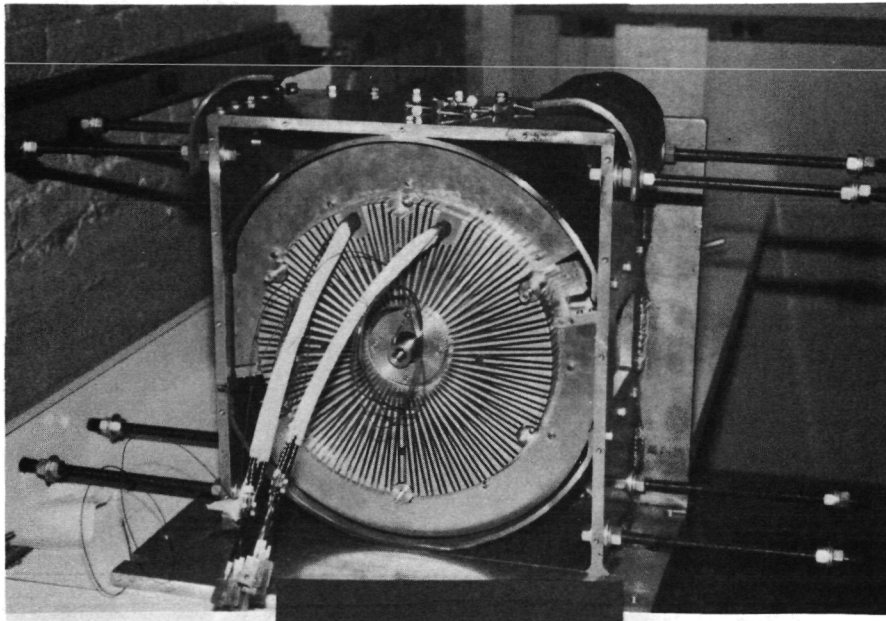


Figure 13-1. Completed Motor in the Mounting/Safety/Ventilation Enclosure

13.2 ACCURACY AND PRECISION

Current transformers were substituted for the F.W. Bell current probe, which the manufacturer guarantees only to 2% at 200 amperes. A Permalloy core current transformer was wound with 2000 turns, and a 5 ohm burden resistor was added. These current transformers were calibrated at 60 and 400 Hz. The oscilloscope probes and amplifiers were frequently calibrated during the test sequence. Voltage and current measurements were accurate to between 1/2% and 1% at worst. Three phase power measurement accuracy should thus be good to approximately 1%.

Torque measurements made with the Himmelstein torque transducer, which was rated at 0.1% of full-scale accuracy, appeared to be systematically high by about 2.5%. Dead weight calibration of the transducer was done and rechecked periodically with no measurable additional error. Heat runs with the motor running as a motor and as a generator at the same speed and similar currents were compared. The temperature rise of the aluminum motor shell was assumed to vary linearly with losses. A correc-

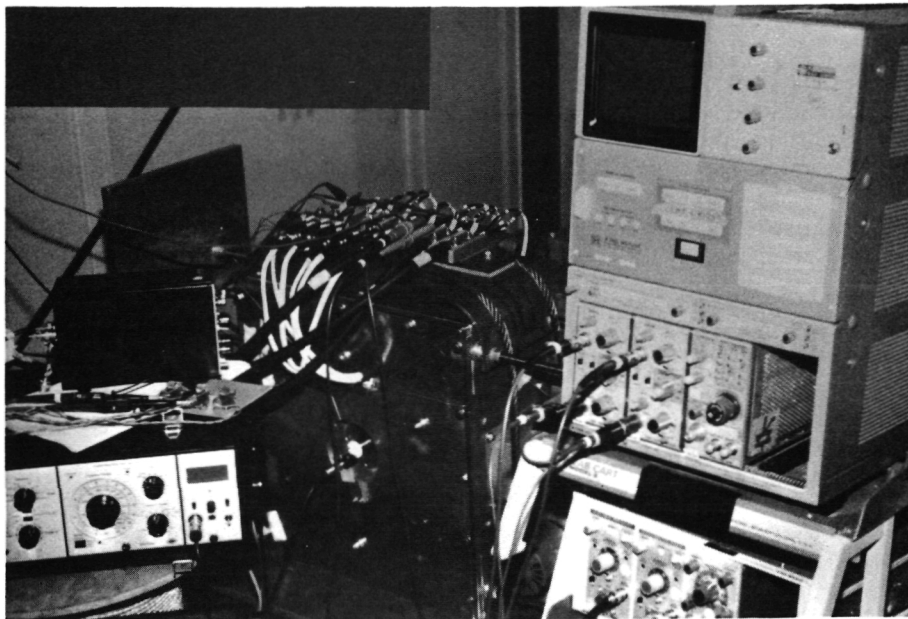


Figure 13-2. Test Setup Showing Terminals, Vibration Instrumentation, and Digital Processing Oscilloscope Cart

tion was applied to the torque (and power) readings to bring the motor and generator results into agreement. A heat transfer coefficient of $50 \text{ W/}^\circ\text{C}$ shell-to-ambient was obtained from the two heat runs at 4000 rpm, and data obtained in heat runs at other speeds and loads agreed closely after the torque was corrected. All data contained in this report has been corrected as described. This systematic source of error in torque measurement has not been identified.

The torque transducer also appeared to exhibit a reversible thermal drift during some tests. This drift was substantially larger than that specified by the manufacturer, and its source has not been identified. Where practical, this thermal drift has been compensated for in the data presented.

The Himmelstein torque transducer and amplifier system have a fundamental limit of resolution in the "least count" of the display. Table 13-1 shows the power associated with one count of the display at the various test speeds. It should be realized that, regardless of any other specification put on the torque measuring system, this one count uncertainty remains.

Data printouts obtained from the DEC data acquisition computer were used as a check of the operating condition, not as primary data for performance calculation. The voltage measurements used by the DEC were made at the inverter terminals, a substantial distance both physically and electrically from the motor. Efficiency as calculated by the DEC thus suffered from the losses in about 60 feet of leads, losses nearly equal to the I^2R loss in the motor itself. All performance data and loss segregation was done utilizing the Tektronix digital processing oscilloscope at the motor terminals and the Himmelstein torque and speed readings; hence no cable correction was required.

Table 13-1
MECHANICAL POWER
MEASUREMENT UNCERTAINTY
DUE TO LEAST COUNT OF
HIMMELSTEIN DISPLAY
AT FULL LOAD

<u>speed (rpm)</u>	<u>power (W)</u>
4000	± 47
5500	± 65
7000	± 83
9000	± 106
11000	± 130

(Least count of display corresponds
to ± 1 lb-in. of torque)

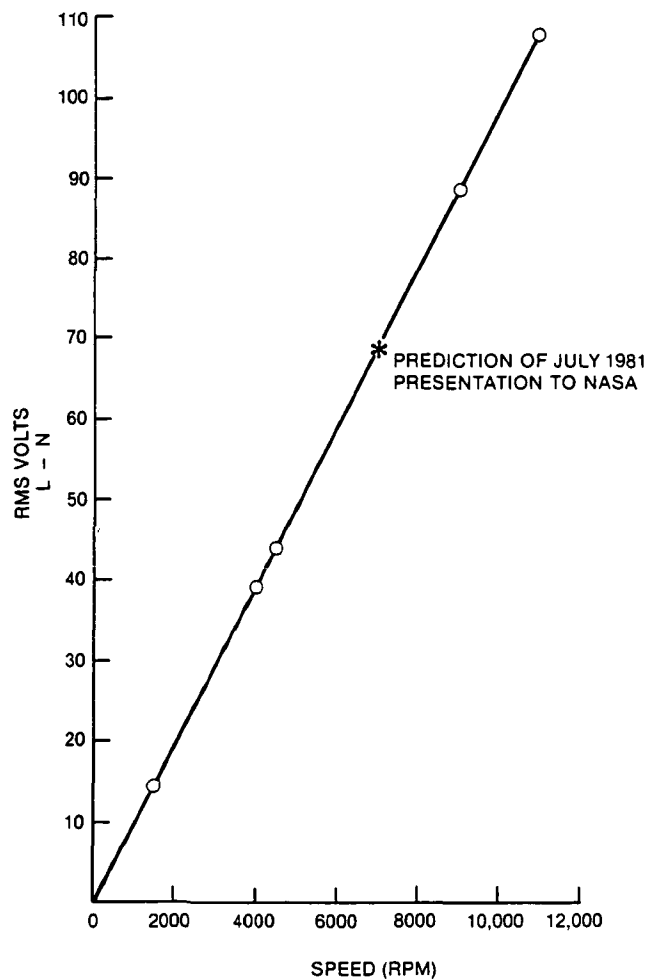


Figure 13-3. Open Circuit Voltage Measurement

13.3 Open Circuit Tests

Open circuit voltage was measured with a Fluke Model 8200A digital voltmeter. Voltage was linearly increasing with speed at 9.85 V/1000 rpm at 25°C (Figure 13-3). Voltage magnitudes and 120° phase relationship were balanced to obtain the 0.005% limits of measurement. Test data is given in Table 13-2. The waveform of line-to-neutral voltage is shown in Figure 13-4, and the fast Fourier transform of this voltage is shown in Figure 13-5. Harmonic content is about 3% third, 4% fifth, 2% seventh, and 1% ninth.

Table 13-2
WINDING BALANCE

<u>RMS Voltage</u>			
<u>V_{A-N}</u>	<u>V_{B-N}</u>	<u>V_{C-N}</u>	
44 30	44 31	44 30	(±0.01%)
<u>V_{A-B}</u>	<u>V_{B-C}</u>	<u>V_{C-A}</u>	
77 73	77 70	77 70	(±0.02%)
NOTE. $44.30\sqrt{3} = 76.73$ (−1.25%)			
<u>Inductance (Before Assembly), μH</u>			
<u>A</u>	<u>B</u>	<u>C</u>	
20.3	20.5	20.5	(±0.5%)
<u>Resistance (mΩ)</u>			
<u>A</u>	<u>B</u>	<u>C</u>	
28.26	28.14	28.14	(±0.3%)

In Table 13-2, the line-to-neutral voltage contains considerable triplen (and other) harmonics which will be reduced in the line-to-line voltage; hence the measurements are consistent.

Also shown are the static measurements of inductance and resistance showing that they too are closely balanced.

Tests of open circuit voltage versus temperature were made in open circuit heat runs at 4,000 and 11,000 rpm. The 2% drop in open circuit voltage in the high-speed run shown in Table 13-3 was used along with Hitachi magnet data showing a reversible temperature coefficient of $-0.045\%/^{\circ}\text{C}$, to predict a rotor temperature of 65.6°C (150°F).

Open circuit loss data for the machine was obtained at speeds from 1,500 to 11,000 rpm. At speeds above 7,000 rpm, noticeable differences between cold and hot machine losses were obtained. These values, as well as a predicted curve are shown in Figure 13-6. For performance prediction, this data was approximated as

$$\text{Watts} = 411.38 - 105.37 * N + 21.88 * N^2$$

for $4 < N < 11 \times 1000$ rpm

PHASE C RMS VALUE IS 39.4464

OFFSET IS 1.02081

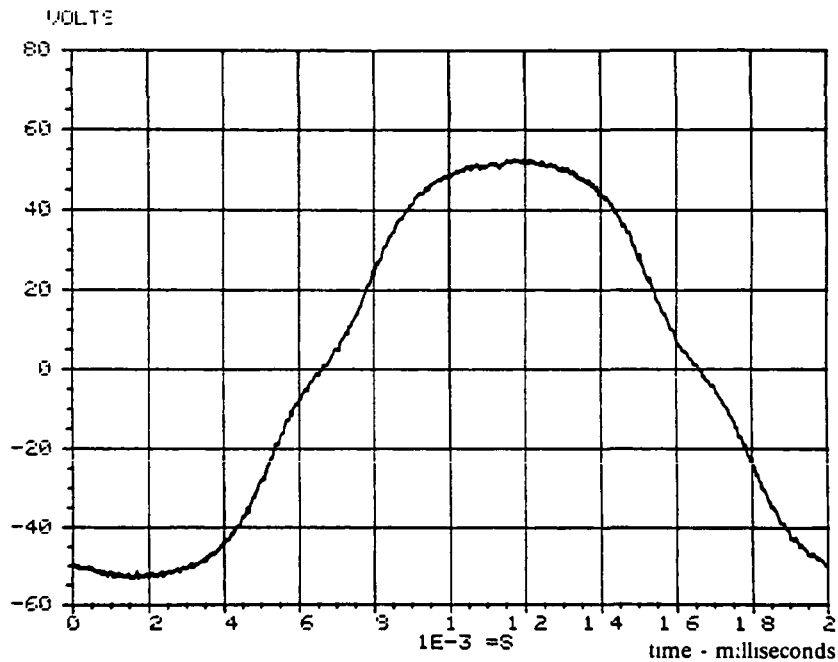


Figure 13-4. Voltage Waveform - Generating, Low Speed

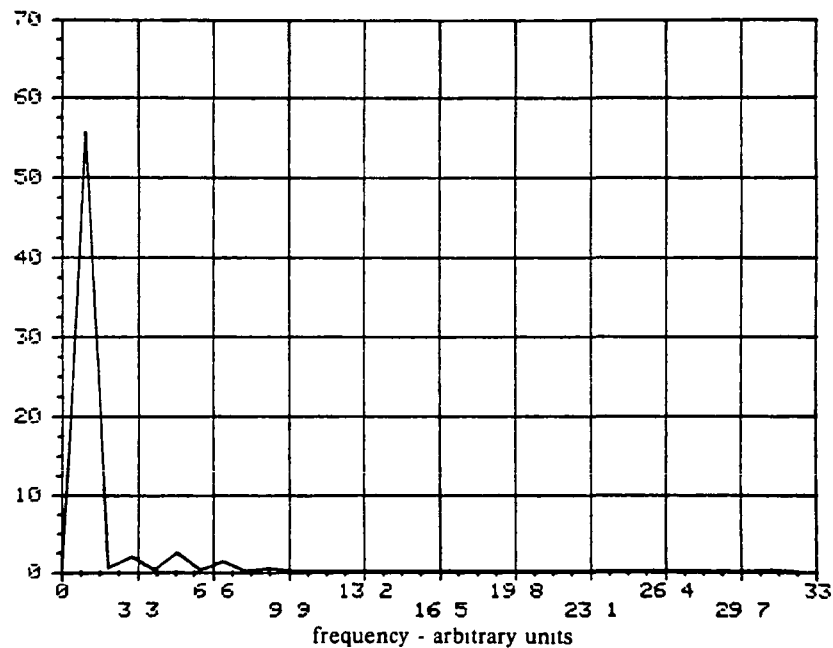


Figure 13-5. Voltage Spectrum - Generating, Low Speed

A Hall-effect clamp-on current probe was placed around one cable of the parallel pair which comprises phase A, and the current signal of Figure 13-7 was recorded. The noise is apparently due to the sampling rate of the digital oscilloscope, but does not appreciably affect the results. Circulating currents between cables on the same phase with peak amplitudes of about one ampere of fundamental, fifth, and seventh harmonics were detected, as shown in Figure 13-8. All other odd harmonics, including third and ninth, were also present.

Table 13-3
MAGNET TEMPERATURE

• Estimated from reversible temperature coefficient		
• 11,000 rpm open-circuit heat run		
Winding	71.1°C (160°F)	} Thermocouples
Case	54.4°C (130°F)	
Spacer	58.9°C (138°F)	
Ambient	26.7°C (80°F)	
Magnet	65.6°C (150°F) Estimated	
(2% drop in open circuit voltage)		

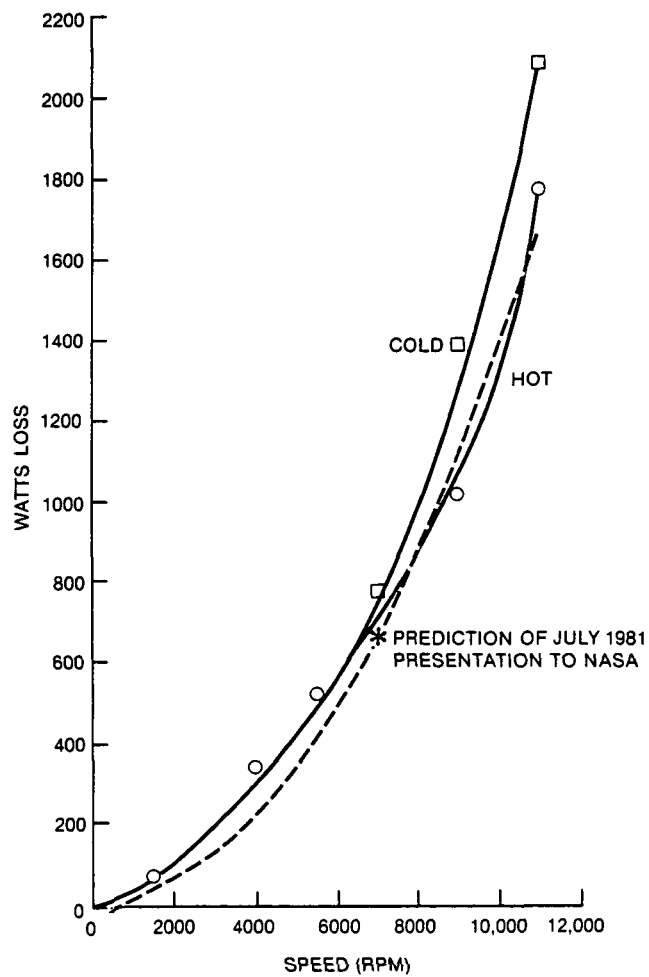


Figure 13-6. Open Circuit Loss Measurement

PHASE A RMS VALUE IS 14.0595

OFFSET IS 0

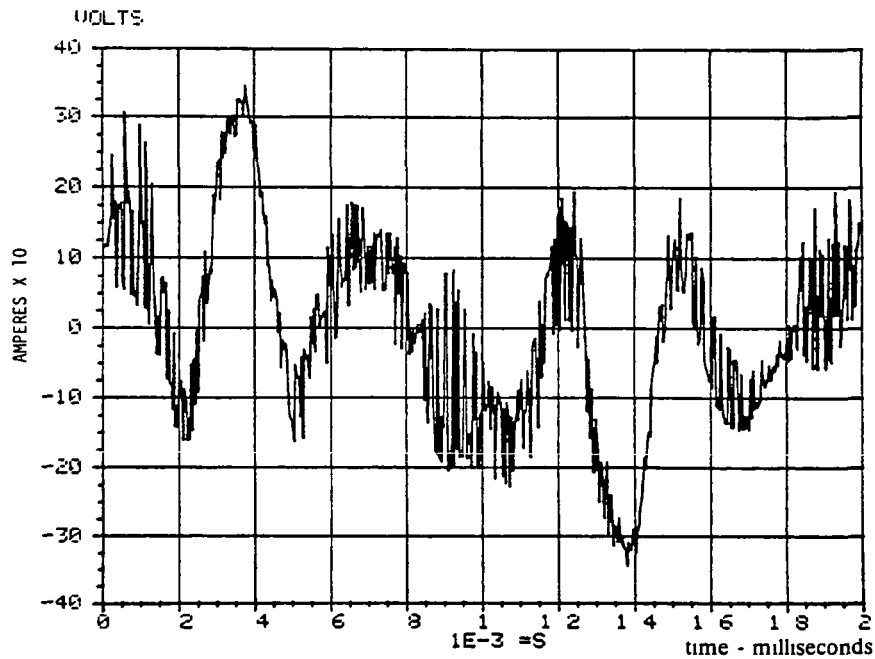


Figure 13-7. Circulating Current Waveform – Low Speed, Open Circuit, Cable-to-Cable

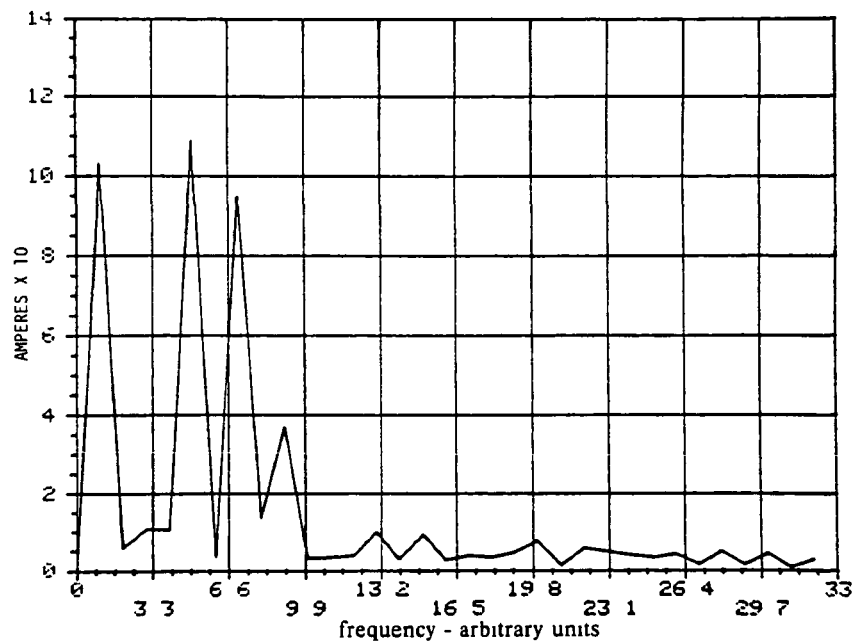


Figure 13-8. Circulating Current Spectrum – Low Speed, Open Circuit, Cable-to-Cable

13.4 GENERATING TESTS

The motor was run as a generator with a resistive load at eight points to characterize its performance. A balanced three-phase resistor bank of cast-iron grids was used. Lead inductance and the inductive nature of the grids resulted in load power factors

between 95 and 98%. The load points, as well as the required performance curve for the motor, appear in Figure 13-9. The data for each of these conditions is summarized in Table 13-4. Note that points 1 and 6 were steady-state (one hour) heat runs, while the other points were held for several minutes. The stray loss measurement should be positive and increasing with speed and load. The variance of this deduced measurement from the theoretical is an indication of the limits of measurement of electrical and mechanical power in the machine. The stray loss measurement could be plotted against load and speed in a three-dimensional regression analysis to improve the accuracy of each point on the basis of the others. This is a fairly complex analysis, and has not been attempted here.

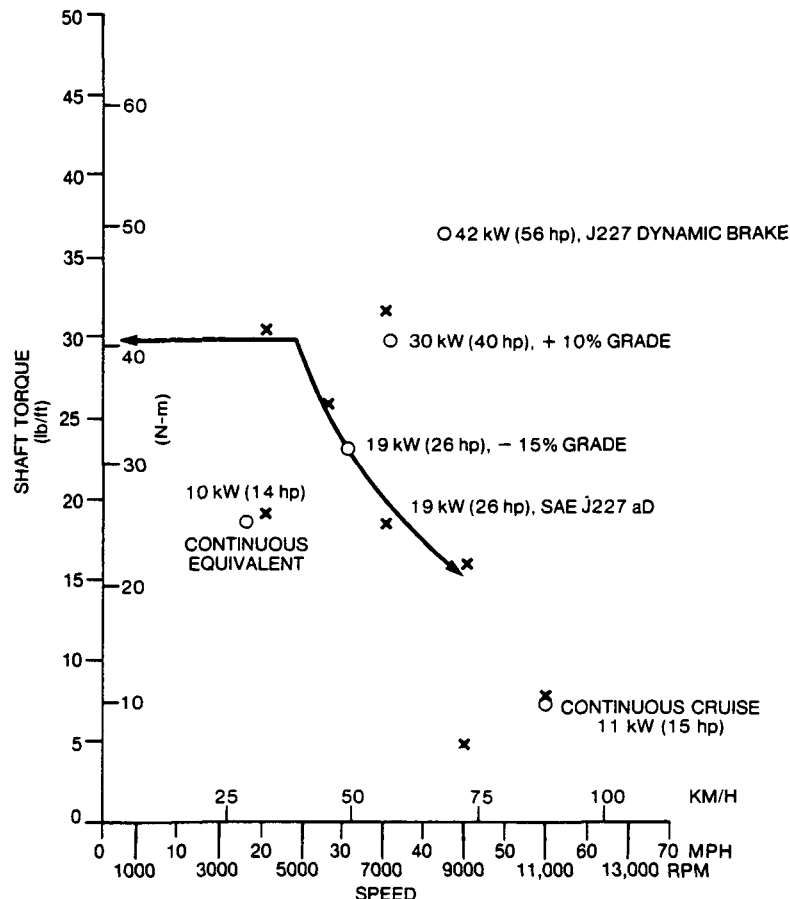


Figure 13-9. Generating Performance Test Points (indicated by X)

The peak power of 33 kW (44 hp) was essentially the limit of the dc drive system, although the disc machine appeared to be capable of significantly more short-time output. The highest efficiency (93%) was achieved at several speeds and loads, and appears to be the best this particular machine can do. The performance of this machine was significantly better than that of either the proof-of-principle motor or the Phase I(A) functional model, as can be seen by comparing Table 13-4 to Table 5-4 in the Phase I(A) report.

Figures 13-10 to 13-14 show the voltage, current, and power waveforms, as well as the harmonic spectra of voltage and current at 7000 rpm, 18.5 kW (24.8 hp) load, point 4 in Table 13-4. Note that all of these, including the instantaneous product of voltage and current, are for Phase A. The power in Phase A is the average of this product.

Table 13-4
GENERATING TESTS WITH RESISTANCE LOAD

	1	2	3	4	5	6	7	8
Speed (rpm)	3998	4038	5443	7005	7091	9000	9000	11005
Torque (lb in)	-231	-368	-309	-223	-382	-67	-195	-88
Shaft Power (hp)	-14.4	-23.5	-26.7	-24.8	-43.7	-9.6	-27.9	-15.3
V_A rms (V)	36.86	35.56	49.2	65.46	63.5	86.4	84.63	105.3
I_A rms (A)	91.0	150.3	126.8	89.3	159.7	24.2	77.0	33.1
Output Power (kW)	10.04	15.922	18.437	17.291	29.872	6.156	19.355	9.722
Shaft Power (kW)	10.750	17.551	19.908	18.526	32.600	7.164	20.780	11.435
Efficiency (%)	93.5	90.7	92.6	93.3	91.6	85.9	93.1	85.0
Power Factor (%)	98.3	97.4	96.8	96.9	97.2	94.8	96.3	94.8
Lead Angle (degrees)	+10	11	14	14	14	22	15	22
Input-Output Loss (watts)	701	1629	1471	1235	2728	1008	1425	1713
I^2R Loss (watts)	387	1129	767	384	1251	28	285	54
Open Circuit Loss (watts)	340	340	520	746	746	1030	1030	1760
Stray Loss (watts)	(-26)	160	184	105	731	(-50)	109	(-101)
(Test - I^2R - Open Circuit)								
Winding Temperature Rise (°C)	25	45	31	34	39	34	34	40
Case Temperature Rise (°C)	14	17	14	19	14	22	19	24
Thermal Resistance (watts/°C)	49.4	-	-	-	-	45.4	-	-

PHASE A RMS VALUE IS 65.623

OFFSET IS -1.49012E-08

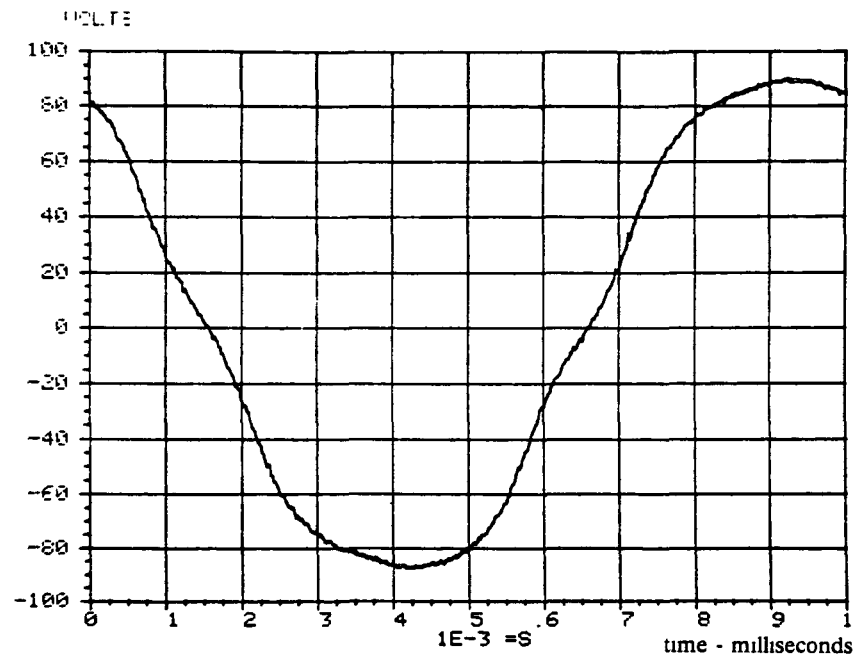


Figure 13-10. Phase A Voltage – Generating at 7000 rpm, 18.5 kW (24.8 hp)

PHASE A RMS VALUE IS 90.4608
-07

OFFSET IS 5.84638E

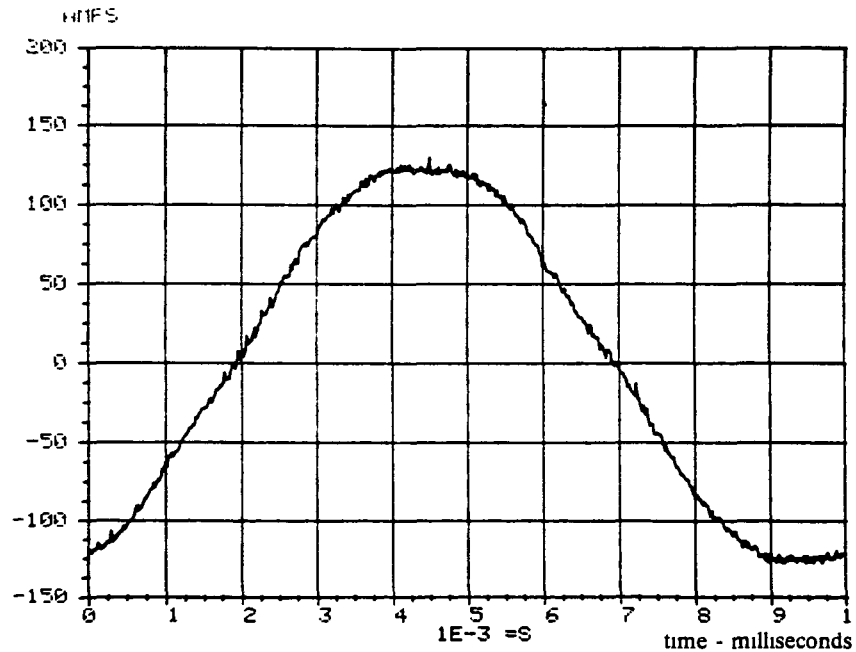


Figure 13-11. Phase A Current – Generating at 7000 rpm, 18.5 kW (24.8 hp)

PHASE A MEAN VALUE 1E-5786 42

1E 3 WATTS

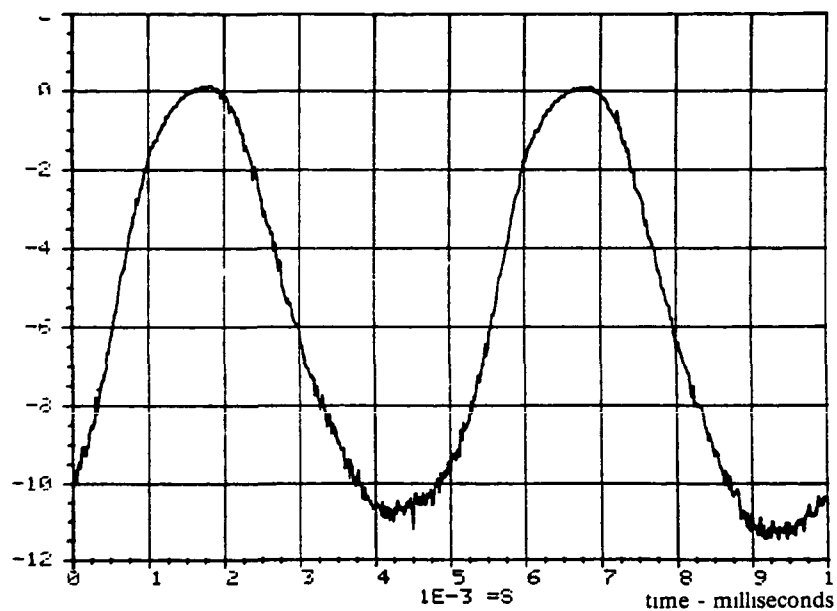


Figure 13-12. Phase A Power — Generating at 7000 rpm, 18.5 kW (24.8 hp)

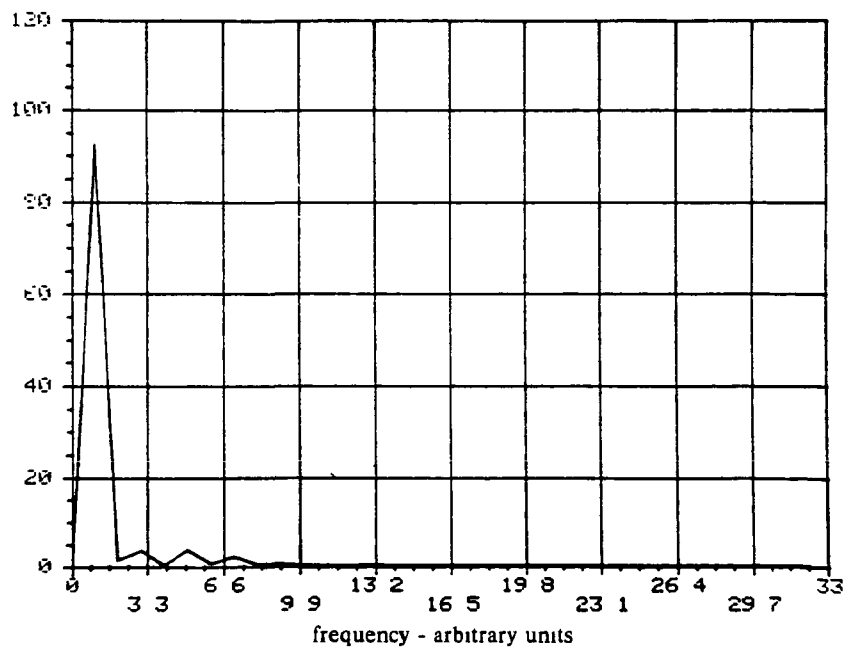


Figure 13-13. Phase A Voltage Spectrum — Generating at 7000 rpm, 18.5 kW (24.8 hp)

13.5 MOTORING TESTS

Figure 13-15 shows twelve motoring test points over the spectrum of loads expected in the application of the motor, as well as nine points at 5500 rpm to identify the peak efficiency within the limits of the test system. The data associated with the

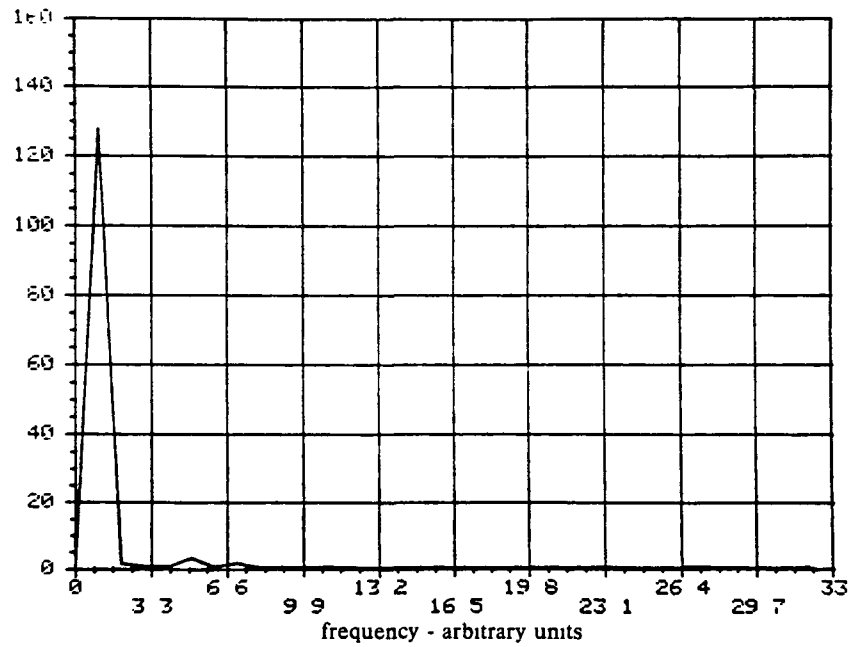


Figure 13-14. Phase A Current Spectrum – Generating at 7000 rpm, 18.5 kW (24.8 hp)

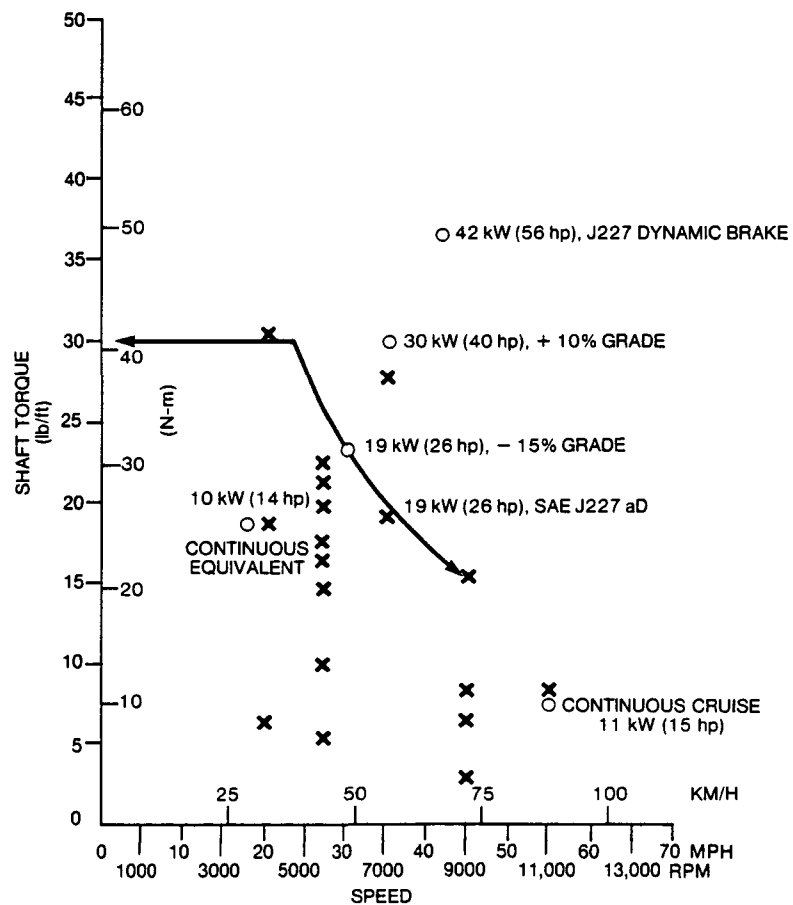


Figure 13-15. Motoring Performance Test Points (indicated by X)

twelve operating points is given in Table 13-5, and includes five steady-state heat runs. As in the generating tests, these were held for about one hour, while the others were held for several minutes.

At speeds below 5500 rpm, the dc bus voltage was adjusted for the minimum “comfortable” commutation margin in the inverter. This resulted in the fundamental component of current leading to the voltage by 22° to 30° , and represented an optimum system operating point. At about 5500 rpm, the voltage limit of the 125V, 250A power supply was reached, and the inverter phase advanced for higher speeds. The larger (43° to 63°) lead angle at speeds above 5500 rpm resulted in a drop-off in motor performance, as power factor moved further from the optimum.

Figures 13-16 to 13-18 show the line-to-neutral voltage, current, and power in one phase of the machine for the 15 hp, 11,000 rpm load, point 12. This was the highest speed of operation. Figures 13-19 to 13-23 show the same quantities as well as harmonic spectra of voltage and current for the 7000 rpm, 24 kW (32 hp) point. This was the highest motoring power obtained, limited by the inverter dc power supply, which was at both voltage and current limit during the test. (Note: 195 amperes ac rms corresponds to 250 amperes dc).

The size of the commutating notches in the voltage waveforms of Figures 13-16 and 13-19 should be compared to those for the proof-of-principle and Phase I(A) motors. The narrow width and small amplitude of the notches for this motor are indicative of its small leakage inductance and the ease with which the system of motor and inverter commutate currents from phase to phase.

Figure 13-24 and Table 13-6 show the results of a series of tests at 5500 rpm. This was the highest speed at which minimum lead angle could be held with the 120 volt dc supply, and was thus the best candidate for high efficiency from the motor. Load points from 3.7 to 18.6 kW (5 to 25 hp) were run; then a heat run was performed at 18 hp, identified as at or near the peak efficiency for the motor. The resulting performance is tabulated in Column 9 of Table 13-6, listed as “estimated” because the motor failed prior to obtaining the shutdown data. Column 8 of the table gives data at the beginning of the heat run, while Column 9 is adjusted to reflect the winding temperature at the end of the run. The efficiency of 92.5% from this test is slightly higher than predicted by the conservative mathematical model, and quite high for a motor of this rating when operating in an LCI system.

As indicated above, the motor failed during the last supplementary heat run to determine the efficiency profile. The motor was running at low speed and low power at the time. there had been no history of electrical, mechanical, or thermal problems. In fact the motor ran remarkably smoothly and well.

A post-failure examination of the motor showed no defects in the windings, even though two phases had experienced severe overtemperature. The third phase showed no signs of deterioration or damage. The focus of damage was the lead entry area (Figure 10-7) just outside of the loaded epoxy filler where heavy arcing and melting of two phases occurred. Damage to the windings was apparently due entirely to large currents through a short circuit between two phases in the entry area driven by the rotating magnets rather than the inverter. Fast fuses in the inverter lines did not blow.

Even though there was considerable distortion of the windings due to high temperatures, no strands were broken. The insulation also retained its integrity as shown by insulation resistance tests, phase-to-phase and phase-to-ground. As a result, HiPot tests were repeated on the damaged windings, proving a remarkable degree of insulation integrity, both phase-to-phase and phase-to-ground.

Although there were no resources available for an exhaustive fault analysis, examination of the evidence and various fault scenarios indicated a likely combination of events and circumstances that could have been responsible for the failure. These are an inverter fault and a weakening of the insulation in the entry area.

It was demonstrated theoretically that an inverter miscommutation could result in high voltages appearing between phases. The insulations used should have easily withstood these voltages. It may be postulated that high temperatures and/or vibration in the entry region could have weakened the insulation sufficiently to breakdown during an inverter fault.

The entry region, for reasons of convenience in the laboratory model, was not impregnated; air flow was restricted there, and the terminals were at some distance. All these factors, which would not be present in a production prototype, could have led to higher than desired temperatures.

In addition, protection could be added to prevent voltage spikes at the motor, such as metal oxide varistors across the phases and monitoring of inverter commutation. Fuses in the center of the "Y" connection would also have prevented extensive damage to the motor.

Table 13-5
MOTORING TESTS ON LOAD-COMMUTATED INVERTER

	1	2	3	4	5	6	7	8	9	10	11	12
Speed (rpm)	4000	4000	3999	5511	5505	6992	6990	9003	8996	8995	9002	10997
Torque (lb in.)	76	221	365	117	294	230	272	34	74	103	184	90
Shaft Power (hp)	4.83	14.06	23.13	10.24	25.65	25.53	30.15	5.01	10.58	14.77	26.47	15.65
V_A rms (V)	39.57	40.01	40.30	54.08	54.37	63.49	63.44	85.38	82.80	81.14	79.3	99.07
I_A rms (A)	37.1	107.9	194.5	58.6	154.0	158.6	192.8	34.89	67.4	92.9	174.4	104.7
Input Power (kW)	3.913	11.415	19.864	8.210	7.637	21.209	25.581	4.791	9.323	12.702	22.956	14.277
Shaft Power (kW)	3.600	10.488	17.253	20.944	19.137	19.042	22.489	3.739	7.882	11.019	19.748	11.674
Efficiency (%)	92.0	91.9	86.9	93.0	91.2	89.8	87.9	78.0	84.6	86.8	86.0	81.8
Lead Angle (degrees)	22	25	29	27	27	43	43	56	56	56	56	63
Input-Output Loss (watts)	313	927	2611	573	1857	2167	3092	1052	1431	3208	3387	2603
I^2R Loss (watts)	62	566	2019	161	1201	1303	1980	59	227	448	1605	539
Open Circuit Loss (watts)	340	340	340	520	520	746	746	1030	1030	1030	1030	1760
Stray Loss (watts)	-89	25	29	-108	136	118	366	-37	174	205	573	304
(Test - I^2R - Open Circuit)												
Winding Temperature Rise (°C)	13.6	36	66	26	49	56	64	35.5	45	57	62	40
Case Temperature Rise (°C)	8.6	19	23	16	23	26	28	22	28	33	28	21
Thermal Resistance (watts/°C)	36.4	49.8	-	-	-	-	-	48	51.5	51	-	-

PHASE A RMS VALUE IS 98.3195

OFFSET IS 264883

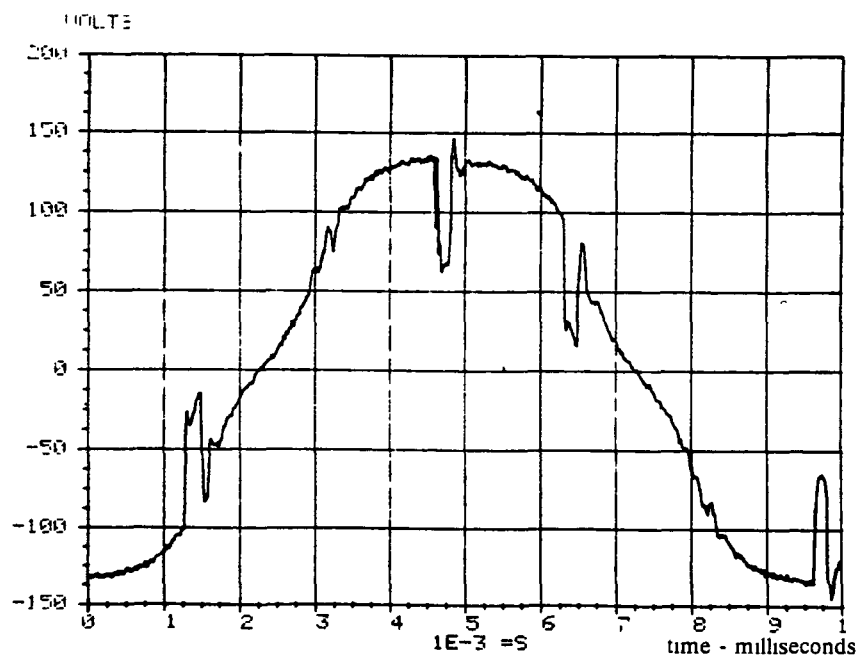


Figure 13-16. Phase A Voltage - Motoring at 11,000 rpm, 11.2 kW (15 hp)

PHASE A RMS VALUE IS 105.396

OFFSET IS 504126

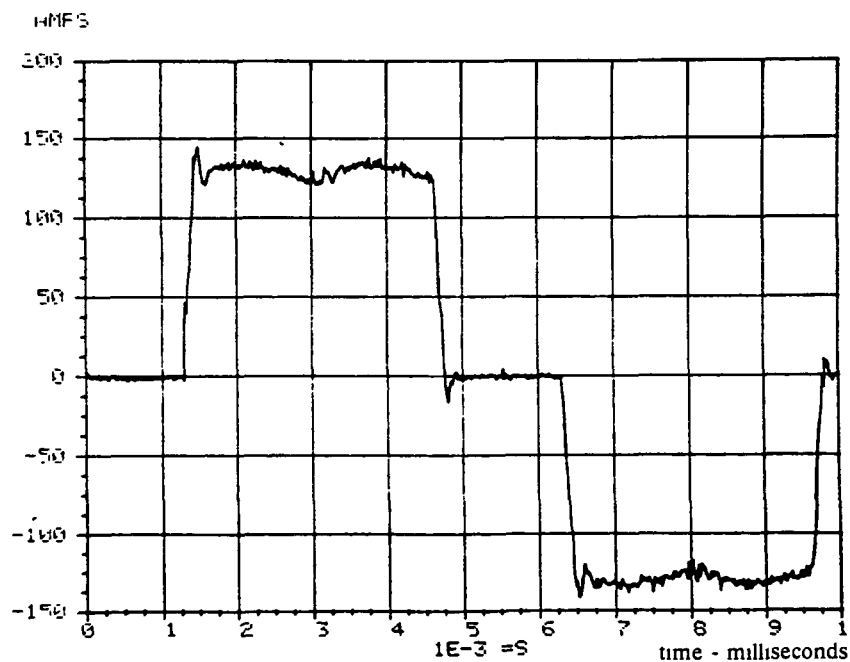


Figure 13-17. Phase A Current - Motoring at 11,000 rpm, 11.2 kW (15 hp)

PHASE A MEAN VALUE IS 4777.72

1E 3 WATTS

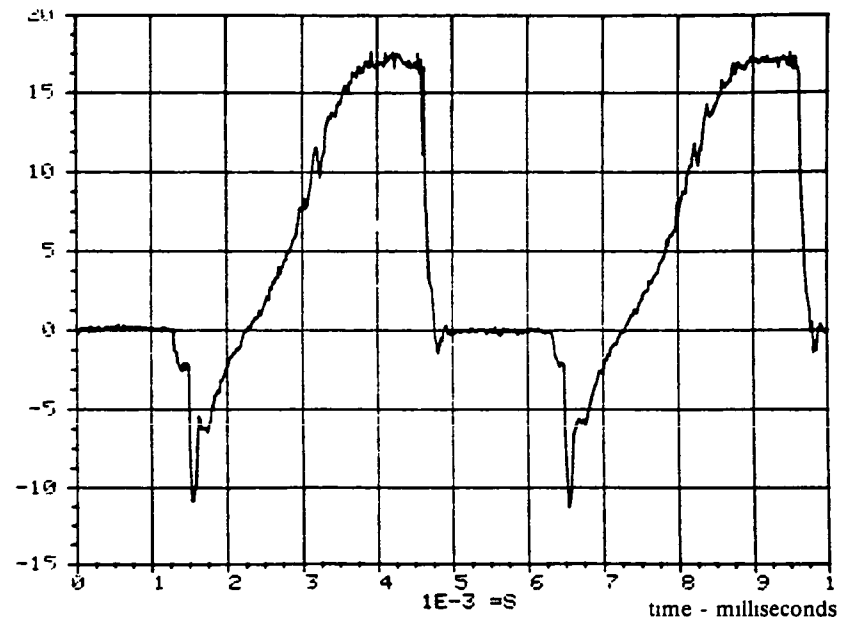


Figure 13-18. Phase A Power – Motoring at 11,000 rpm, 11.2 kW (15 hp)

PHASE A RMS VALUE IS 63.44

OFFSET IS -1.74619

VOLTS

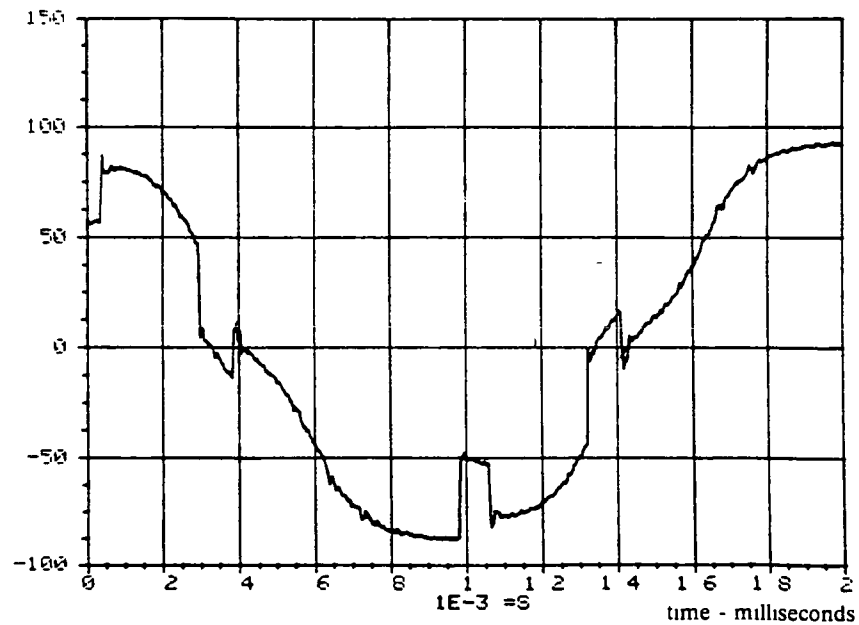


Figure 13-19. Phase A Voltage – Motoring at 7000 rpm, 23.9 kW (32 hp)

PHASE A MEAN VALUE IS 192.837

OFFSET IS -4.87009

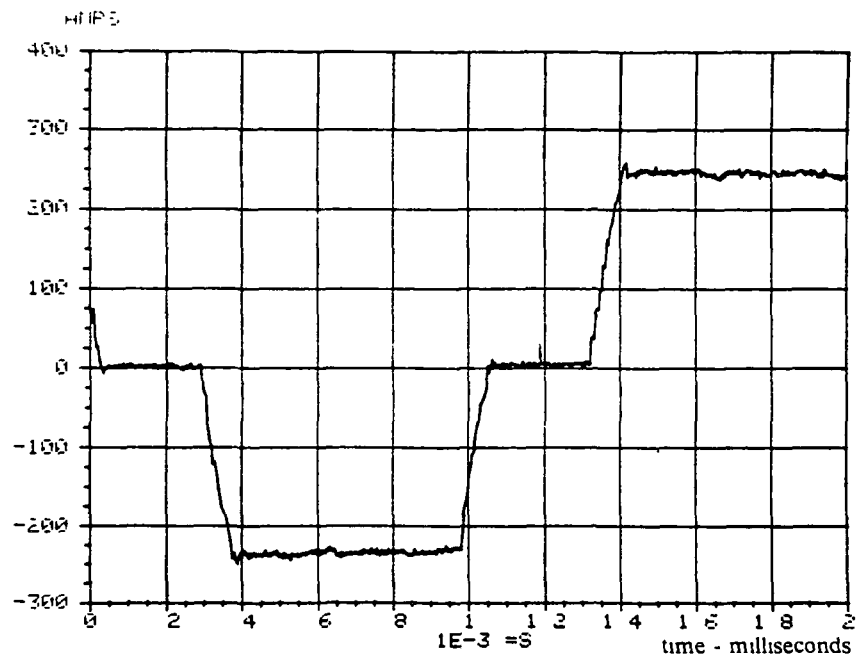


Figure 13-20. Phase A Current – Motoring at 7000 rpm, 23.9 kW (32 hp)

PHASE A MEAN VALUE IS 63.327

1E 3 WATTS

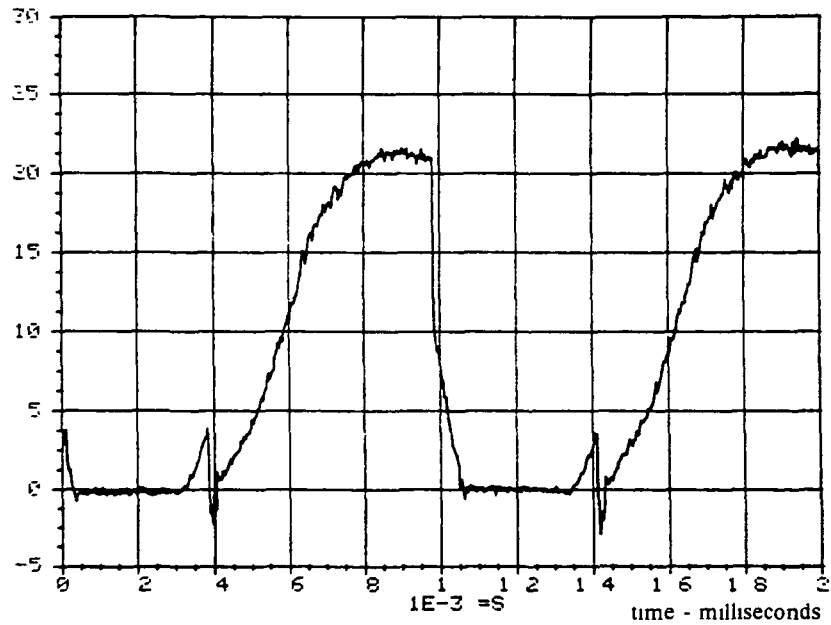


Figure 13-21. Phase A Power – Motoring at 7000 rpm, 23.9 kW (32 hp)

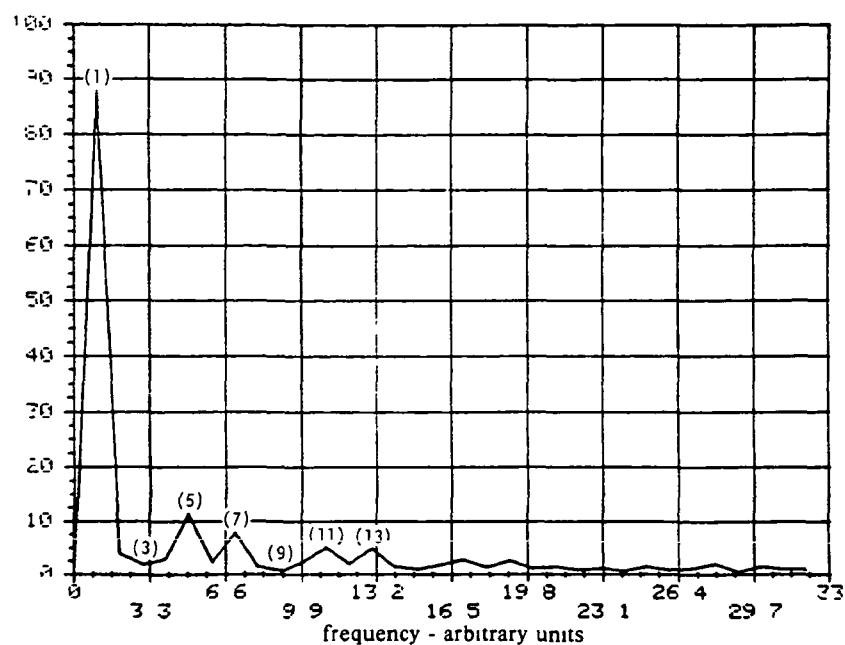


Figure 13-22. Phase A Voltage Spectrum – Motoring at 7000 rpm, 23.9 kW (32 hp)

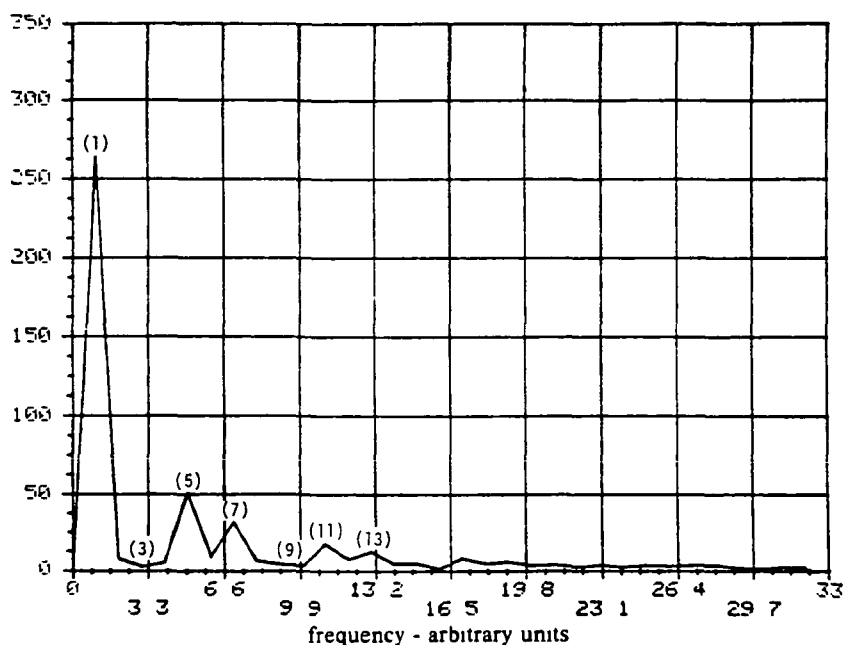


Figure 13-23. Phase A Current Spectrum – Motoring at 7000 rpm, 23.9 kW (32 hp)

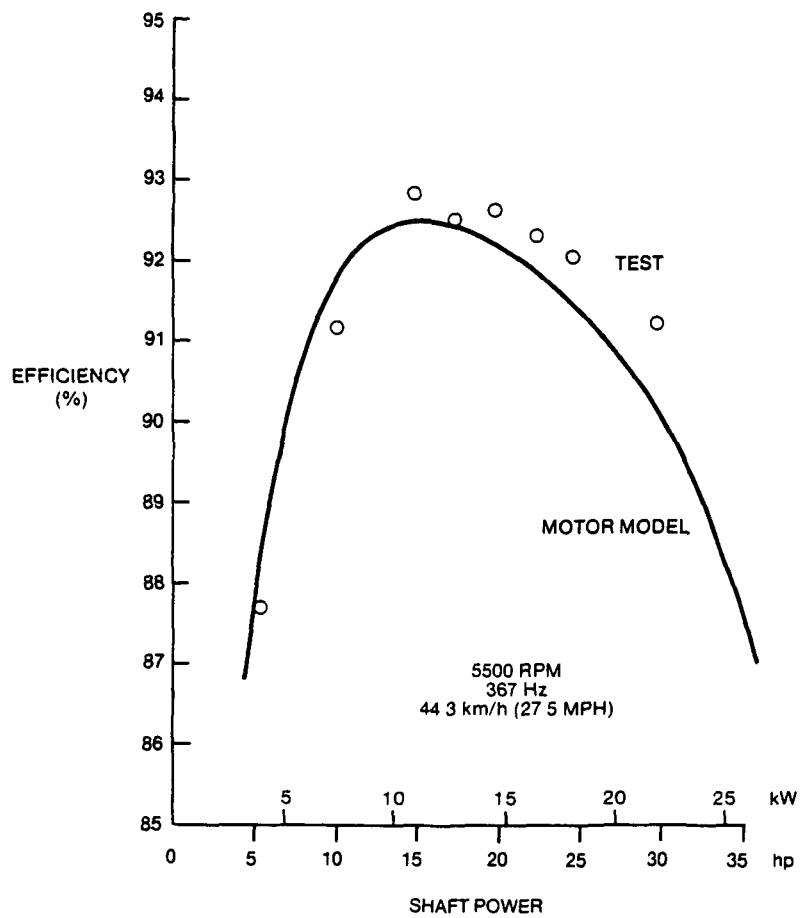


Figure 13-24. Peak Efficiency Determination

Table 13-6
MOTORING TESTS – 5500 RPM RUNS – LOAD-COMMUTATED INVERTER

MOTOR TESTS									
5500 RPM RUNS – 10/5/81									
	1	2	3	4	5	6	7	8	9
Speed (rpm)	5505	5502	5504	5508	5503	5504	5500	5510	5510
Torque (lb in)	63	117	173	200	231	256	286	207	207
Shaft Power (hp)	5.54	10.3	14.98	17.47	20.09	22.46	24.85	18.07	18.07
V_A rms (V)	54.05	54.09	54.24	54.24	54.20	54.17	54.12	54.20	(54)
I_A rms (A)	33.7	59.5	87.1	102.3	118.4	132.4	148.5	106.3	(106)
Input Power (kW)	4.711	8.268	12.041	14.091	16.185	18.157	20.158	14.562	(14.574)
Shaft Power (kW)	4.133	7.557	11.172	13.034	14.991	16.758	18.540	13.478	13.478
Efficiency (%)	87.7	91.4	92.8	92.5	92.6	92.3	92.0	92.6	(92.5)
Lead Angle (degrees)	23	25	25	27	27	27	26	27	(27)
Input-Output Loss (watts)	578	711	869	1057	1194	1399	1618	1084	(1096)
I^2R Loss (watts)	52	162	356	500	680	867	1124	544	(556)
Open Circuit Loss (watts)	520	520	520	520	520	520	520	520	520
Stray Loss (watts)	+6	+29	-7	37	-6	12	-26	20	(20)
(Test – I^2R – Open Circuit)									
Winding Temperature Rise (°C)	17	19	26	32	36	42	51	34	40
Case Temperature Rise (°C)	10	13	14	18	20	23	26	19	23
Thermal Resistance (watts/°C)	—	—	—	—	—	—	—	—	(47.7)
									Estimated At End of Heat Run

14.0 CONCLUSIONS AND RECOMMENDATIONS

14.1 CONCLUSIONS

The motor performed exceedingly well. Performance was verified by test up to the limit of the experimental facilities. Structural integrity was verified and vibration problems in the motor were minimal. A mathematical model for prediction of motor performance matched (or underestimated slightly) actual performance, both electromagnetically and thermally.

Based on the tests and the model predictions, the motor meets all of the contractual requirements. Again, based on preliminary results of the model, it appears likely that the present motor design with minor modifications could accommodate the "Diesel Equivalent Specification." This, of course, will require a more detailed electromagnetic, thermal, and mechanical analysis than was possible in the present circumstances to verify. It is, however, an inherent advantage of the disk type machine that capability may be doubled or tripled rather easily by simply stacking up identical units on a single shaft. This would also reduce unit costs by having only one size of motor to produce. Making a single unit larger, on the other hand, poses rather severe electromagnetic, mechanical, and thermal problems.

14.2 RECOMMENDATIONS

14.2.1 The Functional Model Motor

In the course of designing the Phase I(B) motor, choices were made that led to lower than the ultimate efficiency. Also, some further discrepancies were revealed in testing. In future developments with this motor, a number of improvements can be made leading to as much as 30% reduction losses or an efficiency of over 95%. These have been grouped according to functional areas. In the following tables, losses are labeled "OCL" for open circuit loss and "LL" for load loss — losses which are independent of load and those which are dependent on load.

Improvements to the winding are listed in Table 14-1. The stranding size could be made smaller without much difficulty. Since eddy current losses depend on the fifth power of the diameter, these losses can easily be halved or even further reduced. The cable design used was not fully intermixed, i.e., inner and outer strands did not exchange. Some gains could be made by full transposition but would have to be balanced against packing factor. Tighter packing is possible if more space can be provided for the outside end turns. The cables simply lay in the slots now. Perhaps 20% to 35% more copper could be used with tighter packing. Lead lengths were made artificially large for convenience of connections and electrical measurements. Better than 20% of the resistance, hence the load losses, in each phase are in the lead exten-

Table 14-1
PERFORMANCE IMPROVEMENT WINDING

Smaller Strands (OCL)

Transpose Strands (OCL)

Tighter Packing (LL)

Shorter Leads (LL)

sions. Terminal boxes attached to the motor frame at the end exit points would then save considerable losses and have other benefits as well. The data reported in previous sections included these losses.

Close location of the terminal box impregnation of the leads and air flow over the leads would hold down temperatures on the lead entry area, reducing the likelihood of failure in this area. The addition of varistors at the motor terminals and/or commutation monitoring would then virtually eliminate the possibility of catastrophic failure, as experienced at the end of testing.

Improvements to the case and core area are shown in Table 14-2. High frequency core losses will vary approximately with the square of the lamination thickness. The cores used were made with 12 mil stock but could have been made of 6 mil stock with little penalty, thus reducing core loss to a negligible level. The spacer extension has two functions: (1) to minimize windage losses by controlling the radial gap, and (2) emergency energy absorption in case of a catastrophic rotor failure. This was most directly and cheaply done by making the spacer very thick, as shown in Figure 10-2. Unfortunately, as shown in Figure 11-5, there is some leakage flux from the rotor magnets linking the spacer extension. The magnitude is not large, but the frequency is high and the resistivity is low, leading to considerable losses. Replacement of the spacer extension with a nonconducting energy absorber would be desirable. The surface of the stator ended up somewhat "bumpy" due to the methods of fabrication used. Providing extra material and machining to a flat smooth surface would reduce windage losses.

In the system area (Table 14-3), higher battery voltages would reduce losses by reducing currents in the leads and semiconductors, and the motor could be run with a higher voltage corner point, thus requiring less phase advance. Another strategy for reducing phase advance would be a series-parallel switch to double the corner speed.

Table 14-2

PERFORMANCE IMPROVEMENT CASE AND CORE

- Thinner Laminations (OCL)
- Nonconducting spacer extension (OCL)
- Machined Stator Surface (OCL)

Table 14-3

PERFORMANCE IMPROVEMENT SYSTEM

- Higher Battery Voltage
 - Reduce Inverter Loss
 - Reduce Lead Losses
 - Reduce Phase Advance
- Series/Parallel Switch
 - Reduce Phase Advance

14.2.2 Engineering Model

The engineering model design was discussed in Part One but is resummarized here in light of the Phase I(B) motor. The first option for development into an engineering model is the extension, with improvements, of the Phase I(B) functional model (Table 14-4). This is a satisfactory motor and would require the least additional development work.

Other options for the engineering model would reduce its capability to that required by the contract (Table 14-5). Two such options are shown in Table 14-6 and 14-7, both of which utilize lower speed and slotted steel tapes or iron powder/epoxy composites. Both would require extensive further development of the nature of a functional model before proceeding to the engineering model.

Table 14-4
ENGINEERING MODEL OPTION PHASE I(B) DESIGN

- *Improvements in Electromagnetics*
 - Thinner Laminations
 - Finer Stranding
 - Tighter Slot Packing
 - Smooth Stator Surface
 - Nonconducting Spacer
 - *Mechanical Redesign*
 - *Termination and Lead Entry Redesign*
 - *Performance*
 - Improved Efficiency
 - Cooler
 - Lower Weight
 - *Original Specification*
 - *May be Stretched to Diesel Specification*
 - Thermal Evaluation
- | | |
|-----------------|-------------------|
| Magnet OD | 24.1 cm (9.5 in.) |
| Rotor Thickness | 3.8 cm (1.5 in.) |
| Maximum Speed | 11,000 rpm |

Table 14-5
ENGINEERING MODEL OPTION
MODIFIED DESIGNS

- *Reduce Capability*
 - Reduce Speed
 - Reduce Diameter
- *Performance*
 - Lower Weight
 - Lower Inertia
 - Lower Efficiency
 - Higher Temperature
- *Original Specification*
 - No Chance for Diesel Specification Without Gears

Table 14-6
ENGINEERING MODEL OPTION

- *Slotted Iron Stator, Large OD, Low Speed*
 - Slotted Tape
 - Iron Powder/Epoxy
- *Advantages*
 - Shorter
 - Reduced Weight and Inertia
 - Stretchable to Diesel Specification (?)
 - High Efficiency (~96%)
 - Better Heat Transfer
 - Reduced Fault Current
- *Disadvantages*
 - Poorer LCI Operation
 - Large Diameter
 - More Development

Magnet OD	30 cm (11.8 in.)
Rotor Thickness	2.54 cm (1 in.)
Maximum Speed	8000 rpm

Table 14-7
ENGINEERING MODEL OPTION

- *Slotted Iron Stator, Large OD, Low Speed*
 - Slotted Tape
 - Iron Powder/Epoxy
- *Advantages*
 - Shorter, Reduced OD
 - Low Weight, Low Inertia
 - Reduced Fault Current
 - Better Heat Transfer
 - Modest Efficiency (93%)
- *Disadvantages*
 - Poorer LCI Operation
 - More Development
 - Requires Gear Shift For Diesel Specification

Magnet OD	21.6 cm (8.5 in)
Rotor Thickness	2.54 cm (1.0 in)
Maximum Speed	8000 rpm

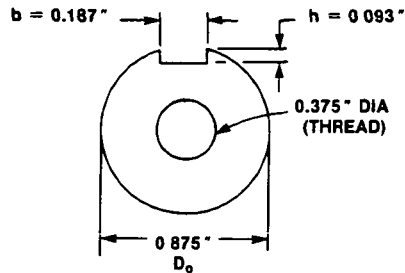
Appendix A
MECHANICAL DESIGN ANALYSIS

Appendix A

MECHANICAL DESIGN ANALYSIS

A1. STRESSES

A1.1 Shaft Stress



Loading: Torsion

Material: 1015 to 1035 steel
 $S_y = 35$ ksi, min tensile
 $S_u = 75$ ksi, min
 $E = 28 \times 10^6$ lb/in.²

Reference: *Machine Design*, Maleev and Hartman, 3rd Ed., Chap. 20

Shear stress (S_s) = $\frac{KTr}{J}$, where

$$K = \frac{0.2b + 1.1h}{D_o} = 1.16$$

$$T = 117 \text{ ft-lb} = 1404 \text{ in.-lb (max)}$$

$$r = \frac{D_o}{2} = 0.4375 \text{ in.}$$

$$J = \frac{\pi}{32} (D_o^4 - D_i^4) = 0.0556 \text{ in.}^4$$

$$S_s = \frac{1.16(1404 \text{ in. lb})(0.4375 \text{ in.})}{0.0556 \text{ in.}^4}$$

$$S_s = 12.8 \text{ ksi} < 1/2 S_y$$

Therefore, the shaft should not fatigue.

A1.2 Rotor Bearings

Type: deep groove, ball, 52100 steel

Size: Bore = 25 mm (0.9843 in.)

OD = 52 mm (2.0472 in.)

Width = 15 mm (0.5906 in.)

Lubricant: Grease (Texaco Unitemp 500, -50°F to $+300^\circ\text{F}$)

Seals: Both ends

Cage: Two piece, ribbon

Speed Limit: 10^4 rpm

Loads: Radial (R) = 16.2 lb (1/2 rotor weight)

Thrust (T) = 50 lb (from 2 preload springs)

Bearing Life (Reference: Barden catalog ST2)

$$L_{10} = \left(\frac{C}{P} \right)^3, \text{ million revolutions, where}$$

L_{10} = minimum life for 90% of typical group of apparently identical bearings

C = basic load rating = 2380 lb

P = equivalent load rating

$$P = XR + YT$$

$$X = 0.45$$

$$Y = 1.55$$

$$P = 0.45 (16.2 \text{ lb}) + 1.55 (50 \text{ lb}) = 84.8 \text{ lb}$$

$$L_{10} = \left(\frac{2380 \text{ lb}}{84.8 \text{ lb}} \right)^3 \times 10^6 \text{ rev} = 2.2 \times 10^{10} \text{ revs at 1000 rpm}$$

at 5000 rpm:

$$L_{10} = \frac{2.2 \times 10^{10} \text{ rev}}{60 \text{ min/hr}} \times \frac{1000}{5000 \text{ rpm}} = 7.3 \times 10^7 \text{ hr}$$

However, according to Barden Engineering, the bearing life should be limited by the lubricant to the order of 2500 hours. With most greases, at approximately 100°C bearing life varies by a factor of 1.5 per 10°C temperature change.

A1.3 Shrink Fit – Hub on Shaft

Hub Material

Aluminum alloy 2024-T3 Carbon Steel (0.15 to 0.35% C)

$$S_y = 50 \text{ ksi}$$

$$E = 10^7 \text{ lb/in.}^2$$

$$\alpha = 23.2 \times 10^{-6}/^\circ\text{C}$$

$$S_y = 35 \text{ ksi}$$

$$E = 2.8 \times 10^7 \text{ lb/in.}^2$$

$$\alpha = 11.5 \times 10^{-6}/^\circ\text{C} \text{ (Metals Handbook, 9th Ed.)}$$

Interference required to transmit maximum torque without slipping (Reference: *Machine Design*, Mallev and Hartman, 3rd Ed., Chap. 13)

$$T = \frac{\pi D^2 L f P_2}{2}, \text{ where}$$

$$T = \text{torque} = 1404 \text{ in. lb, max}$$

$$D = \text{shaft dia.} = 1.75 \text{ in.}$$

$$L = \text{engagement length} = 2.06 \text{ in.}$$

$f = \text{friction coefficient} = 0.125$

$P_2 = S_c = \text{compressive stress, lb/in.}^2$

$$S_c = \frac{2T}{\pi D^2 L F}$$

$$S_c = \frac{(2)(1404 \text{ in. lb})}{\pi (1.75 \text{ in.})^2 (2.06 \text{ in.})(0.125)}$$

$$S_c = 1130 \text{ lb/in.}^2$$

Interference required to transmit torque:

$$i = \frac{S_c r_s}{n} \left[\frac{n}{E_s} + \frac{1}{E_n} \right]$$

$$n = \frac{r_n^2 - r_s^2}{r_n^2 + r_s^2}$$

$$r_n = 2.5 \text{ in.}$$

$$r_s = 0.875 \text{ in.}$$

$$n = 0.78$$

$$i_t = \frac{1.13 \text{ ksi} (0.875 \text{ in.})}{0.78} \left[\frac{0.78}{28 \times 10^3 \text{ ksi}} + \frac{1}{10^4 \text{ ksi}} \right]$$

$$i_t = 0.00016 \text{ in.}$$

(will apply a safety factor to shrink fit at conclusion of analysis)

Dynamic expansion of hub (neglecting ribs) =

$$S_r = \frac{\delta \omega^2}{4g} [(3 + \nu) R_4^2 + (1 - \nu) R_s^2] \text{ at } r = R_s$$

Reference: *Formulas for Stress and Strain*, R.J. Roark, 4th Ed.

Method of determining increase of hub ID: Calculate the tangential (hoop) stress at the ID and the corresponding radial growth.

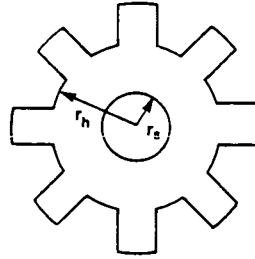
$$\omega^2 = (\text{angular speed})^2 \text{ in } (\text{rad/sec})^2$$

$$\omega^2 = \left(\frac{2\pi}{60 \text{ sec/min}} \times 5000 \text{ rev/min} \right)^2 = 2.74 \times 10^5 / \text{sec}^2$$

$$g = 386 \text{ in./sec}^2$$

$$\delta = \text{density} = 0.10 \text{ lb/in.}^3$$

$$\mu = \text{Poisson's ratio} = 0.33$$



$$S_t = \frac{0.10 \text{ lb/in.}^2 (2.74 \times 10^5 / \text{sec}^2)}{4(386 \text{ in./sec}^2)} [3.33(2.5 \text{ in.})^2 + 0.67(0.875 \text{ in.})^2]$$

$$S_t = 378 \text{ lb/in.}^2$$

$$\Delta D_{DYN} = \frac{S_t}{E_h} D_1 = \frac{378 \text{ lb/in.}^2}{10^7 \text{ lb/in.}^2} (1.75 \text{ in.})$$

$$\Delta D_{DYN} = 6.6 \times 10^{-5} \text{ in. (negligible)}$$

Differential expansion of hub to shaft

$$\Delta D_{TH} = D_1 \Delta \alpha \Delta T = 1.75 \text{ in.} [(23.2 - 11.5) \times 10^{-6} / ^\circ\text{C}] (100 ^\circ\text{C})$$

$$\Delta D_{TH} = 0.0020 \text{ in.}$$

$$\text{Minimum shrink fit} = i_t + \Delta D_{th}$$

$$= 0.00016 + 0.0020$$

$$= 0.00216$$

Applying a design margin of 2

$$\text{Shrink fit } 0.0043 \text{ in.}$$

$$\text{Specify: } i = 0.0043 \text{ to } 0.0045 \text{ in.}$$

Stress resulting from maximum shrink fit:

$$\text{Shaft: } S_c = 1.13 \left[\frac{0.0045}{0.00016} \right]$$

$$S_c = 31.8 \text{ ksi} < S_y$$

$$\text{Hub: } S_t = \frac{i}{\left(\frac{n}{E_3} + \frac{1}{E_4} \right) r_s}$$

$$S_t = \frac{0.0045 \text{ in.}}{\left[\frac{0.78}{2.8 \times 10^7} + \frac{1}{10^7} \right] 0.875 \text{ in.}}$$

$$S_t = 40.2 \text{ ksi} < S_y$$

A1.4 Differential Expansion of Hub to Magnets

If the magnets were preloaded against the aluminum by the rim, potentially large thermal stresses could be developed in the magnets, especially in the direction of magnetization where

$$\alpha_m = 4.6 \times 10^6 / ^\circ\text{C}$$

$$E_m = 23.9 \times 10^3 \text{ ksi}$$

$$S_a = 5 \text{ ksi}$$

Assuming that equal volumes of magnet and aluminum interact, the strain induced in each material is inversely proportional to the modulus of elasticity:

$$\epsilon_m = \Delta\alpha\Delta T \left(\frac{E_{AL}}{E_A + E_{AL}} \right), \text{ where}$$

$$\Delta\alpha = \alpha_{AL} - \alpha_{MAG} = (23.2 - 5.6) \times 10^{-6} / ^\circ\text{C}$$

$$\Delta\alpha = 17.6 \times 10^{-6} / ^\circ\text{C}$$

$$\Delta T = 100 ^\circ\text{C}$$

$$E_{AL} = 10^4 \text{ ksi}$$

$$\epsilon_m = 17.6 \times 10^{-6} / ^\circ\text{C} (10^2 ^\circ\text{C}) \left[\frac{10^4 \text{ ksi}}{(2.4 + 1) \times 10^4 \text{ ksi}} \right]$$

$$\epsilon_m = 5.2 \times 10^{-4} \text{ in./in.}$$

$$S_M = \epsilon_m E_M = 5.2 \times 10^{-4} (2.4 \times 10^4 \text{ ksi})$$

$$S_M = 12.5 \text{ ksi} > S_u$$

This potential failure mode has been eliminated by introducing a 0.020 in. (nominal) gap of relatively low stiffness, low strength material (epoxy) between each magnet and the magnet pockets in the hub. Hysol Adhesive EA934 was selected for its elevated temperature strength. Per Hysol:

<u>Temperature</u>	<u>Tensile Shear Strength</u>
24°C	3.1 ksi
101°C	1.5 ksi

A1.5 Rotor Rim

The rotor rim is a shrink fit on the hub. The rim material is the same as that of the hub (i.e., aluminum alloy 2024-T3) to eliminate thermal stresses associated with differing materials and provide a high strength-to-weight ratio. The rim is designed substantially thicker than that required to resist dynamic loads to reduce rim bending over the magnets which, in turn, could overstress the epoxy in compression. In addition to its own mass, the rim is assumed to support 100% of the magnet mass and the hub arms beyond a 3.5 in. radius (i.e., the tapered portions).

Reference: *Formulas for Stress and Strain*, R.J. Roark, 4th Ed.

$$\Sigma W_{\text{magnets}} = 17.2 \text{ lb}; R_{CG} = 3.5 \text{ in.}$$

$$\Sigma W_{\text{alum}} = 2.0 \text{ lb}; R_{CG} = 4.2 \text{ in.}$$

Rim stress due to magnets and arms:

$$F_{M,A} = \frac{w}{g} r \omega^2 = (W_m R_{CG} + W_A R_{CG}) \frac{\omega^2}{g}$$

$$\omega = 5000 \text{ rpm} = 524 \text{ rad/sec}$$

$$g = 386 \text{ in./sec}^2$$

$$F_{M,A} = [17.2 \text{ lb (3.5 in.)} + 2.0 \text{ lb (4.2 in.)}] \frac{(524 \text{ rad/sec})^2}{386 \text{ in./sec}^2}$$

$$F_{M,A} = 48,700 \text{ lb}$$

Inside area of rim:

$$A_I = \pi D_I L = \pi (9.09 \text{ in.})(2.06 \text{ in.})$$

$$A_I = 58.8 \text{ in.}^2$$

Equivalent average pressure on rim:

$$P_e = \frac{F_{M,A}}{A_I} = \frac{48.7 \times 10^3 \text{ lb}}{58.8 \text{ in.}} = 828 \text{ lb/in.}^2$$

For a thick-walled cylinder:

$$\max ST_{M,A} = P_e \left(\frac{R_o^2 + R_I^2}{R_o^2 - R_I^2} \right), \text{ at } R_I$$

$$R_o = \frac{\text{rim OD}}{2}$$

$$R_I = \frac{\text{rim ID}}{2} = \frac{9.08 \text{ in.}}{2} = 4.54 \text{ in.}$$

$$ST_{M,A} = 828 \text{ lb/in.}^2 \left[\frac{R_o^2 + (4.54 \text{ in.})^2}{R_o^2 - (4.54 \text{ in.})^2} \right]$$

Rim stress from rim mass:

For a disk with a central hole

$$\max S_{tR} = \frac{\delta \omega^2}{4g} [(3+U) R_o^2 + (1-U) R_I^2], A + R_I$$

$$\delta = \text{density of aluminum} = 0.10 \text{ lb/in.}^3$$

$$U = \text{Poisson's ratio} = 0.33$$

$$S_{tR} = \frac{0.10 \text{ lb/in.}^3 (524 \frac{\text{rad}}{\text{sec}})^2}{4(386 \text{ in./sec}^2)} [3.33 R_o^2 + 0.67 (4.54 \text{ in.})^2]$$

$$S_{tR} = 59.2 \text{ lb/in.}^2 [R_o^2 + 4.15]$$

Total tensile stress:

$$S_t = 828 \text{ lb/in.}^2 \left[\frac{R_o^2 + 20.61}{R_o^2 - 20.61} \right] + 59.2 \text{ lb/in.}^4 [R_o^2 + 4.15]$$

The rim stress relationship is also shown in Figure A-1 with rim OD = 10.50 in.

$$R_o^2 = (5.25 \text{ in.})^2 = 27.56 \text{ in.}^2$$

$$S_t = 5737 \text{ lb/in.}^2 + 1877 \text{ lb/in.}^2$$

$$S_t = 7.62 \text{ ksi}$$

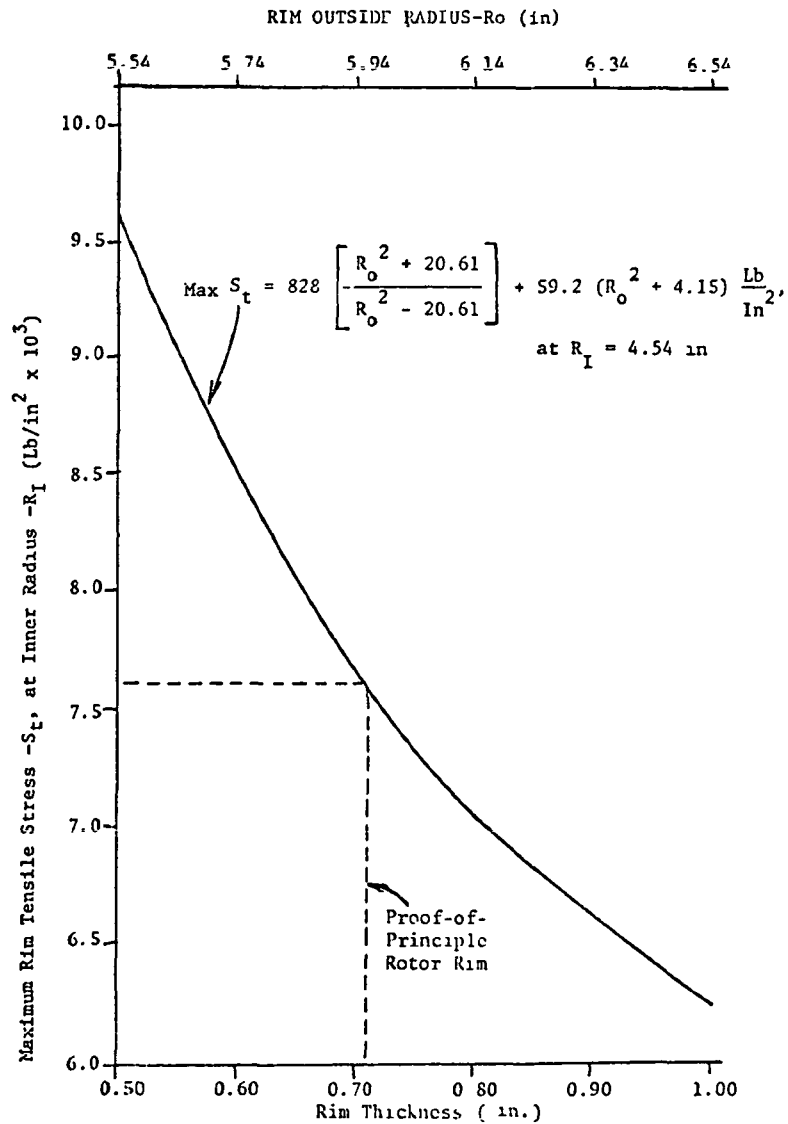


Figure A-1. Dynamic Tensile Stress in Aluminum Alloy Proof-of-Principle Rotor Rim Versus Rim Thickness at 5000 rpm

Increase of ID

$$\Delta ID = \frac{S_t}{E} \times ID = \frac{7.62 \text{ ksi}}{10^4 \text{ ksi}} \times 9.08 \text{ in.}$$

$$\Delta ID = 0.0067 \text{ in.}$$

Allowing a 50% safety margin for shrink fit of rim on hub

$$\text{interference} = 1.5 \times \Delta ID = 0.0104 \text{ in.}$$

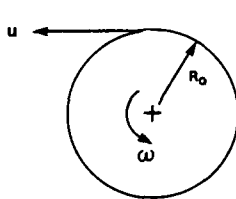
(specified shrink fit = 0.011 to 0.012)

Resulting max rim stress

$$\max S_{tR} = \frac{0.012 \text{ in.}}{0.0069 \text{ in.}} \times S_t = 1.74 (7.62 \text{ ksi})$$

$$\max S_{tR} = 13.3 \text{ ksi}$$

A2. ROTOR WINDAGE LOSS ESTIMATION



Reference: *Boundary Layer Theory*,
Schlichting, 4th Ed.,
pp. 547-5

$$U = R_o \omega$$

$$R_o = \frac{D_o}{2} = \frac{10.5 \text{ in.}}{2} = 5.25 \text{ in.} = 0.44 \text{ ft}$$

$$\omega = 5000 \text{ rpm} = 524 \text{ rad/sec}$$

$$\text{Reynolds number } (R_o) = \frac{u R_o}{J} = \frac{\omega R_o^2}{J}$$

Transition from laminar to turbulent flow occurs for $10^5 < R_c < 3 \times 10^5$

$$J = 0.25 \times 10^{-3} \text{ ft}^2/\text{sec}, \text{ at } T = 100^\circ \text{C}$$

$$R_e = \frac{524 \text{ rad/sec } (0.44 \text{ ft})^2}{0.25 \times 10^{-3} \text{ ft}^2/\text{sec}}$$

$$R_e = 4.06 \times 10^5 \text{ (turbulent)}$$

Drag moment

$$M = \frac{C P \omega^2 R^5}{g} R_e^{-2} \frac{C_M \rho \omega^2 R^5}{g}$$

For a rotor running in a housing with

$$\frac{\text{Clearance gaps}(S)}{\text{Rotor radius}(R_o)} < 0.1, \text{ drag coefficient is significantly less than}$$

for a "free" disk.

$$\frac{S}{R_o} = \frac{0.045}{5.25} = 0.009 < < 0.1$$

$$C_M = 0.0065 \text{ (Ref: Schlichting, Fig. 21.10)}$$

$$\rho = 0.06 \text{ lb/ft}^3, \text{ at } 100^\circ\text{C}$$

$$M = \frac{0.0065(0.06 \text{ lb/ft}^3)(524 \text{ rad/sec})^2(0.44 \text{ ft})^5}{32.2 \text{ ft/sec}^2}$$

$$M = 0.055 \text{ lb-ft}$$

Power dissipated by drag:

$$P = M\omega = 0.055 \text{ lb-ft} (524 \text{ rad/sec}) (1.356 \frac{\text{watt}}{\text{lb-ft/sec}})$$

$$P = 39.0 \text{ watt at } 100^\circ\text{C}$$

Drag will be approximately 15% greater at 40°C primarily due to higher density of air.

Appendix B

PERFORMANCE REQUIREMENTS

Appendix B

PERFORMANCE REQUIREMENTS

B1. THE COMPONENTS OF ROAD RESISTANCE

The components of road resistance are those that oppose the motion of the vehicle. These are:

1. Aerodynamic drag F_a
2. Rolling resistance F_r
3. Force of acceleration (inertia effect) F_i
4. Gravitation effects of a grade F_g

The total resistive force is the sum of the components just listed (they are treated in detail in subsequent sections).

$$F_t = F_a + F_r + F_i + F_g$$

The separate forces are distributed, in different ways, between all wheels and the road. The total force F_t appears at the drive axle and at a radius r (the rolling radius) to form the axle torque

$$T_t = F_t r$$

The wheel rpm is related to the vehicle speed V in mph by

$$n \text{ (wheel rpm)} = 14 V/r$$

where r is the rolling radius in feet.

Consequently, the axle horsepower required to balance "road resistance" is expressed by

$$P_t = T_t n / 5252 \text{ hp}$$

$$= F_t r (14 V/r) / 5252$$

$$= F_t V / 375 \text{ hp}$$

where F_t = total road resistance in pounds

V = vehicle speed mph

B1.1 Aerodynamic Drag

The aerodynamic drag is given by the empirical equation

$$F_a = 2.151 K_a A D V^2 \text{ lb}$$

where A = frontal area (ft^2) = 20 ft^2

D = drag coefficient (dimensionless) = 0.3

V = velocity of vehicle (mph) relative to wind velocity

$$K_a = p/2g$$

K_a for air at standard conditions is

$$K_a = 0.077/2 \times 32.2 = 0.0012.$$

Using this value and assuming the wind velocity is zero so that V becomes the velocity relative to the road,

$$F_a = 0.0026 ADV^2 \text{ lb}$$

B1.2 Rolling Resistance

The rolling resistance is taken to be proportional to the vehicle weight

$$F_r = K_r W \text{ lb}$$

where, from the contract,

$$K_r = 0.008 \text{ (dimensionless)}$$

W = weight of vehicle including passengers
in pounds

B1.3 Gravitation Effects of a Grade

The potential energy of a vehicle that has been raised a distance h is

$$U_p = mgh$$

The power associated with this energy is $P_g = dU_p/dt$ or

$$P_g = mg \frac{dh}{dt}$$

If the vehicle is traveling on an incline of angle θ and with velocity V , then $dh/dt = V \sin \theta$ so that

$$P_g = mgV \sin \theta = WV \sin \theta.$$

Usually the incline is expressed as a grade "gr" or slope defined as $gr = h/x$. The equation, just derived, can be expressed in terms of $gr = \text{grade (fraction)}$ as

$$\begin{aligned} P_g &= WV \sin \theta \\ &= WV h/z \\ &= WV \frac{h/x}{\sqrt{1 + (h/x)^2}} \\ &= WV \frac{gr}{\sqrt{1 + gr^2}} \end{aligned}$$

It should be noted that if the vehicle is accelerating on an incline, or anywhere for that matter, presumably the rotating parts also are accelerating and, hence, W' should be used instead of W . The force along the grade is

$$F_g = W(gr/\sqrt{1 + gr^2})$$

and if W is in pounds, F_g is in pounds.

B1.4 Acceleration

The vehicle as a whole consists of masses that are in translation and rotation. Those parts that are rotating are also being carried along in translation. Let m equal the entire vehicle mass and J_n the moment of inertia of part “ n ” that is rotating.

The kinetic energy is:

$$\begin{aligned} K_e &= (1/2) mV^2 + (1/2) \sum_n J_n \omega_n^2 \\ &= (1/2) mV^2 [1 + \sum_n J_n \omega_n^2 / mV^2] \\ &= (1/2) m' V^2 \end{aligned}$$

where m' is the equivalent vehicle mass including the effect of rotating parts. The power of acceleration is $P_i = dk_e/dt$ or

$$P_i = m' V \frac{dV}{dt} = m' Va$$

where a is the acceleration. The force of acceleration is

$$\begin{aligned} F_i &= m'a \\ &= \frac{w'}{g} a \end{aligned}$$

If the acceleration “ a ” is given in (say) mph/sec, then g should be converted to mph/sec. Values for the gravitational constant are

$$\begin{aligned} g &= 32.2 \text{ (ft/sec)/sec} \\ &= 21.95 \text{ (mph)/sec} \end{aligned}$$

and, therefore

$$F_i = W'a/g = W'a/21.95 = 0.0456 W'a \text{ lb}$$

where

$$a = \text{mph/sec}$$

The power, in the dimension horsepower, is

$$P_i = F_i V / 375$$

where

$$V = \int_{t_1}^{t_2} a \, dt$$

Two special cases emerge at this point: acceleration requirement for constant torque and for constant power. For simplicity, the acceleration to some speed V , will ignore, for the moment, the forces of windage and rolling resistance. The equation for F_i is repeated

$$F_i = 0.0456 W'a . \tag{1}$$

It is seen that F_i will be constant if $a = \text{constant}$. Similarly, the power is

$$P_t = F_t V / 375 \quad (2)$$

Note that a condition of constant power at very low speeds will result in prohibitively large acceleration forces F_t . Consequently, it is better to begin the acceleration process using a constant torque up to some reasonable velocity V_1 at Power P_1 and proceed thereafter with a constant power P_1 to the final velocity V .

Equations (1) and (2) are combined to obtain

$$375 P_t = 0.0456 W' V \frac{dv}{dt} \quad (3)$$

P_t is held constant at P_1 between velocities $V_1 = a_1 t_1$ and the final velocity V ; equation (3) becomes

$$375 P_1 \int_{t_1}^t dt = 0.0456 W' \int_{V_1}^V V dV$$

and, hence, the velocity V is found from

$$V^2 = \frac{2 \times 375 P_1}{0.0456 W'} (t - t_1) + V_1^2 \quad (4)$$

B1.5 Total Force, Torque, and Power at Wheels

The general expression for total force at the wheels when $A = 20 \text{ ft}^2$, $D = 0.3$, $K_r = 0.008$, $g = 21.95 \text{ mph/sec}$ is

$$\begin{aligned} F_t &= F_a + F_r + F_i + F_g \text{ lb} \\ &= 0.0156 V^2 + 0.008 W + 0.0456 W' a + W g r \sqrt{1 + g r^2} \end{aligned} \quad (5)$$

The torque is

$$T_t = F_t r \text{ lb-ft}$$

and the power is

$$P_t = F_t V / 375 \text{ hp}$$

where $V =$ vehicle speed in mph.

B1.6 Motor Torque: Relation to Tractive Effort

The motor torque and tractive effort are related by the system of equations

$$T_t = F_t r$$

$$P_t = F_t V / 375$$

$$P_s = P_t / \eta$$

$$n \text{ (wheel)} = 14 V / r$$

$$n \text{ (motor)} = R n \text{ (wheel)}$$

$$T \text{ (motor)} = 5252 P_s / n \text{ (motor)}$$

which obtains for the motor torque in lb-ft

$$T \text{ (motor)} = F_t r / \eta R$$

where

F_t = tractive effort, lb

r = rolling radius, ft

η = gear train efficiency

R gear ratio

B2. SPECIFIC EVALUATION

The vehicle characteristics and the specifications listed in the Contract were summarized in Section 4.1. From this data, the motor output power and the wheel torque is deduced for three cases:

- a) Cruise, level at 55 mph, continuous
- b) Operation on a 10% Grade, 35 mph for five minutes
- c) Acceleration on the J227a-D cycle

The first case determines the power required during cruise at 55 mph; this power is about 15 hp. The second case determines the power on a 10% grade at 35 mph; this power is about 40 hp. The third case, acceleration during the J227a-D cycle falls between the cruise power and 10% grade power. Hence the 10% grade power is the largest power in this application.

B2.1 Cruise, Level at 55 mph

The force at the wheels during level cruising with no acceleration ($F_t = F_g = 0$) is

$$\begin{aligned} F_t &= F_a + F_r \\ &= 0.0026 ADV^2 + K_r W \end{aligned}$$

where for this vehicle

$$A = 20 \text{ ft}^2$$

$$D = 0.3$$

$$K_r = 0.008$$

$$W = 3000 \text{ lb}$$

and hence at any vehicle speed

$$F_t = 0.0156 V^2 + 24$$

and for $V = 55$

$$F_t = 47.2 + 24$$

$$= 71.2 \text{ lb}$$

The wheel torque is

$$T_t = F_t \times r = 71.2 \times 0.96 = 68.3 \text{ lb-ft}$$

The horsepower at the wheel is

$$P_t = F_t V / 375 = 10.4 \text{ hp}$$

Assuming an efficiency between wheel and motor to be 0.80 (all bearings, gears, and miscellaneous parts) the motor output power is

$$P_s = 10.4 / 0.80 = 13.0 \text{ hp (Use 15 hp)}$$

B2.2 Operation on a 10% Grade, 35 mph for 5 minutes

Since there is no acceleration ($F_t = 0$), the force at the wheel is

$$\begin{aligned} F_t &= F_a + F_r + F_g \\ &= 0.0156 V^2 + 24 + W (gr / \sqrt{1 + gr^2}) \end{aligned}$$

and since $gr = 0.10$ and $W = 3000$

$$\begin{aligned} F_t &= 0.0156 V^2 + 24 + 298.5 \\ &= 0.0156 V^2 + 322.5 \\ &= 342 \text{ lb} \end{aligned}$$

The wheel torque is

$$T_t = F_t r = 328 \text{ lb-ft}$$

and the wheel power is

$$P_t = F_t V / 375 = 31.9 \text{ hp}$$

The power output at the motor shaft using an efficiency of 0.80 is

$$P_s = 31.9 / 0.80 = 40 \text{ hp}$$

B2.3 Acceleration

The acceleration occurs on a level road ($F_g = 0$); hence the force at the wheel is

$$\begin{aligned} F_t &= F_a + F_r + F_i \\ &= 0.0156 V^2 + 24 + 0.0456 W' a \end{aligned}$$

The weight $W' = 1.1 W = 3300 \text{ lb}$, hence

$$F_t = 0.0156 V^2 + 24 + 150.5 a \quad (6)$$

where a is the acceleration in mph/sec. At this point, it is not clear whether a should be constant or variable with respect to time. The specification requires only that the vehicle proceed from 0 to 45 mph in 28 seconds. This subject is treated in Section 4.4.

B2.4 Summary

Cruising Rating

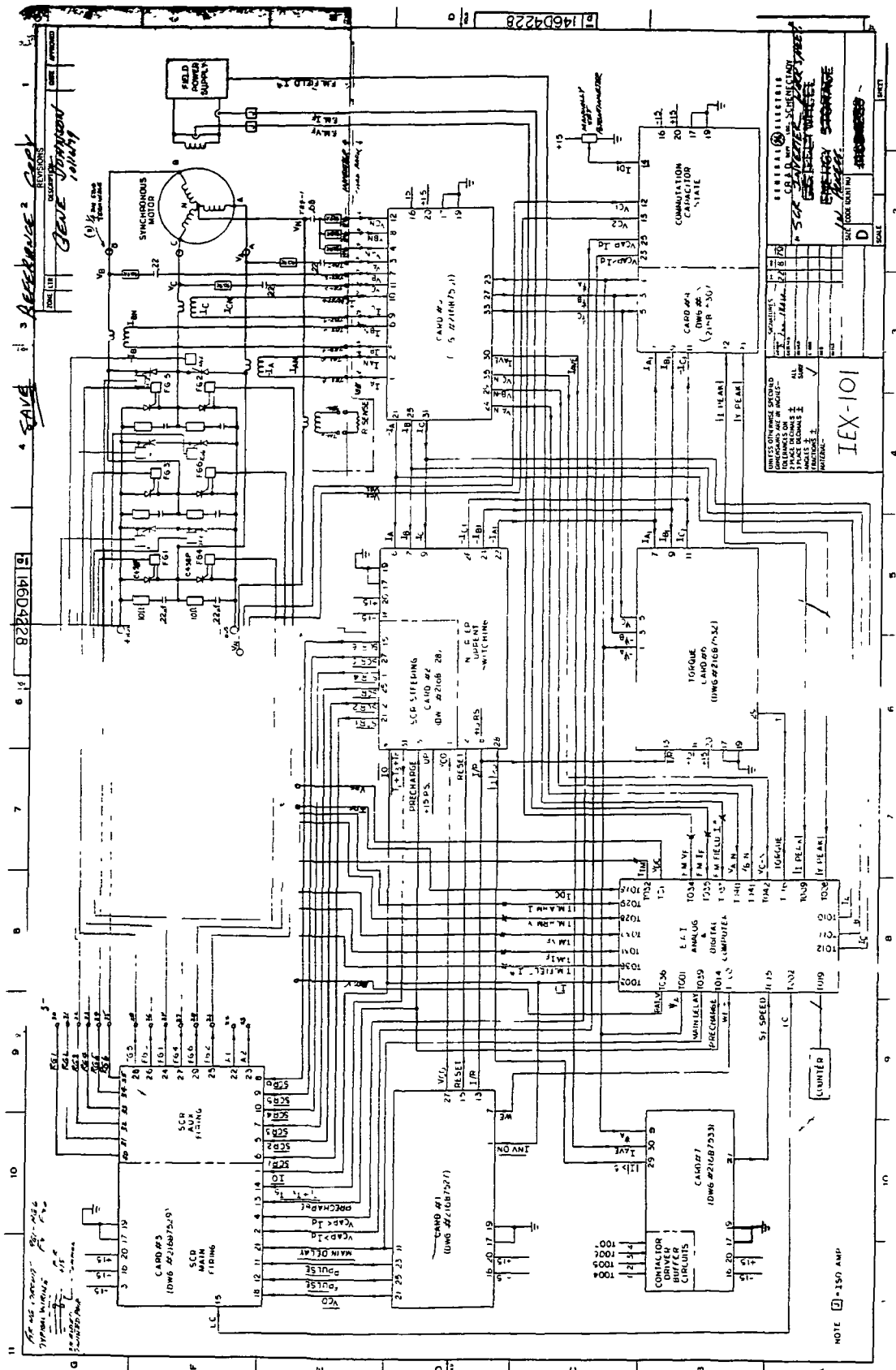
Motor hp	15.0
Vehicle Speed, mph	55
Wheel rpm	802
Gear Ratio <i>R</i>	13.7
Motor rpm	10,987
Tractive Effort, lb	82
Motor Torque, lb-ft	7.2

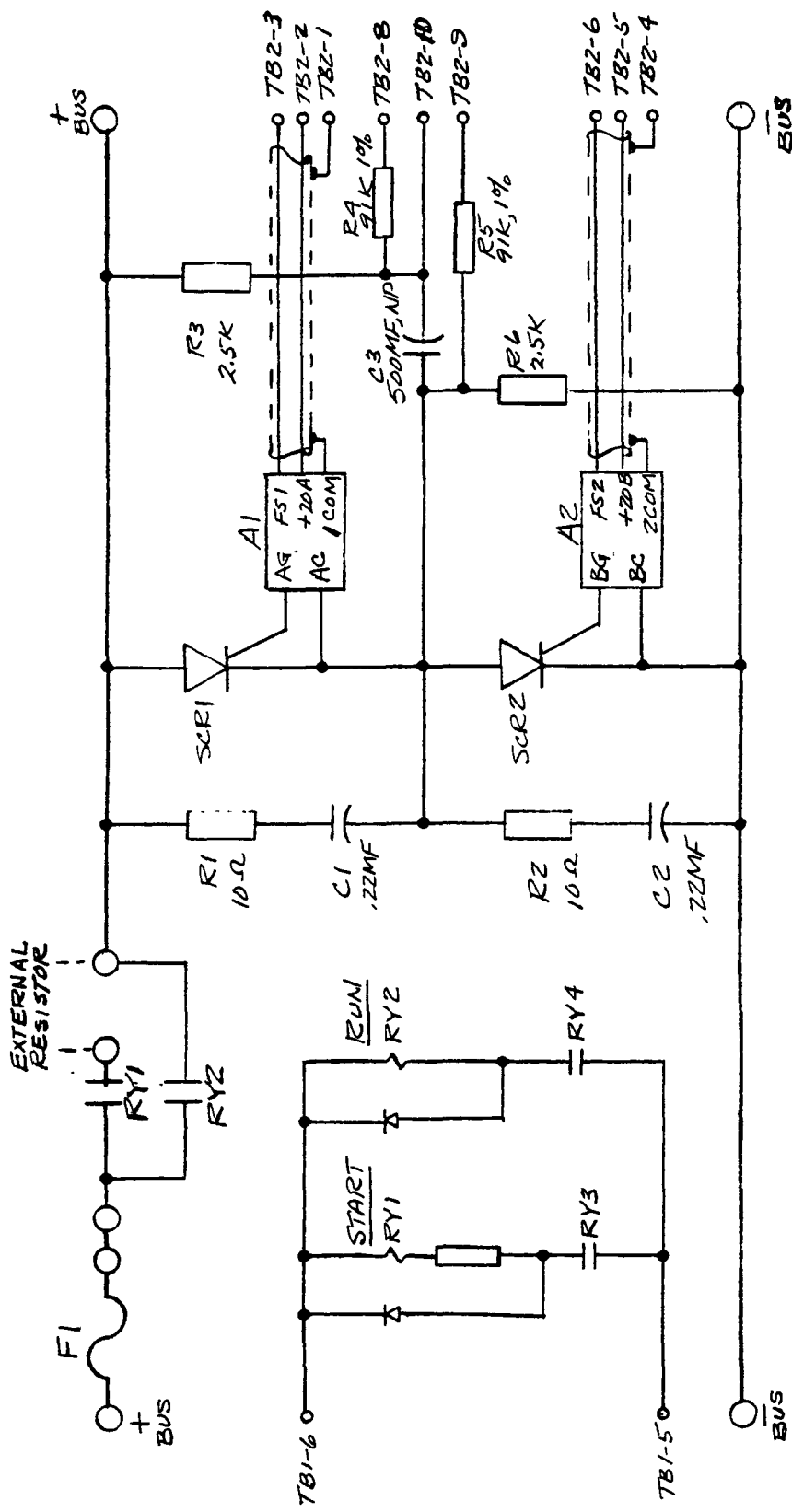
Short-Time Rating: 5 Minutes on a 10% Grade at 35 mph

Motor hp	40.0 (267%)
Vehicle speed, mph	35
Motor rpm	6992
Tractive Effort, lb	342
Time (min)	5
Motor Torque lb-ft	30.0 (417%)

Appendix C
CONTROL SYSTEM SCHEMATICS

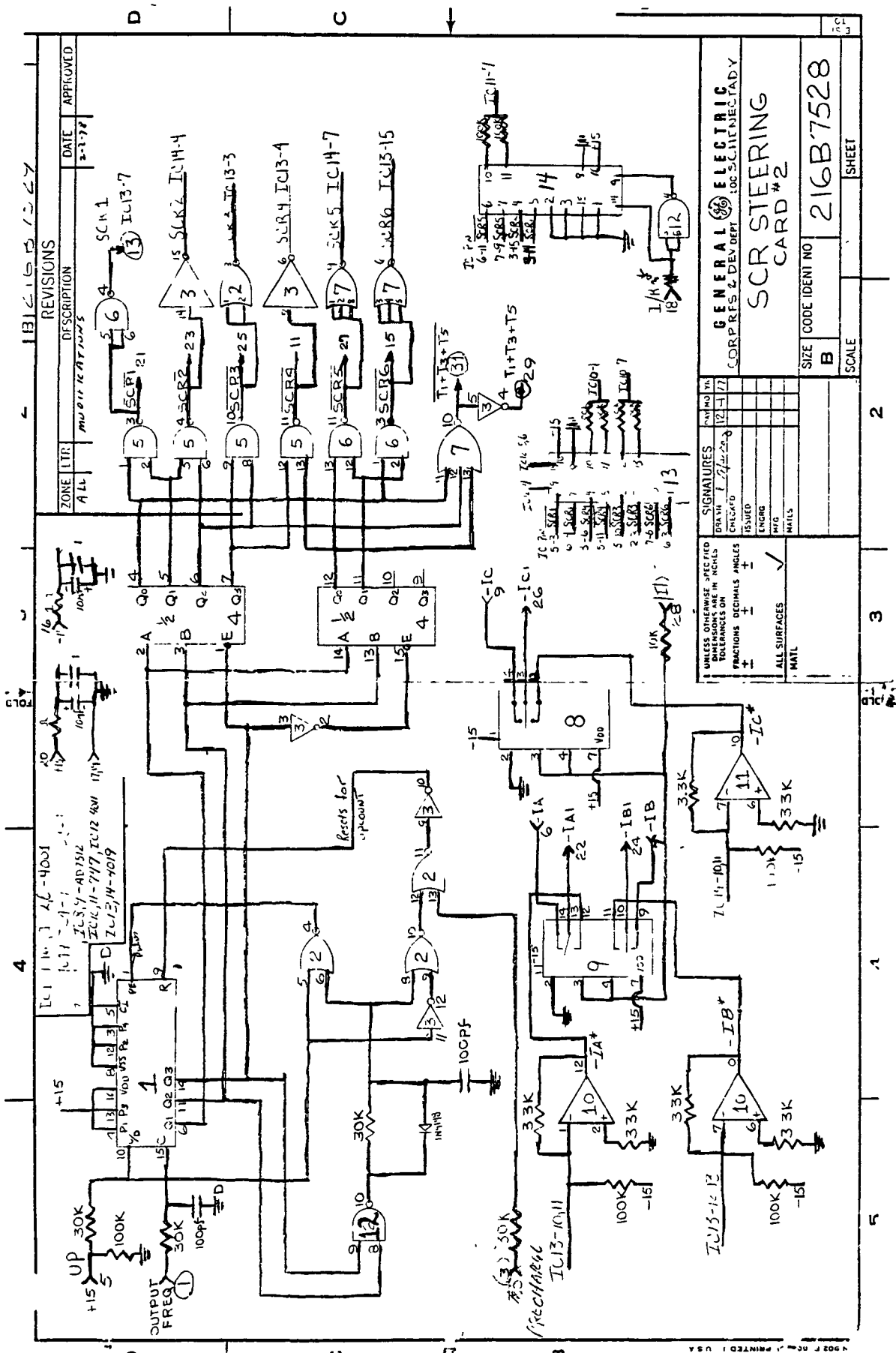
CONTROL SYSTEM SCHEMATICS

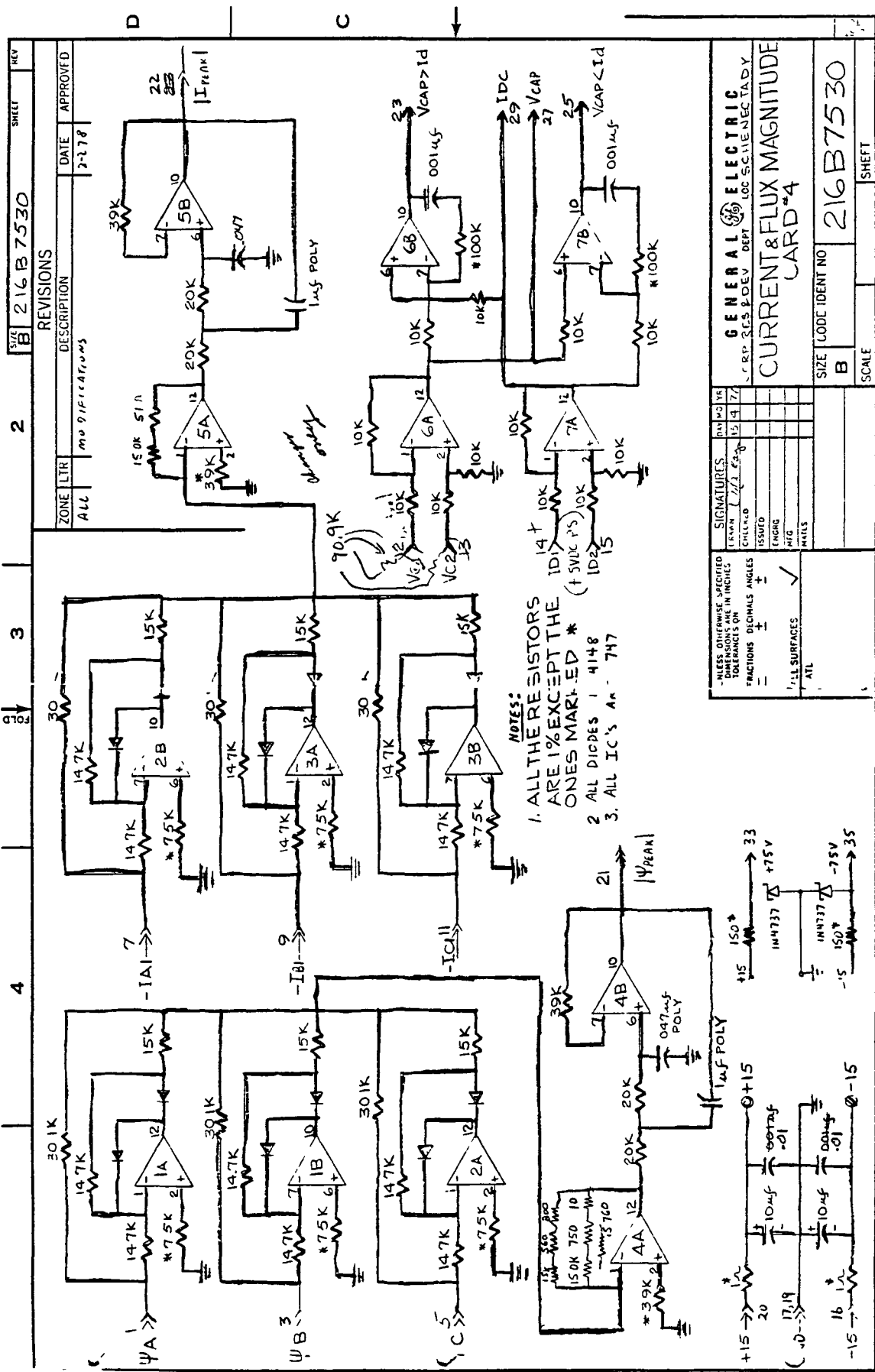




NOTE - AI, A2
PULSE TRANSFORMER CARD
GE TYPE 193X186ABG01

1EX-102
SWITCHING & COMMUTATOR
SCHEMATIC
FMF SCR CONTROLLER
E. L. JOHNSON
10/10/79



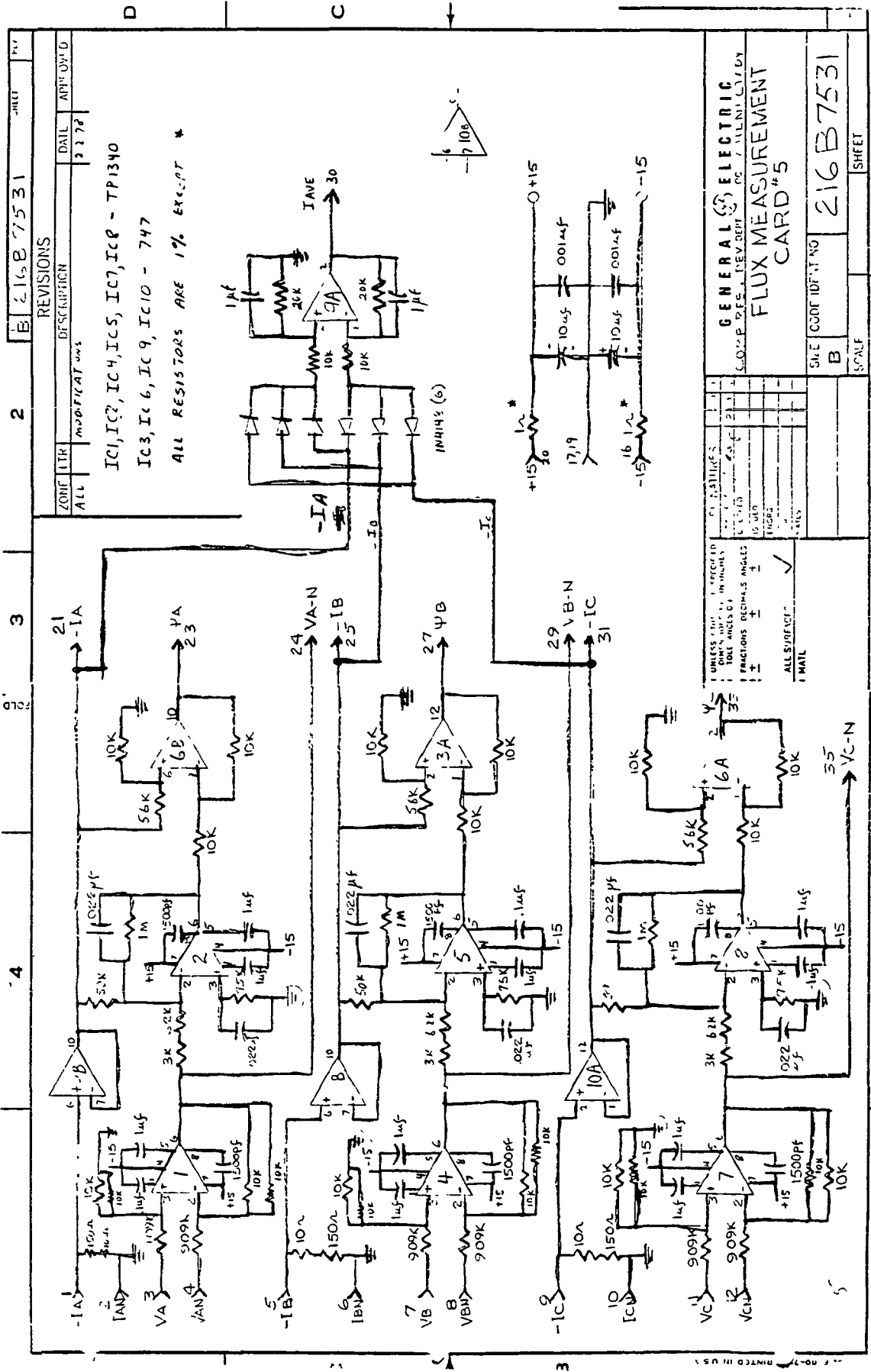


REV	DATE	APPROVED
1	2-2-78	
2		

ZONE	DESCRIPTION
ALL	MODIFICATIONS

GENERAL ELECTRIC CORP. 216 B7530 DEPT. LOC. SCH. ELECT. ADY	
CURRENT & FLUX MAGNITUDE CARD #4	
SIZE: B CODE IDENT NO: 216B7530	SCALE: SHEET:

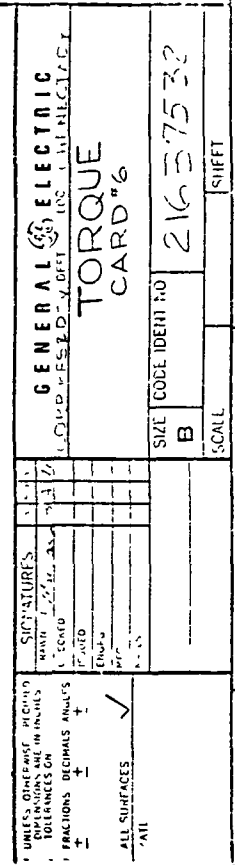
SIGNATURES	DATE	INITIALS
DESIGNED	12/2/77	12/2/77
CHECKED		
ISSUED		
ENG'G		
MTG		
FILE		



REVISIONS		DATE	APPROVED
ZONE	DESCRIPTION		
ALL	MODIFICATIONS	3 3 78	

IC1, IC2, IC4, IC5, IC7, IC8 - TP1340
 IC3, IC6, IC9, IC10 - 747
 ALL RESISTORS ARE 1% EXCEPT *

GENERAL ELECTRIC	
FLUX MEASUREMENT	
CARD #5	
SHEET	216B7531



Appendix D

MAJOR ASSEMBLY DRAWINGS

MAJOR ASSEMBLY DRAWINGS



GENERAL ELECTRIC

PARTS LIST FOR

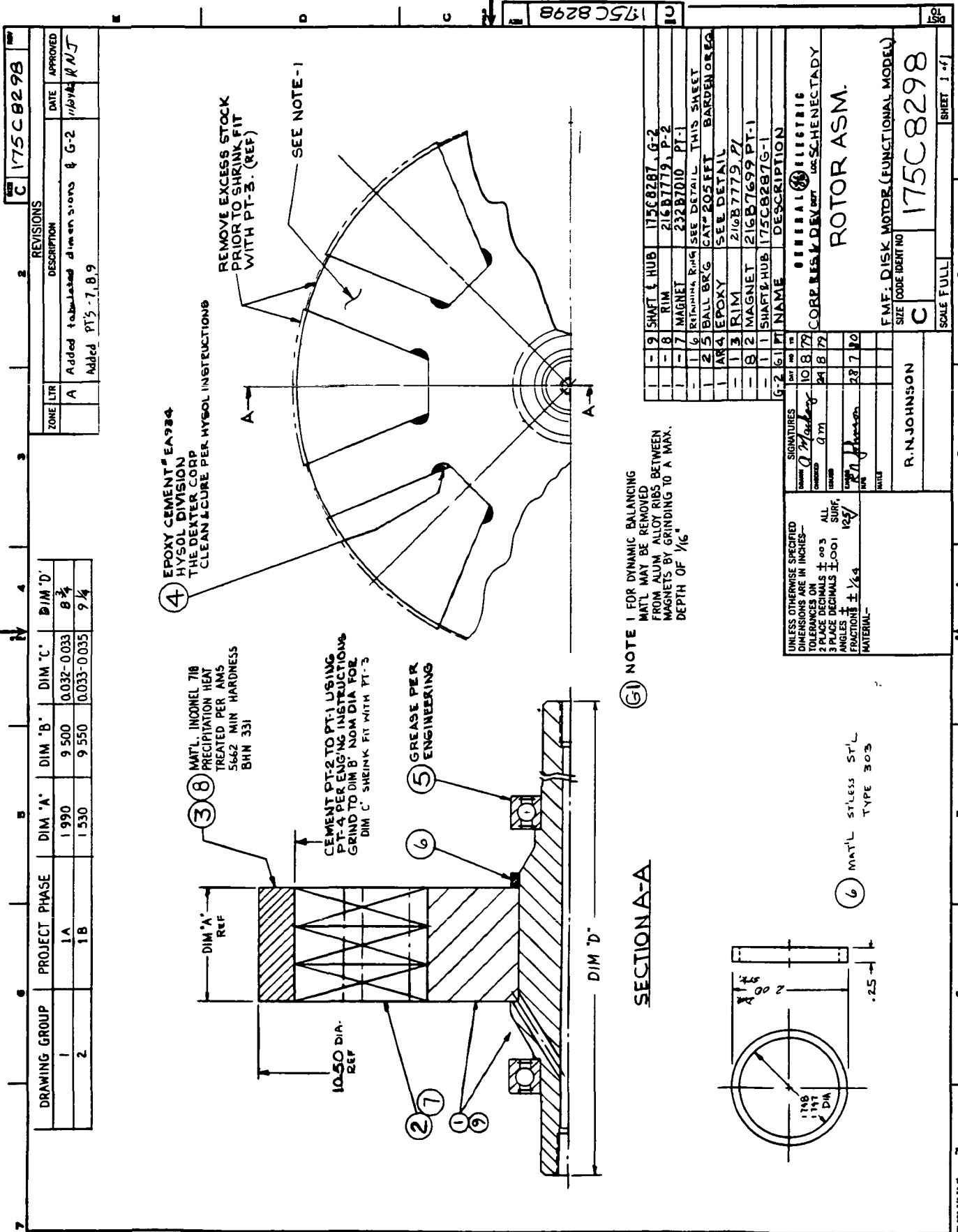
146D4277

CONT ON SHEET —

SH NO 1

[illegible]

FF-804-F 3-72
PRINTED IN U.S.A.



1 Report No NASA CR 167975	2 Government Accession No	3 Recipient's Catalog No	
4 Title and Subtitle ADVANCED AC PERMANENT MAGNET AXIAL FLUX DISC MOTOR FOR ELECTRIC PASSENGER VEHICLE		5 Report Date October 1982	
		6 Performing Organization Code	
7 Author(s) G B Kliman		8 Performing Organization Report No SRD-81-097	
		10 Work Unit No	
9 Performing Organization Name and Address General Electric Company, Corporate Research and Development Schenectady, New York		11 Contract or Grant No DEN 3-76	
		13 Type of Report and Period Covered Contractor Report	
12 Sponsoring Agency Name and Address National Aeronautics and Space Administration Washington, D C 20546		14 Sponsoring Agency Code DOE/NASA 0076-82/1	
15 Supplementary Notes Project Manager, B R Hatvani, NASA Lewis Research Center, Cleveland, Ohio Final Report Report Prepared Under Interagency Agreement DE-A101-77CS51044			
16 Abstract An ac permanent magnet axial flux disc motor was developed to operate with a thyristor load-commutated inverter as part of an electric vehicle drive system. The motor was required to deliver 29.8 kW (40 hp) peak and 10.4 kW (14 hp) average with a maximum speed of 11,000 rpm. It was also required to run at leading power factor to commutate the inverter. Three motors were built in the program. The final version exceeded the performance requirements. It had a peak efficiency (on inverter drive) of 93%, and was tested up to the limit of the experimental facilities. Straightforward proposed revisions of the design were estimated to yield an efficiency of 95% or more.			
17 Key Words (Suggested by Author(s)) synchronous motor permanent magnet ac motor ac disc motor load-commutated inverter electric vehicle		18 Distribution Statement Unclassified — unlimited STAR Category 33 DOE Category UC- 96	
19 Security Classif (of this report)	20 Security Classif (of this page) Unclassified	21 No of Pages 226	22 Price*

For sale by the National Technical Information Service, Springfield, Virginia 22161